ISSN 0915-6348

NATIONAL INSTITUTE FOR FUSION SCIENCE

X-ray Radiation from Hot Dense Plasmas and Atomic Processes

(Received – Oct. 7, 1991)

NIFS-PROC-9 Oct. 1991

RESEARCH REPORT
NIFS-PROC Series

NAGOYA, JAPAN

X-ray Radiation from Hot Dense Plasmas and Atomic Processes

Key words;
radiation process, atomic processes, multiply ionized ions, hot dense plasmas, laser plasmas, astrophysical plasmas, magnetic confiment plasmas,

Preface

In laser, space, astrophysical and magnetic fusion plasmas, radiation energy transport has been recognized to be crucial for space-time evolutions of the plasmas. The analysis of the radiation spectrum is also important for plasma diagnostics. In order to understand the radiation processes in hot dense plasmas, we have to investigate atomic processes which include multiply ionized atoms and to accumulate radiation and atomic data which can be used in plasma hydrodynamic simulations and experimental data analysis.

From 1978 to 1989, several workshops on radiation and atomic processes were held by the supports of Grand-in-Aid for Scientific Researches by Monbusho and Institute of Plasma Physics, at Nagoya University. This meeting (July 1st ~ 2nd, 1991 at NIFS, Nagoya) was held as a joint research program of National Institute for Fusion Science (NIFS). One of the main subjects of this meeting is to review the recent progress of researches on radiation and atomic processes in fusion, space and astrophysical plasmas. Another important subject is organizing a few workshops for numerical models which describe atomic processes, radiation hydrodynamics in fusion, x-ray laser and astrophysical plasmas, and so on. More than 40 scientists participated in presentations and discussions. Presented were the papers on radiation and atomic processes in laser implosion and laser x-ray plasmas, radiation transport in binary stars and tokamak edge plasmas, equation of state of high density plasmas, atomic structure and transition rate of high Z ions, numerical models for rate equation and so on.

In the summary session, critical issues in the atomic and radiation plasma physics and organization of workshops were discussed.

Finally, we thank all participants for very interesting presentations and fruitful discussions.

August, 1991
K. Mima
Y. Kato
ILE, Osaka University

PROGRAM

X-ray Radiation from Hot-Dense Plasmas and Atomic Processes

Date : July 1 (Monday) - July 2 (Tuesday), 1991
Place : National Institute for Fusion Science
Conference Room on the 8th Floor

July 1 (Monday)

Opening

Chairperson : S. Kawata

Lunch

Chairperson : H.Yoneda

Coffee Break

Lunch

Chairperson : T. Kato

LIST OF PARTICIPANTS

Toshihisa Tomie	Electotechnical Laboratory
Eisuke Miura	Electotechnical Laboratory
Michiya Shimada	Japan Atomic Energy Research Institute
Toshio Hirayama	Japan Atomic Energy Research Institute
Kazuhiro Sakimoto	Institute of Space and Astronautical Science
Fumihiro Koike	School of Medicine, Kitasato University
Takayuki Aoki	The Graduate School at Nagatsuta, Tokyo Institute of Technology
Koichi Kasuya	The Graduate School at Nagatsuta, Tokyo Institute of Technology
Akira Sasaki	Institute for Laser Science, University of Electro-Communications
Hitoki Yoneda	Institute for Laser Science, University of Electro-Communications
Kenichi Ueda	Institute for Laser Science, University of Electro-Communications
Tomoharu Suzuki	Faculty of Science, University of Tokyo
Tsuneyuki Ozaki	The Institute for Solid State Physics, University of Tokyo
Masayuki Katsuragawa	The Institute for Solid State Physics, University of Tokyo
Norio Aitani	The Institute for Solid State Physics, University of Tokyo
Harald Bolt	Nuclear Engineering Research Laboratory, University of Tokyo
Shigeo Kawata	Department of Electrical Engineering, Nagaoka University of Technology
Keiji Sawada	Department of Engineering Science, Kyoto University
Tetsuya Kawachi	Department of Engineering Science, Kyoto University
Takashi Kagawa	Department of Physics, Nara Women's University
Noboru Tanizuka	University of Osaka Prefecture

Yoshiaki Kato	Institute of Laser Engineering, Osaka University
Kunioki Mima	Institute of Laser Engineering, Osaka University
Katsunobu Nishihara	Institute of Laser Engineering, Osaka University
Hideaki Takabe	Institute of Laser Engineering, Osaka University
Shinji Nakamura	Institute of Laser Engineering, Osaka University
Takeshi Nishikawa	Institute of Laser Engineering, Osaka University
Takashi Inoue	Institute of Laser Engineering, Osaka University
Susumu Kato	Institute of Laser Engineering, Osaka University
Hiroyuki Furukawa	Institute of Laser Engineering, Osaka University
Kensuke Murai	Institute of Laser Engineering, Osaka University
Gang Yuan	Institute of Laser Engineering, Osaka University
Guan-ming Zeng	Institute of Laser Engineering, Osaka University
Akio Nishiguchi	Institute for Laser Technology, Osaka University
Kazumi Fujima	Faculty of Engineering, Yamanashi University
Sumio Kogoshi	Science University of Tokyo
Kozo Ando	The Institute of Physical and Chemical Research
Tamio Hara	The Institute of Physical and Chemical Research
Hideo Hirose	The Institute of Physical and Chemical Research
Tomoyuki Hanawa	Department of Astrophysics, Nagoya University
Takako Kato	National Institute for Fusion Science
Kuniaki Masai	National Institute for Fusion Science
Mario Ueda	National Institute for Fusion Science
Takaichi Kawamura	National Institute for Fusion Science

Statistical Approach for Calculating Opacities of Partially Ionized High-Z Plasmas

H. Takabe, T. Nishikawa, and K. Mima

Institute of Laser Engineering
Osaka University
Suita, 565 JAPAN

Abstract

A statistical method to evaluate the opacity of hot, high-Z plasmas is considered by taking account of line group steming from the same transitions in different charge states. Structure of the line group is described and used to model effective line profiles in numerically treating radiation transport in fluid codes. Dispersion of line spread is obtained by statistical method with the use of the averaged electron configuration of ions. The validity of the method is studied by reducing the Saha equilibrium relation in local thermodynamic equilibrium limit.

I. Introduction

When an intense laser light is irradiated on a medium- or high-Z material, substantial fraction of the absorbed laser energy is converted into soft x-rays of < 1 keV. Since the x-rays can be applicable, for example, to drive an implosion of fusion capsule target, fundamental studies on such as x-ray conversion efficiency, penetration (transport), and spectra have been carried out experimentally and numerically[1, 2]. Most of the x-ray stems from line radiation and, therefore, atomic modeling of partially ionized plasma has been regarded as a key element especially in numerically simulating the phenomena.

In modeling opacity and emissivity of line radiation of partially ionized high-Z (e.g., gold) plasmas, important elements are

(1) Evaluation of line positions and oscillator strength for given electron configuration

(2) Evaluation of statistical distribution of electron configuration. Some non LTE model is required to be solved.

(3) Modeling of line groups to evaluate spectral opacities and emissivities.

Since huge number of electron configurations must be considered in case of high-Z plasma, we have used a simplified atomic model like average atom model (AAM) [3]. Combining AAM with the screened hydrogenic model (SHM) [3], the line positioning can be done. Then, a difficulty appears especially in solving line radiation transport [4]. AAM can provide the information about the averaged line position. However, it does not directly give information about the dispersion (spread) of the lines corresponding to the same transition such as 5d-4p. Because many of ions in different charge states co-exist at the same place, the line radiation due to the same transition consists of line group with shifted line centers. In order to include all configurations, the detailed configuration accounting (DCA) [5] is solved. However, it is time consuming calculation and more simplified model like hybrid atom model (HAM) [4] has been proposed.

In the present note, we propose a more simplified model to evaluate the detail electron configuration based on AAM and consider how to model the line group profile in installing the line opacities in a fluid code.

II. Structure of Line Group

In dealing with dynamical phenomena where hydrodynamics and radiation transport strongly couple each other, hydrodynamic simulation is itself time consuming calculation and , therefore, some simplification is required to model material opacities. When a laser pulse at intensity of $\sim 10^{14}$ W/cm^2 is irradiated on a gold foil, most of the x-rays are generated in the region with the temperature

of 100 ~ 300 eV. Then, most probable ions have electron configurations in which K, L, and M shells are fully occupied and N-shell is partially occupied. Most of x-rays are generated by single-electron-excited configuration and so-called N-band and O-band emissions form the emitted x-ray spectral profile.

A simple hydrogenic model has been used to model atomic structures. In this model, electronic state is characterized only by the principal quantum number n. With this model and AAM, line emissions are given as shown in Fig. 1-(a), where 5-4, for example, represents the transition from n=5 to n=4. In this case, gold plasma at temperature of ~ 200 eV shows the O-band emission around $h\nu$ = 200 ~ 300 eV and the N-band emission around $h\nu$ = 700 ~ 800 eV. It is obvious, however, that in such partially ionized high-Z plasmas substantial energy split appears due to the difference of the orbital quantum number l (so-called l-splitting) [6]. By including the l-splitting effect, the single line of 5-4 transition [Fig. 1-(a)] is found to consist of significant lines 5g-4f, 5f-4d, and 5d-4p with energy separation of ~ 400 eV [6]. In addition, inner shell transition ($\Delta n = 0$ transition) appears to be important and it is pointed out in Ref. [6] that the x-ray spectra near $h\nu \approx 250$ eV are mainly contributed by 4f-4d and 4d-4p. Such l-splitting effect is schematically shown in Fig. 1-(b).

The average atom model gives only one line to a given transition. However, the plasma consists of ions in different charge states, and for example the line 5f-4d consists of many lines as shown in Fig. 1-(c). This is symbolically shown as $5f4d^k \rightarrow 4d^{k+1}$ (k = 0-10), and the line group has an effective width of 50 -100 eV [6].

The transition energy is also affected by the spin-orbit interaction. The one line of Fig. 1-(c) has micro structure made by many of lines due to **L-S** coupling. This situation can easily understood as an analogy of the line group seen in emission spectra from the rare earths of the lanthanides [7]. Theoretical energy levels of configurations $4f^w 6s^2$ of neutral lanthanide atoms, relative to the center-of-gravity energy E_{av}, are shown in Fig. 2 [Fig. 20-2 of Ref. 7]. When a shell 4f is partially filled, there are many combination of electron spins and many levels are seen. The same sort of energy levels are seen in partially ionized gold ions with partially filled N-shell. Therefore, a single line of Fig. 1-(c) in general consists of many lines as shown in Fig. 1-(d).

Finally, each line of Fig. 1-(d) has a line profile determined by natural broadening and another broadenings due to thermal fluctuations as shown in Fig. 1-(e). Strictly speaking, such hierarchy of line structure should be included in evaluating material opacities. However, it is unrealistic and we need to approximate the line group based on such structure.

Tsakiris and Eidmann [8] proposed to use an artificial line width $\Delta h\nu$ as an adjustable parameter to obtain reasonable opacities from the simplest model of Fig. 1-(a). They have compared material opacities (Rosseland and Planck mean opacities) at LTE derived from the model (a) of Fig. 1 with the tabulated ones given in SESAME table [9]. For the case of Eu (Z = 63), they concluded that

if they impose $\Delta h\nu = 100$ eV to all lines, the material mean opacities can well reproduced in a wide range of density and temperature. However, they do not show physical reason why 100 eV is required. This can be considered to be due to the *l*-splitting effect and the spread of line group by difference in charge state shown in Fig. 1-(b) and (c). Then, it is reasonable that the artificial line width decreases as nuclear charge decreases as pointed out in Ref. [8].

It is also noted that the simple model of Ref. 8 can be well applicable in radiation-hydrodynamic codes to reproduce x-ray conversion rate when an intense laser light is irradiated on a gold foil [2], where $\Delta h\nu \approx 150$ eV is the best fit for gold.

III. Evaluation of Fraction of Ions in Each Charge State

SHM with the screening constants of Ref. 3 is used to model electron energy levels. In order to obtain electron population in each energy level of an averaged atom, a stationary solution of a rate equation is solved. So-called collisional radiative equilibrium (CRE) is obtained. In CRE, photo-excitation and ionization processes are neglected. In the present CRE model, the dielectronic recombination is included.

In Fig. 3, the resultant CRE population of electrons are shown as functions of temperature for gold (Z = 79) of the density of $\rho = 0.1$ g/cm^3. Shown are fractional electron populations P_n / g_n = (the number of electrons) / (statistical weight) for the principal quantum number n = 1-10.

Once the fractional populations P_n / g_n are obtained, the fraction of a given electron configuration can be calculated in the following way.

Let us consider a gold plasma near $T_e \approx 200$ eV. From Fig. 3, it is found that the shells with n = 1 to 3 are fully occupied and n = 4 shell is partially occupied. For example, the fraction of electron configuration where the shells with n = 1-3 are fully occupied, k electrons are in the n = 4 shell and no electrons in the shells $n \gtrsim 5$ can be calculated as

$$f_k = x_1^{g_1}\, x_2^{g_2}\, x_3^{g_3}\, {}_{g_4}C_k\, x_4^k \left(1-x_4\right)^{g_4-k} \left(1-x_5\right)^{g_5} \left(1-x_6\right)^{g_6} \times \cdots \quad , \qquad (1)$$

where $x_n = P_n / g_n$ can be understood the probability that an electron exists in the state n. In Eq. (1), ${}_{g_4}C_k$ is the combination defined by ${}_M C_N = M! / (M-N)!\, N!$. Then, f_k ($k = 1 \cdots\cdots g_4$) shows a binomial distribution [6].

It is straight-forward to evaluate the fraction of ions in excited states. The fraction of a configuration where one electron is excited in n = 5 can be obtained by replacing $(1-x_5)^{g_5}$ by $g_5\, x_5 (1-x_5)^{g_5-1}$ in Eq. (1). According to such process, we can calculate the fractional distribution of each

electron configuration.

In Fig. 4-(a), the fractions of ions with different charge states are shown for CRE gold plasma with density of $\rho = 0.01$ g/cm^3. In the figure, the numbers represent the effective charge. In obtaining Fig. 4, we have included only the electron configurations of ground state and singly-excited state. In Fig. 4-(b), similar figure for ions at the ground state is shown, while Fig. 4-(c) represents the fraction of singly-excited ions. It is seen in these figures that the fraction of the excited ions decreases as the temperature increases and the corona approximation can be applicable. Since the emissivity of radiation is proportional to the fraction of the excited ions, Fig. 4-(c) indicates that the emissivity decreases drastically near $T_e \approx 1$ keV.

For reference, a similar figure for aluminum plasma in CRE is shown in Fig. 5. It is seen that He-like ($Z^* = 11$) ion exists in wide range from $T_e \approx 100$ - 500 eV.

By using the resultant fraction of each electron configuration, we can evaluate line positions of each transition based on SHM. For example, the line group corresponding to 5-4 transition by singly-excited ions of gold plasma near $T_e = 200$ eV is shown in Fig. 6. The line strength is represented by linear scale and proportional to the fraction of excited ions. It is noted that the width of the line group of Fig. 6 is about 150 eV and this can be the reason why $\Delta h\nu = 150$ eV provides a good adjust as mentioned previously.

IV. Validity of the Statistical Model

In order to see whether the present statistical treatment is a good approximation of the detailed configuration accounting calculation, we derive the fraction of ions in LTE limit. If the model is valid, it should reduce to the Saha equilibrium (SE) relation.

The SE relation can be derived by minimizing the free energy of plasma and can be expressed as [10]

$$\frac{N_m}{N_{m+1}} = \frac{Z_m}{Z_{m+1}} e^{-\frac{\mu}{\tau}} \qquad (2)$$

where N_m is the number of ions with m bound electrons, Z_m is one-ion partition function, μ is the chemical potential and $\tau = kT$. The partition function Z_m is defined as

$$Z_m = \sum_{\{i\}} e^{-\frac{\varepsilon_i^m}{\tau}}$$

where {i} represents every possible configuration of electrons and their total energy for a given configuration {i} is represented by ε_i^m. Let us assume that $\varepsilon_i^m = \varepsilon_0^m, \varepsilon_1^m, \cdots$ and the

corresponding statistical weights are g_0^m, g_1^m, · · · · . Then,

$$Z_m = e^{-\frac{\varepsilon_0^m}{\tau}} \left(g_0^m + g_1^m e^{-\frac{w_1^m}{\tau}} + \cdots \right) \quad . \tag{3}$$

Therefore,

$$\frac{Z_m}{Z_{m+1}} = e^{-\frac{\varepsilon_0^m - \varepsilon_0^{m+1}}{\tau}} \times \frac{\sum_{k=0} g_k^m e^{-\frac{w_k^m}{\tau}}}{\sum_{k=0} g_k^{m+1} e^{-\frac{w_k^{m+1}}{\tau}}} \quad , \tag{4}$$

where $w_k^m = \varepsilon_k^m - \varepsilon_o^m$ is the energy difference from the ground state. In Eq. (4), $\varepsilon_0^m - \varepsilon_0^{m+1} = I_{m,m+1}$ is the ionization energy. Inserting Eq. (4) into Eq. (2), we obtain

$$\frac{N_m}{N_{m+1}} = \frac{u_m}{u_{m+1}} e^{-\frac{\mu}{\tau}} e^{-\frac{I_{m,m+1}}{\tau}} \quad , \tag{5}$$

where

$$u_m = g_0^m + g_1^m e^{-\frac{w_1^m}{\tau}} + \cdots \tag{6}$$

Equation (5) is an alternative form of the Saha equilibrium relation.

Let us consider the case of AAM. When the system is in LTE, the averaged electron fraction in the state k is given by the Fermi-Dirac distribution:

$$\frac{\langle P_k \rangle}{g_k} = x_k = \frac{1}{1 + \exp\left\{ \left(\langle \varepsilon_k \rangle - \mu' \right) / \tau \right\}} \tag{7}$$

Then,

$$x_k (1 - x_k)^{-1} = \exp\left\{ \left(\mu' - \langle \varepsilon_k \rangle / \tau \right) \right\} \quad . \tag{8}$$

In Eqs. (7) and (8), we used < > to denote that the values are the averaged ones, and the chemical potential is described to be μ' in order to note that the value is evaluated by AAM.

Since N_m is proportional to the fraction of electron configurations consisted by m bound electrons, we can obtain the relation:

$$N_m \propto \prod_{k'} \left(1 - x_{k'} \right)^{g_{k'}} \sum_{\{i\}} g_i^m \prod_k \left\{ x_k (1 - x_k)^{-1} \right\}^{f_k^{i,m}} \quad , \tag{9}$$

where $f_k^{i,m}$ is integer and represents the number of electrons in the k state for a electron configuration {i} with m bound electrons. By using the relation ;

$$\sum_k f_k^{i,m} = m \quad , \tag{10}$$

we can obtain

$$\prod_k \left\{ x_k (1-x_k)^{-1} \right\}^{f_k^{i,m}} = \exp\left\{ \left(m\mu' - \left\langle \varepsilon_i^m \right\rangle / \tau \right) \right\} \quad , \tag{11}$$

where we have introduced an approximated total energy $<\varepsilon_i^m>$ defined by

$$\sum_k \left\langle \varepsilon_k \right\rangle f_k^{i,m} = \left\langle \varepsilon_i^m \right\rangle \quad . \tag{12}$$

It should be noted that Eq. (12) is good approximation as far as the electron configuration {i} is not so different from the averaged electron configuration.

Using Eqs. (9) and (11), we finally obtain the relation ;

$$\frac{N_m}{N_{m+1}} = \frac{\left\langle u_m \right\rangle}{\left\langle u_{m+1} \right\rangle} \cdot e^{-\frac{\mu'}{\tau}} \cdot e^{-\frac{\left\langle I_{m,m+1} \right\rangle}{\tau}} \tag{13}$$

where $< >$ denotes that the average energy is used to evaluate the values u_m, u_{m+1} and $I_{m,\,m+1}$. By comparing Eq. (13) with Eq. (5), it is concluded that as far as the energy shift due to the difference in the electron configuration which is dominant in calculating the partition function is sufficiently small enough compared to the temperature τ, the Saha relation obtained by the present statistical method can be reasonable.

It is useful to calculate Eq. (13) in the simple case considered previously. We assume that the shells of n = 1, 2 and 3 are fully occupied, k electrons are in the n = 4 shell and no electrons are in the shells with $n \gtrsim 5$. In the corona limit, we take account of only the electron configuration of the ground state in evaluating the partition function. By using Eq. (9) we obtain the fraction of ions with k electrons in n = 4 in the form

$$\frac{N_0^k}{N} = x_1^{g_1}\, x_2^{g_2}\, x_3^{g_3}\, {}_{g_4}C_k\, x_4^k \left(1-x_4\right)^{g_4-k} \left(1-x_5\right)^{g_5} \times \cdots \quad , \tag{14}$$

where N is the total number of ions and $N_0{}^k$ is the number of electrons with k electrons in n=4. Then, we obtain the following relation:

$$\frac{N_0^k}{N_0^{k+1}} = \frac{{}_{g_4}C_k}{{}_{g_4}C_{k+1}} e^{\left(\langle \varepsilon_4 \rangle - \mu'\right)/\tau} \tag{15}$$

In the present limiting case, the ionization energy $I_{k,\,k+1}$ can be $I_{k,\,k+1} = -<\varepsilon_4>$. Therefore, Eq. (15) corresponds to the Saha equilibrium relation of Eq. (5).

V. Summary and Conclusion

In dealing with the radiation transport in laser produced high-Z and medium-Z plasmas, the line radiation transport is most dominant process. Since huge number of level transitions simultaneously contribute to the line radiations, it is required to simplify the line profile based on the

hierarchy of the line group. In the present paper, we have shown the structure of the line group. A partially ionized gold plasma is considered as an example. It is concluded that the l-splitted line with its line width determined by the dispersion of the line position due to mixing of different charge states can be a good approximation in evaluating opacities and line trappings.

It is pointed out that the spread of the line group can be evaluated by a statistical method based on the averaged ion model. The distributions of ion abundance are calculated for LTE gold and aluminum plasmas, resulting reasonable distributions. As a next step, these distributions will be used to evaluate opacities of matters.

In order to show the validity of the present statistical model, we have studied whether the present model can provide the Saha equilibrium distribution in the LTE limit. It has been shown that as far as the energy shift of each electronic level due to the difference in electron configuration is small enough compared to the temperature τ, the present model can be applicable.

References

[1] P. D. Goldstone, S. R. Goldman, W. C. Mead, J. A. Cobble, G. Stradling, R. H. Day, A. Haner, M. C. Richardson, R. S. Marjoribanks, P. A. Jannimagi, R. L. Keck, F. J. Marshall, W. Seka, O. Barnouin, B. Yaakobi, and S. A. Letzring, Phys. Rev. Lett. **59**, 56 (1987).

[2] H. Nishimura, H. Takabe, K. Kondo, T. Endo, H. Shiraga, K. Sugimoto, T. Nishikawa, Y. Kato, and S. Nakai, Phys. Rev. A **43**, 3073 (1991).

[3] R. M. More, J. Quant. Spectrosc. Radiation Transfer, **27**, 345 (1982).

[4] M. Itoh, T. Yabe, and S. Kiyokawa, Phys. Rev. A **35**, 233 (1987).

[5] Y. Lee, G. Zimmerman, D. Bailey, D. Dickson, and D. Kim, "A Time-Dependent Ionization-Balance Model for non-LTE Plasma", LLNL Reprot.

[6] T. Nishikawa, H. Takabe and K. Mima, in this proceedings.

[7] R. D. Cowan, "The Theory of Atomic Structure and Spectra", (Univ. California Press., Los Angels, 1981) Chap. 20.

[8] G. D. Tsakiris and K. Eidmann, J. Quant. Spectrosc. Radiation Transfer **38**, 353 (1987).

[9] T4-Group, Los Alamos National Lab. Reprot No. LALP-83-4, Los Alamos, N.M. (1983).

[10] Ya. B. Zeldovich and Yu. P. Raizer, "Physics of Shock Waves and High-Temperature Hydrodynamic Phenomena" (Academic, New York, 1966), Chap. III.

Figure Captions

Fig. 1 Hierarchy of line group in partially ionized high-Z (e.g., gold) plasmas.

(a) Line spectra obtained by average ion model with electronic levels depending only on the principal number n.

(b) The *l*-splitted lines steering from 5-4 transition and $\Delta n=0$ transition in n=4 shell.

(c) Line group formed by the same transition (5f-4d) of ions in different change states (Z*).

(d) Fine structure of each line in Fig. (c) due to difference in the spin-orbit interaction.

(e) Line profile of a line in Fig. (d) determined by natural broadening and another broadenings due to thermal fluctuations.

Fig. 2 Theoretical energy levels of configuration $4f^w6s^2$ of neutral lanthanide atoms, relative to the center-of-gravity energy E_{av}. The density of levels within each solid block is too great for the levels to be drawn separately. The figure is taken from Fig. 20-2 of Ref. 7.

Fig. 3 Electron population divided by statistical weight (P_n / g_n) for each energy level as a function of temperature for gold (Z=79) with density of $\rho = 0.1$ g/cm^3. Each indicated number represents the principal quantum number of hydrogenic model. The population is obtained by assuming CRE model.

Fig. 4 Fraction of ions with different charges in CRE gold plasmas with density of $\rho = 0.01$ g/cm^3. Each number indicated in figures represents the effective charge.

(a) Fraction of ions in ground state and singly-excited state.

(b) Fraction of ions in ground state.

(c) Fraction of ions in singly-excited state.

Fig. 5 Fraction of ions with different charges in CRE aluminum plasma.

Fig. 6 Normalized line strength for the group of 5-4 transition. In obtaining the figure, it is assumed that the levels below n = 4 are fully occupied and $P_4 / g_4 = 0.5$ and $P_5 / g_5 = 0.02$ and no electrons above n=6.

Line Group Structure

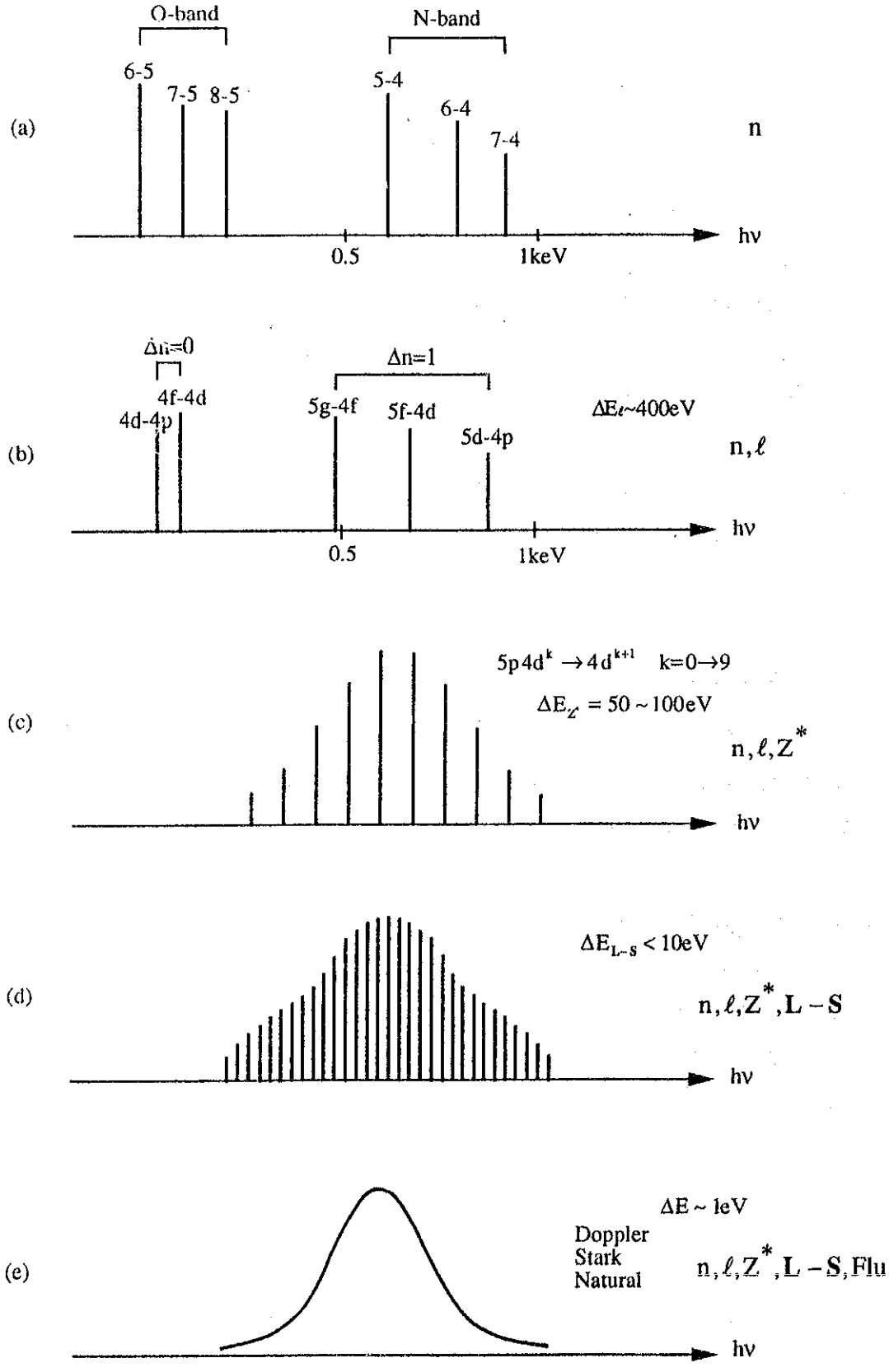

Fig. 1

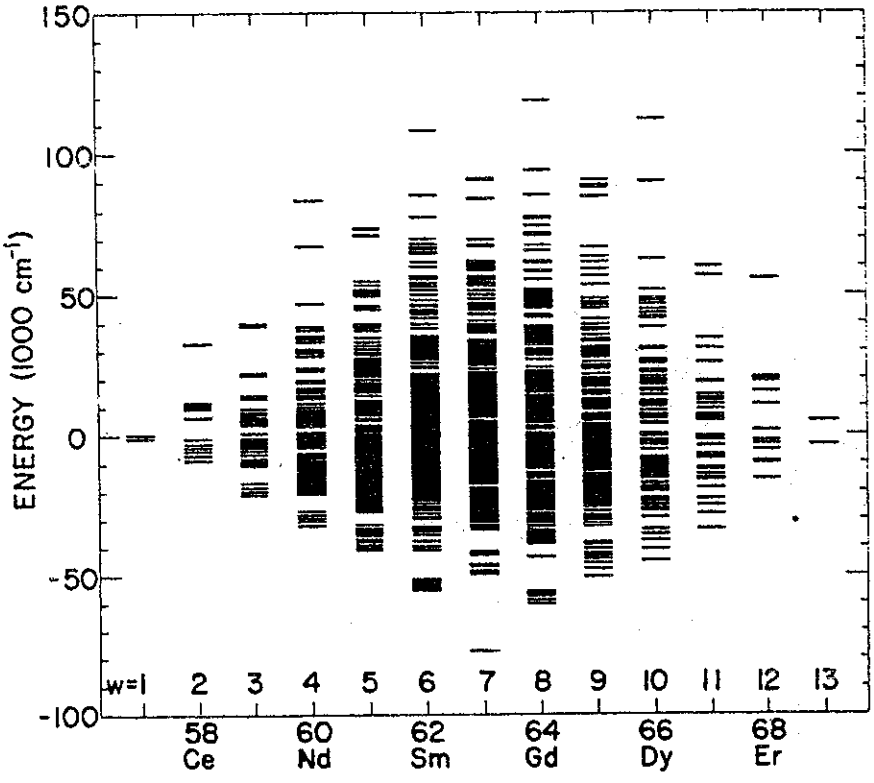
150
100
50
0
-50
-100
ENERGY (1000 cm^{-1})
w=1 2 3 4 5 6 7 8 9 10 11 12 13
58 Ce
60 Nd
62 Sm
64 Gd
66 Dy
68 Er

Fig. 2

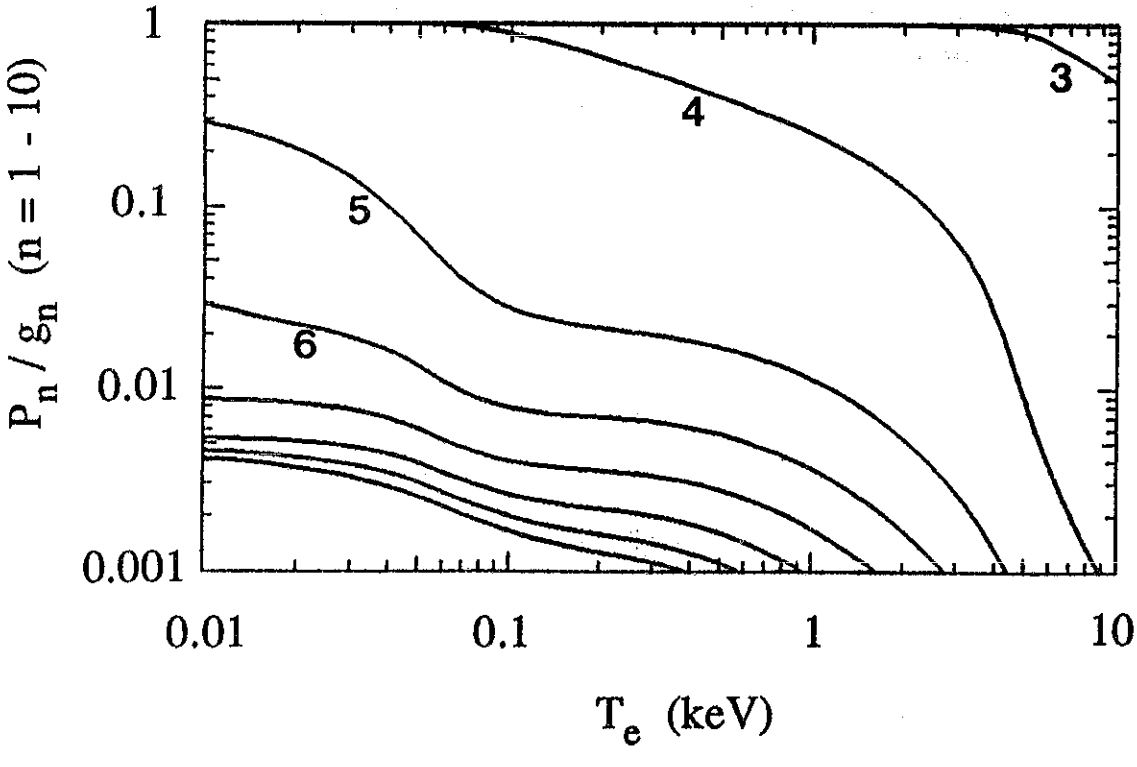
1
0.1
0.01
0.001
P_n / g_n (n = 1 - 10)
3
4
5
6
0.01
0.1
1
10
T_e (keV)

Fig. 3

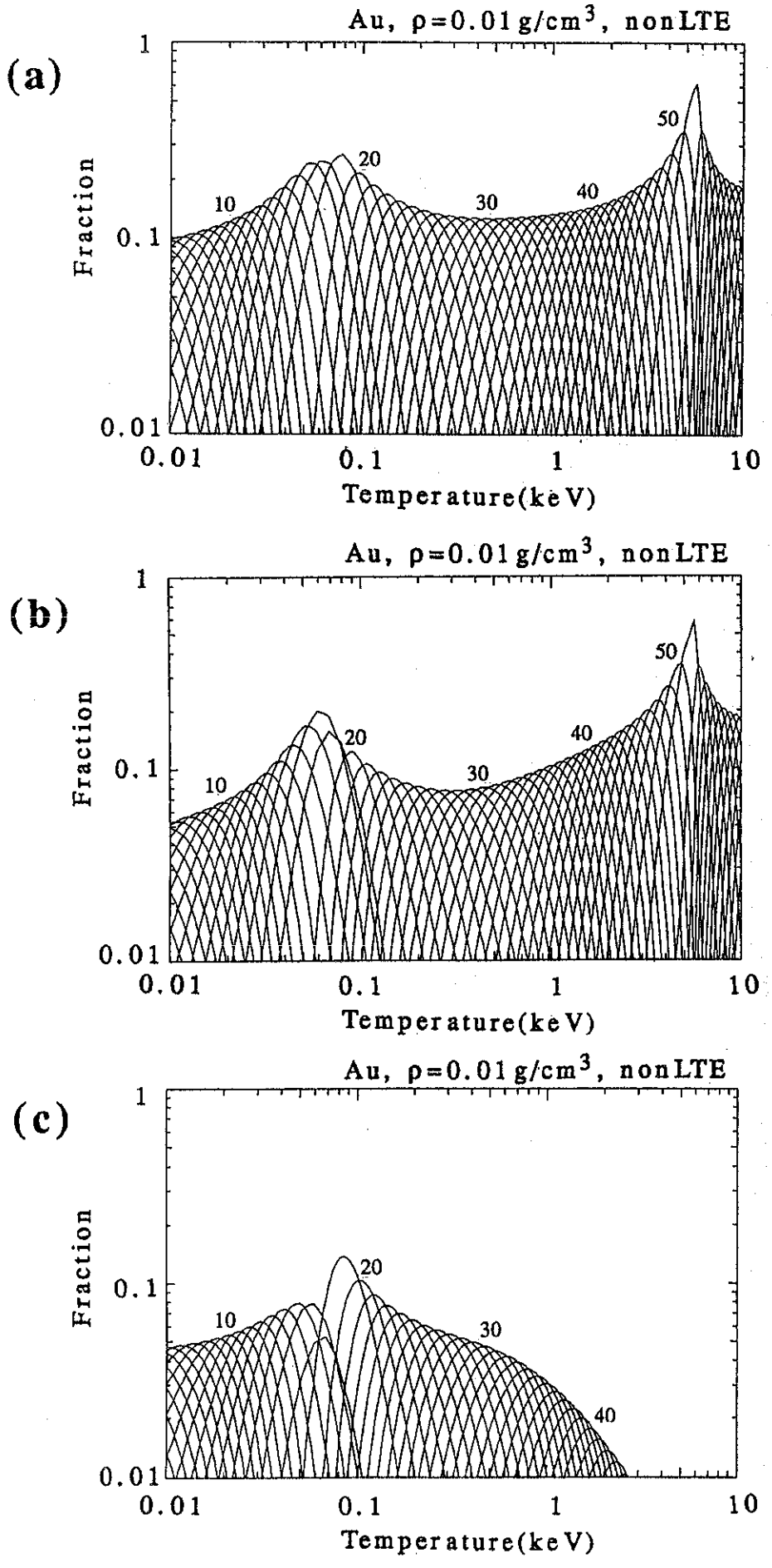
(a)
Au, ρ=0.01 g/cm³, nonLTE
Fraction
1
0.1
0.01
10
20
30
40
50
0.01
0.1
1
10
Temperature(keV)
(b)
Au, ρ=0.01 g/cm³, nonLTE
Fraction
1
0.1
0.01
10
20
30
40
50
0.01
0.1
1
10
Temperature(keV)
(c)
Au, ρ=0.01 g/cm³, nonLTE
Fraction
1
0.1
0.01
10
20
30
40
0.01
0.1
1
10
Temperature(keV)

Fig. 4

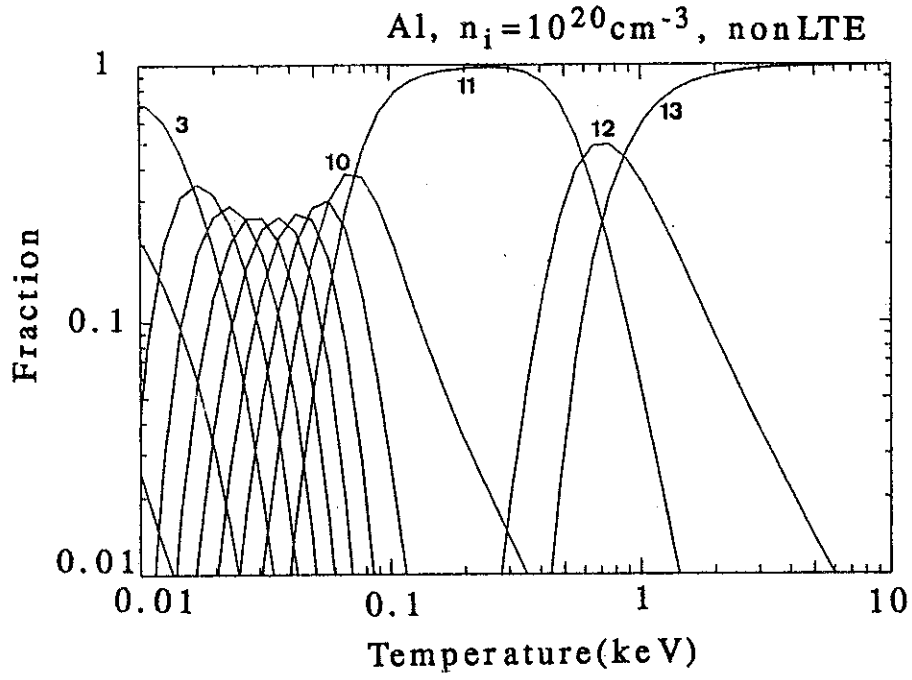
Al, $n_i=10^{20}cm^{-3}$, nonLTE
Fraction
1
0.1
0.01
0.01
0.1
1
10
Temperature(keV)
3
10
11
12
13

Fig. 5

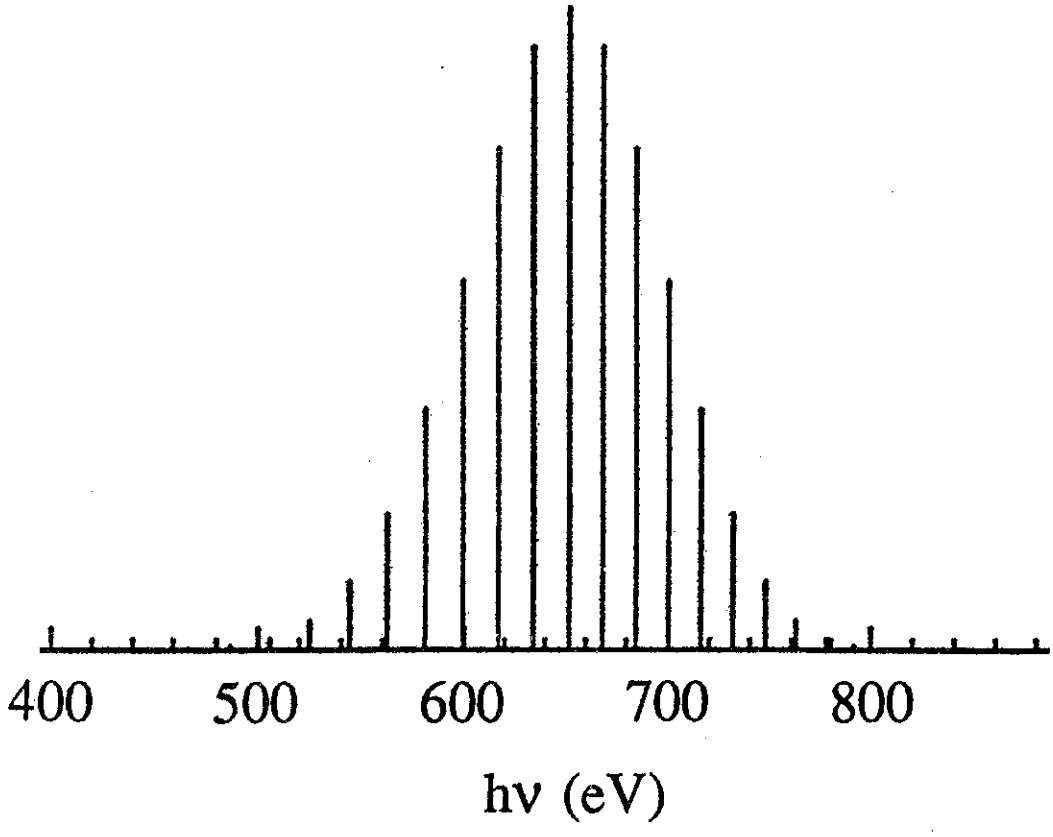
400
500
600
700
800
hν (eV)

Fig. 6

Development of an atomic code for short-wave-length laser irradiated plasmas

Akira Sasaki
Institute for Laser Science, University of Electro-Communications
Chofugaoka, Chofu Tokyo JAPAN 182

Abstract

1-dimensional hydrodynamic code with CRE atomic model and radiation transport for short-wave-length laser irradiated Al plasmas is developed and is used to analyze the excitation of x-ray lasers. It is found that higher plasma temperature is achieved with pulse-train irradiation.

1. Introduction

Atomic processes in the laser irradiated plasmas have particular importance for laser fusion applications. In indirect driven targets, conversion of incident laser to x-rays and ablative compression by x-rays are major concern, and even in direct driven targets, radiation may participate in fuel preheat as well as additional smoothing of irradiation non-uniformity. Furthermore, line and continuum emission from plasmas have been considered as an useful aim for density and temperature diagnostics. For x-ray laser applications higher efficiency is pursued by optimizing atomic excitation processes. We report the development of a 1-dimensional hydrodynamic code which include atomic processes and radiation transport for analyses of above subjects.

2. Code development

We are developing a radiation hydrodynamic code for low- and mid-z plasmas. The code is based on a single fluid, two temperature, 1-dimensional Lagragian hydrodynamic code for laser irradiated target plasmas[1]. The code includes flux limited diffusion thermal-electron heat transport, and absorption of laser light is treated by collisional absorption for underdense region and by anomalous absorption at critical density surface.

Atomic model of Aluminum plasma is generated and implemented into the hydrodynamic code. The model is based on detailed-configuration CRE atomic model[2] to treat line emission and its transport properly, assuming characteristic time of atomic

ionization, recombination, excitation and deexcitation is much shorter than that of hydrodynamics.The model concerns 13 ionic ground states (Al II to Al XIV) and excited states of Be-, Li-, He-, H-like ions in terms of principal quantum number ≤ 5. Energy of bound electrons are determined using screening factor[3]. Rate coefficients for hydrogenic ions[4] are used for collisional ionization, 3-body recombination, radiative recombination, collisional excitation and deexcitation, spontaneous emission, absorption and induced emission.

Two way (forward and backward) transport in 1-dimensional planner geometry of continuum and line emission is concerned, including photo ionization and excitation processes. Continuum transport includes bound-free and free-free transitions which is divided into 30 energy groups from 10eV to 10keV range. 32 discrete line transport mainly belong to K-shell ions are calculated using the opacity represented by the value at the line center assuming Doppler broadened profile.

Hydrodynamic equations, rate equations, and radiation transport equations are coupled together and are solved to give the instantaneous plasma temperature (Te and Ti), level population, and radiation intensity profile.

3. Results and discussion

The code is applied to the analysis of the excitation processes of compact x-ray lasers. It is demonstrated recently by Hara[5] that considerable gain is observed for 3d-4f and 3d-5f transitions (λ=105.7 - 177.8Å) of Be- and Li-like aluminum with pulse-train excitation. It is claimed that this gives efficient heating and production of He-like ions for low average irradiation intensity at the order of 10^{11} - 10^{12}W/cm^2.

We have calculated the time evolution of peak temperature of blowoff plasma as plotted in Fig.1(a) for both constant (I_L=1x10^{12}w/cm^2) and pulse-train irradiation condition. Square pulse is considered with its intensity and duration are 2 and 3x10^{12}W/cm^2, 100 and 67ns in 200ns interval, respectively, so that average intensity is equal for constant pulse and pulse-train excitation. In this series of calculation, opacity of plasma is not concerned. It is found that peak temperature is higher for pulse train excitation as shown in Fig.1(a). For comparison, results calculated by a hydrodynamic code without atomic

model is shown in Fig.1(b). In this calculation plasma assumed to be fully ionized (z=13); discrepancy of temperature between Fig.1(a) and Fig.1(b) can be explained by the fact that in the calculation with atomic model about half of incident energy is consumed by ionization of plasma up to z≈5. Fig.1(b) shows similar time evolution of temperature with Fig.1(a), indicating this should be explained by hydrodynamic response of the plasma rather than atomic processes.

Density and temperature profile calculated by hydrodynamic code without atomic model for constant and pulse-train excitation case are shown in Fig.2(a) and (b) at the time of 400ps from the beginning of irradiation. In pulse-train irradiation, plasma heated by preceding pulse expands outward and the energy of succeeding pulse is absorbed by expanding plasma. It is shown from the figure that absorption is occurring nearby critical density surface, ≤ 40μm from ablation front for constant irradiation case, whereas it is occurring at the low density region, 10 to 50μm from ablation front for pulse-train irradiation case, small heat capacity of low density plasma (≈1/10 ρ_c) is the cause of rapid temperature rise of absorption region.

(References)

1) J.P.Christiansen, D.E.T.F.Ashby, and K.V.Roberts, Comput. Phys. Commun. 7,271(1974).

2) D.Duston and J.Davis, Phys. Rev. A21, 1664(1980).

3) W.A.Lokke and W.H.Grasberger, Lawrence Livermore Laboratory Report No. UCRL-52276, 1977 (unpublished).

4) M.Itoh, T.Yabe, and S.Kiyokawa, Phys. Rev. A35, 233(1987).

5) T.Hara, K.Ando, Y.Aoyagi, Y.Kusakabe, and H.Yashiro, Jpn. J. Appl. Phys. part. 2, 28, 1010(1989).

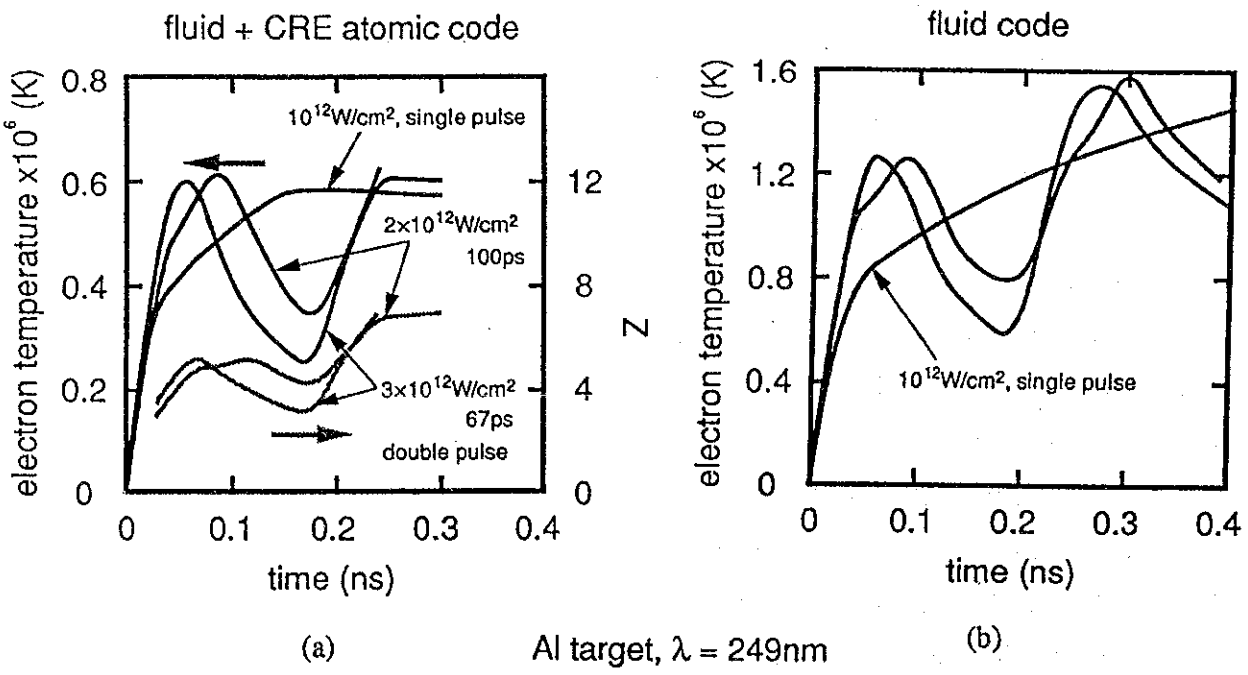

(Fig.1) Peak blowoff temperature as a function of time calculated by hydrodynamic code (a) with atomic model and (b) without atomic model.

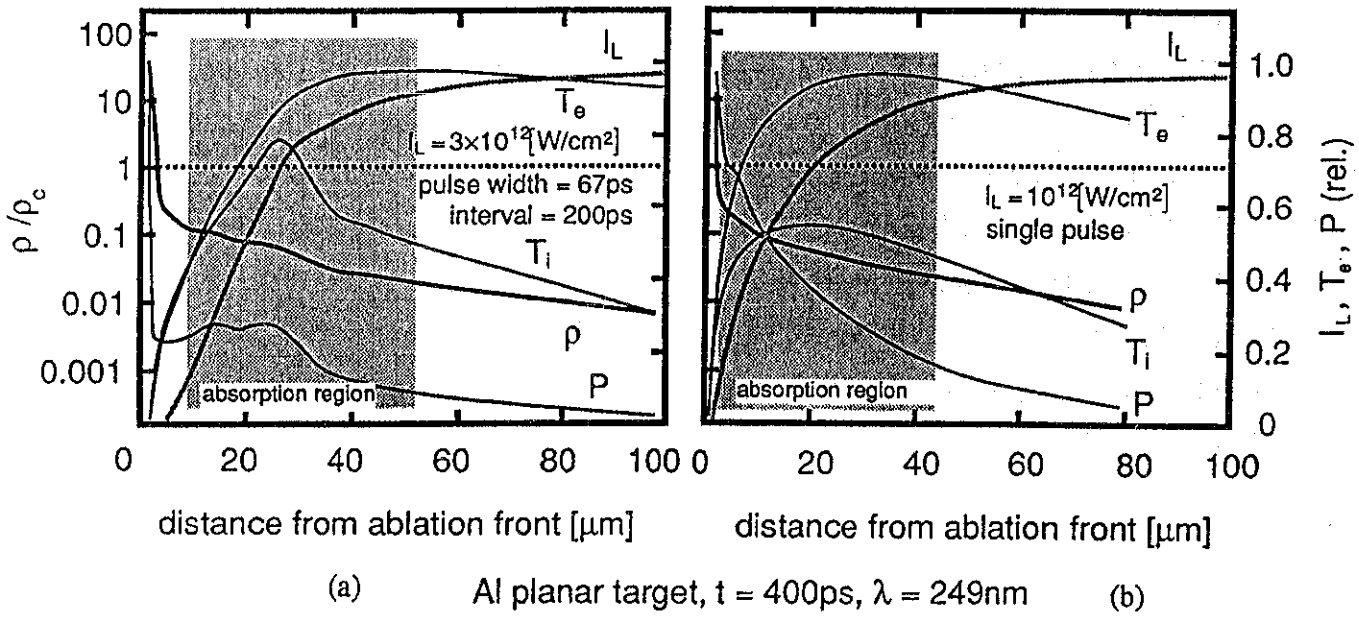

(Fig.2) Density, temperature, and incident laser intensity profile; (a) constant irradiation, (b) pulse-train irradiation.

L-Splitting Effect and Line Profile Modeling for Average Atom Model

T.Nishikawa, H.Takabe and K.Mima
Institute of Laser Engineering, Osaka University, Suita, Osaka 565

Abstract

We have developed a model in which the l-splitting effect is treated in calculating spectral opacities and emissivities of partially ionized high-Z plasma. The average ion model is used to describe the electronic state of the plasma. In order to model the line groups made of the line emissions from ions in different charge states, we have used a statistical method and calculated the distribution of the charge states from the averaged electron population in each bound state. The spectral opacities and emissivities are calculated with the electron distribution given from the collisional-radiative balance relation, and used to simulate experiments carried out by irradiating high intensity 3 ω (0.35μm) laser lights on gold foils. It is found that the $\Delta n=0$ transition (n:principal quantum number) can explain the peaked spectra near $h\nu$=200eV and l-splitted emission of n=5-4 transition can explain the flat spectra in the region of $h\nu$=400~800eV seen in the experiments.

I Introduction

When an intense laser light (~10^{14}W/cm^2) of short wavelength (0.26~0.35μm) is irradiated on a high-Z material, most of the absorbed energy (70~80% of incident energy) is converted into soft X-rays as shown in experiments[1),2)]. There are many applications of such soft X-rays. Therefore, many experiments have been carried out to study the X-ray conversion rate, spectra and transport[1)-4)], and sophisticated fluid codes have been used to analyze the experimental results[3),4)].

With the simulation codes, for example, the X-ray conversion efficiency defined as total X-ray energy divided by absorbed laser energy can be well-reproduced. However, the numerical X-ray spectra do not coincide with the corresponding experimental ones. In Fig.1, the time-integrated spectra of the X-rays measured from a laser irradiation side are shown[4)], where the experimental spectrum is shown by the solid line and the numerical one

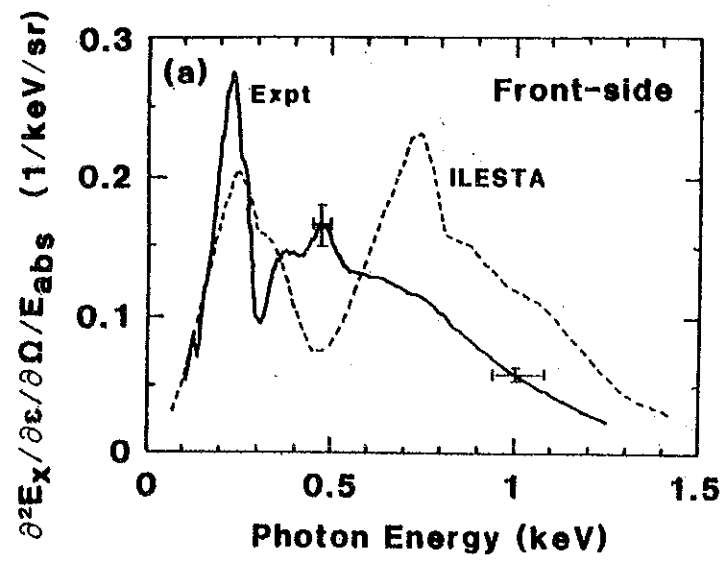

Fig.1 Time-integrated spectra of X-rays at the laser irradiation side, where the experimental result is shown by the solid line and the simulation result is shown by the dashed line. This is the case where six beams with wavelength of 0.35 μm are irradiated with large spot size (radius~0.5mm) at intensity of 3.3×10^{14}W/cm^2 with 800ps pulse duration. The target is a gold foil with 0.436μm in thickness.

is shown by the dashed line. In the experiment, six beams with wavelength of 0.35μm are irradiated on a large spot size (radius~0.5mm) with intensity of 3.3×10^{14}W/cm^2 and pulse duration of 800ps. The beams are focused on a gold foil of 0.436μm in thickness. It is typically seen that the experimental spectra have a strong peak near 200eV and flat area in 400~800eV. The same structure in spectra has also been measured in OMEGA experiments[3]. In contrast, the numerical spectra consist of two peaks; one is near 200eV stemming from line emissions due to deexcitation into the 4th shell, and the other is near 700~800eV stemming from the line emissions due to the deexcitation into the 5th shell, where the 4th and 5th mean the principal quantum number n. It is clear that the X-ray spectra seen in the simulation are harder than in the experiment.

We develop a new method for calculating reliable spectral coefficients of radiation transport within the average atom model. We treat non-LTE plasmas being in the collisional radiative equilibrium, and include transitions between electron energy levels distinguished by

not only the principal quantum number but also the azimuthal quantum number. Since the calculation is relatively simple, it is easy to use the present modeling to the hydrodynamic simulation codes.

In Sec.II, we see the importance of the energy level splitting owing to difference in the azimuthal quantum number in the case of partially ionized plasmas. We calculate a spectral emissivity based on the average atom model in which the electron energy levels are distinguished by the principal (n) and azimuthal (l) quantum numbers. We compare this emissivity with that obtained when the azimuthal quantum number dependence is excluded. In Sec.III, we describe our line profile modeling based on the average atom model. In the modeling, the effect of line center shift due to the difference of the charge state is taken into account for each distinguished transition. New spectral opacities and emissivities are calculated to install in a fluid code and a numerical simulation is carried out to see a change in X-ray spectra generated from a gold foil plasma shown in Fig.1. Summary and discussions are given in Sec.IV.

II Effect of L-splitting on Radiation Coefficients

First, we see the splitting of the electron energy levels owing to the difference in the azimuthal quantum number. Figure 2 shows the electron energy levels of gold as a function of the number of the bound electrons in the ground state. The electron energy levels are

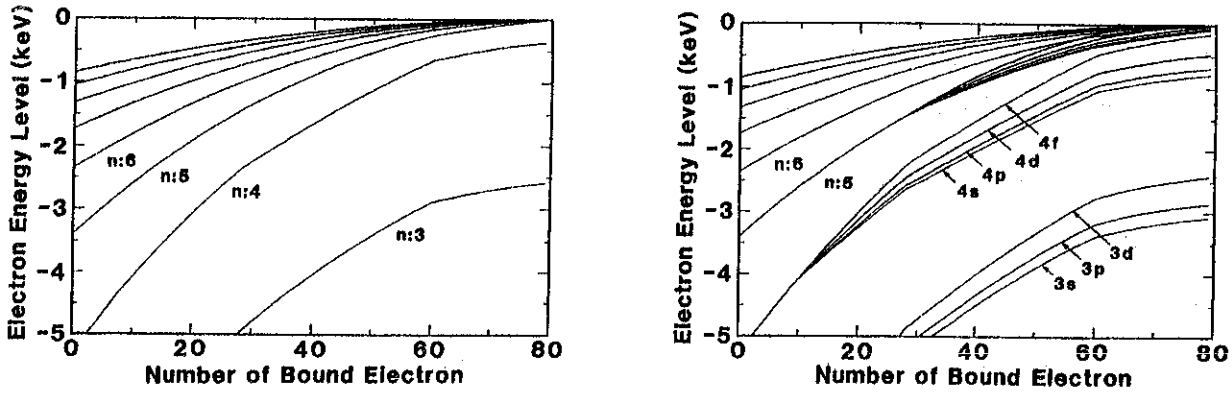

(a) l-splitting (b) l-splitting

Fig.2 Electron energy levels of gold as a function of the number of bound electrons in the ground state.

calculated from the screened hydrogenic model[5)-7)]. In Fig.2(a), the case without l-splitting (l-degenerate) is shown, while the case with l-splitting is shown in Fig.2(b). From Fig.2, it is found that the electron energy level of n=4 of Au^{+40}, for example, splits with the width of about 300eV by including the l-splitting effect. As the number of bound electrons increases, energy gaps between different principal quantum numbers decrease, while the energy splits in the same principal quantum number increase.

When the population, P_n the occupation number of electrons in the n-th shell, is given for each shell, spectral coefficients of radiation transport can be calculated. There are three processes by which an atom or ion emits or absorbs photons: i.e., free-free, bound-free and bound-bound processes[8)]. The emissivity η^E due to spontaneous emission and opacity χ^E consisting of pure absorption minus induced emission are given in the forms;

$$\eta^E = \eta^E_{ff} + \sum_k \eta^E_{fb} + \sum_{k',\, k \le k'} \eta^E_{bb} , \qquad (J / s / cm^2 / keV / str) \qquad (1)$$

$$\chi^E = \chi^E_{ff} + \sum_k \chi^E_{bf} + \sum_{k',\, k \le k'} \chi^E_{bb} . \qquad (cm^{-1}) \qquad (2)$$

Details of each coefficient can be seen in Ref.5.

Now, we show a spectral emissivity of gold in the collisional radiative equilibrium with T=200eV and plasma density ρ=0.1g/cm^3. In the calculation, we use the electron populations P_n's (n=1~10) obtained previously by employing the collisional radiative equilibrium (CRE) assumption[9)]. In obtaining the populations, the dielectronic recombination[10)] is also taken into account. The populations P_n's are tabulated as a functions of the electron temperature T and plasma density ρ. These tabulated population P_n's are used to calculate the opacities in the simulation code ILESTA[11)].

Figure 3 shows the emissivity of gold in the CRE, where T=200eV and ρ=0.1g/cm^3. The case without the l-splitting is shown in Fig.3(a), while the case with the l-splitting is shown in Fig.3(b). In Fig.3, the line profile is assumed to be a Lorentz profile.

It is found that the relatively strong line emission stemming from 5-4 transition (about 570eV) seen in Fig.4(a) splits into three relatively strong lines due to the transitions of 5g-4f

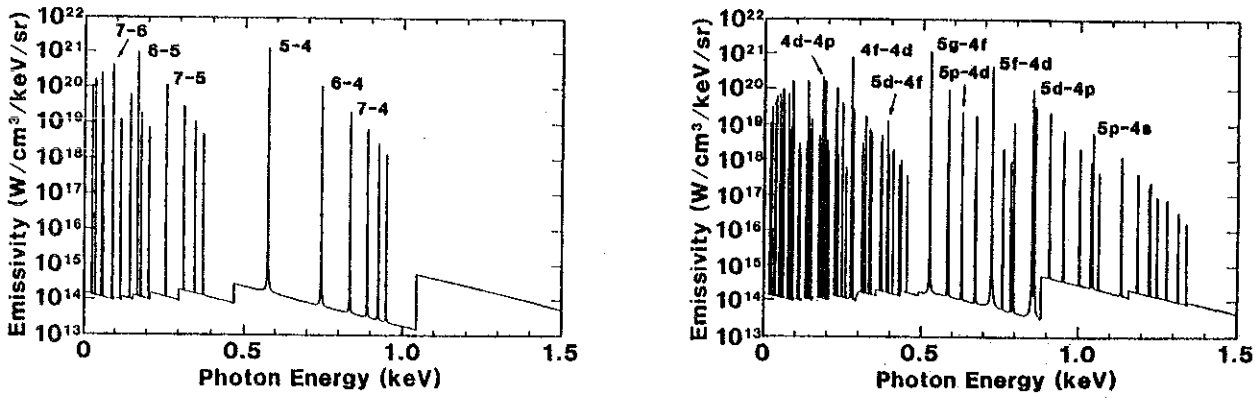

(a) l-splitting (b) l-splitting.

Fig.3 Emissivity of gold in the collisional radiative equilibrium, where electron temperature T=200eV and plasma density ρ=0.1g/cm^3.

(about 520eV), 5f-4d (about 730eV) and 5d-4p (about 850eV). The lines of 5d-4f (about 390eV), and 5p-4d (about 630eV) are relatively weak, because the oscillator strengths of these lines are small.

In Fig.4(a), the relative intensity of the lines due to the 6-5 transition is as strong as that of the 5-4 transition. However, the inclusion of the l-splitting effect makes the lines due to the transition relatively insignificant. This is caused by the fact that the emissivity given by Eq.(5) is proportional to E^3. The line of the highest intensity (6h-5g) of the 6-5 transition is located at about 60eV, while the line of transition in Fig.4(a) is located about 160eV. As the result, the intensity of 6h-5g decreases by a factor of $(60/160)^3$~0.05 due to this energy dependence. The lines seen at about 280eV and 180eV are 4f-4d and 4d-4p, respectively. These lines are due to the transitions between the subshells and stem purely from the inclusion of the l-splitting effect.

III Line Profile Modeling for X-Ray Radiation Transport Coupled with Hydrodynamics

In the case of high-Z plasma like gold treated in this paper, the largest splitting is due to the effect of the l-splitting (hundreds eV), the second largest splitting is due to the effect of line shifts arising from the difference in charge state(tens eV), and the third largest splitting is due to the effect of the j-splitting (tens eV). We can include the effect of l-splitting in our model as described in Sec.2. Therefore, we estimate the effective line width due to the line shifts arising from the difference in charge state.

Let us consider the fraction of ion which has x electrons in the n-th shell. We assume that P_n/g_n is the probability of electron occupation in the each quantum state in the n-th shell. Then, the fraction of ion which has x electrons in the n-th shell can be given with the binomial distribution;

$$f(x)_n = {}_{g_n}C_x \left(\frac{P_n}{g_n}\right)^x V_n^{\,g_n - x}, \qquad (3)$$

where V_n=1-P_n/g_n is the fractional vacancy of the n-th shell. Since the line position of a given transition shifts according to the number of the bound electrons, many lines are emitted with the strength proportional to the fraction given by Eq.(3). In the case of large g_n, the binomial distribution Eq.(3) can be approximated by Gaussian distribution. Namely,

$$f(x)_n = \frac{1}{\sqrt{2\pi}\,v} \exp\left(-\frac{(x-a)^2}{2v^2}\right), \qquad (4)$$

$$a = P_n, \qquad (5)$$

$$v = \sqrt{P_n V_n}. \qquad (6)$$

By assuming that the each line emission from each charge state overlaps each other and form a line group, we can approximate the line group profile in the form;

$$\phi_{kk'}(E) = \frac{1}{\sqrt{2\pi}\,v\Delta E_{kk'}} \exp\left(-\frac{(E-E_{kk'})^2}{2(v\Delta E_{kk'})^2}\right). \qquad (7)$$

Here, $\Delta E_{kk'}$ is the line shift when the ionization stage changes by unity. We use an $\Delta E_{kk'}$ averaged over the values obtained by changing P_n from 1 to g_n. The free-bound and bound-free opacities and emissivities are obtained by using the same way discussed in the case of the bound-bound transition.

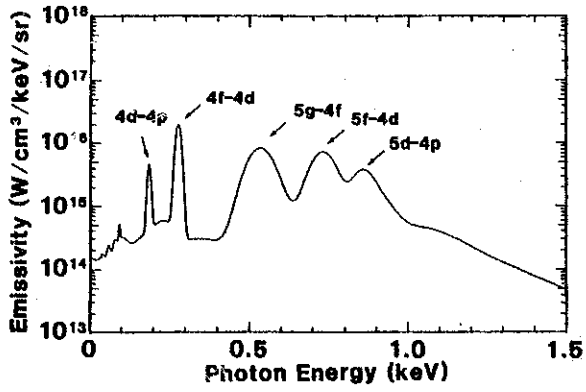

Fig.4 Emissivity of gold in the collisional radiative equilibrium with l-splitting. The electron temperature T=200eV and plasma density ρ=0.1g/cm^3. The line profile modeling is taken into account.

Figure 4 is the emissivity calculated by employing the line profile Eq.(7). Figure 3 changes its profile as shown in Fig.4. From Fig.4, it is found that the full width at half maximum of the typical lines are about 93 eV (5g-4f), about 86eV (5f-4d), and about 19eV (4f-4d). The effective line widths of $\Delta n=0$ transitions are relatively narrow, because these lines are not so affected by the change in the number of bound electrons. The effective line width of $\Delta n=0$ transition is determined by the j-splitting. In Fig.4, the j-splitting width of Ref.12 is used.

With the simulation code ILESTA, we carry out a simulation for the case shown in Fig.1. In Fig.5, the X-ray spectra with the l-splitting effect are shown. By comparing Fig.5 with the numerical results shown in Fig.1, it is found that the peaked spectra at 700eV~800eV in Fig.1 becomes flat due to the l-splitting effect. However, the intensity in 200~300eV region becomes week compared with the case without the l-splitting, although the experimental intensity shown by the solid line in Fig.1 is very strong there. It is noted that the emission of the 4f-4d transition is dominant in 200eV~300eV region compared to the lines due to the 6-5 transition, which was dominant in Fig.1. It is also noted that as seen below this emission due to the $\Delta n=0$ transitions is very sensitive to how to redistribute P_n into P_{nl}.

We have distributed the electrons in the n-th shell into the subshells by using Fermi function with the effective temperature T^{eff}, which is obtained as the best fit of the occupation

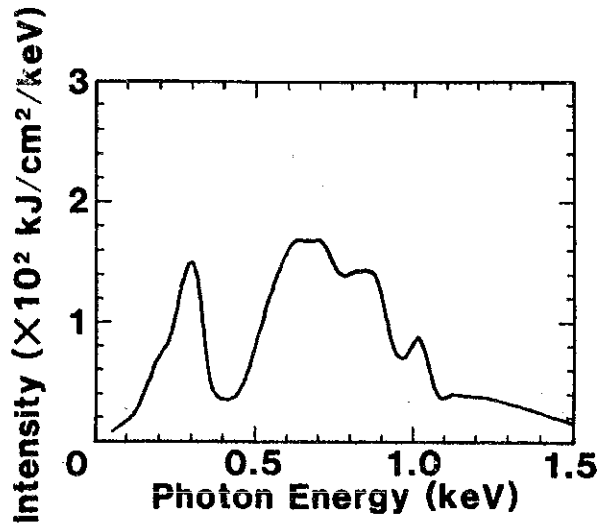

Fig.5 The X-ray spectra at the laser irradiated side calculated by the ILESTA-1D code with the new coefficients of radiation transport. The l-splitting effect and the line profile modeling for the average atom model are included. The same parameter as in Fig.1 is used.

numbers of the excited levels and is smaller than the temperature T because of the radiative deexcitation effect. However, if the collisional redistribution among the subshells of a given n takes place predominantly, it is reasonable to assume that the effective temperature determining the distribution in the subshells is higher than T^{eff} and the value between T^{eff} and T. Therefore, we replace T^{eff} by T^{w} defined as

$$T^{w} = f\,T^{eff} + (1-f)\,T. \qquad (8)$$

Figure 5 corresponds to the case of f=1.0. As the factor f decreases, the intensity of the emission due to the $\Delta n=0$ transitions gradually increases. In Fig.6, the X-ray spectra for the case of f=0.7 is shown. By comparing Fig.6 with the experimental spectra, it is found that the value of f=0.7 provides reasonable spectra to explain the experimental results. It is suggested from this results that the electron distribution in subshells is highly excited into the upper-subshells and this may be the reason why we see the strongly peaked intensity near hν=200~300eV in our experiments.

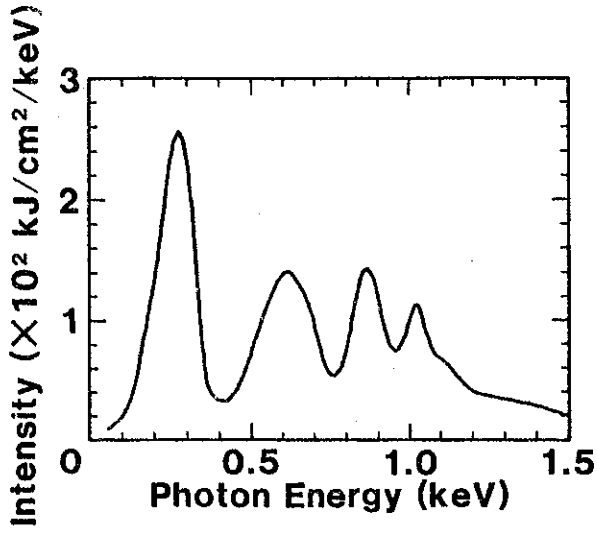

Fig.6 The X-ray spectra at the laser irradiation side calculated by the ILESTA-1D code with the new coefficients of radiation transport. In redistributing the electrons into the subshells, the effective temperature defined by Eq.(8) with the value of f=0.7 is used.

IV Summary and Conclusions

We have developed a new method for calculating spectral coefficients of radiation transport by taking account of the l-splitting effect in the non-LTE plasma. As the results, the 4th shell of gold plasma whose energy is several hundreds eV splits into subshells with the width of about 300eV. It is pointed out that the transitions in the subshells such as 4f-4d is an important element to understand the strong peak near 200eV in the experimental spectra. We also developed a line profile modeling for the average atom model. The line profile is approximated to be a Gaussian profile with the width determined by the dispersion of charge states. The calculated opacities and emissivities are installed into a fluid code to examine the experimental spectra. As the results of the simulation, it is found that the peaked soft X-ray near 200 eV seen in the experiment stems from the lines due to the $\Delta n=0$ transition in the subshells with n=4. In addition, relatively flat spectra in hv=400~800eV seen in the experiment can be explained as a results of the l-splitting of the line due to the 5-4 transition. The line group of 5g-4f, 5f-4d, and 5d-4p mainly forms these flat regions. Finally, it is pointed out that the electron distribution in the subshells is highly excited one compared with the distribution of the shells and this allows the peaked spectra near

hν=200~300eV.

Acknowledgements

The authors thanks Prof.M.Finkenthal of Hebrew University, Prof.Y.Kato, Dr.H.Nishimura and Mr.K.Murai for valuable discussions and Prof.S.Nakai for his support and encouragement.

References

1) H.Nishimura, F.Matsuoka, M.Yagi, K.Yamda, S.Nakai, G.H.McCall, and C.Yamanaka, Phys.Fluids 26 (1983) 1688.
2) R.Kodama, K.Okada, N.Ikeda, M.Mineo, K.A.Tanaka, T.Mochizuki, and C.Yamanaka, J.Appl.Phys.59 (1986) 3050.
3) P.D.Goldstone, S.R.Goldman, W.C.Mead, J.A.Cobble, G.Stradling, R.H.Day, A.Hauser, M.C.Richardson, R.Marjoribanks, P.A.Jaanimagi, R.L.Keck, F.J.Marshall, W.Seka, O.Barnouin, B.Yaakobi, and S.A.Letzring, Phys.Rev.Lett.59 (1987) 56.
4) H.Nishimura, H.Takabe, K.Kondo, T.Endo, H.Siraga, K.Sugimoto, T.Nishikawa, Y.Kato, and S.Nakai, Phys.Rev.A.43 (1991) 3073.
5) T.Nishikawa, H.Takabe, K.Mima, Technology Report, Osaka University.
6) R.M.More, J.Quant.Spectrosc.Radiat.Transfer 27 (1982) 345.
7) F.Perrot, Phys.Scripta 39 (1989) 332
8) W.A.Lokke and W.H.Grasberger, Lawrence Livermore National Laboratory Report No.UCRL-52276 (1977).
9) M.Itoh, T.Yabe and S.Kiyokawa, Phys.Rev.A 35 (1987) 233.
10) D.E.Post, R.V.Jesen, C.B.Tarter, W.H.Grasberger, and W.A.Lokke, At.Data Nucl.Data Table 20 (1977) 397.
11) H.Takabe, Research Report, Institute of Laser Engineering, ILE9008P (1990).
12) M.Finkenthal, private communication.

Effects of Radiative Ionization and Excitation on Radiation Transport

Katsunobu Nishihara

Institute of Laser Engineering, Osaka University

2-6, Yamada-oka, Suita, Osaka 565

Abstract

When a gold foil is irradiated by an intense laser of the order of 10^{14} W / cm^2, more than a half of an absorbed laser energy is converted to soft x-ray. Radiation energy density is therefore very large near the surface and radiative processes of excitation and ionization can not be neglected. Effects of radiative processes on the ionization state and radiation spectrum are investigated.

1. Introduction

When an intense laser of the order of 10^{14} W/cm^2 is irradiatied on a high-z matter such as a gold, more than a half of an absorbed laser energy is converted to soft x-ray. Radiation energy density is therefore very large near the surface and radiative processes of excitation and ionization can not be neglected. In this report, we estimate effects of radiative excitation and ionization on the ionization state and radiation spectrum by using density and temperature obtained by the hydrodynamic simulation code "HISHO". In the HISHO, the average atom collisional radiative equilibrium(CRE) model and the multi group diffusion model of radiation transport are used.

2. Effects of Radiative Processes on Ionization State

Figure 1(a) shows spatial profiles of ion density (n_i), electron density (n_e), electron temperature (T_e), and brightness temperature of radiation (T_r), as a function of the areal mass density from the surface at the laser peak for the case that a blue (0.35μm) laser of 3.5×10^{14} W/cm^2 and 1ns full width of a half maximum is irradiated on a gold foil. The laser energy is absorbed in the under dense region ($n_e<n_c$), approximately $\leq 0.13\times10^{-3}$ g/cm^2. The electron temperature is more than 1 keV near the critical density, $n_e\sim 9\times10^{21}$cm^{-3}. The electron heat conduction transfers the absorbed energy inward and drives an ablation and a shock wave. In the over dense region, the electron temperature is approximately 200eV and the brightness temperature of the radiation is comparable to the electron temperature. The ratios of the radiative ionization rate to the collisional ionization rate for N-shell and O-shell are shown in Fig.1 (b), which are calculated by using the radiation energy spectra obtained in the HISHO. It is clear from the figure that in the overdense regions the radiative ionization rate is larger than the collisional ionization rate for N-shell.

Fig. 1 (c) shows the spatial profiles of th ionization states obtained by the conventional CRE model (CR-CRE), LTE model and the CRE model taking the radiative processes into account. In the over dense region the ionization state obtained by R-CRE model is close to that obtained by LTE model, as easily expected from the result shown in Fig. 1 (b). On the other hand, in the under dense region the ionization state by the R-CRE model is not approximated by nether the LTE model nor the conventional CRE model.

3. Radiation spectra

As shown in the previous section, the radiative ionization and excitation processes results in the large ionization state, especially enhances the ionization from the N-shell. Thus the high energy emission above 800eV may increase compared with that obtained by the conventional CRE model. The comparison of the spectra obtained by the R-CRE model and the conventional CRE model is shown in Fig.2 (a) and (b). The solid line in the figure is the corresponding experimental result. The increase of the emission above 800eV agrees well with the experiment. The discrepancy near the energy 200 ~ 300eV is due to the fact that the principal quantum states are treated in the model. Those emission comes from the transition within the same principal quantum state.

The optical depth is also estimated and it is found that the optical depth where the opacity becomes one is approximately 0.2×10^{-3} g/cm^2 for the radiation below 500eV, and that it becomes larger for that above. As shown in Fig. 1(a), the spatial nonuniformity of the temperature is very large within the distance of the optical depth. Thus the radiation spectrum can not be approximated by the single Planckian.

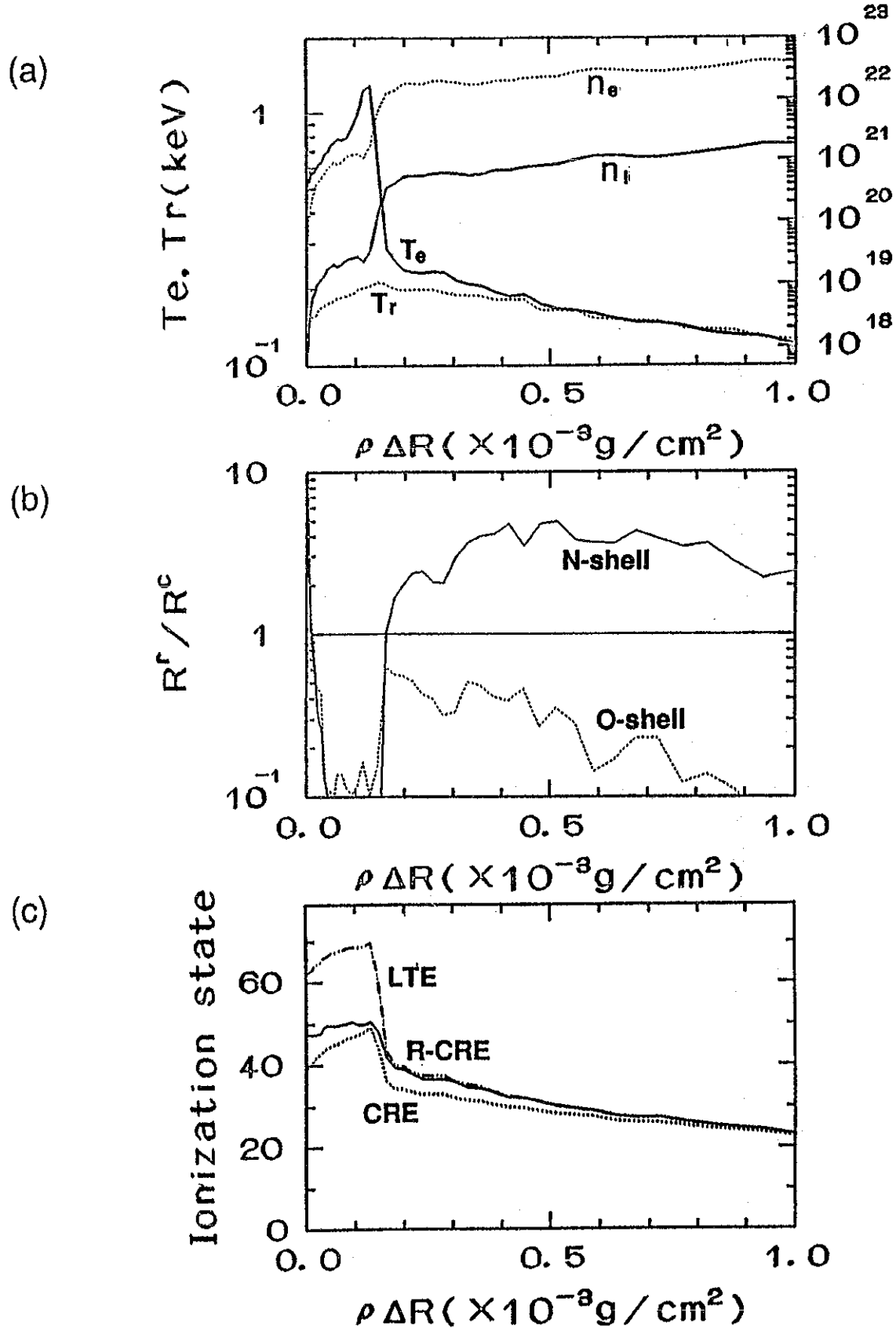

Fig. 1 (a) Spatial profiles of electron density (n_e),ion density (n_i), electron temperature (T_e), brightness temperature of radiation (T_r), at the laser peak. The horizontal axis is the distance from the surface measured by areal mass density.

(b) Ratio of radiative ionization rate to collisional ionization rate for N-shell and O-shell as a function of distance.

(c) Ionization states obtained by LTE model (dash dotted line), conventional CRE model (dotted line), and R-CRE model (solid line).

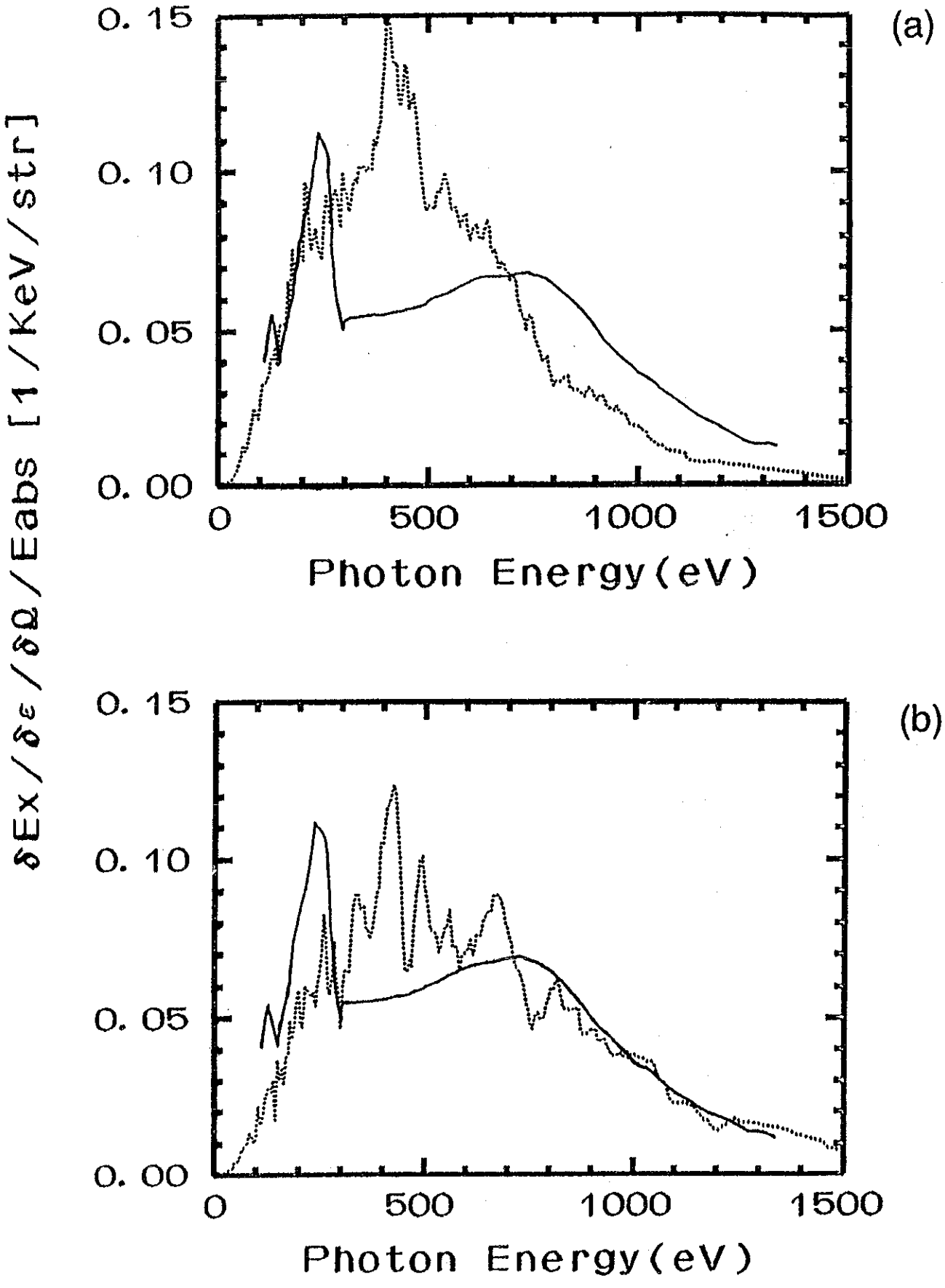

Fig. 2 Radiation spectra obtained by CRE model (a), and R-CRE(b) model. Solid line is the experimental result.

Practical Inertial Confinement Fusion and Its Numerical modeling

S.Kawata, T.Teramoto, S.Wada, M.Shiromoto, S.Kiyokawa#,
S.Kato,M.Aoyagi,and T.Saitoh
Department of Electrical Engineering, Nagaoka University of Technology,
Nagaoka 940-21, Japan.
#Department of Physics, Nara Women's University,
Kitauoyanishi 630, Japan.

Abstract

We introduce and discuss the concept of practical inertial confinement fusion(ICF) in which a fuel pellet contains deuterium-tritium fuel more than 1000mg. In the practical ICF the fuel compression ratio is less than 100 times of the solid density. Because of that, required constraints for fuel compression are relaxed compared with those for the high-compression implosion of a small pellet: The implosion nonuniformity of 10% can be allowed and the low implosion speed, that is 10^6cm/sec, is sufficient. This concept serves a practical alternative way realizing ICF. In addition, we also present the improvement for the shielding constant being used in the screened-hydrogen energy level in the average ion model which is widely used in the numerical model for the ICF pellet implosion. The improvement is performed by using energy level and population derived from the computation based on the Dirac-Fock-Slater model.

1.Introduction

In inertial confinement fusion(ICF)[1] it has been studied that a small fuel capsule is compressed to about 1000 times of solid density in order to extract fusion energy in a short time with the high burning rate and save the input driver energy. In this high-compression scheme the requirement for the implosion uniformity is quite severe and the instability-free compression is also essential. However recent works presented some solutions to these requirements. On the other hand an alternative candidate can be a low-compression scheme which is presented and discussed in this paper. In the low-compression scheme a fuel pellet should contain a large mass more than 1000mg in order to attain a high $\rho R>3g/cm^2$ with the low ρ. Because of the low compression ratio and a large size of a pellet, this scheme, called practical ICF,

relaxes the uniformity requirement and the requirement for the driver beam focusing, which is a severe problem especially in light-ion beam ICF. However it has a disadvantage of the total input energy which should be larger than 10 to 50 MJ. Such a large driver producing the larger energy is not yet developed in the world, because the requirement for the beam power is so high for a conventional small-pellet implosion that a long pulse cannot be produced by a present machine. In this practical ICF a long low-power pulse is required and the constraint on a driver machine is different from that on a present one.

In this paper we present the concept of this practical ICF and discuss its numerical modeling. In addition, we also present the improvement of the shielding constant which is used in the screened-hydrogen enegy level in average ion model. This improvement is performed by using energy level and population based on the Dirac-Fock-Slater(DFS) average ion model[2]. The improved shielding constant reproduces the DFS energy level well compared with the More shielding constant.

2.Concept of Practical ICF and Numerical Modeling

One of main objectives in practical ICF is to reduce fuel compression ratio to several tens to 100 times of the solid density with a large fuel mass which is more than 1000mg. In conventional ICF a few-mg fuel is compressed to 1000 times of the solid density(n_s). Therefore the constraints of the uniformity of fuel implosion is quite severe. It is well known that the nonuniformity should be suppressed less than a few % in order to obtain the high compression ratio[3]. In this practical ICF a fuel radius is about 1cm to several cm or more depending on a pellet structure and on the total fuel mass being contained in the capsule. Because of that, the required compression ratio is rather low compared with that in the conventional ICF, in order to attain $\rho R>3g/cm^2$. This fact relaxes the uniformity requirement for the pellet implosion.

2.1.Power-plant system

First we would like to introduce a simple power-reactor system in order to find an idea for this practical ICF (Fig.1). An energy balance is described by

$$P_a+P_d+P_e=\eta_t P_t. \qquad (1)$$

Here P_t is the output thermal energy which is presented by $(MQ+1)E_b$, M

is the multiplication factor at the blanket, $Q=R_rG$, R_r the repetition rate, G the pellet gain, η_t the conversion efficiency from the thermal to the electric energy, P_e the net electric output energy, P_d the energy supplied to a driver machine and $P_a=f_aP_e$ the energy required to drive the reactor system. Then we obtain the expression for Q:

$$Q=\{1+(1+f_a)P_e/P_d\}/(\eta_t M\eta_b)-1/M \qquad (2)$$

The input energy being required to compress and heat the fuel is estimated by the sum of heating energy $W_h(J)=38.3M_{DTh}(mg)T_i$ (eV) and the energy(pressure work) to compress the fuel which is derived from the perfect-degenerate gas equation of state. Here M_{DTh} is a part of fuel $M_{DT}(mg)$ heated up to T_i by the input energy and its radius is 1 to 3 times of the radius at which a produced alpha particle stops. The pressure work is $W_p(J)=114(\kappa^{2/3}-1)M_{DT}$, where κ is the compression ratio. In our estimation $\rho R=3g/cm^2$, the implosion efficiency 5%, $\eta_b=20\%$, M=1.1, $f_a=0.1$ and $\eta_t=45\%$. Finally we obtain the relation between the compression ratio and the beam input energy, as shown in Fig.2. For a large pellet containg more than 1000mg of DT, the required compression ratio is rather low and is less than 100. Figure 3 presents the pellet gain versus the input beam Energy. These figures show that the practical ICF can be a promising candidate in ICF.

2.2.DT-fuel adiabatic compression

Following Kidder's solution[4] we present a solution for the adiabatic compression. Assuming homogeneous compression, we introduce a scale factor h(t) by $dV=h(t)^3dV_0$. Here dV shows the Lagrangian-element volume. Then we obtain that $r(r_0,t)=r_0h$, $u(r_0,t)=r_0dh/dt$, $\rho(r_0,t)=\rho_0(r_0)/h^3$ and $P(r_0,t)=P(r_0)/h^{3\gamma}$. The transformed equation of motion is $h^{3\gamma-2}d^2h/dt^2=-(1/\rho_0r_0)dP_0/dr_0=$ constant. We choose a solution of constant =0 for our solution. In this solution, h(t) is proportional to time t and is set to $1-t/\tau_c$ in this paper. Here τ_c is the collapse time. The mechanical power for pellet compression is $P_M=(4\pi R_0^3/\tau_c)P(R_0)/(1-t/\tau_c)^{3\gamma-2}$ and $\rho R(t)=\rho R(t=0)/h^2$. The mach number $M(r_0)<R_0/(\tau_cC_s(R_0))$ should be less than 1 in order for the adiabatic compression. Here C_s is the sound speed.

In our solution the pressure does not depend upon the space coordinate. The implosion speed does not change in time and $-r_0/\tau_c$. The space dependency of density and temperature is arbitrary in our solution.

In general a shock wave drives the DT fuel into motion at the very initial time. After the first shock propagates through the DT fuel, we may expect that the implosion process is adiabatic and some space profile is realized. We may use this profile as the initial condition for our solution. In the practical ICF the initial ρR is about $0.2g/cm^2$. Therefore $h^{-2}(t_f)=(\rho R(t_f)/\rho R(t=0))=3/0.2=15$, where t_f is the time at which $\rho R=3g/cm^2$ is achieved. The pressure at the outer surface of pellet is $P=P(R_0)/(1-t/\tau_c)^5$, the mechanical-power density is $P_{Md}(W/cm^2) = 10^{11}R_0(cm)P(R_0)(Mbar)/[\tau_c(\mu sec)h^5]$ and the time-averaged pressure at the outer surface is $<P>=P(R_0)/[4t_f/\tau_c h(t_f)^4]$. If the initial pressure $P(R_0)=0.1Mbar$, the averaged pressure $<P>$ is 7.6Mbar. In order to keep the mach number $M(r_0)$ less than 1, $\tau_c>R_0/C_s(R_0)=396(nsec)R_0(cm)/T(eV)^{0.5}$ should be held; For the initial temperature $T=0.1eV$, $\tau_c>1.25\mu sec$ and then $t_f=0.742\tau_c$. From this result, the implosion time is about $1\mu sec$ and the implosion speed is R_0/τ_c is about $8\times10^5cm/sec$ for $R_0=1cm$. The total energy of DT fuel after compression is $E_{DT}(MJ)= 8.8\ P(R_0)(Mbar)R_0(cm)^3$.

2.3. Radiation-ablation pressure and radiation intensity

The fuel pellet may be irradiated by the thermal radiation being produced by laser, particle beam, projectile and so on. The radiation-driven-ablation pressure is estimated in this subsection[5,6].

When we assume that the isothermal expansion region follows the ablation (deflagration) wave, the total incident energy flux I_R is about 4PsCs and the energy flux I_{Rs} sustaining the ablation wave at the sonic point is about 3PsCs, where Ps is the pressure and Cs the sound speed at the sonic point[6,7]. From the approximate radiation transport equation[5,8] $d^2I/d\tau^2=3I$, we can obtain a relation of $\ln(I_R/I_{Rs})=\ln(4/3)=0.866t_fC_s/L_{Rs}$. Here $d\tau$ is dx/L_R, L_R is the Rosseland mean free path[8]. The relation of $I_R=4PsCs$ gives another one: $(1+z)n_s=I_{Rs}/(4C_sT_s)$, where T_s is the temperature at the sonic point. Then we can obtain the expression for the ablation pressure[7] Pa: $Pa(Mbar)=[\gamma/(1+z)+1]Ps=2.95(\gamma/(1+z)+1)\ A^{11/24}(I_R/10^{13})^{5/6}/[z^{1/12}(t_f^{1/12}/10^{-10})]$.

If we assume that the ablation pressure Pa is about the averaged mechanical pressure $<P>$, we can estimate the averaged radiation intensity $<I_R>$ being required : $<I_R>=13.1TW/cm^2$ for $z=10$, $A=27$ and $<P>=7.6Mbar$.

2.4. Pellet gain

In order to find the pellet gain in the practical ICF, first we estimate

the total input energy Ein: $Ein=4\pi R0^2<I_R>t_f=154MJ$. The final ρR in our pellet is $3g/cm^2$ and then the burning fraction f_b being estimated by ρR /(6+ρR) is about 1/3; The fusion energy output Ef is about $88.6R0(cm)^3GJ$ for a void-less DT pellet. The pellet gain is Q=Ef/Ein=575 for a 1cm pellet. The repetition rate may be about 1/30 in a practical ICF reactor of 10^6kW level.

2.5. Uniformity requirement

The nonuniformity of the implosion speed δVimp can be estimated as follows: From approximated relations of $R0=Vimpt_f$ and $\delta R=\delta Vimpt_f$, $\delta Vimp/Vimp=\delta R/R0=(\delta R/R)(R/R0)=(\delta R/R)\kappa^{-1/3}$. Here R0 is the initial radius and R is the final radius of the pellet. On the other hand ρR is proportional to R^{-2} and $\delta(\rho R)/(\rho R)_0=(1+\delta R/R)^{-2}$. Then $\delta R/R=[\delta(\rho R)/(\rho R)_0]^{-1/2}-1$. Combining these relations, we obtain $\Delta=\delta Vimp/Vimp=[(\delta(\rho R)/(\rho R)_0)^{-1/2}-1]/\kappa^{1/3}$. From this result $\Delta_{practical}/\Delta_{high-\rho}=[\kappa_{high-\rho}/\kappa_{practical}]^{1/3}$ for the fixed allowable $\delta(\rho R)/(\rho R)_0$. Here $\Delta_{high-\rho}$ shows the nonuniformity in the conventional high-compression scheme and $\Delta_{practical}$ presents one in the practical ICF. For the high-compression scheme the volume compression ratio $\kappa_{high-\rho}$ is about 10000 and for the practical ICF $\kappa_{practical}$ is about 58.1 in our pellet presented above. Therefore the factor of $\Delta_{practical}/\Delta_{high-\rho}$ is about 5.56; Consequently the tolerable nonuniformity in the practical ICF is 5.56 times larger than that in the high-compression ICF: Probably 10% order of the nonuniformity can still bring the sufficiet fusion energy output in the practical ICF.

2.6. Numerical modeling

Next we would like to discuss numerical modeling of the practical ICF. Because of the low compression ratio, only the electron degeneracy should be included in equation of state. For the radiation transport, the Rosseland mean free path L_R is much smaller than the scale of the pellet: For the tamper, $L_R=7.74\times10^{-4}$cm for the temperature T=1keV, ionization degree Z=10 and the solid density $n=n_s/50$, and $L_R=9.15\times10^{-3}$cm for T=100eV,Z=4 and $n=n_s/50$. For the DT fuel, $L_R=1.02\times10^{-3}$cm for T=10eV and $n=n_s$. On the other hand, the pellet radius is $r(cm)=[M_{DT}(mg)/795.9]^{1/3}$ for a void-less pellet; 1.08cm for 1000mg and 2.32cm for 10000mg. Therefore photons emitting from any point in space are absorbed at the immediate vicinity of that point. Consequently the radiation is almost in

equilibrium and can be described by the Planck formula. As a model for the radiation transport, we can employ the diffusion approximation with the flux limiter in the three temperature model. For the fuel behavior we use the two-dimensional fluid model with the adaptive grid in order to avoid severe grid distortion.

3.Improvement of More's Shielding Constant

In the averaged ion model being widely used in the ICF-pellet simulation the More shielding constant[8] may be used for the computation of the screened-hydrogen energy level. A set of the More shielding constant is derived from the fitting procedure to the Hartree-Fock computational results of the energy level for all elements. The More shielding constant provides a rather good fit to the Hartree-Fock result with an error of a few percent. However we found that an error of a few % leads unacceptable deviation from the real energy level in many cases[10]. In this section we present the improved shielding constant based on the Dirack-Fock-Slater(DFS) computation[2].

In our computation the shielding constant was derived with the dependence upon temperature for each element. In order to specify the electron configuration we fixed the temperature and the density. The electron population and the level energy of a fictitious averaged ion were computed self-consistently by the DFS computation in many sets of the temperature and density for each element. With these data we obtained the new shielding constant for each element by fitting procedure to the DFS results.

Figures 4 and 5 show the level energy dependence on the temperature for Al and Pb. The level energy being computed by using our new shielding constant (see Tables 1 and 2) presents better fit to the DFS result. Figures 6 and 7 present the difference of the level energy by the More shielding constant and by ours from the DFS results. These figures show that the error of the level energy was improved by one order.

4.Discussions

In this paper we presented the concept and the analytical estimation for the pellet and incident radiation parameters, and the numerical modeling in the practical ICF in which a DT pellet contains more than 1000mg of DT fuel. The compression ratio is less than 100. In order for this low compression the requirement for the implosion nonuniformity is

quite relaxed compared with that in the high-density compression ICF. In our pellet being presented in this paper the nonuniformity of 10 % can be allowed in order to extract the sufficient fusion energy output. The radiation input power is low and the implosion speed is less than about 10^5cm/sec. However the pulse duration is about 1μsec and the total input energy is more that 100MJ. We believe that the scheme of practical ICF, that is the low-compression scheme, is also one of the promising branch in ICF.

In addition, we also performed the improvement of the shielding constant which is used to compute the screened-hydrogen energy level. This work was based on the Dirac-Fock-Slater computation which provides the electron population and the level energy for a fictitious averaged ion. The new shielding constant being obtained reproduces the DFS level energy very well compared with the result by using the More shielding constant.

Acknowledgement

This work is partly supported by the cooperating project in National Institute of Fusion Science in Japan and also in part supported by the Scientific Research Fund of the Ministry of Education, Science and Culture in Japan.

References

1) J.J.Duderstadt and G.A. Moses, "Inertial Confinement Fusion", (John Wiley and Sons, New York, 1981).
2)F.Rozsnyai, Phys. Rev. A5, 1664(1980).
3)S.Kawata and K.Niu, J. Phys. Soc. Jpn, 53, 3416(1984).
4)R.E.Kidder, Nuclear Fusion, 14, 53(1974).
5)K.Nishihara, Jpn. J. Appl. Phys., 21, L571(1982).
6)T.Yabe, S.Kiyokawa, T.Mochizuki, S.Sakabe and C.Yamanaka, 22, L88(1983).
7)H.Takabe, K.Nishihara and T.Taniuchi, J.Phy.Soc.Jpn., 45, 2001(1978).
8)Ya.B.Zel'dovich and Yu.P.Raiser, "Physics of Schock aves and High Temperature Hydrodynamic Phenomena", (Academic Press,New York, 1966).
9)R.M.More, Lawrence Livermore National Lab.Rept. UCRL-84991,(1981).
10)E.Bandoh, T.Teramoto, S.Kawata and S.Kiyokawa, J.Advanced Science, 2, (1989).

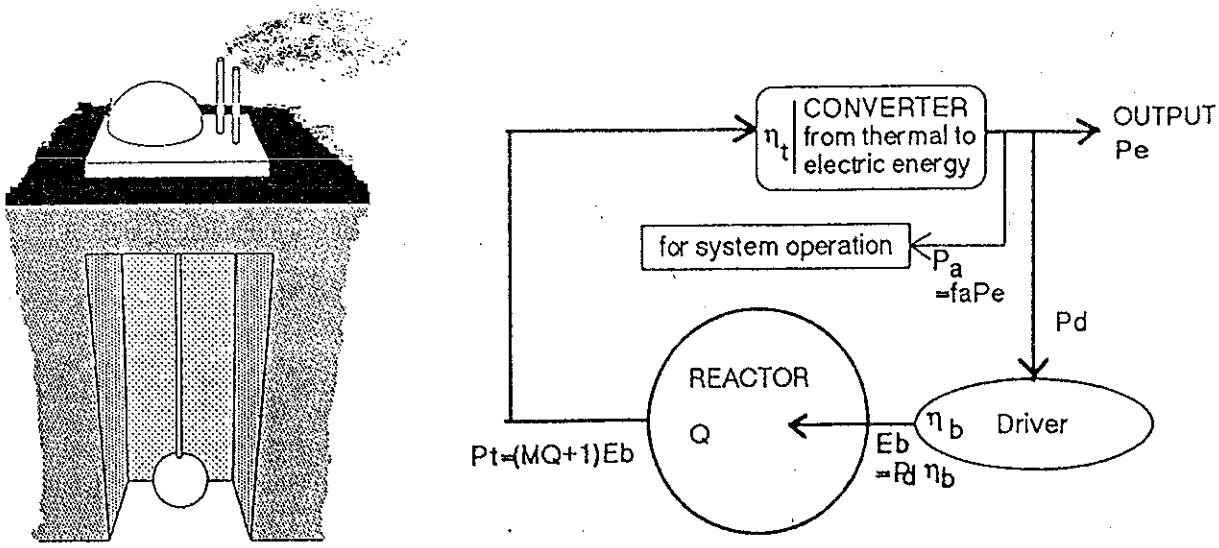

Fig.1 Power system of practical inertial confinement fusion.

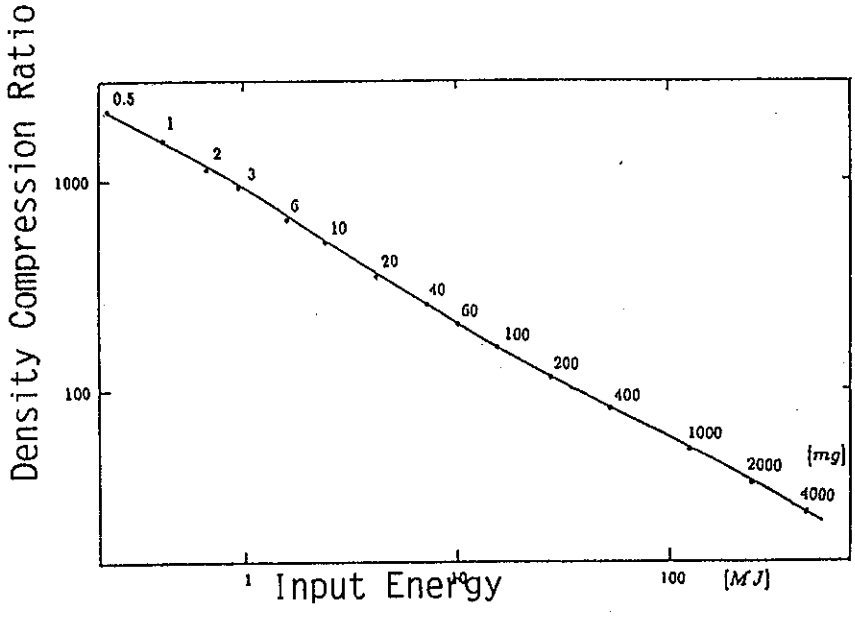

Fig.2 Density compression ratio versus input energy.

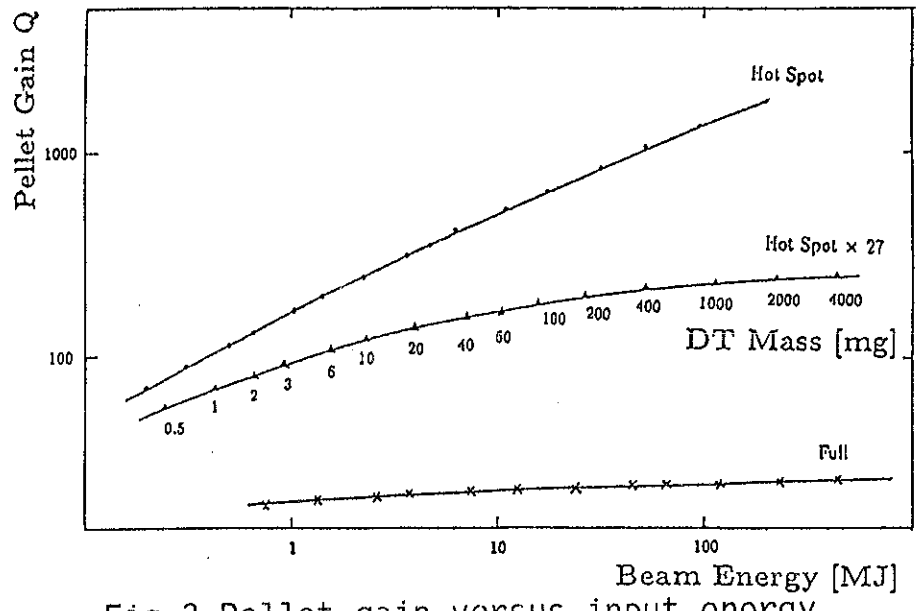

Fig.3 Pellet gain versus input energy.

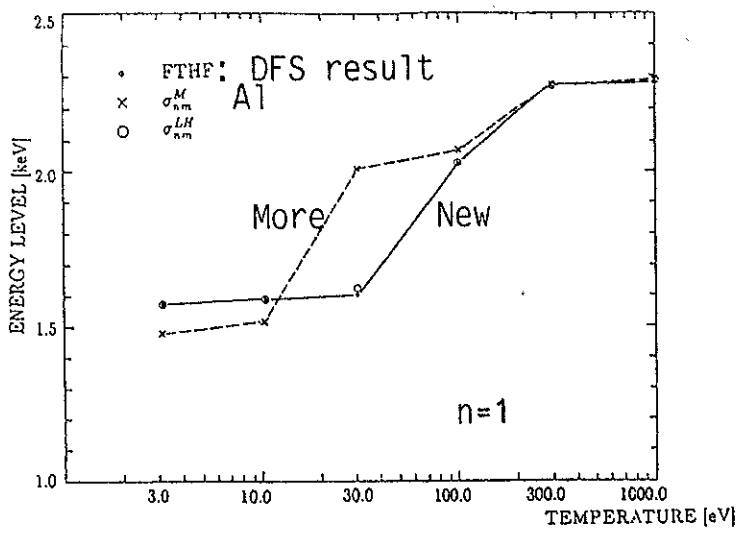

Fig.4 Energy level for Al at the density of $6.00 \times 10^{19}/cm^3$.

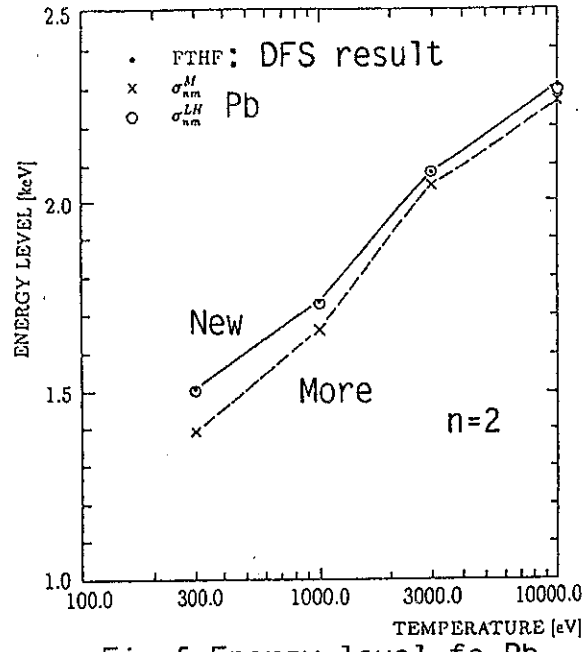

Fig.5 Energy level fo Pb at the density of $3.30 \times 10^{22}/cm^3$.

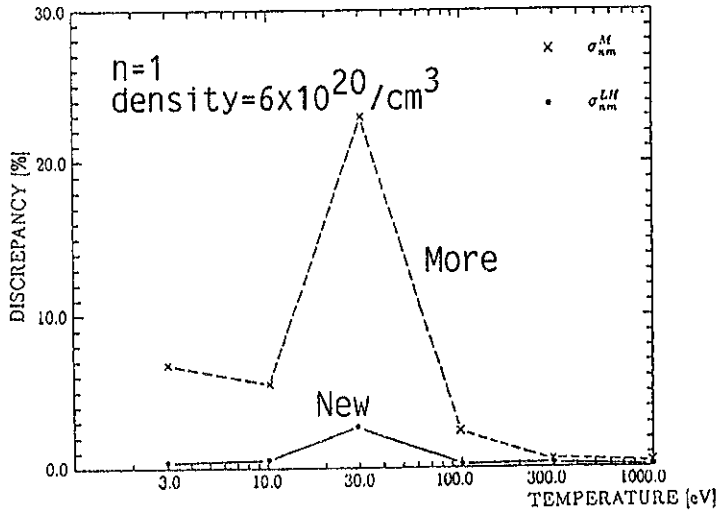

Fig.6 The difference of level energy from DFS result for Al.

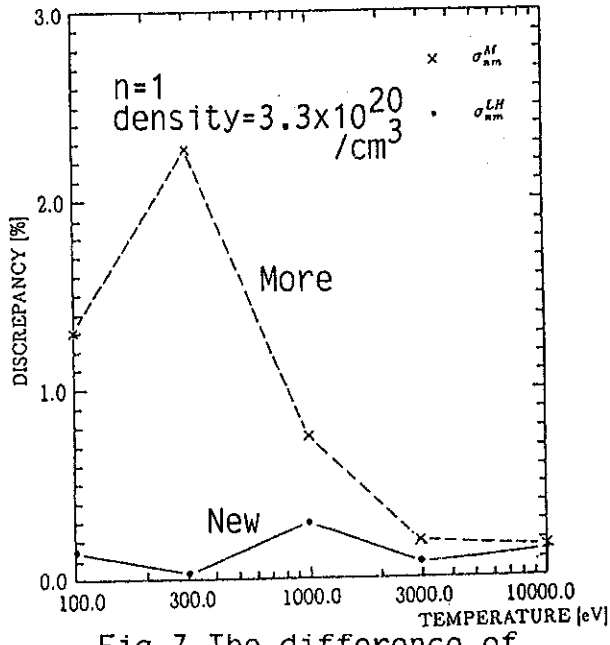

Fig.7 The difference of level energy from DFS result for Pb.

σ^L_{nm} ($\leq$ 30eV)

m \ n	1	2	3	4	5	6	7	8	9	10
1	.9898	.9870	.9840	.9954	.9970	.9970	.9990	.9999	.9999	1.000
2	.0295	.6521	.9040	.9722	.9979	.9880	.9900	.9990	.9990	1.000
3	.0295	.3829	.6800	.9155	.9796	.9820	.9860	.9900	.9920	1.000
4	.0293	.2424	.5150	.7100	.9200	.9600	.9750	.9830	.9860	.9900
5	.0282	.1596	.3527	.5888	.7320	.8300	.9000	.9500	.9700	.9800
6	.0220	.1098	.2455	.4267	.5764	.7248	.8300	.9000	.9500	.9700
7	.0218	.0808	.1811	.3184	.4592	.6098	.7374	.8300	.9000	.9500
8	.0170	.0624	.1392	.2457	.3711	.5062	.6355	.7441	.8300	.9000
9	.0124	.0493	.1102	.1948	.2994	.4222	.5444	.6558	.7553	.8300
10	.0100	.0400	.0900	.1584	.2450	.3492	.4655	.5760	.6723	.7650

σ^H_{nm} (> 30eV)

m \ n	1	2	3	4	5	6	7	8	9	10
1	.3824	.9788	.9840	.9954	.9970	.9970	.9990	.9999	.9999	1.000
2	.2611	.9465	.9040	.9722	.9979	.9880	.9900	.9990	.9990	1.000
3	.0681	.2548	.6800	.9155	.9796	.9820	.9860	.9900	.9920	1.000
4	.0645	.0860	.5150	.7100	.9200	.9600	.9750	.9830	.9860	.9900
5	.0630	.0724	.3527	.5888	.7320	.8300	.9000	.9500	.9700	.9800
6	.0487	.0351	.2455	.4267	.5764	.7248	.8300	.9000	.9500	.9700
7	.0450	.0226	.1811	.3184	.4592	.6098	.7374	.8300	.9000	.9500
8	.0366	.0032	.1392	.2457	.3711	.5062	.6355	.7441	.8300	.9000
9	.0227	.0020	.1102	.1948	.2994	.4222	.5444	.6558	.7553	.8300
10	.0100	.0090	.0900	.1584	.2450	.3492	.4655	.5760	.6723	.7650

Table 1 New shielding constant for Al.

σ^L_{nm} ($\leq$ 100eV)

m \ n	1	2	3	4	5	6	7	8	9	10
1	.3150	.9609	.9840	.9954	.9970	.9970	.9990	.9999	.9999	1.000
2	.2431	.6956	.9040	.9722	.9979	.9880	.9900	.9990	.9990	1.000
3	.1345	.6083	.6800	.9155	.9796	.9820	.9860	.9900	.9920	1.000
4	.0341	.1520	.5150	.7100	.9200	.9600	.9750	.9830	.9860	.9900
5	.0333	.1467	.3527	.5888	.7320	.8300	.9000	.9500	.9700	.9800
6	.0258	.1049	.2455	.4267	.5764	.7248	.8300	.9000	.9500	.9700
7	.0202	.0820	.1811	.3184	.4592	.6098	.7374	.8300	.9000	.9500
8	.0155	.0637	.1392	.2457	.3711	.5062	.6355	.7441	.8300	.9000
9	.0123	.0504	.1102	.1948	.2994	.4222	.5444	.6558	.7553	.8300
10	.0100	.0404	.0900	.1584	.2450	.3492	.4655	.5760	.6723	.7650

σ^H_{nm} (> 100eV)

m \ n	1	2	3	4	5	6	7	8	9	10
1	.3689	.7349	.9840	.9954	.9970	.9970	.9990	.9999	.9999	1.000
2	.2154	.5850	.9040	.9722	.9979	.9880	.9900	.9990	.9990	1.000
3	.0745	.3344	.6800	.9155	.9796	.9820	.9860	.9900	.9920	1.000
4	.0441	.2259	.5150	.7100	.9200	.9600	.9750	.9830	.9860	.9900
5	.0275	.1152	.3527	.5888	.7320	.8300	.9000	.9500	.9700	.9800
6	.0273	.1159	.2455	.4267	.5764	.7248	.8300	.9000	.9500	.9700
7	.0236	.0965	.1811	.3184	.4592	.6098	.7374	.8300	.9000	.9500
8	.0179	.0715	.1392	.2457	.3711	.5062	.6355	.7441	.8300	.9000
9	.0134	.0502	.1102	.1948	.2994	.4222	.5444	.6558	.7553	.8300
10	.0100	.0297	.0900	.1584	.2450	.3492	.4655	.5760	.6723	.7650

Table 2 New shielding constant for Pb.

Atomic Processes of the Low and Medium Z ions in the Laser-Produced Plasmas ~Advanced Mixed Model~

T. Inoue , T. Nishikawa , H. Takabe and K. Mima
Institute of Laser Engineering , Osaka University , Suita , Osaka 565 , Japan

A. Nishiguchi
Institute for Laser Technology , Suita , Osaka 565 , Japan

Abstracts

To decide the ion fractional abundance of every charge state in the short computation time, we must build a suitable atomic model. In 1982, Busquet proposed a mixed model, where he assumed two superlevels. They are related to a ground state and ioned states, respectively, and partial local-thermodynamic equilibrium(LTE) is assumed over the superlevel. In order to treat the atomic processes more accurately, we introduce the three levels for describing bound states. The transition rates between them are evaluated by using Burguess formula to be used for the rate equations. Consequently, present model(Advanced Mixed Model; AMM) gives results more close to the collisional and radiative(CR) model than the original mixed model.

I.INTRODUCTION

In the recent laser fusion experiments, the silicon(Si) at a few percentage is doped in the deuterated and tritiated plastic(CD) targets for the neutron activation measurement. According to the experimental results, x-ray emission from Si affects the implosion by the preheating. Otherwise, the implosion fluid simulations which use the average-ion model don't agree with the experimental results. So we propose a simple but accurate rate equation model for the atomic processes of the medium Z ions.

Busquet proposed the simple model, called the mixed model(MM)[1], in 1982. In the MM the all excited states and ioned states of a same-charge state are combined into one superlevel and populations of those states included one superlevel are assumed to satisfy the Boltzmann Saha law. Then transition rates between the superlevels are calculated by the rate equations. There, he insisted that the MM extended the local-thermodynamical equilibrium(LTE) to electron density one to three orders of magnitude lower. So, by treating ground level and the first excited level separately(non-superlevel) and taking more configurations into consideration, we can get the results which reproduce the collisional-radiative(CR) model relatively, with short computation time.

In section II, we describe the structure of the present model and the included atomic processes and bound electron configurations. The evolution of the population for the superlevel is also described. Finally, the reduced rate equations are derived.

In section III we show the results of the present model, which are compared with the original MM and the CR model on mean ion charge ($\langle Z \rangle$).

II. DERIVATION OF AN ADVANCED MIXED MODEL

The higher excited bound levels and free states are combined into one superlevel (see Fig. 1). In this superlevel, the distribution of electrons is assumed to be given by the Saha equation;

$$\frac{N_z N_e}{N_{z,p}} = 2\left(\frac{2\pi m k T_e}{h^2}\right)^{3/2} \frac{g_z}{g_{z,p}} \exp\left(-\frac{E_{z,n}}{kT}\right) \qquad (1),$$

where $N_{z,p}$, $E_{z,p}$ and $g_{z,p}$ are the population,the energy and the statistical weight of an ion in charge state z with an excited electron in the pth level, respectively. ; N_e, T_e are the electron density and temperature. The population of the superlevel, N_z^*, is then given by

$$N_z^* = N_z + \sum_{p=3}^{p_c} N_{z,p} \qquad (2),$$

where p_c is the upper limit of the principal quantum number for the bound state(which is decided by equating the orbit radius to the ion sphere radius or the Debye length[2]). We then consider the rate equations between the first excited states and the superlevels in various charge states(see Fig.2), which are equivalent to the CR model. In general CR model, the rate equation for the population $N_{z,p}$ satisfies

$$\begin{aligned} dN_{z,p}/dt = &-\sum_n I_{z,p;z+1,n} N_{z,p} N_e - \sum_m R_{z,p;z-1,m} N_{z,p} N_e + \sum_{n'} I_{z-1,n';z,p} N_{z-1,n'} N_e \\ &+ \sum_{m'} R_{z+1,m';z,p} N_{z+1,m'} N_e - \sum_k E_{z,p;z,k} N_{z,p} N_e - \sum_l D_{z,p;z,l} N_{z,p} N_e \\ &+ \sum_l E_{z,l;z,p} N_{z,l} N_e + \sum_k D_{z,k;z,p} N_{z,k} N_e \qquad (3), \end{aligned}$$

where $z=0,1,2,.....,z_0$(z_0 is the nuclear charge) and $p=1,2,.....,p_c$. Here I, R, E, and D are the rate coefficients for collisional-ionization, three body-, dielectronic- and radiative-recombination, collisional-excitation, and collisional and radiative- deexcitation, respectively. These rates coefficients are estimated by the formulas for the hydrogenlike ion approximately[3-8].

If we consider homogeneous plasmas, the electron density N_e is given by

$$N_e = \sum_z \sum_n z N_{z,n} \qquad (4).$$

From Eqs.(3) and (4) we obtain the self-consistent solution for the electron density and the bound state electron populations.

III.NUMERICAL RESULTS

We consider equilibrium plasmas, in which of the quasi-steady-state for atomic processes can be assumed. That is, the left-hand side of Eq.(3) is approximated to be 0 for all states. The present model has been applied to homogeneous aluminum plasmas. We present the temperature dependence of $\langle Z \rangle$.

Fig. 3 shows the comparison of $\langle Z \rangle$ values obtained by the present model(AMM), with those by MM, and the CR model[9] for the ion densities (a) 10^{20}, (b) 10^{24} cm^{-3}. The figure shows that AMM gives much better results than MM. Especially, in the high temperature region(> a few hundred eV) our model reproduce the CR model very precisely. Since this temperature range(100eV~1keV) is very important region for the x-ray emission from the laser-produced plasmas, this model may be useful for analyzing the radiation and atomic processes in those plasmas.

IV.SUMMARY

In summary, we propose the improved MM by solving the rate equations for the populations of the first excited states separately from the higher excited states. It turns out that this improvement is useful and effective for describing for the laser-produced medium-z plasmas where electron density and temperature typically range from 10^{20} to 10^{24} cm^{-3} and from 100 eV to a few keV, respectively. Furthermore, this model is valid not only for low and medium-plasmas, but for high-z plasmas, as it was discussed in the MM. For the excited state of He-like ion, however, we must separately treat singlet and triplet levels. They are strongly isolated because of the selection rule, so we have to treat their transition separately.

In the near future, this model will be applicant to the simulation code for implosion of laser-fusion. We estimate the x-ray emission from Si doped in a plastic target to investigate by the simulation code with AMM whether the x-ray emission from Si preheat the compress core plasma in the implosion.

References

[1] M. Busquet, Phys. Rev. A **25**, 2302 (1982).

[2] I. Shimamura and T. Fujimoto, Phys. Rev. A **42**, 2346 (1990).

[3] M. Itoh, T. Yabe and S. Kiyokawa, Phys. Rev. A **35**, 233 (1987).

[4] R. K. Landshoff and J. D. Perez, Phys. Rev. A **13**, 1619 (1976).

[5] W. Lotz, Z. Phys. **216**, 241 (1968).

[6] M. J. Seaton, in *Atomic and Molecular Processes*, edited by D. R. Bates (Academic, New york, 1962), p. 375.

[7] R. W. McWhirter, in *Plasma Diagnostic Techniques*, edited by R. H. Huddlestone and S. L. Leonard (Academic, New york, 1965).

[8] A. Burgess, Astrphys. J. **141**, 1588 (1965).

[9] D. Saltzmann and A. Krumbein, J. Appl. Phys. **49**, 3229 (1978).

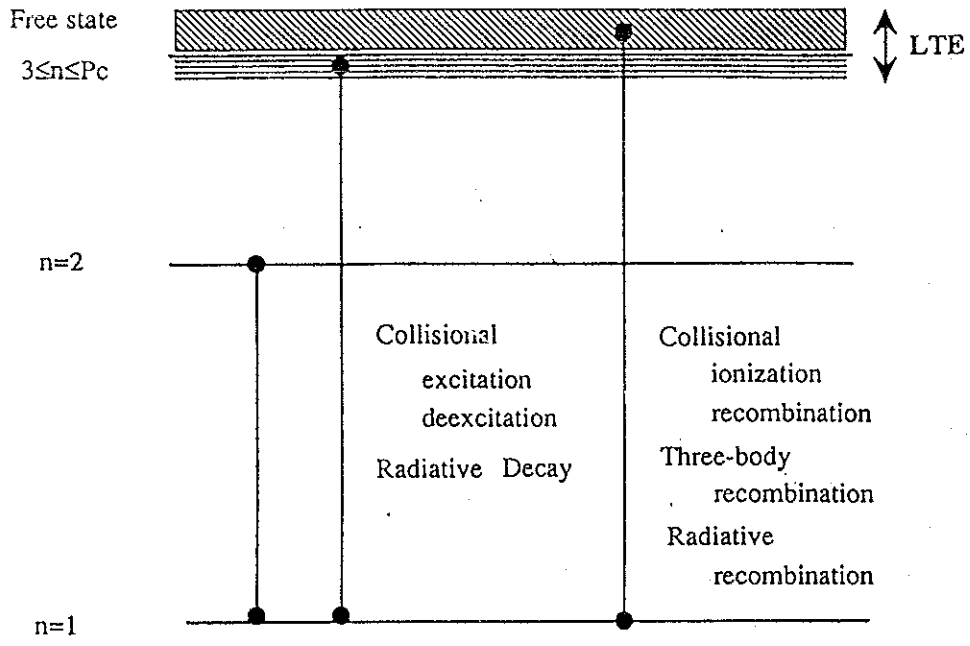

Fig. 1 The Atomic Processes of This Model

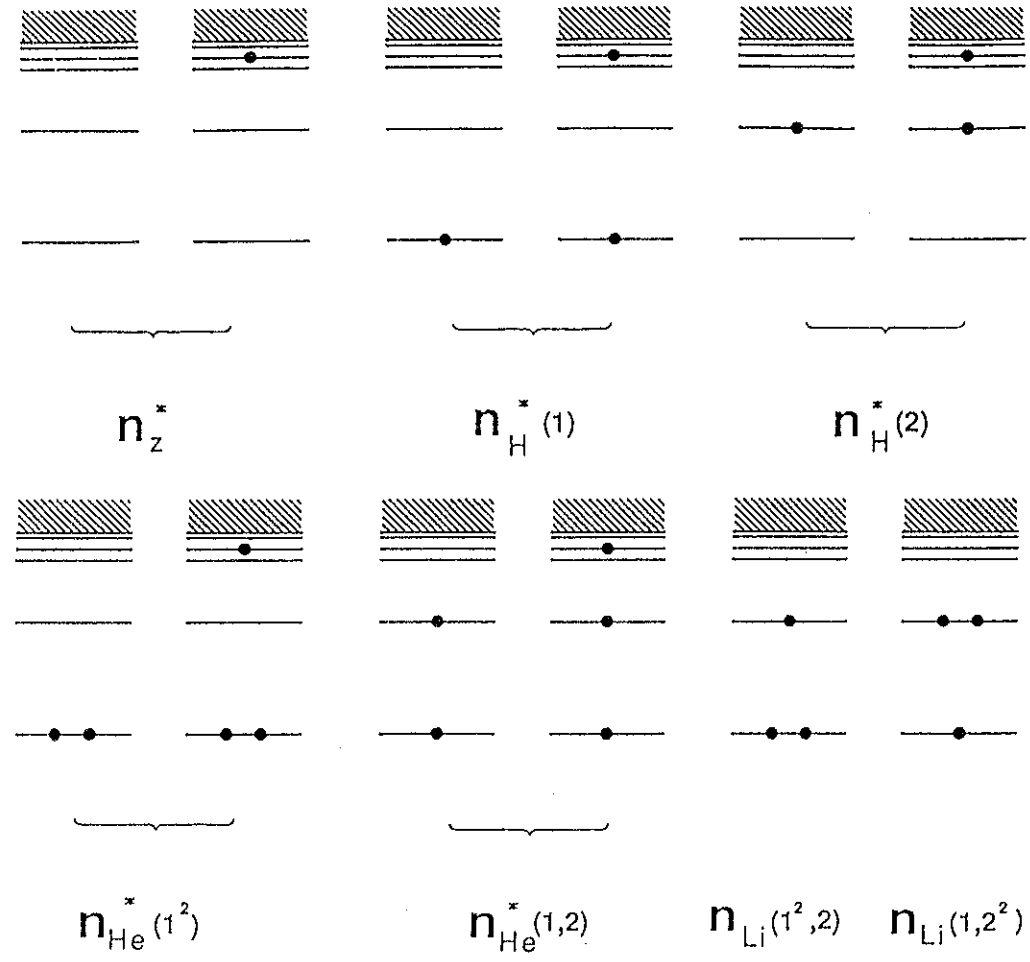

Fig. 2 Configurations of Bound Electrons

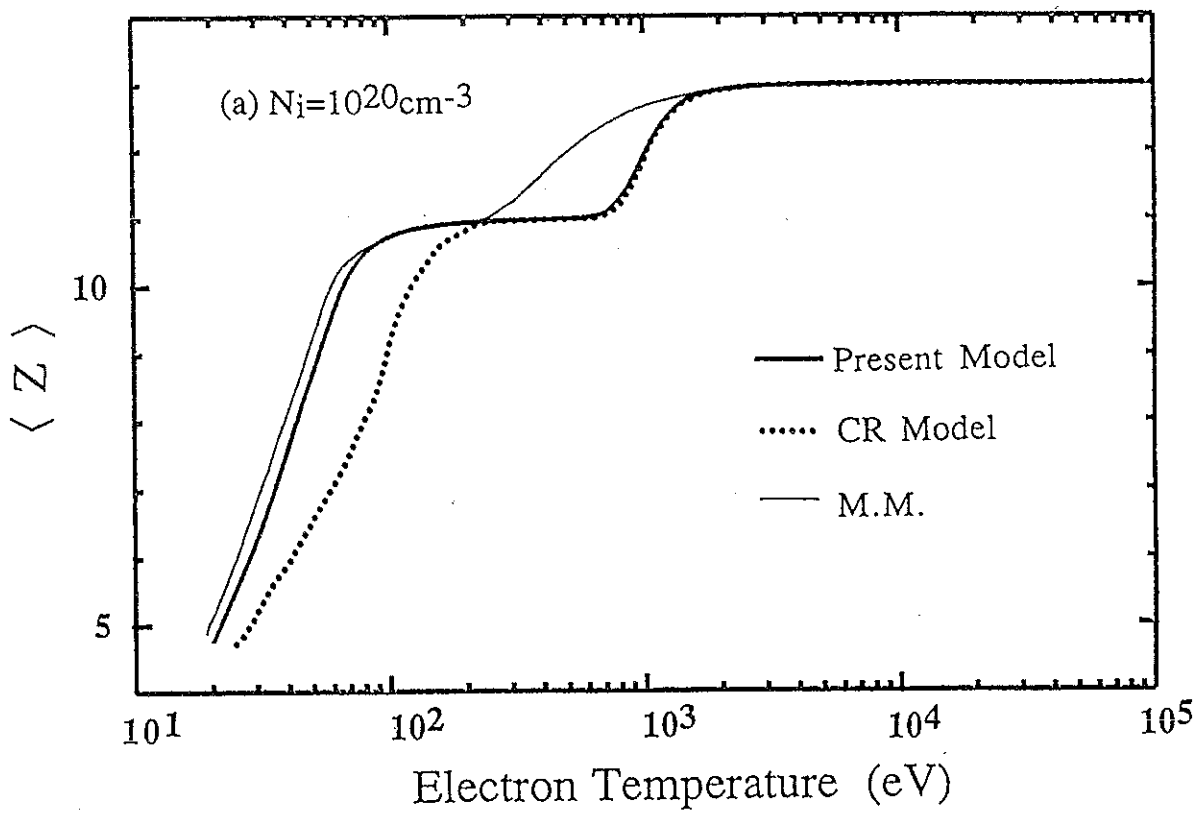

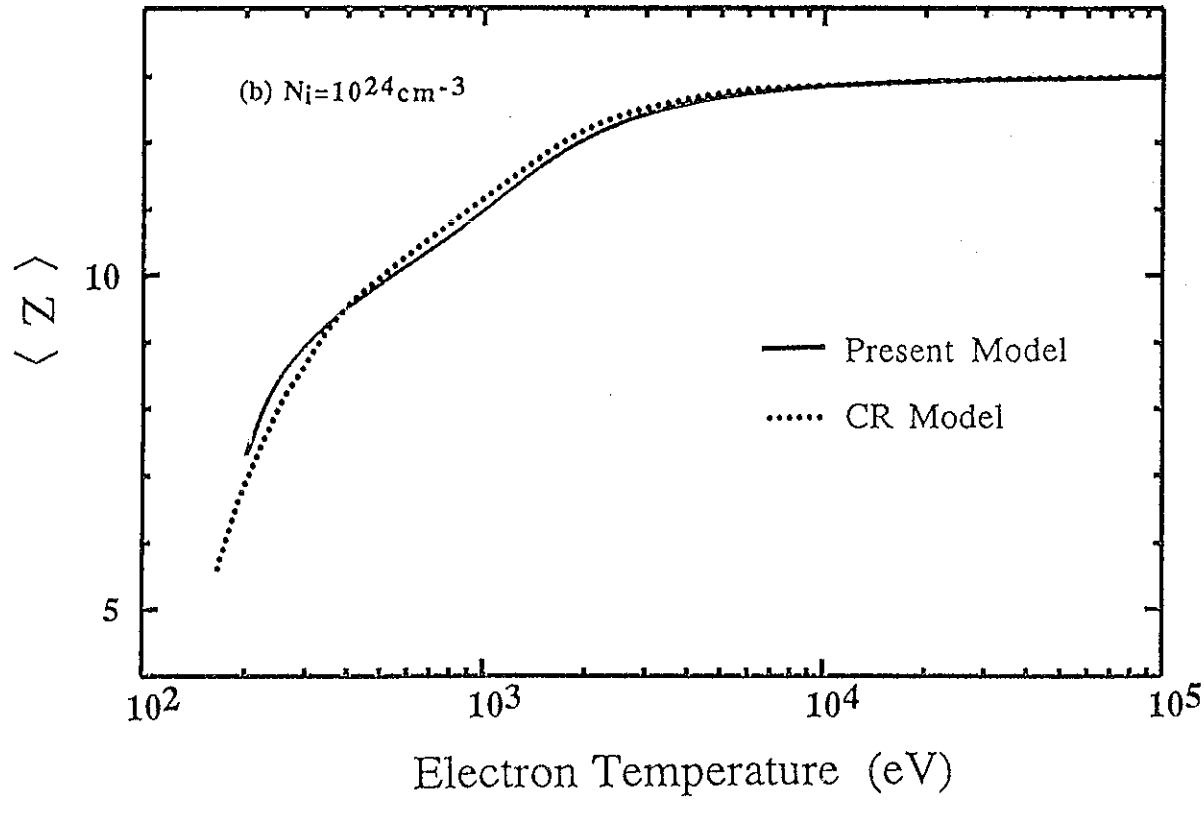

Fig. 3 Comparison of ⟨Z⟩ Values by the Present Model, M.M., or the CR Model (a) $N_i=10^{20}cm^{-3}$ (b) $N_i=10^{24}cm^{-3}$

Oscillator Strength of Partially Ionized High-Z Atom on Hartree-Fock Slator Model

S.Nakamura, T.Nishikawa, H.Takabe, K.Mima
Institute of Laser Engineering, Osaka University

Abstract

The Hartree-Fock Slator (HFS) model has been solved for the partially ionized gold ions generated when an intense laser light is irradiated on a gold foil target. The resultant energy levels are compared with those obtained by a simple screened hydrogenic model with l-splitting effect (SHML). It is shown that the energy levels are poorly model by SHML as the ionization level becomes higher. The resultant wave functions are used to evaluate oscillator strength of important line radiations and compared with those obtained by a simple model using hydrogenic wave functions. Its demonstrated that oscillator strength of the 4p-4d and 4d-4f lines are well modeled by the simple method, while the 4-5 transitions such as 4f-5g, 4d-5f, 4p-5d, and 4f-5p forming the so-called N-band emission are poorly modeled and HFS results less strong line emissions.

Introduction

When an intense laser light is irradiated on a high-Z material, most of the absorbed laser energy is converted into the X-ray radiation. In numerically simulating such phenomena, it is required to model (1) hydrodynamics, (2) radiation transport kinetics, (3) LTE and non LTE atomic modeling and (4) atomic data base. In the present note, we focus on the atomic data base; namely, energy levels of line radiations, and their oscillator strengthes. Since most of the X-rays in laser irradiated gold plasmas stem from the line radiations generated by partially ionized ions with partially filled n=4 shell (n; principal quantum number), we evaluate the atomic data for such partially ionized gold ions.

In Fig.1, a typical X-ray spectra obtained in an experiment and a one-dimensional hydrodynamic simulation are shown for the case where a 3ω laser pulse at the intensity of 2×10^{14} W/cm^2 is irradiated on a gold foil. In the numerical simulation, the screened hydrogenic model with l-splitting effect (SHML) proposed by Perrot [1] is used to evaluate each line position and an effective line width given by an statistical model is used [2]. The oscillator strength of each line radiation is evaluated following the method [3], in which hydrogenic wave functions with spatial scale determined by an screened nuclear charge are used to calculate the dipole moment for each transition. By comparing the experimental spectrum with the numerical one in Fig.1, it is found that the inner shell transition in n=4 (4f-4d) generate a strong peak at $h\nu \cong 200$-300 eV, and the transition from n=5 to n=4 (4f-5g, 4d-5f, and 4p-5d) generate most of the X-ray in the region of $500\ \mathrm{eV} \lesssim h\nu < 1$ keV.

It is our purpose of the present note to check the accuracy of the atomic data

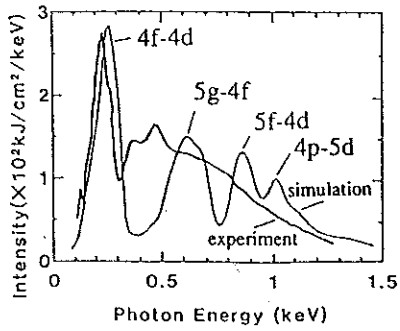

Fig.1 Typical result of X-ray spectra obtained by experiment and simulation on irradiating 3 ω laser incidence upon plane Au target

for these line radiation by solving the Hartree-Fock Slator (HFS) model in a self-consistent field for the partially ionized gold ions. Actually, the numerical spectrum has a dip near $h\nu = 400$ eV, while the line radiation of 4f-5d exists there. The oscillator strength of this line is so small that the radiation cannot be seen as the result. To check the strength of this line by HFS model is one of the purpose.

In the present note, we compare the energy levels of electrons in the n=4 and 5 shells obtained by SHML model with those by HFS model. The oscillator strengthes used in the simulation are also compared with those obtained by HFS model. Dependencies of these data on the electron configuration are finally shown for the partially ionized gold ions by varying the number of bound electrons in the n=4 shell.

Calculation Models

The SHML which we have used for calculating energy levels is an extended version of the screened hydrogenic model (SHM). The screening constants $\sigma_{nn'}$ which is given by More (4) are used. With the nuclear charge Z and $\sigma_{nn'}$ and the occupation number P_{nl} of the subshell (n,l) and the total occupation P_n of n shell, the screened nuclear charge Q_{nl} is given as follows,

$$Q_{nl} = Z - \sum_{n \le n'} P_{n'} \sigma_{nn'} \left(1 - \frac{1}{2}\delta_{nn'}\right) + \sum_{l=0}^{n-1} x_{nl} g_{nl} \sum_{n'} P_{n'} q_{nn'} \qquad (1)$$

where

$$E_{nl} = \frac{P_{nl}}{P_n} \qquad (2)$$

$$g_{nl} = \frac{1}{4n^2}\left(n^2 - 2l(l+1) - 1\right) + \nu_n \qquad (3)$$

In equation (1), $g_{nn'}$ are for $2n^2 > n'^2$

$$q_{nn'} = \frac{1}{\pi}\left(\frac{n'}{n}\right)^5 \left(2 - \left(\frac{n'}{n}\right)^2\right)^{\frac{1}{2}} \qquad (4)$$

and otherwise

$$q_{nn'} = 0 \qquad (5)$$

The third term of equation (1) is additional part for the structure of l-splitting, and second term is for that of degenerate n shell. In this theory constructed by the

equation (1) to (5), v_{nl} is a adjustable parameter which has important influence on accurate energy levels, and screening constant is also.

In second place, basic equations of HFS which is used for comparison can be written in the following manner.

$$-\frac{d^2}{dr^2}R+\frac{1}{\varepsilon_0}(V-\varepsilon)R=0 \qquad (6)$$

and

$$\nabla^2\varphi=-4\pi e(Z\delta_{(r)}-\rho_{(r)}) \qquad (7)$$

where

$$\rho_{(r)}=\frac{\sigma_{(r)}}{4\pi r^2} \qquad (8)$$

$$\sigma_{(r)}=-\sum_{nl}\omega_{nl}P_{nl}(r)^2 \qquad (9)$$

and

$$V=V_0+V_{exc.} \qquad (10)$$

$$V_{exc.}=-Ry\ (\frac{24}{\pi}\rho)^{\frac{1}{3}} \qquad (11)$$

In schroedinger equation (6), R is the electron's radial wave function with radius r, and ε is the eigen value of the energy level when the electron of (n,l) orbit moves in a central potential V. The potential V is determined with Poisson equation (7) in which φ=eV, and ρ is the electron density distribution as the result of equations (8) and (9) where ω is the population in the (n,l) orbit. And P satisfies $P=r^{-1}RY$ where Y is a spherical harmonic function. Farthermore in order to include the exchange energy, Slator's local approximation of equation.(11) is used, which is simple model at the base of Slator matrix. This approximation can't obtain full exchange energy unlike multi body theory, and the accuracy of present calculation in the region of heavy or highly ionized atoms is been under consideration now. Present HFS model is one body problem, and HFS computation can be carried out by solving the equations (6) to (11) self-consistently by the iteration method.

By the use of resultant wave functions and energy levels, the oscillator strength of bound-bound transition can be given by the following equation [5].

$$f_{nl}^{n'l'}=\frac{1}{3}\frac{max(l,l')}{2l+1}\frac{\Delta E}{Ry}(R_{nl}^{n'l'})^2 \qquad (12)$$

In this equation, $(R_{nl}^{n'l'})^2$ is the dipole moment and ΔE is the transition energy between the state (n,l) and (n',l).

Electron Configuration

When an intense laser light of the intensity near 10^{14} w/cm^2 is irradiated on a gold foil, most of the X-ray is generated in the region where the temperature is about 200 eV and the density 0.1 g/cm^3. In Fig.2, the non LTE (non Local

Thermodynamic Equilibrium) electron population of gold at the density of 0.1 g/cm^3 is given [6] for the case where the screened hydrogenic model including only the principal quantum number dependence is used. In Fig.2 the number attached each line represents the principal quantum number ,and the population P_n divided by the statistical weight g_n is shown. It is found from Fig.2 that the shells up to the M-shell (n=3) are fully occupied and the N-shell (n=4) is partially occupied with $P_n/g_n \cong 50$ %. Therefore, in the present note we treat the electron configuration where the shells up to n=3 are fully occupied and the shell of n=4 is partially occupied.

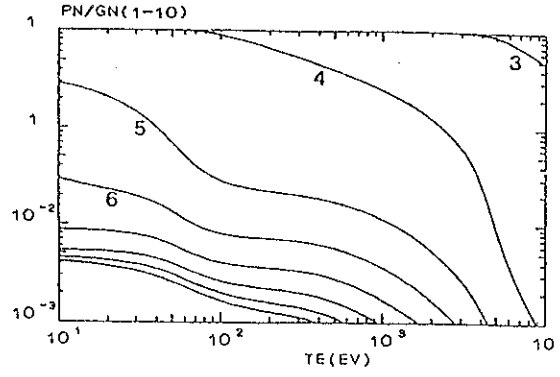

Fig.2 The relation between occupation number of each shell and electron temperature with the result of Collisional Radiative Equiliblium in the case of Au

In present calculation, all configurations are the ground state and farthermore the presence of excited electron is neglected, because it has almost no influence on the atomic data.

Calculation and Discussion

Fig.3 shows the energy levels of N-shell and O-shell with various atomic models. SHML has two adjustable parameters, one is $\sigma_{nn'}$ which is the screening constant and two dimensional tabulated parameter, and the other is v_{nl} which is one dimensional parameter. These two parameters are fitted so that energy levels of SHML have good agreements with those obtained by HFS for neutral atoms. However SHML dose not fit well in the region of highly ionized atom as seen in Fig.3. In Fig.3 the difference of energy levels between SHM or SHML and HFS is shown for the case with the number of bound electrons 44 and 55. It is seen that SHML better fits HFS for the case with larger number of bound electrons. If we vary the constants $\sigma_{nn'}$ and v_{nl} according to the ionization state, it's possible to apply this model even for highly ionized atoms.

Fig.4 shows the comparison of oscillator strengthes of transitions related to the N- and O-shells calculated with HFS to those obtained by a simple model with SHML and modified hydrogenic wave functions. As seen in Fig.4, the transition energy and oscillator strength of the transition in the same shell are well reproduced by the simple model compared with those between the different shells. The disagreement about the 4-5 transition is considerable. It is noted that at the 4f-5d

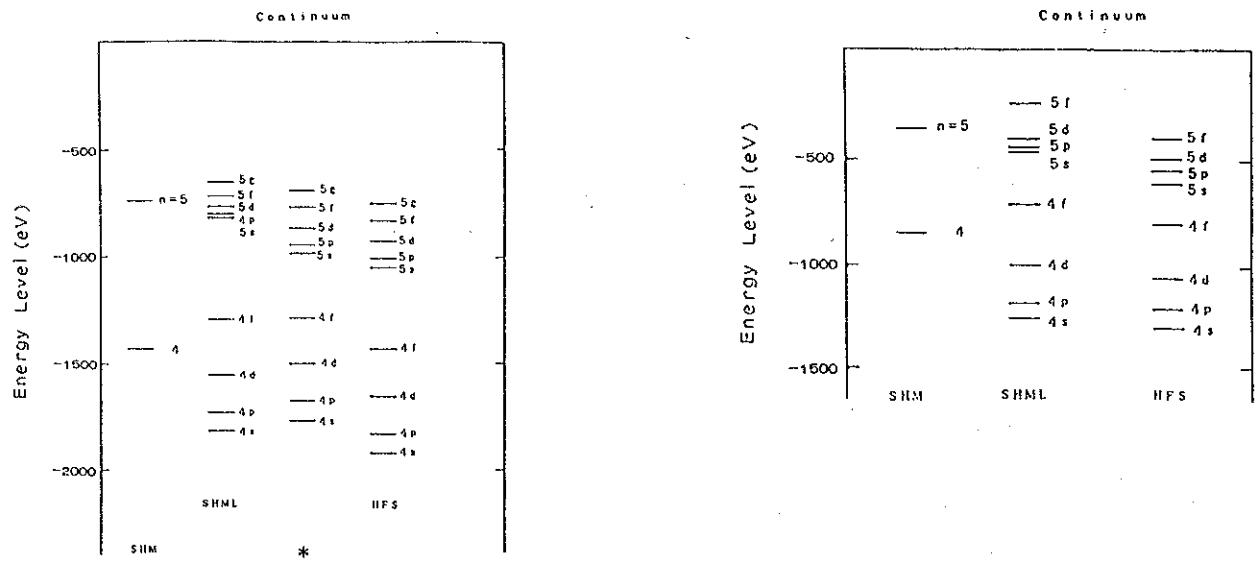

44 electrons bounded　　55 electrons bounded

Fig.3 The energy levels of N-shell and O-shell obtained by various atomic models (* ; No Slator term is included)

transition the oscillator strength of 4f-5d by HFS is relatively small, but it's about eight times larger than that by SHML. Though the profile of radiation spectrum depends on the balance of population in each orbit , the vacancy at 400 eV on the numerical spectrum seen in Fig.1 will be filled by employing the atomic data of HFS. It should be also noted that the oscillator strengthes of 4f-5g,4d-5f,4p-5d, and 4s-5p which give the so-called N-band emission are overestimated in the simple model.

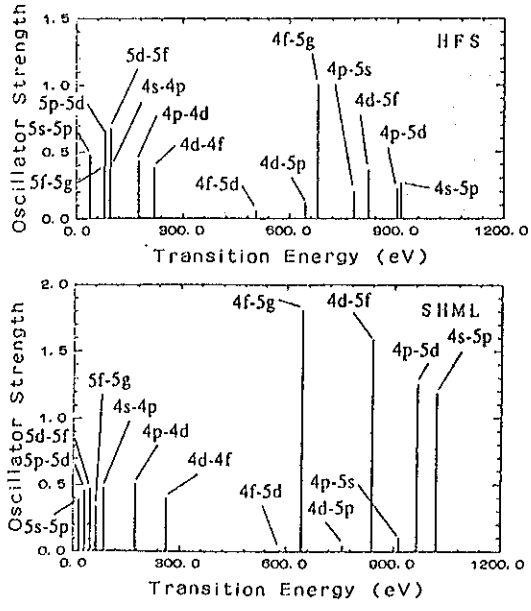

Fig.4 Oscillator strength relating to the N-shell and O-shell obtained by HFS and SHML where 44 electrons are bounded in the ground state

In Fig.5, the oscillator strength and transition energy for the important transitions are shown as the functions of the number of bound electrons in the n=4 shell. It is noted that they are simply varying functions and can be used as a data base for line radiations due to singly excited electron configuration.

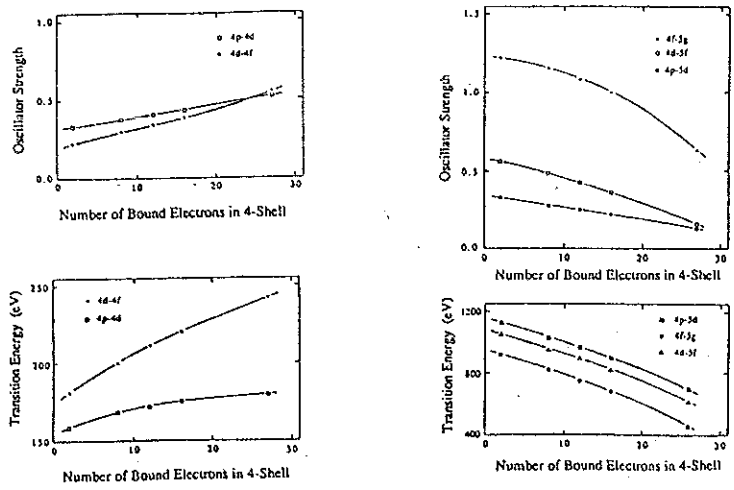

Fig.5 Oscillator strength and transition energy related with the occupation number of N-shell

Conclusion

We have calculated the atomic data of energy levels and oscillator strength by solving Hartree-Fock Slator model for partially ionized gold ions. The resultant data have been compared with the corresponding ones used in the numerical simulation in which a simple screened hydrogenic model with l-splitting effect is used.

It is found that the discrepancy of energy levels is enhanced as the ionization level becomes higher. This may be due to the fact that the screening constants are obtained so that the energy levels coincide with those obtained by HFS model for the case of almost neutral atoms.

The oscillator strength for 4p-4d and 4d-4f lines are found to be well modeled by the simple method, while those for 4f-5g, 4d-5f, 4p-5d, and 4s-5p forming so-called N-band emission are poorly modeled and HFS results less strong line emission. The line emission of 4f-5d which is located at $h\nu$=400 eV, and has sufficiently weak transition probability in the simple model, is found to have eight times larger probability in HFS model. This may help to fill up the dip near 400 eV seen in the simulation of Fig.1.

References

(1) F.Perrot, Physica Scripta, Vol. 39, P.332-337, 1989.
(2) T.Nishikawa, H.Takabe, and K.Mima, in the same proceedings.
(3) A.Rickert, and J.Meyer-Ter-Vehn, Laser and Particle Beams, Vol.8, No.4, 1990.
(4) R.M.More, Quant. Spectrosc. Radiat. Transfer, Vol.27, P.345-357, 1982.
(5) H.A.Bethe, and E.E.Salpeter, Quantum Mechanics of One- and Two- Electron Atoms, Plenum Publishing Corporation, New York, 1977.
(6) H.Takabe, Research Report, Institute of Laser Engineering at Osaka University, ILE 9008p, 1990.

Radiation Transport Dependence on Modeling in Laser-Produced Plasmas

A.Nishiguchi and K.Mima*

Institute for Laser Technology
*Institute of Laser Engineering

The radiation transport property is examined with several different modeling especially the collisional ionization rate coefficient and bound-bound opacity treatment(line transport) in laser produced plasmas. The rate equation is solved coupled with the implosion hydrodynamic. The difference of total emitted radiation energy loss for different rate coefficient is up to 35% and especially the difference of the K-shell emission is up to 110%. The difference due to the bound-bound opacity treatment is about 50%.

The high density compression by laser considerably depends on the effects of radiation transport. There are many modeling of atomic physics. Here we investigate the dependence of radiation property on ionization rate and bound-bound opacity. The typical experimental parameter of the high density compression in ILE is used for calculation. The silicon doped CDT shell target of radius 247μm and thickness 8.71μm is irradiated by the stacked laser pulse of energy 8.14kJ and pulse width 1.91nsec. The total radiation energy emitted from the surface is observed. The following four collisional ionization rates are examined.

Landshoff-Perez[1)]

$$1.24\times10^{-6}T^{-\frac{3}{2}}\left\{\frac{0.915}{(u+0.64)^2}+\frac{0.42}{\left(u^2+0.5\right)^2}\right\}\exp(-u)$$

Lotz[2)]

$$3\times10^{-6}T^{-\frac{3}{2}}\frac{Ei(u)}{u}$$

Seaton[3)]

$$2.15\times10^{-6}T^{-\frac{3}{2}}\frac{\exp(-u)}{u^2}$$

Mcwhirter[4)]

$$2.34\times10^{-7}T^{-\frac{3}{2}}\frac{\exp(-u)}{u^{\frac{7}{4}}}$$

The dependence of ionization probability on plasma temperature is shown in Fig.1 for each model. The results for each model is shown in Table I. The difference of total emitted radiation loss is 50%. Especially the K-shell line emission of Landshoff Perez model is two times larger than that of Lotz model.

The bound-bound opacity has the structure of Fig.2(b),but Fig2(a) in the average ion model[5]. In the treatment of radiation with multigroup model, the one bound-bound opacities added to the group opacity. The addition method of two extremes is considered;one is the conserving of the area and another the conserving of the value(height)(see Fig.3). The radiation loss dependences on the two case for Landshoff-Perez and Seaton are shown in TableII. The difference of the two case is about 50% for both models.

References

1.R.K.Landshoff and J.D.Perez, Phys. Rev. A**13**,1619(1976).

2.W.Lotz, Z.Phys. **216**,241(1968).

3.M.J.Seaton, in Atomic and Molecular Processes, edited by D.R.Bates (Academic, New York,1962), p.375.

4.R.W.P.McWhirter, in Plasma Diagnostic Techniques, edited by R.H.Huddlestone and S.L.Leonard (Academic, New York, 1965).

5.M.Itoh, T.Yabe, and S.Kiyokawa, Phys. Rev. A**35**,233(1987).

Collisional-ionization model	K-shell line (J)	Radiation loss (J)	ρR(g/cm^2)
Landshoff-Perez	2.01	90.1	0.649
Lotz	0.95	70.6	0.757
Seaton	1.02	66.6	0.761
McWhirter	2.10	91.1	0.640

Table I. Model dependence of emitted radiation energy and ρR.

Collisional ionization model	case 1 (J)	case 2 (J)
Landshoff-Perez	105.2	74.6
Seaton	99.1	66.6

Table II. Radiation loss energy dependence on the treatment of Bound-Bound opacity treatment.

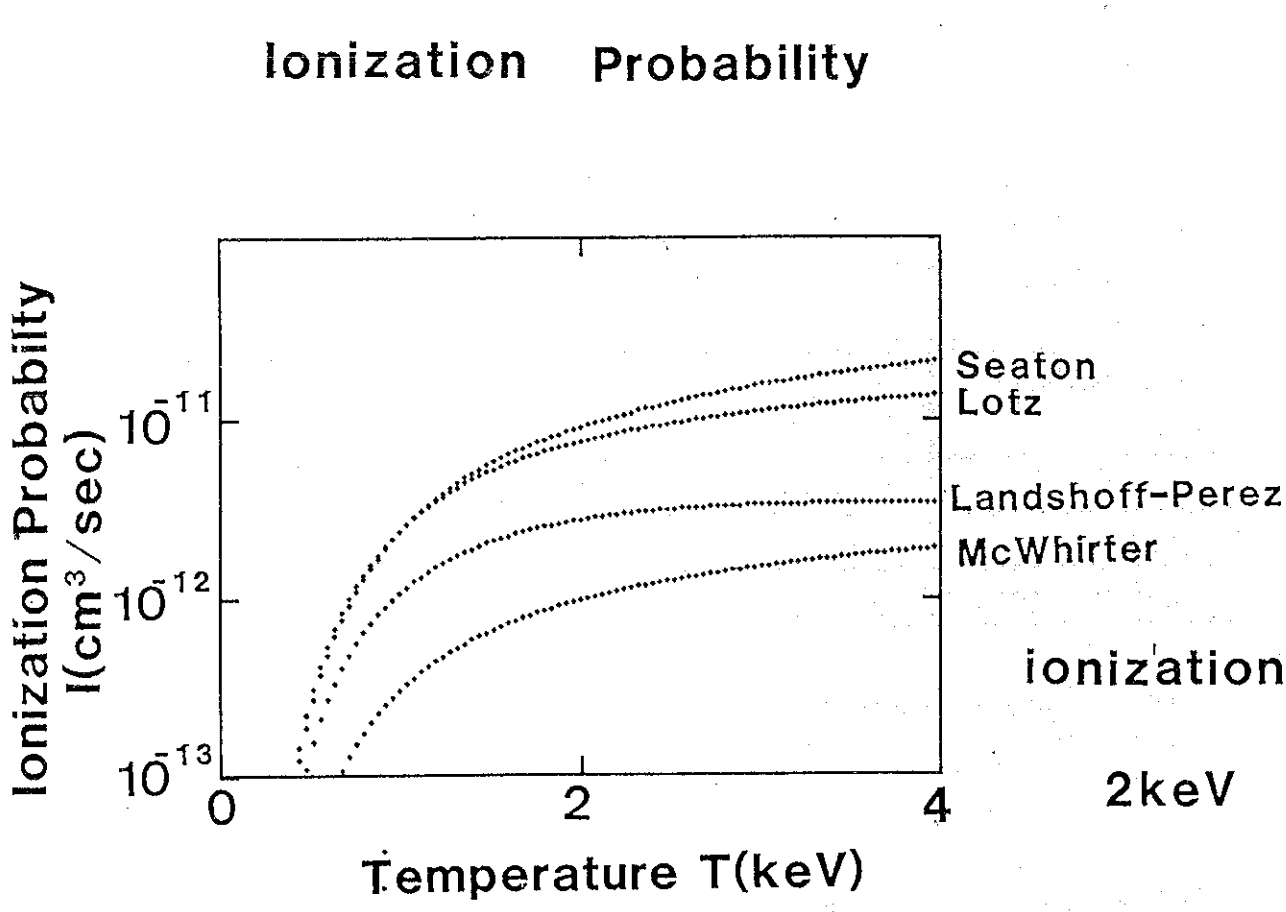

Fig.1 The collisional ionization rate of four model as a function of plasma temperature. The ionization energy is 2keV.

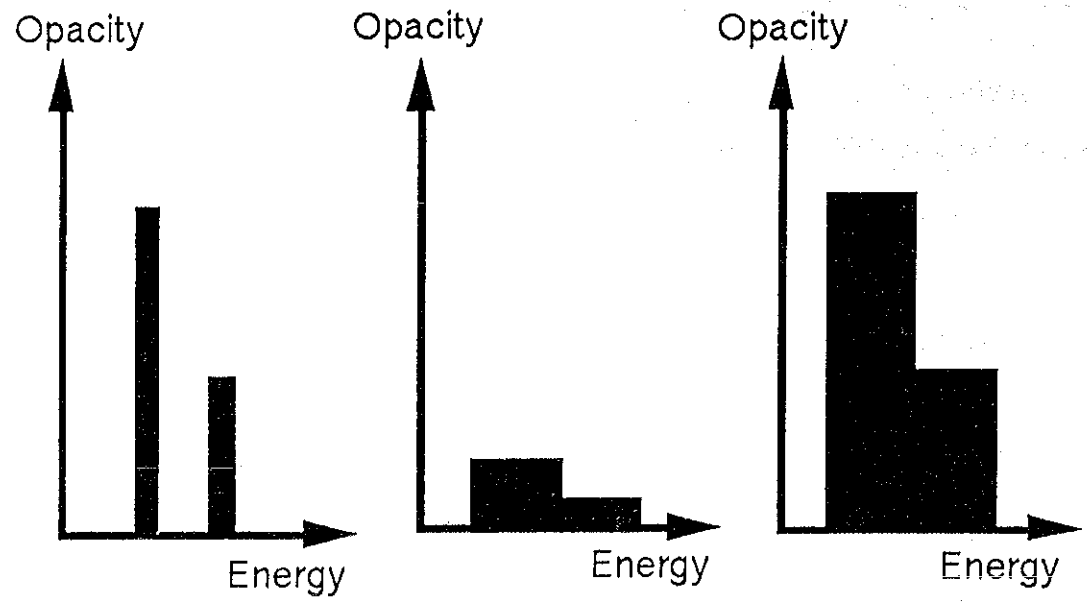

(a) line opacity (b) case 1 (c) case 2

Fig.3 Two addition method of bound-bound opacity to the multigroup. (a)shape of line opacity. (b)the conserving of the value. (c)the conserving of area.

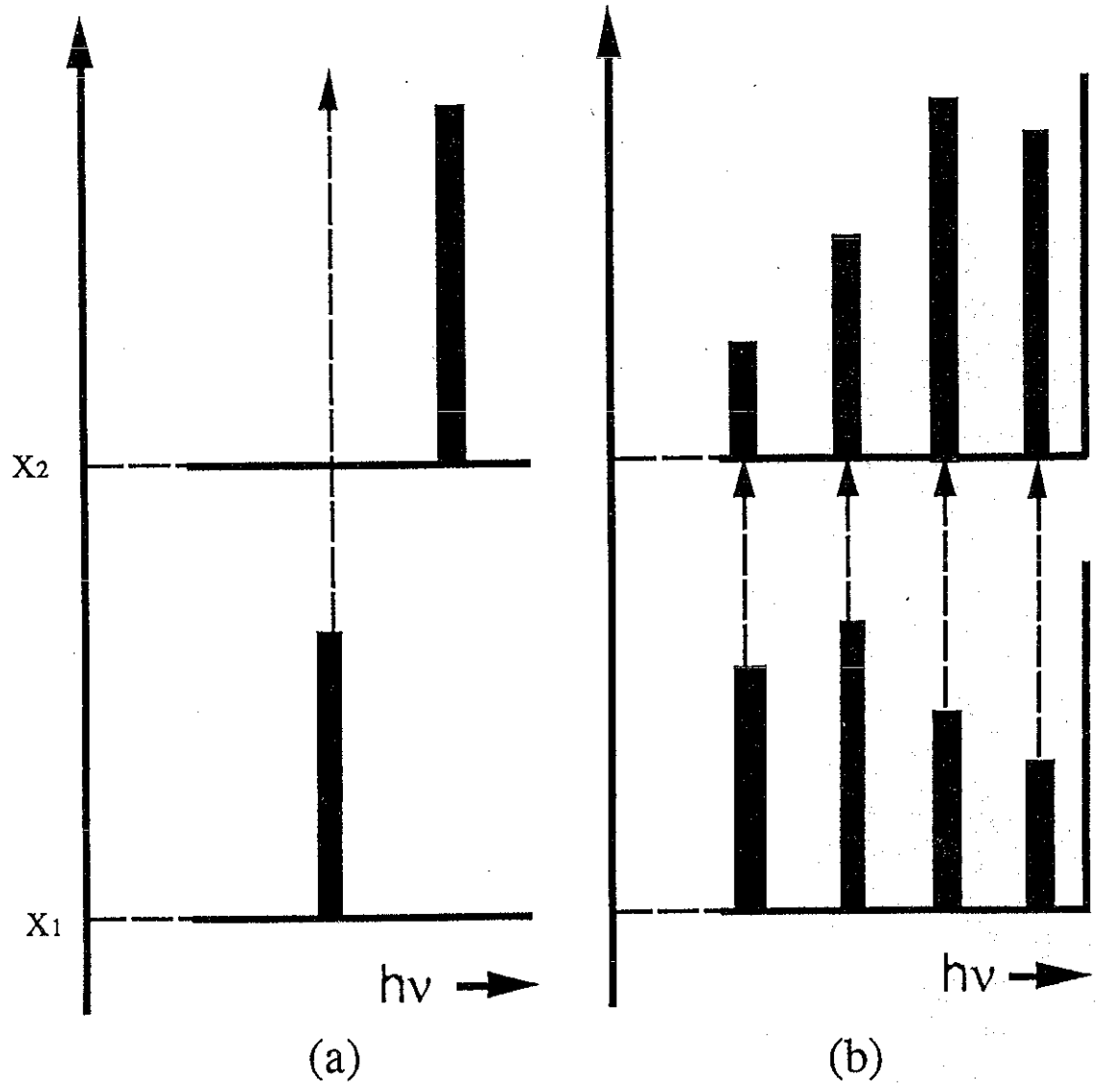

Fig.2 The line radiation is emitted at some point x_1 and absorbed at x_2. (a)In the average-ion model, there is only one fictitious ion at each space. The level energy of ion changes from space to space depending on the average charge z^a which follows physical parameters. Consequently, the level energy shift between x_1 and x_2,which does not occur in actual plasmas, exists and the line radiation emitted at x_1 is no more absorbed by the same spectral line at x_2. (b)In the real situation, there exists an ion having the same charge z in all region although the abundance Nz changes from space to space. This means that a spectral line emitted at one region can always be absorbed by the same line in whole space with varying amount.

Relativistic Configuration Interaction Theory for Atomic Systems

Takashi Kagawa, Yoshie Honda and Shuji Kiyokawa

Department of Physics, Nara Women's University
Nara 630, Japan

Abstract: The relativistic configuration interaction (RCI) method with analytical relativistic Hartree-Fock-Roothaan (RHFR) basis functions for atomic systems is presented. One-electron functions used for constructing configuration state functions (CSF's) are obtained with the RHFR method in which the large and small components of the radial part of a four-component wavefunction are expanded in terms of an analytical basis set consisting of Slater-type orbitals.

Numerical application of the method to neonlike atomic systems is carried out. It is shown that calculated excitation energies with the method are in good agreement with experiment.

Highly ionized atoms have attracted special interest in modern atomic physics and other related fields such as astrophysics and plasma physics. Lines emitted from highly ionized atoms such as the first transition elements immersed in solar, stellar and laboratory plasmas have been playing a very important role in modelling these matters. In the analysis of the spectra observed, accurate level structures and optical oscillator strengths for an atom in various charge states are required.

Using the Dirac-Breit Hamiltonian for many-electron atoms, various relativistic atomic structure theories such as the Dirac-Hartree-Fock (DHF) one by use of the finite difference numerical method[1], analytical relativistic Hartree-Fock-Roothaan (RHFR),[2,3] multiconfiguration Dirac-Fock (MCDF)[4,5], analytical multiconfiguration relativistic Hartree-Fock-Roothaan (MCRHFR)[6] ones.

For the purpose of calculating energies for states consisting of a large number of multiplet terms in highly ionized atoms systematically, the relativistic configuration interaction method (RCI) is also one of the most powerful and efficient methods. Hagelstein[7] has made RCI calculations for highly ionized atoms, where a basis set for constructing the configuration state functions (CSF's) is obtained with the DHF calculation for corresponding fictitious closed-shell systems which have an electronic configuration containing excited orbitals with fractional occupation numbers. However, there have so far been reported few RCI calculations for atoms with large basis sets and the effectiveness of the method has not been investigated sufficiently. The whole scheme of the method is much more simple than that of the MCDF one, since the latter method requires to solve extra coupled self-consistent field equations to determine one-electron wave functions in each calculation. Naturally accuracy of a RCI calculation deeply depends on one-electron functions used as a basis set.

In this report, we present the relativistic configuration interaction (RCI) method with a basis set in terms of analytical relativistic Hartree-Fock-Roothaan (RHFR) functions. By using Slater-type orbitals (STO's) with noninteger powers of r, a set of one-electron functions (OEF's) for constructing CSF's are obtained from the RHFR calculations[3] for not only the ground state but also some singly-excited states in the systems under consideration. The RHFR calculations for excited states are carried out when OEF's belonging to the different symmetry from those contained in the ground-state configuration are needed in the RCI calculation.

The operator $H_B(i,j)$ due to the Breit interaction between two electrons is neglected in the RHFR calculations but is treated by using the first-order-perturbation theory in the RCI calculation. The QED corrections or the Lamb-shift energies such as the self energy and the vacuum polarization energy are not included in the present theory

because they are higher-order corrections compared with the Coulomb or Breit interaction energies. The optical oscillator strengths for various transitions in a system are calculated relativistically with the RCI energies and the wavefunctions obtained.

Using 23 OEF's consisting from the 1s up to $5f_{7/2}$ RHFR functions, we carry out the RCI calculations to obtain the energies for the ground and singly-excited states in neon isoelectronic sequence. Here we show the calculated resuts in Fe^{16+} to see the effectiveness of the theory.

In Table, we compare the RCI transition energies for the E1 transitions in Fe^{16+} with the experimental ones[8]. For the states up to n=4, experimental data are complete. It is seen from the table that the RCI excitation energies are in good agreement with experiment. Error in the RCI transition energies for some n=2-5 transitions especially for the $2p_{1/2}$-$5d_{3/2}$ one becomes large compared with those for the n=2-3 and the n=2-4 transitions because of the insufficient basis set to describe wavefunctions for these excited states adequately.

Concerning the oscillator strength for the E1 transitions considered in this ion, the RCI oscillator strengths in the length form f_L for all the transitions except the n=2-5 ones are consistent with those with other theoretical methods,[8] where the f_L values for the 2p-3s and 2p-3d transitions listed in the last column in the table are the RRPA ones of Shorer[9].

The present RCI method has a merit that one can save much computaion time when obtaining a large number of multiplet states in atomic systems because of an analytical form of the basis set. The theoretical transition energies and oscillator strengths for various transitions obtained for an atomic isoelectronic sequence will be very useful in identifying the lines observed.

References

1. I.P. Grant, Adv. Phys. 19, 747 (1970).

2. Y.-K. Kim, Phys. Rev. 154, 17 (1967).
3. T. Kagawa, Phys. Rev. A12, 2245 (1975).
4. J.P. Desclaux, Comput. Phys. Commun. 9, 31 (1975).
5. I.P. Grant, B.J. McKenzie, P.H. Norrington, D.F. Mayers and N.C. Pyper, Comput. Phys. Commun. 21, 207 (1980).
6. T. Kagawa: Phys. Rev. A22, 2340 (1980).
7. P.L. Hagelstein, Phys. Rev. A34, 924 (1986).
8. T. Shirai, Y. Funakata, K. Mori, J. Sugar, W. L. Wiese and Y. Nakai, J. Phys. Chem. Reference Data 19, 127 (1990).
9. P. Shorer, Phys. Rev. A20, 642 (1979).

Table. Transition energies and oscillator strengths with the length form f_L for the E1 transitions from the ground state in neonlike Fe(Z=26).

State	Transition Energy (cm^{-1})			f_L	
	RCI	Exp.[a]	ΔE	RCI	Others[a]
$2s^22p^53s$ $(\frac{3}{2},\frac{1}{2})_1^o$	5875609	5864770	10839	0.0829	0.122
$2s^22p^53s$ $(\frac{1}{2},\frac{1}{2})_1^o$	5969957	5960870	9087	0.0447	0.105
$2s^22p^53d$ $(\frac{3}{2},\frac{3}{2})_1^o$	6482760	6471800	10960	0.0049	0.001
$2s^22p^53d$ $(\frac{3}{2},\frac{5}{2})_1^o$	6564236	6552200	12036	0.6189	0.629
$2s^22p^53d$ $(\frac{1}{2},\frac{3}{2})_1^o$	6680481	6660000	20481	2.5501	2.31
$2s2p^63p$ $(\frac{1}{2},\frac{1}{2})_1^o$	7225645	7198900	26745	0.0305	0.029
$2s2p^63p$ $(\frac{1}{2},\frac{3}{2})_1^o$	7260860	7234300	26560	0.3148	0.28
$2s^22p^54s$ $(\frac{3}{2},\frac{1}{2})_1^o$	7900034	7885800	14234	0.0133	0.022
$2s^22p^54s$ $(\frac{1}{2},\frac{1}{2})_1^o$	7997853	7983000	14853	0.0067	0.025
$2s^22p^54d$ $(\frac{3}{2},\frac{3}{2})_1^o$	8132412	8116000	16412	0.0033	0.004
$2s^22p^54d$ $(\frac{3}{2},\frac{5}{2})_1^o$	8168769	8154000	14769	0.4095	0.40
$2s^22p^54d$ $(\frac{1}{2},\frac{3}{2})_1^o$	8260958	8249000	11958	0.4168	0.53
$2s^22p^55s$ $(\frac{3}{2},\frac{1}{2})_1^o$	8773600	8757000	16600	0.0043	0.007
$2s^22p^55s$ $(\frac{1}{2},\frac{1}{2})_1^o$	8872484	8860000	12484	0.0002	0.004
$2s^22p^55d$ $(\frac{3}{2},\frac{5}{2})_1^o$	8899330	8887000	12330	0.2105	0.13
$2s2p^64p$ $(\frac{1}{2},\frac{1}{2})_1^o$	9085388	9056000	29388	0.0183	0.016
$2s2p^64p$ $(\frac{1}{2},\frac{3}{2})_1^o$	9097026	9072000	25026	0.1117	0.11
$2s^22p^55d$ $(\frac{3}{2},\frac{3}{2})_1^o$	9689956			0.1157	
$2s^22p^55d$ $(\frac{1}{2},\frac{3}{2})_1^o$	9829893	8982000	847893	0.4604	0.18
$2s2p^65p$ $(\frac{1}{2},\frac{1}{2})_1^o$	9925981	9878000	47981	0.0003	
$2s2p^65p$ $(\frac{1}{2},\frac{3}{2})_1^o$	9929645	9878000	51645	0.0727	

a) Reference 8.

Atomic Process in High Intensity Electromagnetic Field

S. Kato and K. Mima

Institute of Laser Engineering, Osaka University,
Suita, Osaka, 565, Japan

abstract

Recently, plasmas produced by an intense ultrashort pulse (pulse width < 1ps) laser has attracted much interest. In such a case, the above-threshold-ionization (ATI) or multiphoton ionization process is dominant is comparison with the collisional ionization. In plasmas produced by such lasers, the plasma density is almost solid density and the temperature is lower than or comparable to the Fermi temperature. Then electrons are degenerate. Since ions are strongly coupled in such plasmas, the ion-ion correlation is described by the hypernetted-chain (HNC) equation. On the other hand, the electron-ion correlation is described by the linear response theory. By using those correlation functions, evaluated are the ion potential. The behaviors of the free and bound electron in the strong laser field are investigated by the Schrödinger equation which is transformed to the Kramers-Henneberger (K-H) frame. The Schrödinger equation is numerically solved to found the temporal evolution of the electron wave function.

I. INTRODUCTION

Recently, plasmas produced by an intense ultrashort pulse (pulse width < 1ps) laser has attracted much interest. Ultrashort-pulse lasers heat a solid target before any expansion occurs. In such a case, the plasma scale length is less than the laser skin depth. Consequently, the ultrashort-pulse-laser radiation directly interacts with a solid-density plasma. Nonlinear inverse bremsstrahlung of high intensity laser is discussed by the previous paper.[1] In that paper, it shows that the inverse bremsstrahlung absorption rate decreases in the high intensity range, namely, $v_0/v_e > 1$, where v_0 is a electron quiver velocity. The inverse bremsstrahlung absorption process is a free-free transition process. However, the above-threshold-ionization (ATI) or multiphoton ionization process (bound-free transition) is more important than absorption by inverse bremsstrahlung. In the isolated system, it was reported by the one-dimensional simulations that the ionization is suppressed by high-frequency intense field.[2] In order to investigate a bound-free or bound-bound transition in a solid-density plasma, the ion potential is determined and the basic equation is derived.

The Schrödinger equation for a one-electron moving under the combined forces of a potential $\phi(\mathbf{r})$ and a radiation field $\mathbf{A}(t)$ is

$$i\hbar\frac{\partial\tilde{\Psi}(\mathbf{r},t)}{\partial t}=\frac{1}{2m}\left[\frac{\hbar}{i}\nabla-\frac{e}{c}\mathbf{A}(t)\right]^2\tilde{\Psi}(\mathbf{r},t)+\phi(\mathbf{r})\tilde{\Psi}(\mathbf{r},t) \qquad (1)$$

Under such circumstances, the very convenient treatment was proposed by Henneberger[3] for laser-atom interactions. It assumes that the laser field can be described by the dipole approximation. By applying the time-dependent translation $\mathbf{r}\rightarrow\mathbf{r}+\mathbf{r}_0(t)$ with

$$\mathbf{r}_0(t)=-\int_0^t\frac{e}{mc}\mathbf{A}(\tau)d\tau \qquad (2)$$

from Schrödinger equation of Eq.(1) we get

$$i\hbar\frac{\partial\Psi(\mathbf{r},t)}{\partial t}=-\frac{\hbar^2}{2m}\nabla^2\Psi(\mathbf{r},t)+\phi\big(\mathbf{r}+\mathbf{r}_0(t)\big)\Psi(\mathbf{r},t) \qquad (3)$$

II. BASIC FORMALISM

A. Ion Potential

It assumes that the ions do not moving during the laser pulse width. In the K-H frame, the Poisson's equation is give by

$$-\nabla^2\phi(\mathbf{r},t)=4\pi e\left[Z^*\delta(\mathbf{r}+\mathbf{r}_0(t))+Z^*n_i g(\mathbf{r}+\mathbf{r}_0(t))-n_e(\mathbf{r},t)\right] \quad , \tag{4}$$

where n_i and Z^*e are the ion number density and effective ion charge, and $g(\mathbf{r})$ and $n_e(\mathbf{r},t)$ are the radial distribution function of ion and electron number density. The background plasmas are assumed to be neutral : $Z^*n_i = n_e$. We give

$$-\nabla^2\phi(\mathbf{r},t)=4\pi e\left[Z^*\delta(\mathbf{r}+\mathbf{r}_0(t))+Z^*n_i h(\mathbf{r}+\mathbf{r}_0(t))-\delta n_e(\mathbf{r},t)\right] \quad , \tag{5}$$

where

$$h(\mathbf{r}+\mathbf{r}_0(t))=g(\mathbf{r}+\mathbf{r}_0(t))-1 \quad , \tag{6}$$

$$\delta n_e(\mathbf{r},t)=n_e(\mathbf{r},t)-n_e \quad , \tag{7}$$

and $\delta n_e(\mathbf{r},t)$ is the electron density fluctuation. The Fourier transform of Eq.(5) yields

$$\phi(\mathbf{k},\omega)=\frac{4\pi e}{k^2}\left[Z^*S(\mathbf{k})\sum_{n=-\infty}^{\infty}J_n(\mathbf{k}\cdot\mathbf{r}_0)2\pi\delta(\omega-n\omega_0)-\delta n_e(\mathbf{k},\omega)\right] \quad , \tag{8}$$

and

$$S(\mathbf{k})=1+n_i\int d\mathbf{r}h(\mathbf{r})\exp(-i\mathbf{k}\cdot\mathbf{r}) \quad , \tag{9}$$

where ω_0 is the laser frequency and we assumed that $\mathbf{r}_0(t) = \mathbf{r}_0\sin\omega_0 t$. Due to the linear response theory, $\delta n_e(\mathbf{r},t)$ is given by

$$\delta n_e(\mathbf{k},\omega)=[\varepsilon(\mathbf{k},\omega)-1]\frac{k^2\phi(\mathbf{k},\omega)}{4\pi e} \quad . \tag{10}$$

Using Eqs.(5) and (6), the shielding ion potential : $\phi(\mathbf{k},\omega)$ is given by

$$\phi(\mathbf{k},\omega)=\frac{4\pi Z^*e}{k^2}\frac{S(\mathbf{k})}{\varepsilon(\mathbf{k},\omega)}\sum_{n=-\infty}^{\infty}J_n(\mathbf{k}\cdot\mathbf{r}_0)2\pi\delta(\omega-n\omega_0) \quad . \tag{11}$$

The inverse Fourier transform of Eq.(7) yields

$$\phi(\mathbf{r},t)=\sum_{n=-\infty}^{\infty}\phi_n(\mathbf{r})\exp(in\omega_0 t) \quad , \tag{12}$$

where

$$\phi_n(\mathbf{r}) = \int \frac{d\mathbf{k}}{(2\pi)^3} \frac{4\pi Z^* e^2}{k^2} \frac{S(\mathbf{k})}{\varepsilon(\mathbf{k}, -n\omega_0)} J_n(\mathbf{k}\cdot\mathbf{r}_0)\exp(i\mathbf{k}\cdot\mathbf{r}) \quad . \tag{13}$$

The laser light is assumed to be linearly polarized field. Then, the ion potential (Eq.(13)) is given by

$$\phi_n(r,z) = \frac{Z^* e^2}{\pi^2} \int_0^\infty dk \frac{S(k)}{\varepsilon(k,-n\omega_0)} \int_0^{2\pi} d\theta \exp(in\theta) \frac{\sin kr'}{kr'} \quad , \tag{14}$$

where

$$r' = |\mathbf{r} - \mathbf{r}_0 \sin\theta| = \left(r^2 + (z - r_0 \sin\theta)^2\right)^{1/2} \quad . \tag{15}$$

The Eq.(14) shows the potential is cylindrically symmetric. Using this potential, the Schrödinger equation will be solved, and we will evaluate the ionization rate or excitation rate.

B. Schrödinger Equation

The Schrödinger equation (in atomic units) in the Kramers-Henneberger (K-H) frame is

$$i\frac{\partial \Psi(\mathbf{r},t)}{\partial t} = \hat{H}(\mathbf{r},t)\Psi(\mathbf{r},t) \quad , \tag{16}$$

where

$$\hat{H}(\mathbf{r},t) = \sum_{n=-\infty}^{\infty} \phi_n(r,z)\exp(in\omega_0 t) - \nabla^2 \quad , \tag{17}$$

and

$$\Psi(\mathbf{r},t) = \sum_{\mathbf{m}} a_{\mathbf{m}}(t)\psi_{\mathbf{m}}(\mathbf{r})\exp(-i\omega_{\mathbf{m}} t) \quad . \tag{18}$$

$\psi_{\mathbf{m}}(\mathbf{r})$ and $\omega_{\mathbf{m}}$ are the orthogonal function and its eigenvalue. This Hamiltonian has cylindrical symmetry so that we can expand on the interval $0 \le r \le a$ in a Fourier-Bessel series and on the interval $-d \le z \le d$ in a Fourier series :

$$\psi_{\mathbf{m}}(\mathbf{r}) = C_{\mathbf{m}} J_0(\lambda_{0,m_r} r / a)\exp(-i\pi m_z z / d) \quad , \tag{19}$$

where $\mathbf{m} = (m_r , m_z)$, $J_0(x)$ is a Bessel function of the first kind of order zero and $C_{\mathbf{m}}$ is the normalization factor :

$$C_{\mathbf{m}} = [2\pi d a^2 J_1^2(\lambda_{0,m_r})]^{-1/2} \quad , \tag{20}$$

λ_{0,m_r} is the m_r th root of $J_0(x) = 0$. In this expansion, $\omega_{\mathbf{m}}$ is

$$\omega_{\mathbf{m}} = \frac{1}{2}\left[(\lambda_{0,m_r}/a)^2 + (\pi m_z/d)^2\right] \quad (21)$$

Substituting Eqs.(13) - (16) into Eq.(12), we get

$$\frac{da_{k_r k_z}(t)}{dt} = \sum_n \sum_{m_r,m_z} a_{m_r,m_z}(t)\exp\left[-i(n\omega_0 + \omega_{\mathbf{m}} - \omega_{\mathbf{k}})t\right] \times \frac{-i}{d\,a^2 J_1(\lambda_{0,k_r}) J_1(\lambda_{0,m_r})} \int_{-d}^{d} dz \exp\left[-i\pi(m_z - k_z)z/d\right] \times \int_0^a r\,dr\, J_0(\lambda_{0,k_r} r/a) J_0(\lambda_{0,m_r} r/a)\phi_n(r,z) \quad (22)$$

C. Ionization Rate

The ionization rate is obtained by

$$P(t) = \int d\mathbf{W}\left|\langle \mathbf{W}|\Psi(\mathbf{r},t)\rangle\right|^2 , \quad (23)$$

or

$$P(t) = 1 - \sum_{\mathbf{n}}\left|\langle \mathbf{n}|\Psi(\mathbf{r},t)\rangle\right|^2 , \quad (24)$$

where **W** and **n** are free and bound state wave function.

III. SUMMARY

We derive a ion potential in solid-density plasmas under intense laser field. In order to calculate the ionization rate, a basic concept is discussed in sec.II. The ionization rate and laser absorption rate will be discussed in a future paper.

Reference

1. S.Kato, R.Kawakami and K.Mima, Phys.Rev. **A43**, 5560 (1991)
2. Q.Su and J.H.Eberly, Phys.Rev. **A43**, 2474 (1991)
3. W.C.Henneberger, Phys.Rev.Lett. **21**, 838 (1968)

Improvement of Spherical Cell Model and Its Application to Hot, Dense Plasmas

H. Furukawa

Institute of Laser Engineering, Osaka University

Within the framework of the Density Functional Theory (DFT), a new atomic model based on the Spherical Cell Model (SCM) is developed (Ref. 1, 2). Calculated are the correlation functions among particles and the effective potential acting on an electron and an ion by solving a set of the coupled modified Poisson - quantal hyper-netted chain (QHNC) - Schrödinger equations for hot, dense plasmas numerically. The results are compared with other theoretical models (Ref. 3, 4).

1. Introduction

For highly compressed plasmas, for an example, the plasma of six hundred times of solid density which has been recently made with the use of a deuterated polystyrene shell target[5] at ILE, the thermal de Broglie wavelength defined by $\lambda\!\!\!^{-}_e=\hbar/(2\pi m_e k_B T)^{1/2}$ and the electron sphere radius defined by $a_e=(3/4\pi n_e)^{1/3}$ are comparable. Where m_e is the electron mass, k_B is the Boltzmann constant, T is the plasma temperature and n_e is the electron number density. In such a region, the Coulomb coupling constant for ions defined by

$$\Gamma=\frac{\langle Z^{5/3}\rangle e^2}{a_e k_B T} \quad , \qquad (1)$$

is approximately equal to 1~10, and the electron degeneracy defined by

$$\theta=k_B T/\varepsilon_F \quad , \qquad (2)$$

is approximately equal to 0.1~1. Where Z is the atomic number, e is unit charge and ε_F is Fermi energy. It is very important for laser fusion to calculate various thermodynamics functions of plasmas in such a region. In order to investigate such highly compressed partially degenerate plasmas, the quantum diffraction effects should be taken into account through the Schrödinger equation, many body effects are also important because of high density, the nonlinear electric shielding and Fermi degeneracy effects should be taken into account. The spherical cell model[1,2] (SCM) is developed by Perrot and Dharma-wardana. By the SCM, it is possible to determine various effective pair potentials, pair distribution functions, bound states, and the effective charge of ions $Z^*=Z-N_{be}$, with N_{be} a mean number of bound electrons per ion in a self-consistent manner. But in the SCM, the treatments of bound electrons, Fermi degeneracy effects and free electron-free electron correlation effects are not enough to describe such plasmas. I have developed a new atomic model which includes the treatments mentioned above based on the SCM. In the next section, described are the outline of the new atomic model.

2. Outline of atomic model

The outline of the calculation is as follows.

1). Using modified T-F model[4], the initial potential of the Schrödinger equation is obtained.

2). Using the initial potential, the Schrödinger equation is solved and the initial electron-ion pair distribution function is calculated.

3). Solving OCP HNC equations, obtained are the initial ion-ion and electron-electron pair distribution functions.

4). Using the pair distribution functions, calculated are the effective potentials.

5). Using the effective potentials calculated are the pair distribution functions.

6). I repeat 4) and 5) until the iteration is converge.

In Fig. 1, the schematic diagram of the present atomic model is illustrated.

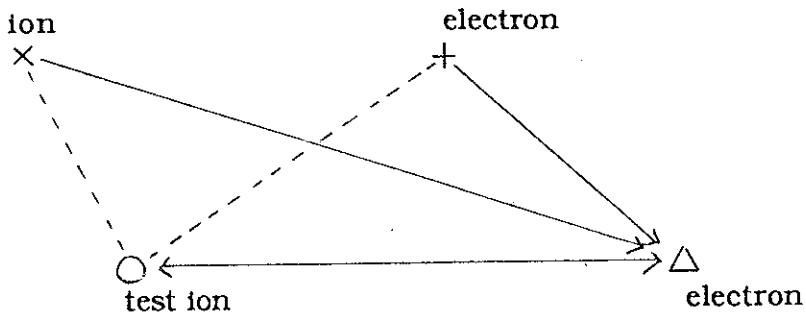

Fig. 1 The schematic diagram of the present atomic model.
x and + are the ions and electrons around the test particle.
The allows means the potentials V_{e-i}.
And the dashed lines are the correlation taking into account.

3. Electron number density around a test ion

The boundary conditions of solving the Schrödinger equation in hot, dense plasmas are described in Refs. 1,2 and 6 in detail.

The elementary quantum theory tells us that the local electron density around a test ion can be written as

$$n_{e-i}(r) = \bar{n}_{fe} + n_{be}(r) + \Delta n_{fe}(r) \quad , \qquad (3)$$

with

$$n_{be}(r) = \sum_{n,\ell} (2\ell+1)\left|R_{n,\ell}(r)Y_{\ell,0}(\theta,\varphi)\right|^2 f(E_{n,\ell}) \quad , \qquad (4)$$

and

$$\Delta n_{fe}(r) = \frac{1}{\pi^2}\int_0^\infty dk\, k^2 f(k) \sum_{\ell=0}^{\infty} (2\ell+1)\left[R_{k,\ell}{}^2(r) - R_{k,\ell}{}^{(0)2}(r)\right] \quad , \qquad (5)$$

where $\bar{n}_{fe}$ is the average free electron number density, $n_{be}(r)$ is the bound electron number density, $\Delta n_{fe}(r)$ is the displaced free electron number density in atomic unit, $R_{n\ell}$ and $R_{v\ell}$ are the radial wave functions, $Y_{\ell 0}$ is the spherical harmonics and f is Fermi distribution function. Since the magnetic

effects are not included in this model, in the spherical harmonics $Y_{\ell m}$ the magnetic number m is always zero and the factor $2\ell+1$ originates in the summation about the magnetic number m. In Eq. (5) the $R_{k\ell}^{(0)}$ is the solution of the Schrödinger equation when $V_{e\text{-}i}(r)=0$, and are compensate $R_{k\ell}$ in the asymptotic region and rapid convergence of ℓ-sum.

The self-consistency of whole calculation can be tested by the finite-temperature version of Friedel sum rule[7]

$$Z^* S_{ii}(0) = \frac{2}{\pi}\int_0^\infty f(k)dk \sum_{\ell=0}^{\infty}(2\ell+1)\frac{d\delta_\ell(k)}{dk} \quad , \qquad (6)$$

where S_{ii} is the ion structure factor, δ_ℓ is the phase shift and

$$Z^* = Z - N_{be} \quad , \qquad (7)$$

$$N_{be} = \int n_{be}(r)\, d\mathbf{r} \quad . \qquad (8)$$

An integration by parts gives, with the convention $\delta_\ell(0)=0$,

$$Z^* S_{ii}(0) = \frac{2}{\pi k_B T}\int_0^\infty k\, f(k)[1-f(k)] \sum_{\ell=0}^{\infty}(2\ell+1)\delta_\ell(k)dk \quad . \qquad (9)$$

The r_{max} should be determined satisfying the condition of Eq. (6) or Eq. (9).

4. Effective potentials

The effective potentials $V_{fe\text{-}fe}(r)$, $V_{e\text{-}i}(r)$ and $V_{i\text{-}i}(r)$ are determined as follows[8-10].

$$-\beta V_{fe-fe}(r) = -\beta\frac{e^2}{r} + \gamma_{fe-fe}(r) \quad , \qquad (10)$$

$$-\beta V_{e-i}(r) = \beta\frac{Ze^2}{r} + \gamma_{fe-i}(r) - \beta\upsilon_{be}(r) \quad , \qquad (11)$$

$$-\beta V_{i-i}(r) = -\beta \frac{Z^{*2} e^2}{r} + \gamma_{i-i}(r) \quad , \quad (12)$$

where

$$\upsilon_{be}(r) = \int \upsilon(|\mathbf{r}-\mathbf{r}'|)\, n_{be}(r')\, d\mathbf{r}' + \mu_{xc}(n_{be}(r)+\bar{n}_{fe}) - \mu_{xc}(\bar{n}_{fe}) \quad , \quad (13)$$

$$\upsilon(r) = e^2 / r \quad , \quad (14)$$

where $\beta=1/k_BT$ and μ_{xc} is the exchange-correlation potential[11]. γ_{fe-fe}, γ_{fe-i} and γ_{i-i} are determined as

$$\hat{\gamma}_{\mu-\nu}(k) = \sum_j \bar{n}_j \hat{c}_{\mu-j}(k) \hat{p}_{j-\nu}(k) \quad , \quad (15)$$

where

$$p_{\mu-\nu}(r) = n_{\mu-\nu}(r) / \bar{n}_\mu - 1 \quad . \quad (16)$$

$c_{\mu-\nu}$ is the direct correlation function and the suffix $\mu-\nu$ denotes μ-type particles around ν-type particles. Note that if both of μ and ν denote free electron, $p_{\mu-\nu}$ is not equal to $h_{\mu-\nu}$, where $h_{\mu-\nu}$ is pair correlation function. Otherwise $p_{\mu-\nu}$ is equal to $h_{\mu-\nu}$. Within the quantal hypernetted-chain (QHNC)[8] approximation, $p_{\mu-\nu}$ and $c_{\mu-\nu}$ satisfy the Ornstein-Zernik relation for a two-component plasma

$$\hat{p}_{fe-fe}(k) - \tilde{\chi}_{fe}{}^0(k) \hat{c}_{fe-fe}(k) = \tilde{\chi}_{fe}{}^0(k)\, \hat{\gamma}_{fe-fe}(k) \quad , \quad (17)$$

$$\hat{p}_{fe-i}(k) - \tilde{\chi}_{fe}{}^0(k)\, \hat{c}_{fe-i}(k) = \tilde{\chi}_{fe}{}^0(k)\, \hat{\gamma}_{fe-i}(k) \quad , \quad (18)$$

$$\hat{p}_{i-fe}(k) - \tilde{\chi}_{fe}{}^0(k) \hat{c}_{i-fe}(k) = \tilde{\chi}_{fe}{}^0(k)\, \hat{\gamma}_{i-fe}(k) \quad , \quad (19)$$

$$\hat{p}_{i-i}(k) - \hat{c}_{i-i}(k) = \hat{\gamma}_{i-i}(k) \quad , \quad (20)$$

where

$$\tilde{\chi}_{fe}{}^{0}(k) = \chi_{fe}{}^{0}(k) / \{-\beta \bar{n}_{fe}\} \quad , \quad (21)$$

$$\chi_{fe}{}^{0}(k) = -\frac{\bar{n}_e}{k_B T}\frac{3\theta}{4K} \int_0^\infty dx \frac{x}{1+\exp\{(x^2-M)/\theta\}} \ln\left|\frac{2x+K}{2x-K}\right|^2 \quad , \quad (22)$$

$$K = \frac{k}{(3\pi^2 \bar{n}_e)^{1/3}} \quad . \quad (23)$$

Note that $\bar{n}_e$ is average total electron number density and is equal to $<Z>n_i$, but $\bar{n}_{ef}$ is equal to $<Z^*>n_i$. M is chemical potential normalized by Fermi energy ε_F and determined by the equation

$$\frac{1}{3}\frac{\langle Z^* \rangle}{\langle Z \rangle} = \int_0^\infty dx \frac{x^2}{1+\exp\{(x^2-M)/\theta\}} \quad . \quad (24)$$

The hat mark means the Fourier-transform. In the classical limit[12], quantal hypernetted-chain (QHNC) approximation reduces to classical hypernetted-chain (HNC) approximation

$$\hat{h}_{\mu-\nu}(k) - \hat{c}_{\mu-\nu}(k) = \sum_{\gamma} \bar{n}_\gamma \, \hat{c}_{\mu-\gamma}(k) \, \hat{h}_{\gamma-\nu}(k) \quad . \quad (25)$$

The ion-ion pair distribution function $g_{i-i}(r)$ is calculated using $V_{i-i}(r)$ as

$$g_{i-i}(r) = \exp\{-\beta V_{i-i}(r)\} \quad . \quad (26)$$

The free electron distribution function around a free electron is calculated using $V_{fe-fe}(r)$ as

$$n_{fe-fe}(r) = \frac{1}{\pi^2} \int dk\, k^2 f_{fe-fe}(k) \quad , \quad (27)$$

and

$$f_{fe-fe}(k) = \frac{1}{1+\exp\left[\beta\left\{k^2/2 + V_{fe-fe}(r) - \mu\right\}\right]} \quad , \quad (28)$$

where μ is chemical potential defined by Eq. (24).

5. Results and discussions

The correlation functions among particles are obtained by the atomic model. The parameters are Z=1, r_s=1 and T=25eV (Γ=1.088, θ=0.4989 and n_i=1.611x10^{24} cm^{-3}). r_s is defined as

$$r_s = \frac{a_e}{a_B} \quad . \quad (29)$$

Figure 2 shows the free electron distribution functions around a free electron. The horizontal axis represents the distance normalized by the electron sphere radius a_e. The solid line shows that obtained by presented model using the QHNC equation, solid-dashed line shows that obtained by presented model using the classical HNC equation and the dashed line shows that by S. Ichimaru et al[3] by the approximation of classical electron one component plasma. The solid line is enhanced compared with the dashed line, because in the Ichimaru model the degeneracy effects and ion correlation effects are not included. And the solid line is almost the same as the solid dashed line. It means that the quantal diffraction effects on the free electron distribution functions around a free electron is very smaller than the Fermi degeneracy effects on that.

Figure 3 shows the electron-ion pair distribution functions. The horizontal axis represents the distance normalized by the ion sphere radius a. The solid line shows the electron-ion pair distribution function obtained by presented model using the QHNC equation, the solid-dashed line shows that by presented model using the classical HNC equation and the dashed line

shows that by modified T-F model. As shown in Fig. 3, the solid-dashed line is reduced compared with the dashed line because of the quantum diffraction effects in the Schrödinger equation and the value at r=0 is finite. And the solid line is reduced compared with the solid-dashed line because of the quantum diffraction effects in the QHNC equation. Note that for this case there is no bound state, namely Z*=1, because of the pressure ionization effects.

Figure 4 shows the ion-ion pair distribution functions. The horizontal axis represents the distance normalized by the ion sphere radius a. The solid line shows the ion-ion pair distribution function obtained by presented model using the QHNC equation, the solid-dashed line shows that by presented model using the classical HNC equation, and the dashed line shows that by the approximation of ion one component plasma with linear electric shielding. As shown in Fig. 4, for the case using the QHNC equation, it becomes difficult to close the ions each other compared with other cases. Because the linear shielding is slightly over-estimation, and for the case using the QHNC equation the shielding effects becomes weak compared with using the classical HNC equation as Fig. 3 shows.

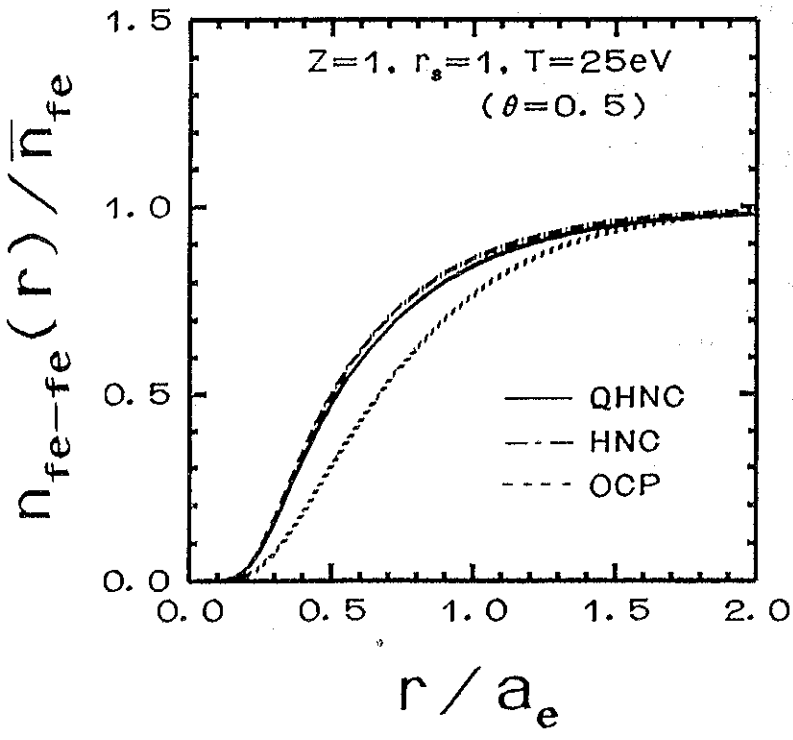

Fig. 2 The free electron distribution functions around a free electron for the case of Z=1, r_s=1,T=25eV.
The horizontal axis represents the distance normalized by the electron sphere radius a_e.

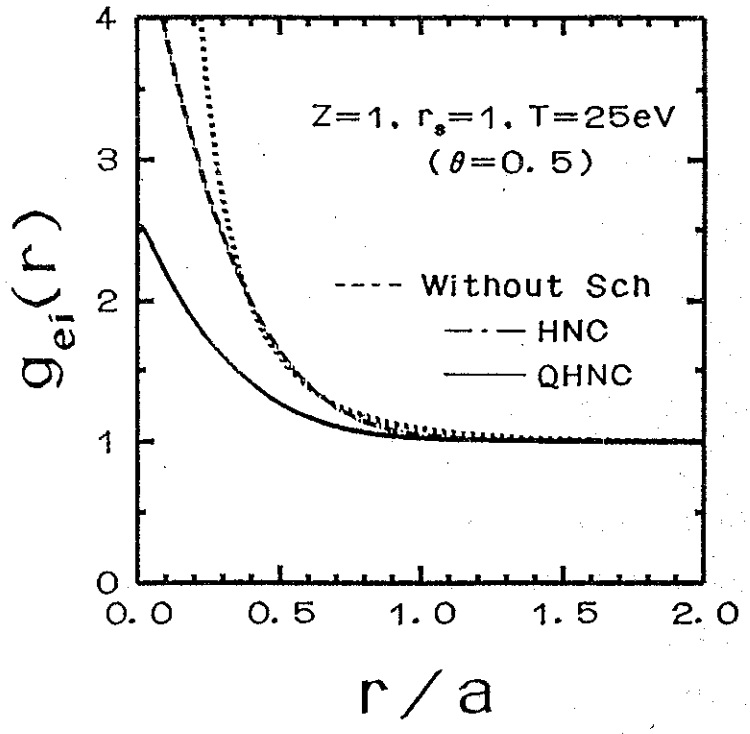

Fig. 3 The electron-ion pair distribution functions for the case of Z=1, r_s=1, T=25eV. The horizontal axis represents the distance normalized by the ion sphere radius a.

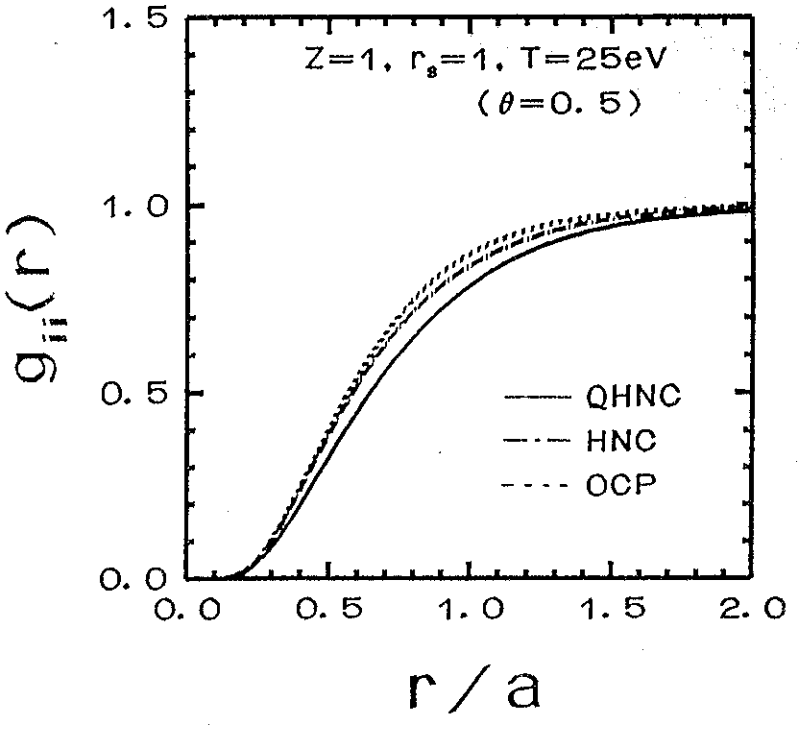

Fig. 4 The ion-ion pair distribution functions for the case of Z=1, r_s=1, T=25eV. The horizontal axis represents the distance normalized by the ion sphere radius a.

References

1). F. Perrot, Phys. Rev. A **25,** 489 (1982).

2). M. W. C. Dharma-wardana and F. Perrot, Phys. Rev. A **26,** 2096 (1982).

3). S. Ichimaru, S. Mitake, S. Tanaka and Xin-Zhong Yan, Phys. Rev. A **32,** 1768 (1985).

4). R. Kawakami, K. Mima, H. Totsuji and Y. Yokoyama, Phys. Rev. A **38,** 3618 (1988).

5). S. Nakai, Bull. Am. Phys. Soc, **34,** 2040 (1989).

6). For example; L. I. Schiff, "Quantum Mechanics, Third Edition" (McGraw Hill, Inc., 1968).

7). J. Chihara, Prog. Theor. Phys. **55,** 340 (1976).

8). J. Chihara, Phys. Rev. A **33,** 2575 (1986).

9). J. Chihara, Phys. Rev. A **40,** 4507 (1989).

10). F. Perrot, Y. Furutani and M. W. C. Dharma-wardana, Phys. Rev. A **41,** 1096 (1990).

11). F. Perrot and M. W. C. Dharma-wardana, Phys. Rev. A **30,** 2619 (1984).

12). A. K. Fetter and J. D. Walecka, "Quantum Theory of Many-Particle Systems" (McGraw Hill, New York, 1971).

Atomic and Radiative Processes in Tokamak Plasmas

Takako KATO
National Institute for Fusion Science

Abstract

The temperature and density range in tokamak plasmas are from 10 eV to 10 keV and 10^{10} to $10^{14} cm^{-3}$, respectively. Various atomic processes involve in plasma physics and plasma diagnostic. We discuss density effects on atomic processes related to two topics; one is neutral beam injection and the other is divertor plasmas.

1 Introduction

Some problems in tokamak plasmas have to be treated by taking into account the atomic processes; plasma spectroscopy for diagnostics, deposition of the neutral beam, remote radiative cooling, energy balance in plasmas etc. The main important processes are ionization, recombination and excitation by electron impact as well as charge exchange with neutral hydrogen. For high energy neutral beam, ionization and excitation by proton and impurity ions are more significant than electrons. In divertor plasmas, neutral atoms and low ionized ions, and possibly molecules play important role. The atomic data for these elements in low temperature plasmas are not sufficient yet.

At the beginning of the discharge, sometimes the suprathermal electrons are produced and they ionize the ions effectively. Then inner-shell ionization, inner-shell excitation, two electron excitation would not be negligible. The highly ionized ions produced by suprathermal electrons give the recombination emissions in thermal plasmas. These phenomena should be considered in non equilibrium ionization condition. Near the center of the plasma where highly ionized ions are dominant, ion-ion charge exchange processes, $A^{z+} + B^{z'+} \rightarrow A^{(z-1)+}(n, \ell) + B^{(z'+1)+}$, can produce different spectra than those by electron excitation.
In this article, we discuss atomic processes on neutral beam and divertor plasmas.

2 Neutral beam injection

2.1 Emission from the beam

Neutral beam injection is currently used for heating plasmas and plasma diagnostics. The characteristics of the neutral beam penetration and energy deposition are important for plasma parameters control as well as plasma diagnostics. The penetration of the neutral beam in a plasma depends exclusively on the atomic processes. After the ionization of the beam, the motion of ionized beam particles is determined by the magnetic field, and their energy is dissipated in Coulomb collisions with the charged plasma particles. The effect of ladder-like (multistep) processes on the beam attenuation is one of the problems especially for large tokamak such as ITER where the electron density is high. The energy range of the beam is between 10 keV/amu and 1 MeV/amu.

In order to know the effect of the ladder-like ionization of the beam, it is necessary to calculate them by a collisional radiative model. The motional Stark effect should be considered. Since the electron temperature is high, the recombination process is not important; the beam can be considered as in an ionizing state. The population of the i-th level n(i) in the neutral beam can be written as,

$$v_0 dn(i)/dx = -(\sum_j R_{ij} + \sum_j A_{ij} + S_i)n(i) + \sum_i (R_{ji} + A_{ji})n(j) \qquad (1)$$

where R_{ij} indicates the excitation rate by electron, proton and impurities impact from i to j level levels, S_i sum of the ionization rate by electron, proton and impurities impact and the charge transfer rate with proton and impurities from the level i, A_{ji} the transition probabilities from j to i, v_0 the velocity of the beam, respectively. The relative velocity of the beam to the charged particles in the plasma is comparable to the velocity of the electrons in plasmas, then both electron and proton collisional processes are significant for the beam penetration.

We consider here for the case of He beam. Since He atom has the metastable state $1s2s(^3S)$, the ionization from the metastable state is important as well as the excitation-ionization through excited states. It is necessary to know how much the population of the metastable states in the incident beam itself. Atomic data relating to the metastable states are not sufficient. For the beam energy below 100 keV/amu the charge exchange process $He + H^+ \rightarrow He^+ + H$ is effective, whereas the ionization $He + H^+ \rightarrow He^+ + H^+ + e$ become important at high energies above 100 keV/amu. Electron excitation processes are predominant for the beam of low energies below 10 keV/amu and always effective even for that of high energies. The excitation cross sections by impurity impact do not follow z^2 scaling at low energies, where z is the charge of the impurity ions. It is reported that z scaling is better than z^2 scaling from the experimental results, but it depends also on the transitions. The data for the interaction between neutral beam and impurity ions in the plasma should be investigated more.

Transfer ionization $A^{z+} + He \rightarrow A^{(z-1)+} + He^{2+} + e$ and double ionization becomes more and more important when z becomes large. The transfer ionization process is comparable with single ionization for the collision between He^{2+} and He at the energies below 40 keV/amu.

We have calculated the collisional radiative ionization rate coefficients for the He beam with the collisional radiative model which includes all the sublevels up to n = 4, and include the levels up to n = 20[1]. The calculated results are shown in Fig. 1 for the case that He beam is injected into a 10 keV temperature plasma. The solid and dashed lines indicate the results for the electron density of the plasma to be 10^{10} and $10^{16} cm^{-3}$. The results by Korotov[2] is shown by the dot-dashed line for $10^{14} cm^{-3}$. Our values are smaller than his values at high beam energies. This difference is considered due to the differences of the atomic data and the models.
In order to know the population of the metastable state in the beam, we propose to measure the ratio of the spectral line intensities of the singlet to the triplet system. The calculated line intensity ratios I(3888.7A $1s2s(^3S) - 1s3p(^3P)$)/I(5015.7A $1s2s(^1S) - 1s3p(^1P)$) is shown in Fig.2 as a function of electron density with parameters η which is the ratio of the population of the metastable state to the ground state $\eta = N(2^3S)/N(1^1S)$.

In tokamak plasmas, the strong magnetic fields B of the order of Tesler(10^4 Gauss) produce electric fields F by motional Stark $F = v_0$ x B, which is the order of 10 kV/cm. The Stark profile for the visible line spectra of the transition n = 2 - 3 (6520 - 6535 A)is observed from JET tokamak for the neutral hydrogen beam[3]. From the Stark profile we can estimate the magnetic field in the plasma. It is expected to know the direction of the magnetic field from the polarization of the spectra. We have to take into account the Lorentz field ionization. The principal quantum number of ionization limit n_l is given as,

$$n_l \sim 1/(2F^{1/4}). \tag{2}$$

Under the condition of tokamak plasmas the ionization limit by the Lorentz field ionization n_l is 5 - 7, and the effect on the effective ionization is estimated to be less than 20 %. Since the neutral beam is in the ionizing state, the effect of the field ionization is not so large.

2.2 Charge exchange spectroscopy

When the beam energy is not so high (10 keV/amu - 200 keV/amu), charge exchange process with impurity ions is dominant. The impurity ions emit spectral lines by radiative stabilization after charge exchange;

$$H + A^z \rightarrow H^+ + A^{(z-1)+}(n,\ell), \quad A^{(z-1)+}(n,\ell) \rightarrow A^{(z-1)+}(n',\ell') + h\nu \tag{3}$$

Here n and ℓ mean the principal and azimuthal quantum number. The spectral line intensities emitted following the cascades to the lower states depend greatly on the ℓ distributions of the charge exchange process[4]. Since visible lines are easy to measure, the emissions from highly excited states n = 8 or 7 of hydrogen like carbon and oxygen ions are currently used for plasma diagnostics. The broadening of the line gives the ion temperature T_i of the plasma and the lineshift gives the toroidal rotation in the plasma. This also allows to detect the fully-stripped carbon and oxygen ions, which are not normally observable by line emission spectroscopy. In this case, quantitative estimates for the effective charge exchange recombination rates including cascades and level mixing are necessary. For the level mixing with the same n and different ℓ, the excitation by proton and impurity ions have to be considered as well as by electrons. The Stark effect has to be taken into account as mentioned in the previous subsection. The critical value of n for which the energy separation by motional Stark field and the fine structure splitting are the same is given as[5],

$$n_c = 2(z^{11}/(T_i(keV)B(T)^2))^{1/12}. \tag{4}$$

We consider here the line intensity by charge exchange recombination for the emission n = 8 - 7 of hydrogen like carbon ions. The intensity I of the line from n = 8 to 7 can be expressed with the population density at n = 8, N(8ℓ)

$$I(8-7) = \sum_{\ell} N(8\ell) \sum_{\ell'} A(8\ell - 7\ell') \tag{5}$$

where A indicates the radiative transition probability. The charge exchange cross section has the maximum value at n = 4 and decreases towards large n approximately as $n^{-\gamma}$ where γ has the value greater than 3. The cascade effects from higher n for I(8-7) is about 20% for $\gamma = 3$. Since the value of γ increases with low incident energy E_0 very sharply($\gamma \simeq 9$ at $E_0 = 10$ keV), the contribution from higher levels is considered negligible for low energy beam. The emission cross section σ^{em} for the line from n to n' by charge exchange is defined as,

$$\sigma^{em}(n - n') = \sum_{\ell} N(n\ell) \sum_{\ell'} A(n\ell - n'\ell')/(v_0 N_H N(C^{6+})) \tag{6}$$

where N_H is the density of the neutral hydrogen and $N(C^{6+})$ the density of the fully stripped carbon ions.
In the low density regions where the collisional processes are not important, the line intensity is affected by only cascades to the lower states,

$$I(n - n') = \sum_{\ell} < \sigma_{CE}(n\ell)v_0 > B(n\ell - n')N_H N(C^{6+}) \tag{7}$$

where $\sigma_{CE}(n\ell)$ is the charge exchange cross section captured to the nℓ state, $B(n\ell - n') = \sum_{\ell'} A(n\ell - n'\ell') / \sum_{n"\ell"} A(n\ell - n"\ell")$ is the branching ratio from nℓ state to n'.

In this case, the emission cross section is determined as,

$$\sigma_0^{em}(n-n') = \sum_{\ell} \sigma_{CE}(n\ell) B(n\ell - n'). \tag{8}$$

When the density becomes high, ℓ mixing begins from the levels with large ℓ since the radiative transition probabilities from these states are smaller than those from the levels of small ℓ, especially $\ell = 1$. The density for complete ℓ mixing is derived,

$$n_e \geq \sum_{n'\ell'} A(np - n'\ell') / \sum_{\ell} R(np - n\ell). \tag{9}$$

At high densities where complete ℓ mixing is realized, the population $N(n\ell)$ follows the statistical weight w of the level. Then the emission cross section, assuming no collisional process among different n levels, is given as follows,

$$\sigma_l^{em}(n-n') = \sum_{\ell} \sigma_{CE}(n\ell) \sum_{\ell} w(n\ell) \sum_{\ell'} A(n\ell - n'\ell') / \sum_{\ell} w(n\ell) \sum_{n'\ell'} A(n\ell - n'\ell') \tag{10}$$

σ^{em}(8-7) $= 0.16 \sum_{\ell} \sigma_{CE}(8\ell)$ is obtained for n = 8 and n' = 7. The density dependance of the σ^{em} depends on the ℓ distribution of the charge exchange cross section $\sigma_{CE}(\ell)$. When the ℓ distribution is steeper than the statistical weight towards the larger ℓ, the σ^{em} decreases for high densities; $\sigma_l^{em} < \sigma_0^{em}$. In Fig.3 we show the ℓ distribution calculated by three different authors; [6], [7] and [8]. The peak values of ℓ for σ_{EC} are $\ell = 5$, 2 and 3 respectively. The calculated emission cross sections for these different ℓ distributions are shown in Fig.4 as a function of electron density taking into account only ℓ mixing among the levels with the same n but without the excitation from different n levels. The excitation rate coefficient by proton impact C_p is taken to be equal to the electron's C_e for ℓ mixing rate coefficients and did not include the contribution of impurity ions. Then the emission cross section by [6] is decreased at high densities as shown in [5]and [9]. On the contrary the emission cross section by [7] increases for high densities, since the σ_{CE} decreases very rapidly for large ℓ. In the case of [8], the emission cross section dose not change very much.

We consider the density dependence of σ^{em} for σ_{CE} by [8] in Fig.4. The radiative decay rate $A(8\ell)$ is the largest at $\ell = 1$ and decreases for larger ℓ. For the densities where the collisional rate R $= \sum_i N_i C_i$ is comparable to A at large ℓ, $\ell \sim 7$, σ^{em} is increased for the increase of the density, because the population at $\ell \sim 7$ is increased due to the collisional process from the levels $\ell < 7$ where $\sigma_{CE}(n\ell)$ is larger. On the contrary, when $R(8\ell - 8\ell')$ is nearly equal to $\sum_{n\ell'} A(8\ell - n\ell')$ at $\ell \sim 1$, the emission cross section is decreased, since the branching ratio for the emission at $\ell = 1$ is very small due to the large radiative decay rate to n = 1. Finally the emission cross section reaches the value given in eq.(10) at the densities sufficiently high. The emission cross section begins to change from the electron density around $10^{14} cm^{-3}$ for $C_p = C_e$ and $10^{12} cm^{-3}$ for $C_p = 100 C_e$ where C_p and C_e indicate the excitation rate coefficients by protons and electrons. In Fig.5 we have calculated $\sigma^{em}(8-7)$ including all the collisional and radiative processes up to n = 9 with different ℓ sublevels using σ_{CE} by [8] shown in Fig.3

as an example. The density dependances are illustrated for different collisional rates, $C_p(\ell - \ell') = C_e(\ell - \ell')$, $30C_e(\ell - \ell')$ and $100C_e(\ell - \ell')$ by solid, dot-dashed and dashed lines respectively, where $C_e(8\ell - 8\ell') = 4$ - 9 x $10^{-6} cm^3 s^{-1}$. Dotted line indicates the values neglecting collisional process among different n levels with the value $C_p = C_e$ as shown in Fig.4. It is seen that σ^{em} begins to increase from the densities $10^{13} cm^{-3}$ and increases more and more for high densities by the excitation from the lower levels in the case of $C_p = C_e$. At high densities, the collisional excitations from/to different n levels become important. For the excitation with different n, electron collisions are predominant and proton collisions are negligible. The excitation to higher levels and ionization make the emission cross section decrease whereas the excitation from lower levels makes it increase. Since the charge exchange cross section increases for lower n values than 8, the excitations from lower levels are significant at high densities. For the rate coefficient $C_p = 100C_e$, the emission cross section begins to increase at $10^{15} cm^{-3}$, because the ℓ mixing rate is much larger than that by electron excitation from lower levels. In this case the collisions from the lower states can be neglected at tokamak density regions. It is necessary to investigate more collisional data for ℓ mixing.

3 Divertor plasma

In divertor plasmas, the electron temperature is low ($\sim$ 20 eV) and the electron density is comparatively high ($\sim 10^{14} cm^{-3}$). Then the radiation emitted from atoms and low ionized ions such as oxygen or carbon are affected very much by collisions; it is not in the corona regime. The emissions have the temperature and density dependence and the spectral lines could be used for density and temperature diagnostics. Unfortunately the atomic data, especially excitation cross sections, for these atoms and ions are lacking for visible lines which are emitted from highly excited states, n = 3 - 5. It is very difficult to discuss the line intensities of visible lines quantitatively at the moment. In Table I, we list the visible spectral lines of carbon atoms and ions for which we need atomic data.

We have investigated the effective ionization rate coefficients for carbon ions including the n = 2 and n = 3 levels of all the ions using the collisional radiative model. The inner-shell ionization processes, such as from CII $2s^2 2p(^2P)$ to CIII $2s2p(^3P)$ metastable state, are included. The effective ionization rate coefficients in ionizing state are shown in Fig.6 as a function of the electron density. For CIII ions, the density effects is about 20 % at 10 eV assuming N(CII)=N(CIII). In divertor plasmas it is considered to be ionizing state for low ionized ions since the neutral atoms are always supplied and the electron temperature is high compared to the ionization temperature in which the ions are in the ionization equilibrium. But we have to be careful for the contribution of the charge exchange recombination with thermal neutral hydrogen.

References

[1] T. Fujimoto, *J. Quant. Spectrosc. Radiat. Transfer, 21 (1979) 439*

[2] M.P. Petrov, *IAEA Consultant Meeting on "He Beam Data Base for Alpha Particle Diagnostics of Fusion Plasmas", (1991)*

[3] A. Boileau, M von Hellermann, W. Mandl, H.P. Summers, H. Weisen and A. Zinoviev, *J Phys. B , 22 (1989) L145*

[4] T. Kato, K. Masai, T. Fujimoto, F. Koike, E. Kallne, E.S. Marmar and J.E. Rice, *Phys. Rev. A (1991) to be published, NIFS-69 (1991)*

[5] R.J. Fonck, D.S. Darrow and K.P. Jaehnig, *Phys. Rev. A 29 (1984) 3288*

[6] H. Ryufuku, *Rep. JEARI-M-82-031 (1982)*

[7] F. Koike, *J. Phys. Soc. Jpn, 57 (1988) 2344, data from private communication*

[8] W. Fritsch, *Phys. Rev. A 30, 3324 (1984), data from private communication (1991)*

[9] A. Boileau, M. von Hellermann, L.D. Horton, J. Spence and H.P. Summers, *Plasma Physics and Cont. Fusion, 31 (1989) 779*

Table 1: Visible lines from carbon atoms and ions

CI	$3s(^1P) - 4p(^1P)$	5380.3A
	$3s(^3P) - 4p(^3P)$	4771 - 4772A
	$3s(^3P_2) - 3p(^3P_2)$	9094.8A
CII	$2s2p3d(^2D) - 2s2p4f(^2F)$	4411.4A
	$2s2p3d(^4D) - 2s2p4f(^4F)$	4076A
	$2s2p3d(^4F) - 2s2p4f(^4G)$	3876A
CIII	$4f(^3F) - 5g(^3G)$	4070A
	$4f(^1F) - 5g(^1G)$	4186.9A
	$2s3s(^3S) - 2s3p(^3P)$	4647-4651A

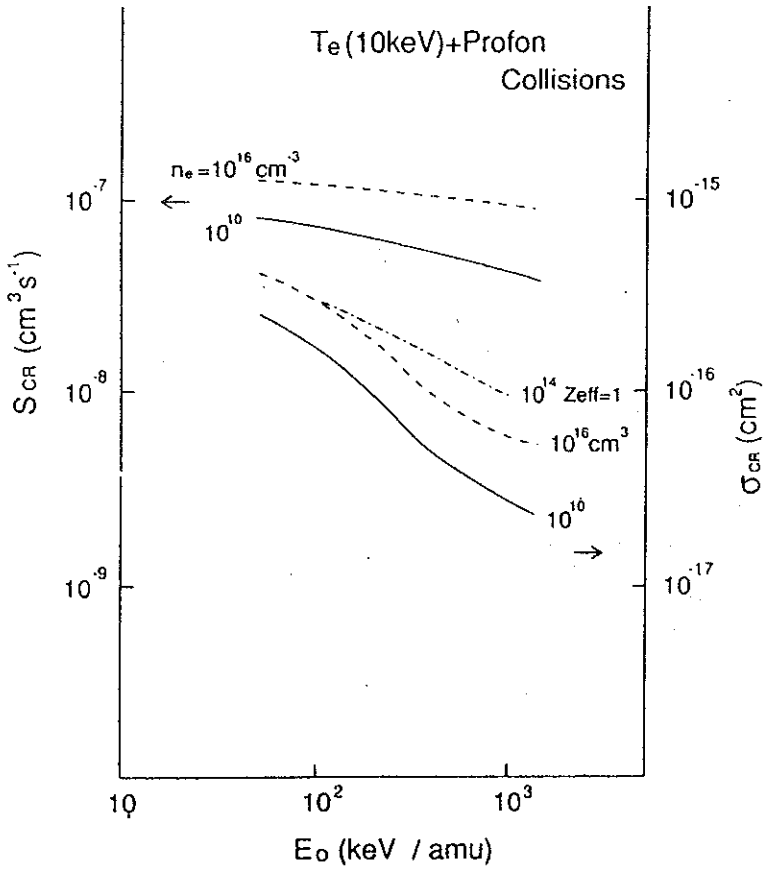

Fig.1 The effective ionization cross sections in 10 keV plasmas for He beam as a function of the beam energy. The solid and dashed lines are our results for $n_e = n_p = 10^{10}$ and 10^{14}, respectively. The dot-dashed line is the result from [2].

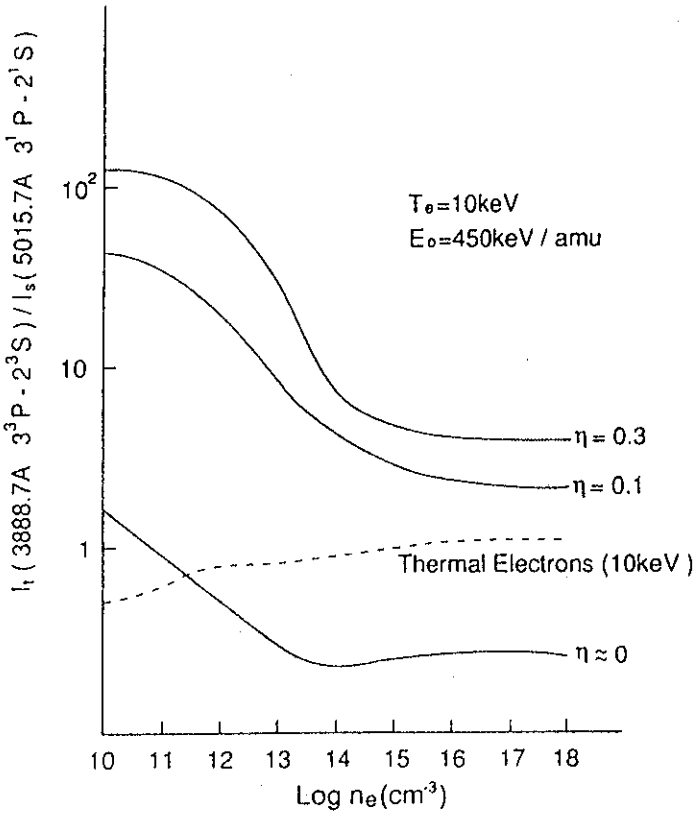

Fig.2 The intensity ratios of the spectral lines of the transition $2^3S - 3^3P(3888.7\text{A})$ to $2^1S - 3^1P(5015.7\text{A})$ from He beam as a function of electron density. η is the population density ratio $N(2^3S)/N(1^1S)$.

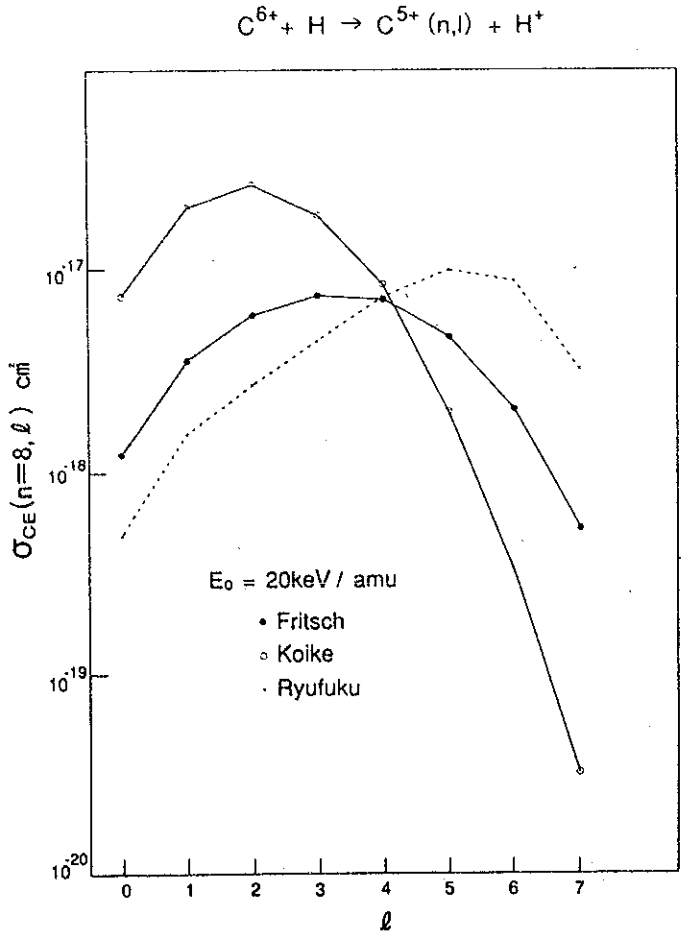

Fig.3 The partial charge exchange cross sections $\sigma(n,\ell)$ for $H + C^{6+} \rightarrow H^+ + C^{5+}(8,\ell)$ by three methods, [6], [8], [7].

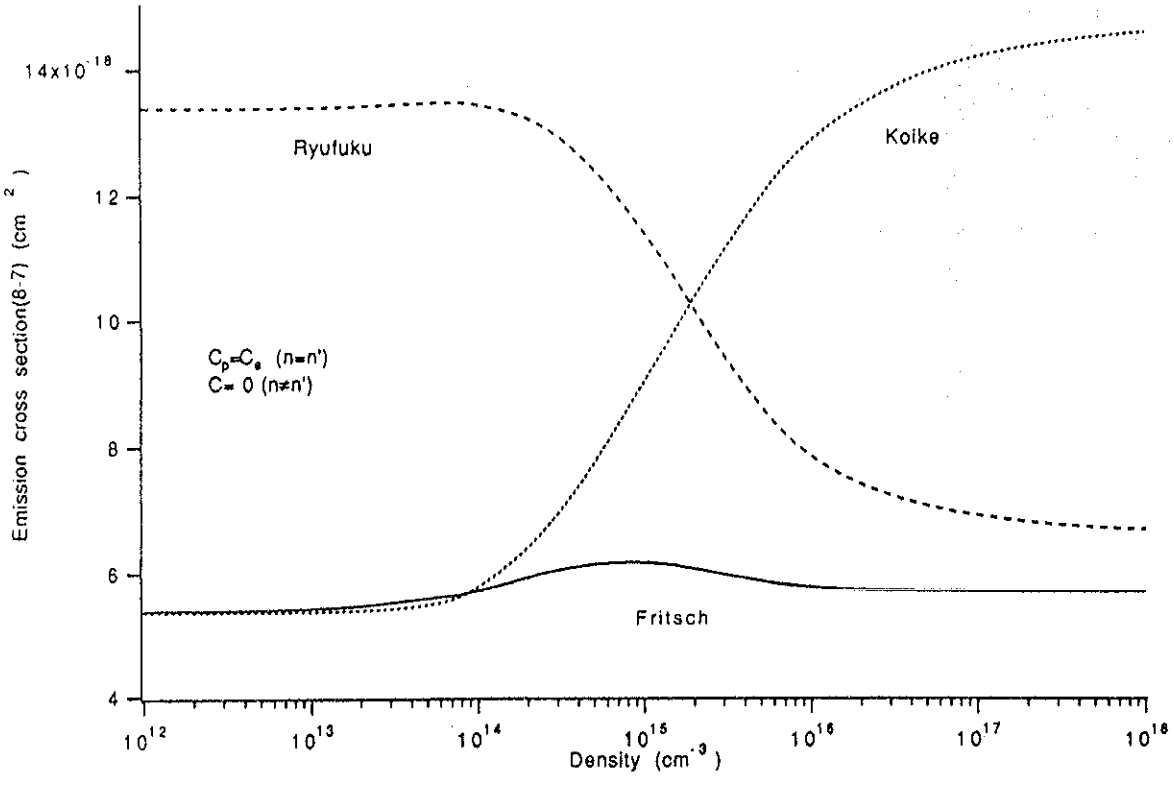

Fig.4 The emission cross sections $\sigma^{em}(8-7)$ as a function of electron densities for three different cross sections without excitation process among different n.

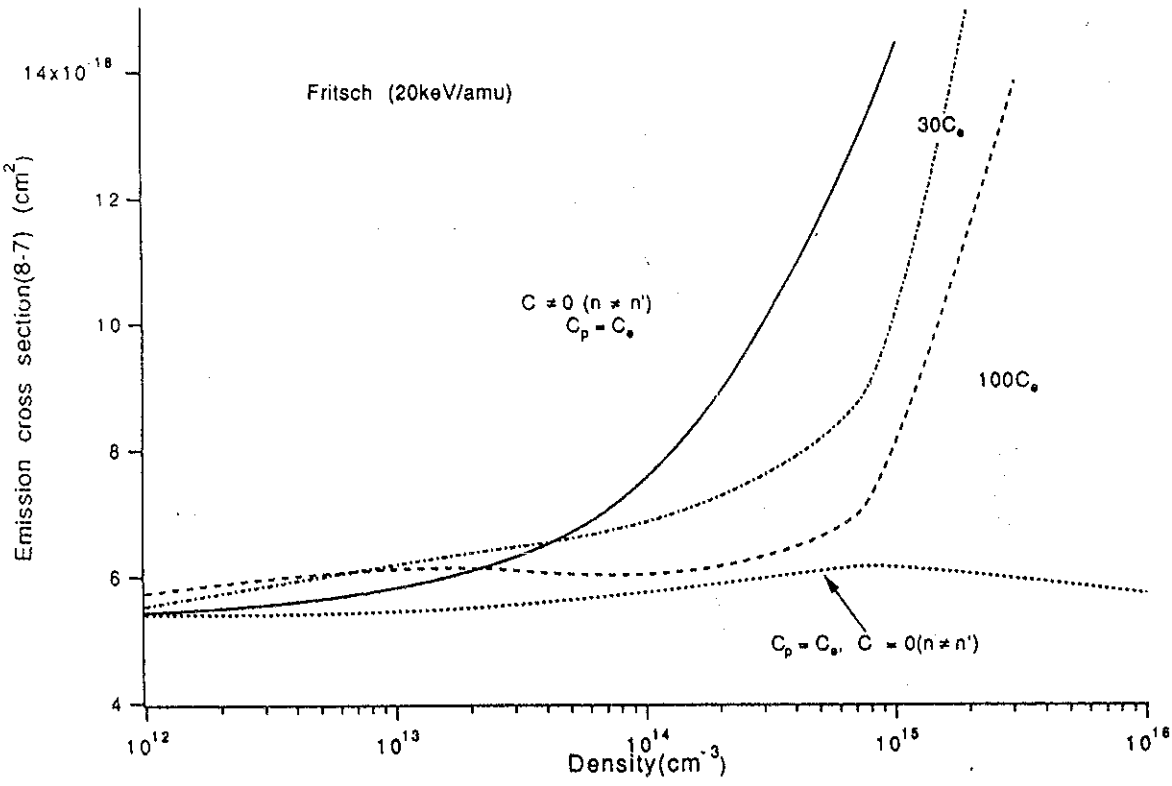

Fig.5 The emission cross sections including collisional processes among different n.

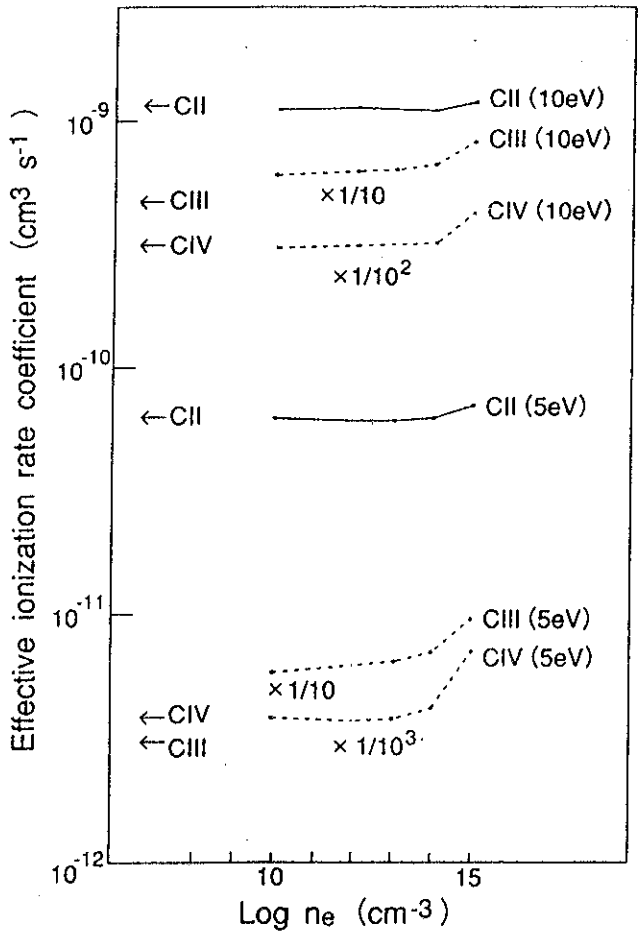

Fig.6 The effective ionization rate coefficients for carbon ions as a function of electron density. The arrows indicate the values at low density limit.

Numerical Scheme for Solving Stiff Equation and Impurity Transport Analysis of pellet fuelled plasmas

T. Hirayama

Naka Fusion Research Establishment
Japan Atomic Energy Research Institute
Naka-machi, Naka-gun, Ibaraki-ken, 311-01, Japan

A numerical scheme which employes the full implicit difference method is described for solving the stiff equation associated with impurity transport in a tokamak plasma. Using an impurity transport code developed with the numerical scheme, intrinsic titanium impurity behavior in pellet fuelled plasmas was studied by applying the neoclassical impurity transport calculation to temporal evolutions of Ti XX and Ti XIX spectroscopically observed. Ti impurity accumulates in the plasma core region, correlated with peaked density profile and the absence of sawtooth oscillation. Impurity accumulation is caused by a strong ion density gradient driving force, as the neoclassical impurity transport theory predicts.

1. Introduction

The study of impurities in tokamaks provides excellent opportunities to measure transport coefficients. Since individual impurities are readily identifiable through their characteristic line radiation, it is possible to follow the spatial and temporal evolution of ion densities. The most interesting aspect of impurity transport is the often observed correlation between long impurity particle confinement and improved energy confinement. This result has been seen in discharges exhibiting transport changes after pellet fuelling. In the context of the present effort to understand transport in tokamaks, one needs to numerically solve the diffusion equations of impurity ions. This kind of diffusion equation, however, poses a numerically difficult problem. This is because of various eigenvalues originating from source terms, with quite different order ranging from about 1 to about 10^8 sec^{-1}. On the other hand, the time constant of impurity ion transport is generally ~10^{-2} to 1.0 sec in tokamak plasmas. Therefore, using conventional schemes of solution of the impurity ion transport equation, the time step is severely restricted by the maximum eigenvalue. The diffusion equation of impurity ions is generally referred to as a stiff equation. Because of this, the set of equations does not lend itself readily to numerical solution by classical methods. In this paper we present the numerical scheme for solving the stiff equation and the results of an impurity transport study in JT-60.

The numerical scheme is presented in Section 2. The transport analysis of Ti impurity in pellet fueled plasmas is described in Section 3. Finally, the main results are summarized in Section 4.

2. Numerical Scheme for Impurity Ion Diffusion Equation

The diffusion equation for impurity ions is typically expressed as,

$$\dot{\vec{u}} = A\vec{u} + B\vec{u} + \vec{a} \tag{1}$$

where $\vec{u}$ is the vector of impurity ion densities, A and B the coefficient matrixes, and $\vec{a}$ the constant vector of the source term. Since Eq. (1) is a stiff equation, the following relation is assumed,

$$|A| << |B|. \tag{2}$$

Applying the full implicit scheme to the second term in R. H. S. of Eq. (1) and using the Crank-Nicholson approach for the rest of the terms, the difference equation is written as,

$$\vec{u}^{i} = \frac{1}{1-\Delta tB}\left[\vec{u}^{old} + \Delta t\theta\vec{a} + \Delta t(1-\theta)\vec{g}^{old} + \Delta tA\vec{u}^{i-1}\right] \tag{3}$$

where,

$$\vec{g}^{old} = A\vec{u}^{old} + \vec{a}, \tag{4}$$

$$\theta = \frac{1}{2}, \tag{5}$$

and "i" represents the iteration number. Since the common denominator is

$$\left|\frac{\Delta tA}{1-\Delta tB}\right| \cong \left|\frac{A}{B}\right| << 1, \tag{6}$$

the convergence of iteration is expected to be fast. As for the propagation of error, the common denominator of error for an iteration is given by

$$\left|\frac{1}{1-\Delta t(A+B)}\right| \tag{7}$$

Therefore, if $B < 0$, the error will not be propagated independently of the time step size, Δt.

The continuum equations of impurity ions are the hierarchy equation,

including the neutral density. The number of equations is always one less than the number of variables. Accordingly, the neutral density as one of the variables is generally given by a Limiter-Scrape off model,

$$\frac{1}{2}n_1 v_1 = \frac{1}{2\pi r_p}\sum_k \int_0^{r_p} (S_k - \dot{n}_k)d\sigma \qquad (8)$$

where n_1 and v_1 are the impurity neutral density and thermal velocity, n_k the impurity ion density with k-th charge, S_k the source term, r_p the plasma radius, and $d\sigma$ the element of plasma surface. Therefore, one can take the neutral density for the boundary condition of the diffusion equations relating to impurity ion charge states. From Eq. (8), one needs $\dot{n}_k$ to estimate n_1. Since $\dot{n}_k$ is always determined one time-step later, it is difficult to conserve the number of impurity ions from the Limiter-Scrape-off model. This numerical error caused by the lack of particle conservation unquestionably makes for worse convergence of lower charge state ion densities.

To settle the numerical problem, the equation prescribing the total number of impurity ions is taken for the restricted condition and solved with the ion diffusion equations. The particle conservation law is that the increment of impurity ion density from the neutral particles is the same as a recycled flux, i.e.,

$$S = \gamma(S - \dot{N}) , \qquad (9)$$

where $S = \sum \int S_k d\sigma$, $\dot{N} = \sum \int \dot{n}_k d\sigma$, and γ is a recycling coefficient. At the j-th time step, Eq. (9) is rewritten as follows,

$$(1 - \gamma)S^j + \frac{\gamma}{\Delta t}N^j = \frac{\gamma}{\Delta t}N^{j-1}. \qquad (10)$$

As γ is unity, Equation (10) becomes $N^j = N^{j-1}$, which represents conservation of the total number of impurity ions. Coupling with the impurity ion

diffusion equations, one obtains the following matrix equation,

$$\begin{bmatrix} A & \vec{P} \\ \vec{Q}^{t} & R \end{bmatrix} \begin{bmatrix} \vec{u} \\ \chi \end{bmatrix} = \begin{bmatrix} \vec{a} \\ C \end{bmatrix} \tag{11}$$

where

A ; coefficient matrix,
$\vec{P}$; ionization rates of neutral particle,
$\vec{a}$; constant terms,
$\vec{u}$; ion densities,

$\vec{Q}^{t}$; coefficients summed over ion densities,
R ; surface-integrated value of normalized neutral density profile,
C ; constant terms,
χ ; neutral density at a plasma boundary.

Accordingly, by solving the matrix equation of Eq. (11), one can estimate the impurity ion densities and the neutral density as the boundary condition, with the strict conservation of total number of impurity ions[1].

3. Neoclassical impurity transport analysis of pellet fueled plasmas

Centrally peaked electron density profiles lasting for one second were obtained by injection of four hydrogen pellets into JT-60 neutral beam heated discharges. Steep density gradients first developed in a zone inside q=1. Sawteeth were suppressed for one second and the energy confinement time was enhanced by up to 40 % over that of gas fuelled plasmas at a medium neutral beam heating power up to 15 MW[2]. A four-barrel pneumatic pellet injector installed on JT-60 produces cylindrical hydrogen pellets with velocities approaching 1.6 km/s. The pellet sizes are 2.7 mm (dia.) × 2.7 mm (length) and 3.8 mm (dia.) × 3.8 mm (length). The small

and the large pellets contain 0.7×10^{21} and 2.0×10^{21} atoms. The improved discharges are characterized by a strongly peaked pressure profile around the magnetic axis (inside the sawtooth inversion radius) and degrades when a large sawtooth occurs or when the pressure gradient reaches a critical value[3]. We present calculations of the neoclassical predicted equilibrium profiles of intrinsic Ti-impurity in JT-60. This calculation was performed for comparison with time evolutions of Ti XX and Ti XXI emissivity lines observed after pellet fuelling.

Figure 1 shows the temporal evolutions of the profiles of electron density and electron temperature of a pellet fueled plasma. The four hydrogen ice pellets are injected at around 6.0 sec into a helium discharge with $I_p = 3.1$ MA and $B_t = 4.8$ T. The combination of pellet sizes is two 2.7 ϕ and two 3.8 ϕ. The typical time interval adopted for each pellet is 50 msec, and the pellets are injected at low heating power of 7 MW to avoid the ablation due to beam fast ions. The NB heating power increases up to 15 MW after the pellet injection. The electron density abruptly increases due to the pellet injections at around 6.0 sec, and the density profile seems to shrink later and is relaxed at 7.0 sec by the reappearance of sawtooth oscillation. Figure 2 shows the temporal evolution of Ti XIX, XX and XXI emissivity lines measured by the crystal spectroscopy. The line density at half the plasma radius, central electron temperature and the central soft X-ray signal are also shown in Fig. 2. The intensities of Ti XIX and Ti XX rapidly increase due to the sudden reduction of the electron temperature by pellet injection. Conversely, the intensity of Ti XXI decreases at once and comes back to increase until the reappearance of sawtooth at ~7.05 sec. The central soft X-ray signal also shows the same behavior as the temporal evolution of Ti XXI. The fundamental question is whether the titanium impurity accumulates or not in pellet fuelled plasmas showing the improved confinement characteristic. Because plasma profiles dynamically change as shown in Fig. 1, there is still a possibility to explain the temporal evolutions of Ti intensity from the changes of electron temperature and density profiles in time and space.

A one-dimensional and time dependent, multi-species impurity code is employed to calculate the impurity ion density and the emissivity lines. In this discussion, we will be concerned with the study of the impurity transport alone. In order to provide a framework for this, let us consider a conventional diffusive/convective model. The conventional approach assumes the impurity flux Γ_k to be given by

$$\Gamma_k(r) = -D_A(r)\frac{\partial n_k}{\partial r} + V_A(r)n_k \qquad (12)$$

where n_k is the impurity ion density in the k-th charge state, $D_A(r)$ an anomalous diffusion coefficient and $V_A(r)$ an anomalous convective velocity. From the diffusive/convective model, the convective velocity is related to the anomalous diffusion coefficient through a form such as

$$V_A(r) = -C_V D_A \frac{2r}{r_p^2} \qquad (13)$$

where C_V is a dimensionless peaking parameter. As $C_V = 1$, Equation (12) provides a gaussian profile of impurity ion density at steady state. Higher values of C_V lead to more peaked density profiles. The diffusion coefficient D_A and the peaking parameter C_V are to be determined from the simulations and are assumed to be the same for all ionization states. Following a previous analysis of Ti impurity in NB heated, L-mode plasmas[4], we take D_A to be spatially uniform and its value to be 1.0 m^2/s.

Figure 3 shows the comparison of the observed line emissivities with the calculated time evolutions of Ti XX and Ti XXI, for systematic parameter scans of C_V from 1 to 4. The measured and calculated values are normalized to the values before the pellet injection. The calculated temporal evolution of Ti XXI needs a larger value of C_V in order to meet the observation. The result of Ti XX, however, reveals that the peaking parameter must be less than two. The contribution of the conventional diffusive/convective transport model is eventually very unsuccessful in explaining the observed

response of line emissivities to density and temperature profile changes.

This situation is reminiscent of the neoclassical transport that provides impurity accumulation due to large density gradients through the electron density evolution in pellet fueled plasmas as shown in Fig. 1. Since impurity collisionality in pellet fueled plasmas lies in the Pfirsch-Schluter regime, we take the neoclassical transport flux proposed by Samain[5] into the anomalous particle flux of Eq. (12). In Fig. 4, comparison of measured emissivity lines with simulation results based on neoclassical transport theory demonstrates that the contribution of neoclassical flux is at least an order of magnitude smaller than the anomalous transport flux. Accordingly, the simple combination of anomalous and neoclassical transport fluxes cannot account for the observed response of line emissivities.

Returning to the individual behavior of titanium impurities and soft X-ray signals, it is certainly found that the temporal evolution of Ti XXI is correlated with the duration of disappearing sawtooth oscillation. Concerning the effect of the sawtooth oscillation on impurity transport, some experiments have reported a continuous increase in the central soft X-ray emission followed by a rapid decrease with large m/n=1 MHD oscillations[6]. These results indicate improvement of central confinement in the sawtooth free phase. We propose a two zone model; the inner plasma zone with reduced transport extending to the q=1 surface, and the outer plasma zone continuing to be dominated by anomalous transport. As for reduced transport, the anomalous diffusion coefficient in the inner zone is assumed to be a factor of ten smaller than that in the outer zone. Figure 5 shows the behavior of TI XXI and XX emissivity lines simulated by the two-zone model. The predicted titanium evolutions are in good agreement with observation. Therefore, impurity transport appears to be reduced to a level close to neoclassical in the central good confinement region of in pellet fuelled discharges.

4. Summary

The stiffness can be successfully removed from the continuum equation for impurity ions by using a difference scheme combining a full-implicit approach with the Crank-Nicholson method. It then becomes possible to calculate the temporal behavior of impurity ions in plasmas using a reasonable amount of cpu-time.

Impurity transport analysis shows that the titanium impurity ions accumulate in a plasma deeply fueled by pellet. This impurity behavior is well described by the combination of reduced anomalous diffusion and neoclassical transport in the plasma interior. The outer zones continue to be dominated by anomalous transport.

Acknowledgment

We are indebted to the entire JT-60 team and in particular to the diagnostics and data management groups for providing the basic data for this study.

References

[1] HIRAYAMA, T., SHIRAI, H., SHIMIZU, K., et al., J. Nucl. Mater. **145&147** (1987) 854.

[2] KAMADA, Y., YOSHINO, R., NAGAMI, M., et al., Nucl. Fusion **29** (1989) 1785.

[3] OZEKI, T., AZUMI, M., KAMADA, Y., et al., Nucl. Fusion **31** (1991) 51.

[4] KOIDE, Y., HIRAYAMA, T., SUGIE, T., et al., Nucl. Fusion **28** (1988) 1835.

[5] SAMAIN, A., WERKOFF, F., Nucl. Fus. **17** (1977) 53.

[6] Doublet III Group, J. Nucl. Mater. **93&94** (1980) 2509.

Figure Captions

Fig. 1 Time evolutions of a) the electron density profile, and b) the electron temperature profile.

Fig. 2 Temporal behaviors of plasma parameters of a pellet fueled plasma: a) the line electron density $n_e l$ at about half the plasma radius and the central electron temperature T_e ; b) the Ti XXI emissivity line ; c) the emissivity lines of Ti XX and Ti XIX ; d) the NB heating power, P_{NB}, and the central soft X-ray intensity, I_{SX}.

Fig. 3 Comparison of measured emissivity lines with simulation results for scanning Cv from 1 to 4, holding the uniform $D_A = 1.0\ m^2/s$: a) Ti XXI ; b) Ti XX.

Fig. 4 Temporal behavior of the emissivity lines of a) Ti XXI, and b) Ti XX calculated by taking the neoclassical impurity transport flux into the anomalous transport driven flux with the uniform $D_A = 1.0\ m^2/s$.

Fig. 5 Comparison of measured lines with the simulation results based on the two zone model assuming the improved transport inside the q=1 surface : a) Ti XXI ; b) Ti XX.

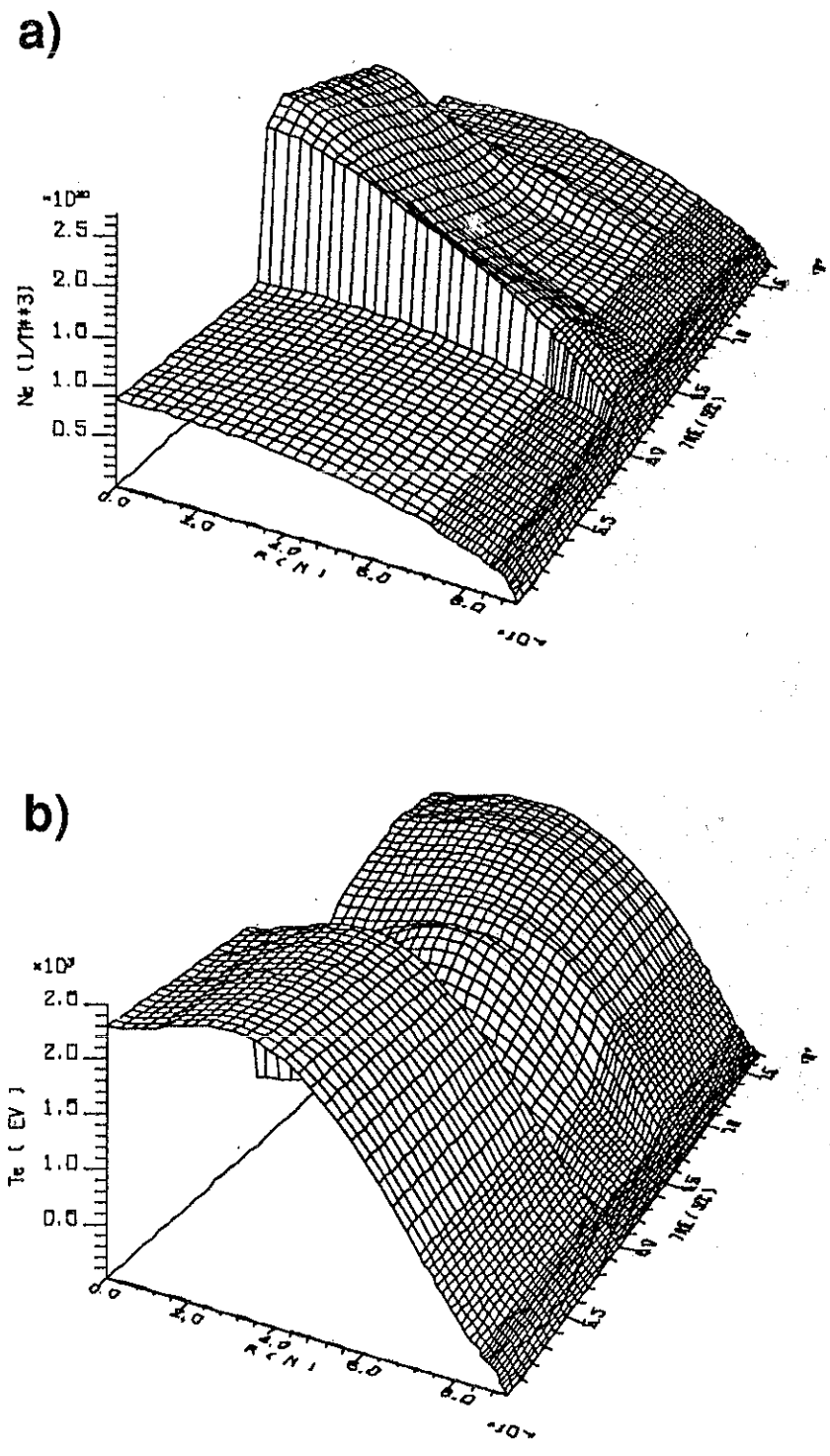

Fig. 1

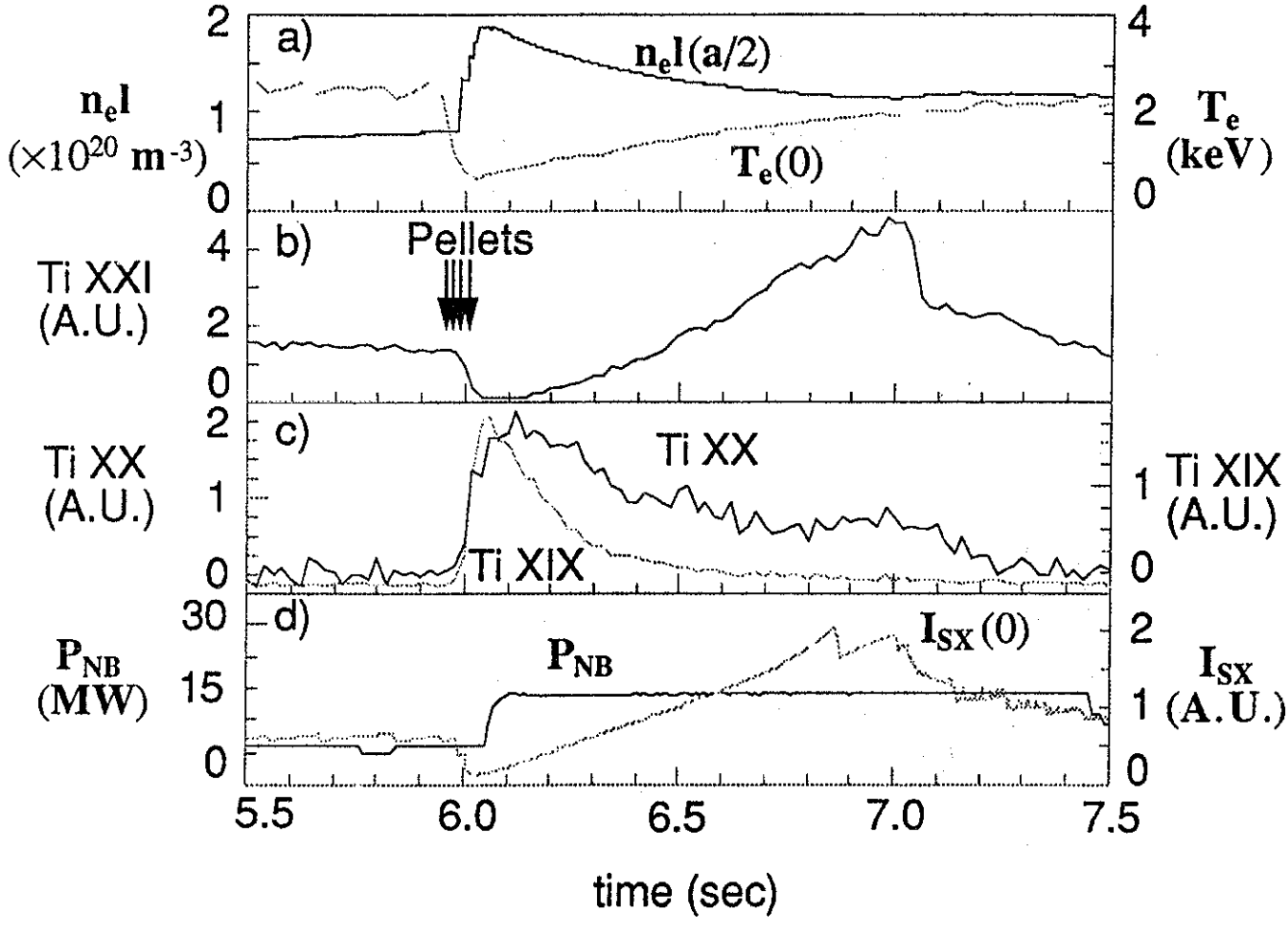
a)
$n_e l(a/2)$
$T_e(0)$
$n_e l$ ($\times 10^{20}$ m^{-3})
T_e (keV)
b)
Pellets
Ti XXI (A.U.)
c)
Ti XX
Ti XIX
Ti XX (A.U.)
Ti XIX (A.U.)
d)
P_{NB}
$I_{SX}(0)$
P_{NB} (MW)
I_{SX} (A.U.)
5.5
6.0
6.5
7.0
7.5
time (sec)

Fig. 2

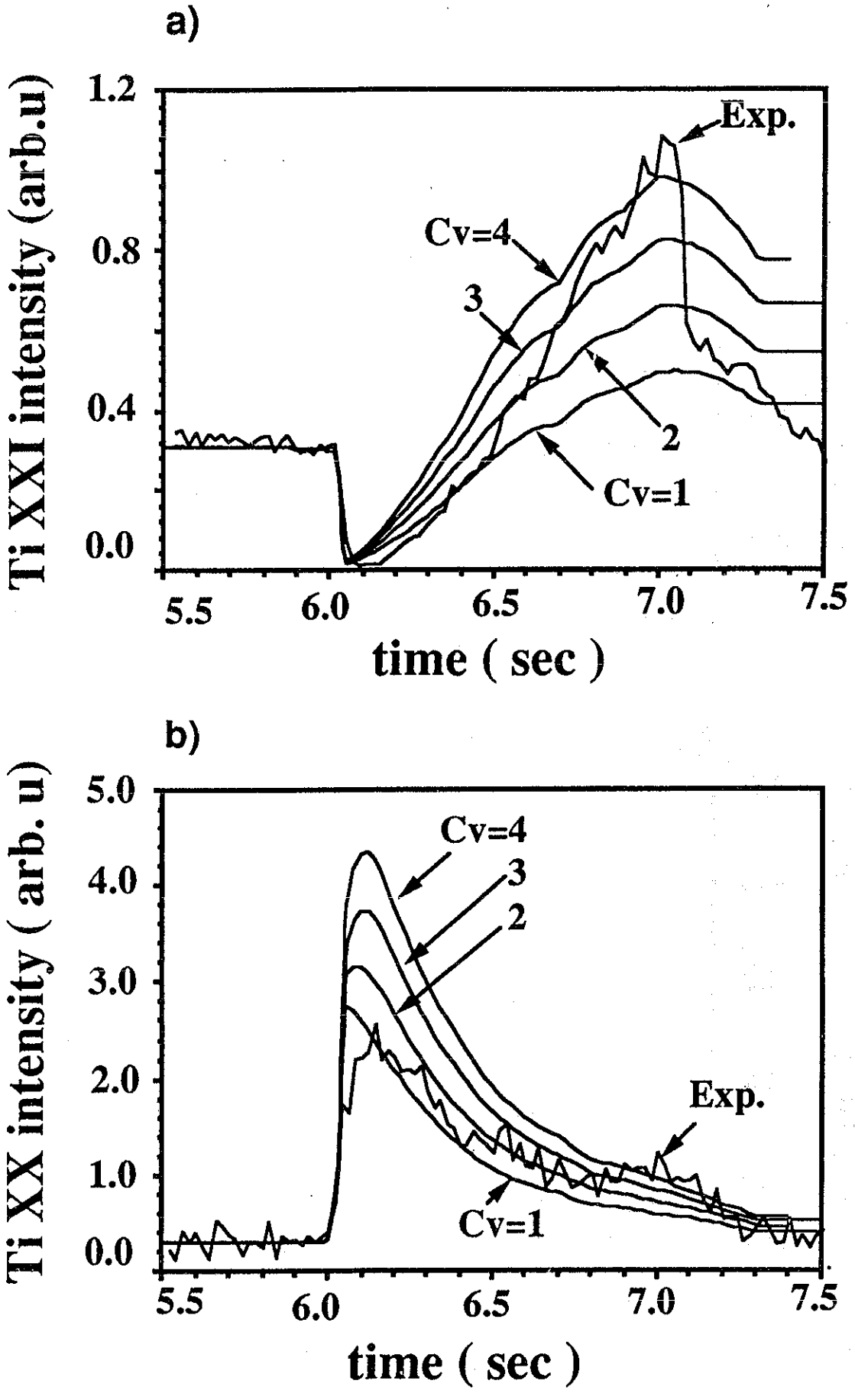
a)
Ti XXI intensity (arb.u)
1.2
0.8
0.4
0.0
Exp.
Cv=4
3
2
Cv=1
5.5
6.0
6.5
7.0
7.5
time (sec)
b)
Ti XX intensity (arb. u)
5.0
4.0
3.0
2.0
1.0
0.0
Cv=4
3
2
Exp.
Cv=1
5.5
6.0
6.5
7.0
7.5
time (sec)

Fig. 3

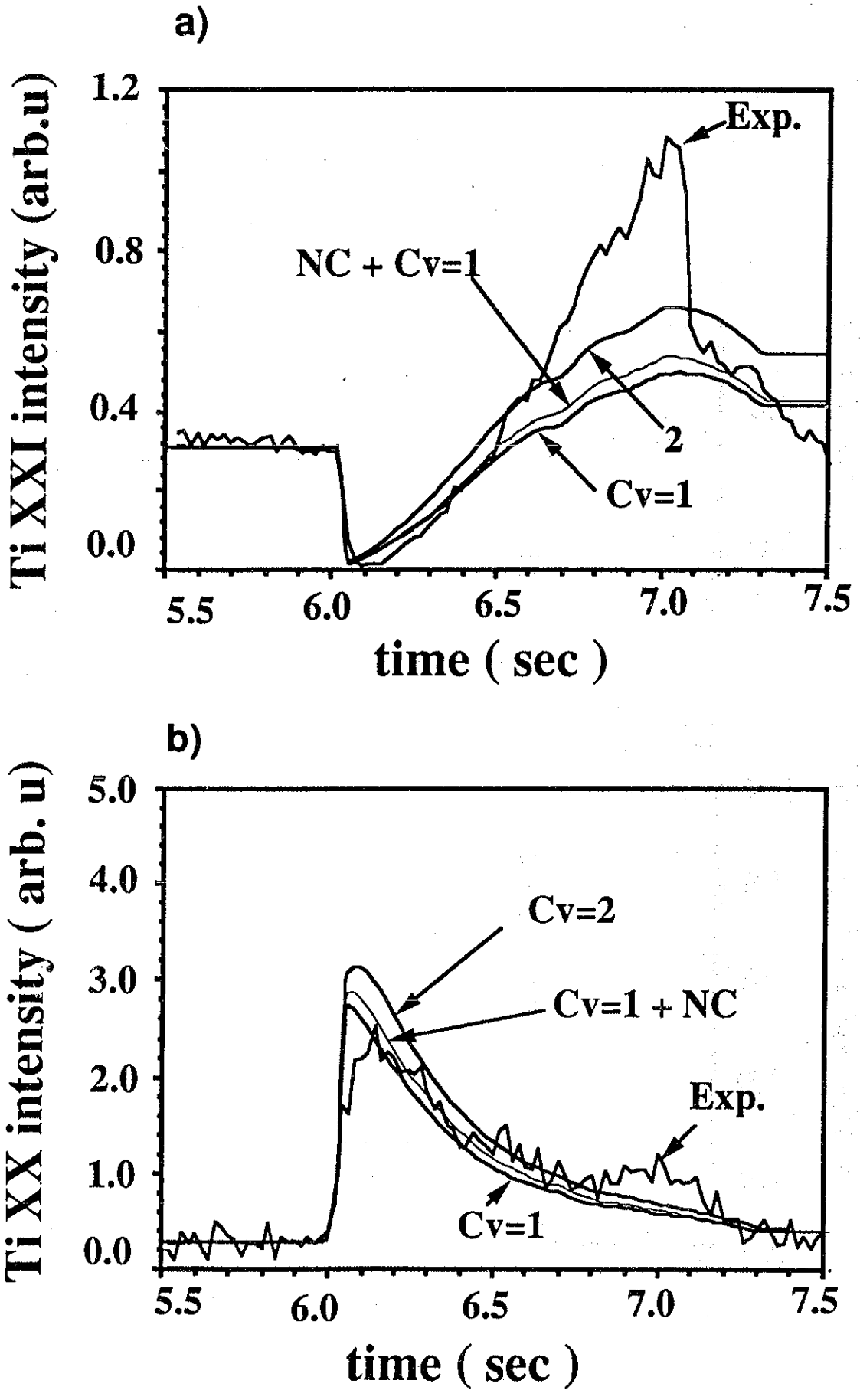
a)
Ti XXI intensity (arb.u)
1.2
0.8
0.4
0.0
Exp.
NC + Cv=1
2
Cv=1
5.5
6.0
6.5
7.0
7.5
time (sec)
b)
Ti XX intensity (arb. u)
5.0
4.0
3.0
2.0
1.0
0.0
Cv=2
Cv=1 + NC
Exp.
Cv=1
5.5
6.0
6.5
7.0
7.5
time (sec)

Fig. 4

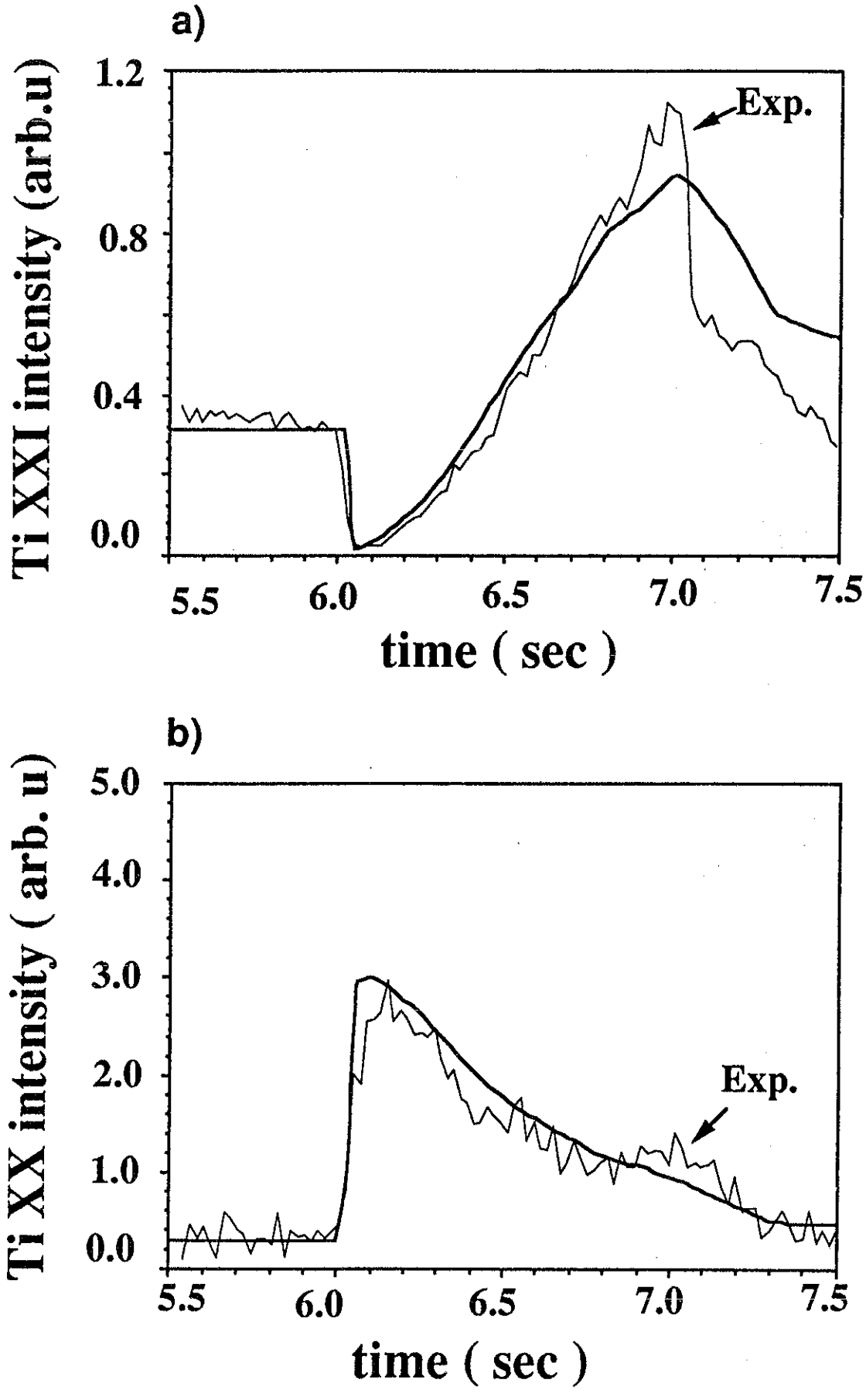
a)
Ti XXI intensity (arb.u)
1.2
0.8
0.4
0.0
Exp.
5.5
6.0
6.5
7.0
7.5
time (sec)
b)
Ti XX intensity (arb. u)
5.0
4.0
3.0
2.0
1.0
0.0
Exp.
5.5
6.0
6.5
7.0
7.5
time (sec)

Fig. 5

Opacity of laser-plasma and x-ray lasers

T.Tomie, E.Miura, and M.Yano

Electrotechnical Laboratory
1-1-4, Umezono, Tsukuba, Ibaraki, 305 Japan

Abstract

The importance of plasma opacity in x-ray lasers is briefly discussed. Some example comparisons of calculations and experiments for recombination lasers are presented to show the presently discussed mystery on the radiation trapping. It is suggested that recombination processes may not be well modelled in simulations, which could explain the mystery on the trapping.

1. Introduction

There are many reports of gain observations in the extreme-ultra-violet (XUV) region. Among many schemes for achieving ultrashort wavelength lasers, recombination pumping scheme is the most promising one for scaling to shorter wavelength, because of its potential high efficiency. However, observed gain length products (gl value) for recombination lasers are only 3 to 4. Only one exception is the experiment at Princeton University, where gl of 8 was observed. Many attempts of increasing gl value have failed so far. Our understanding of recombining plasmas may be incomplete.

The other big issue in the recombination scheme is disagreement between theories and experiments. Peak gains obtained in numerical calculations agree well with the experimental values when radiation trapping is neglected. However, we can not justify the neglection of trapping. If trapping effects are included in calculations, the calculated gains are smaller than experimental values. The disagreement may come from some errors in experiments or from some inadequate treaments in calculations. In this paper, we would like to point out the possibility that calculations may not be simulating the recombining plasmas accurately.

2. Radiation trapping

In the XUV region, population inversion is achieved by the rapid radiative decay of the lower lasing level. Radiative life time of a level is proportional to the square of the radiation wavelength from the level. In the steady state, the population ratio of levels 3 and 2, shown in Fig.1, is given by,

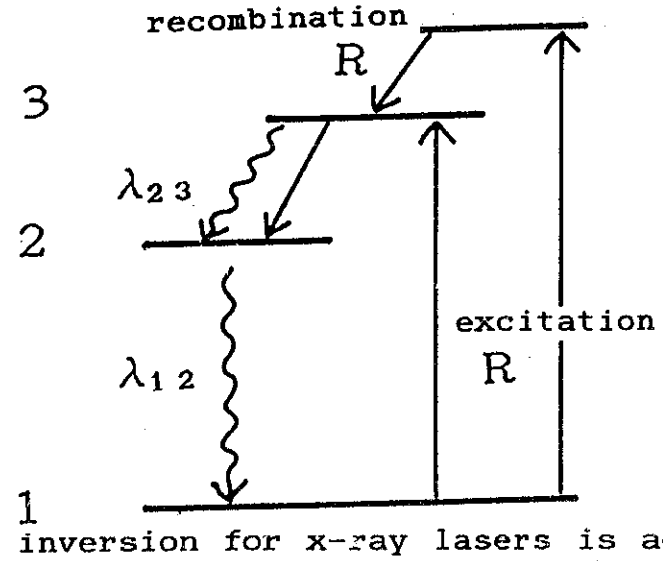

Fig.1: Population inversion for x-ray lasers is achieved by the rapid radiative decay of the lower lasing level 2. If the plasma is optically thick, escape probability of the radiation λ_{12} to the ground state 1 becomes low, and the effective radiative life time of level 2 becomes long, leading to the destruction of population inversion.

$$\frac{n_3/g_3}{n_2/g_2} = \frac{g_1 f_{12}}{g_2 f_{23}} \left(\frac{\lambda_{23}}{\lambda_{12}}\right)^2$$

Here, n_i and g_i are the population density and statistical weight of level i, λ_{ij} and f_{ij} are the wavelength and oscillator strength of the transition between level i and j, respectively. Population inversion between the levels 3 and 2 can be achieved if λ_{12} is well shorter than λ_{23}. For a hydrogen-like recombination laser, radiation from level 2 can be Lyman α and Balmer α can be the transition from level 3 to 2. In this case, the population ratio is given by,

$$\frac{n_3/g_3}{n_2/g_2} \approx 4.7 \quad .$$

If the population of the ground state 1 is not negligible and the plasma size is large, Lyman α will be self absorbed and effective radiative life time of level 2 becomes long. If the escape probability of Lyman α radiation from the plasma is smaller than 0.2, then there will be no population inversion. At high density and high temperature, electron collision could also destroy population inversion by thermalizing levels.

In a laser-produced plasma, expansion velocity of outer plasma is faster and that of inner plasma is slow. This velocity gradient brings about motional Doppler decoupling, and the opacity problem is substantially relaxed.

3. Comparison of calculation with experiment

Figure 2 shows the comparison of numerical calculation result with the experiment[1] for a H-like fluorine laser. The calculated gain including radiation trapping effect is less than half of the experimentally observed value of 4 cm^{-1}. The another example is shown in Fig.3 for the H-like carbon laser. The agreement of the peak gain bewteen the calculation[2] and experiment[3] is better when radiation trapping is neglected. One explanation of the disagreement is some possible error in esimating gains experimentally. There are also efforts to seek theoretical explanations for reduced opacity.

However, we would like to point out that the peak gain is not the single disagreement between experiments and calculations. As seen in Figs.2 and 3, the calculated gain duration is shorter than that experimentally observed. Neglection of trapping extends the gain region toward earlier time, as seen in Figures, leading to the increase of the peak gain. However, inclusion of trapping in calculation does not change the gain profile at later times, because the plasma density is low and the opacity becomes low at later times. Experimental evaluation of gain could carry some uncertainties. Therefore, it will be better to compare the life time of line emissions. In experiments, emission life time was comparable to the gain duration. Although only the gain profile is given in theoretical papers, we expect similar temporal profile for

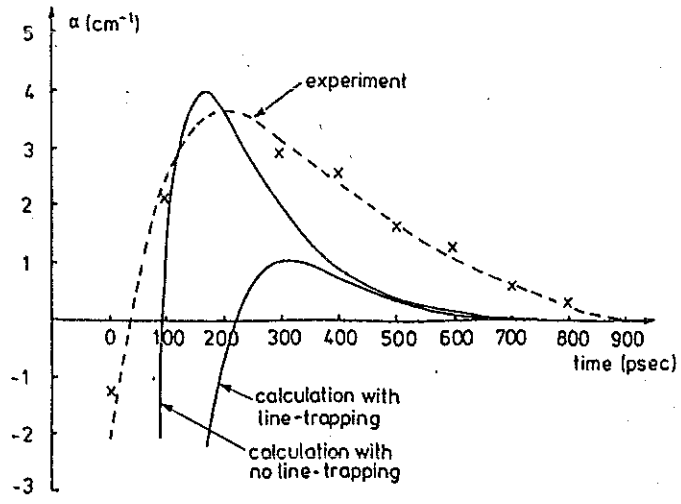

Fig.2: Experimentally observed gain and numarical calculations for H-like fluorine laser. (ref.1)

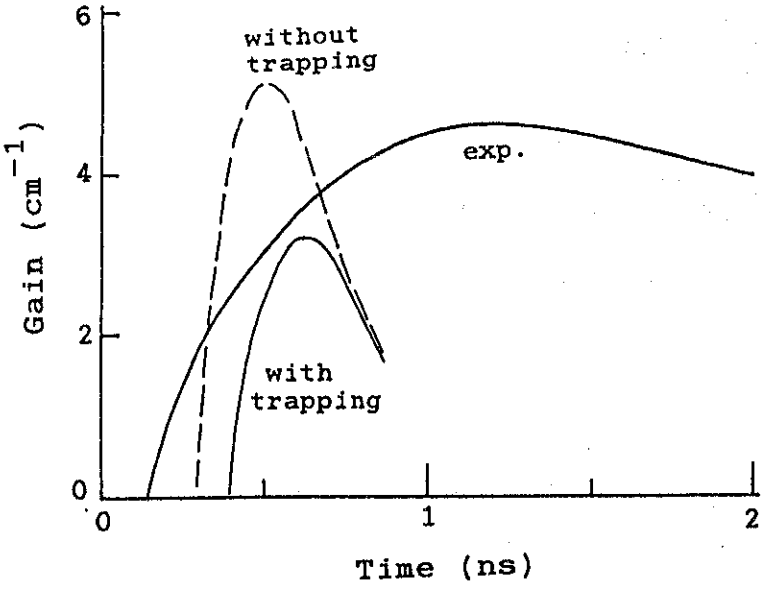

Fig.3: Experimentally observed gain[3] and numarical calculations[2] for H-like carbon laser. The experimentally observed peak gain is well explained by the calculation without trapping. The big difference between the calculation and experiment is the gain duration, which may suggest inadequate modelling of recombination processes in simulations.

calculated line emissions with that of the gain because both are proportional to the number of bare ions. To the best knowledge of the authors, calculated gain duraions are always shorter than experiments. In calcuations, recombination processes may not be adequately treated.

Figure 4 shows our result, showing an x-ray spectrum from a carbon plasma at 100μm from the axis of a fiber target. Although strong Balmer series lines are observed, corresponding emissions from He-like ions are very weak. This spectrum indicates that the number of H-like ions in the ground state is small compared to that of bare ions. If the ground state population of H-like ions is small, trapping of Lyα radiation could be negligible. We are not sure how the ground state of H-like ion can decay so quickly to He-like ions. The detailed study of atomic processes is needed.

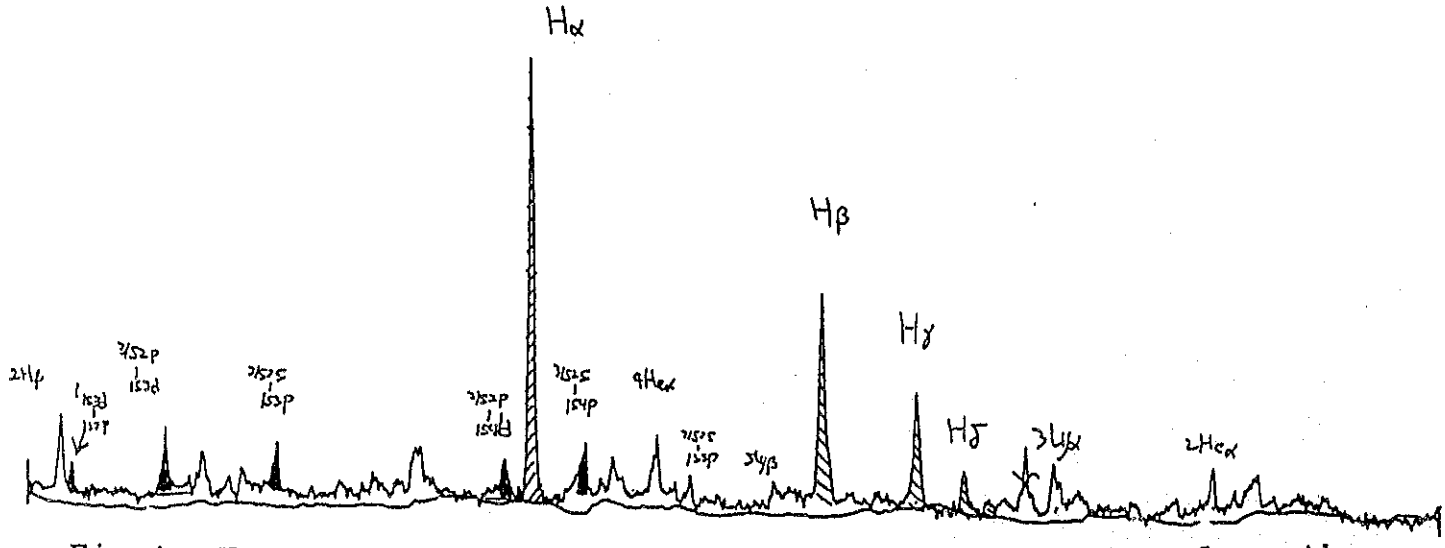

Fig.4: X-ray spectrum from a carbon plasma at 100μm from the axis of a fiber target. Although Balmer series lines (hatched) are strong, corresponding lines from He-like ions (filled) are very weak, indicating small population of H-like ions in the ground state.

4. Conclusion

Radiation trapping is the very important issue in XUV and x-ray lasers of all scheme. In discussions of recombination lasers, only the disagreement of the peak gain between calculations and experiments have been stressed. However, from the temporal behaviour of the gain in calculations and experiments, we would like to suggest that calculations may not be simulating recombination processes adequately. For understanding and optimizing recombination lasers, we should study atomic processes in more detail, and the validity of models should be checked by comparing emission profiles not only by the comparison of the peak gain.

References

1) M.Grande et al.: Opt. Commun. 74 309 (1990)
2) G.Pert and S.Rose: Appl.Phys. B50 307 (1990)
3) C.Chenais-Popovics et al.:Phys.Rev.Lett. 59 2161 (1987)

Characteristics of Soft X-ray Laser Beam Emitted from Laser Produced Ge Plasma

K.Murai, G.Yuan, H.Shiraga, H.Daido, M.Yamanaka and Y.Kato
Institute of Laser Engineering, Osaka University
Suita, Osaka 565 Japan

C.L.S.Lewis, D.M.O'Neill and D.Neely
Department of Pure and Applied Physics, The Queen's University of Belfast
Belfast BT7 1NN, Northern Ireland

Abstract

Experimental results on Ne-like Ge soft X-ray laser are reported. Exponential increase in axial intensity, narrowing of the spectral width and decrease of the divergence angle with increase in the target length have been observed. Characteristics of the lasing lines, such as spectral width, brightness, and spatial coherence are presented.

1.Introduction

Ge soft X-ray laser beam is emitted from Ge plasma column produced by irradiation with the pump laser[1-5]. Population inversion in the 3p-3s transitions in the Ne-like Ge ions is generated by electron collisional excitation in the Ge plasma. The possible lasing transitions are shown in Fig.1. Since different laser lines have different gain regions in the plasma, it is useful to investigate detailed characteristics of the laser lines for understanding atomic processes in the plasma.

Coherence properties of the X-ray laser beam play an important role in applications to lithography, holography and others. In this paper, brightness and spatial coherence of the Ge soft X-ray laser are also evaluated.

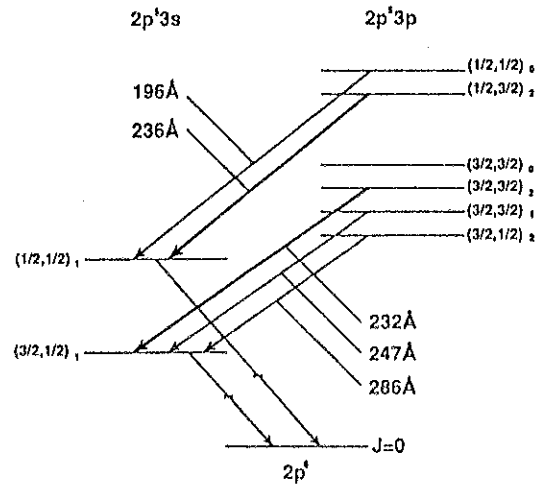

Fig.1 Five lasing transitions in Ne-like Ge

2.Experiment

Figure 2 illustrates the various kinds of targets that we have used in the X-ray laser experiment. The "slab target" is easy to fabricate but the X-ray laser beam is refracted due to electron density gradient in the plasma. The "double plasma target" is designed to compensate for this refraction by guiding the soft X-ray laser beam in a zig-zag path. The "exploding foil target" is pumped by two laser beams and the X-ray laser beam propagates in the middle of the column plasma. The X-ray mirror placed at one end of the target is expected to lengthen the effective target length.

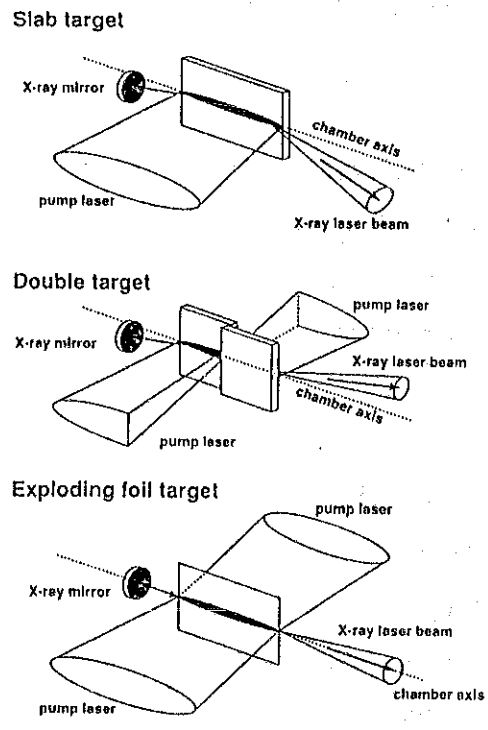

Fig.2 Target configurations used in this experiment

The experimental setup is illustrated in Fig.3. Two beams of the GEKKO XII glass laser were used for pumping. Each beam delivered an energy of 1.1 kJ on the target with 1ns pulse width and 1 μm wavelength. Two pump beams were used for the exploding foil and double targets and one beam was used for the slab target. Each laser beam was line focused to 6 cm length by combination of a cylindrical lens and an aspherical lens. Figure 4 shows the focusing pattern, recorded by an X-ray slit camera, and the distribution of the irradiation intensity. The focus pattern has two beam waists of 50 μm width. The average irradiation intensity of each beam is approximately 1.7×10^{13} W/cm^2. Irradiation intensity becomes less than 1.0×10^{13} W/cm^2 over ±20 mm from the center of the line focus.

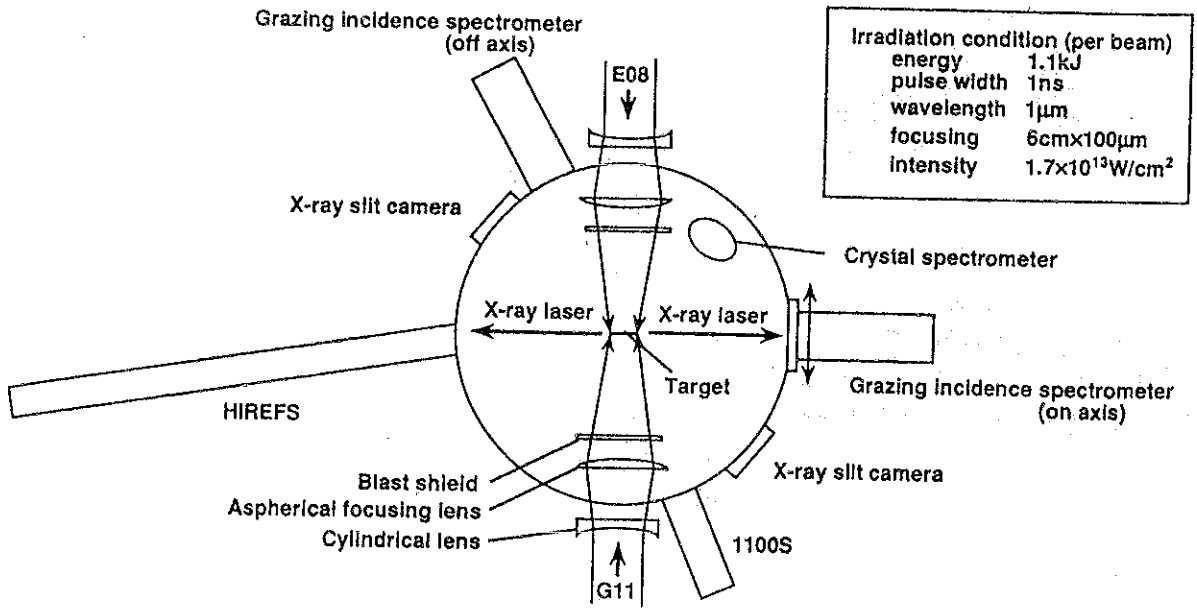

Fig.3 Experimental arrangement

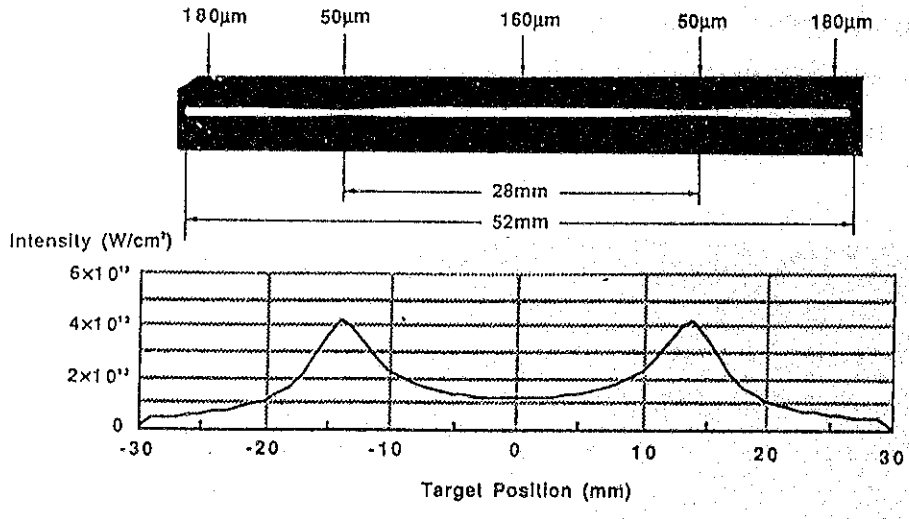

Fig.4 X-ray image of the line focus and the intensity distribution

The diagnostic instruments of the X-ray laser beam are illustrated in Fig.5. A grazing incidence spectrometer was mounted on axis of the X-ray laser to record either a time-integrated spectrum and angular divergence with an X-ray film or a time-resolved spectrum with an X-ray streak camera. On another side, we measured either spectral width with a high spectral resolution grazing incidence spectrometer or spatial coherence of the X-ray laser beam with a pinhole array.

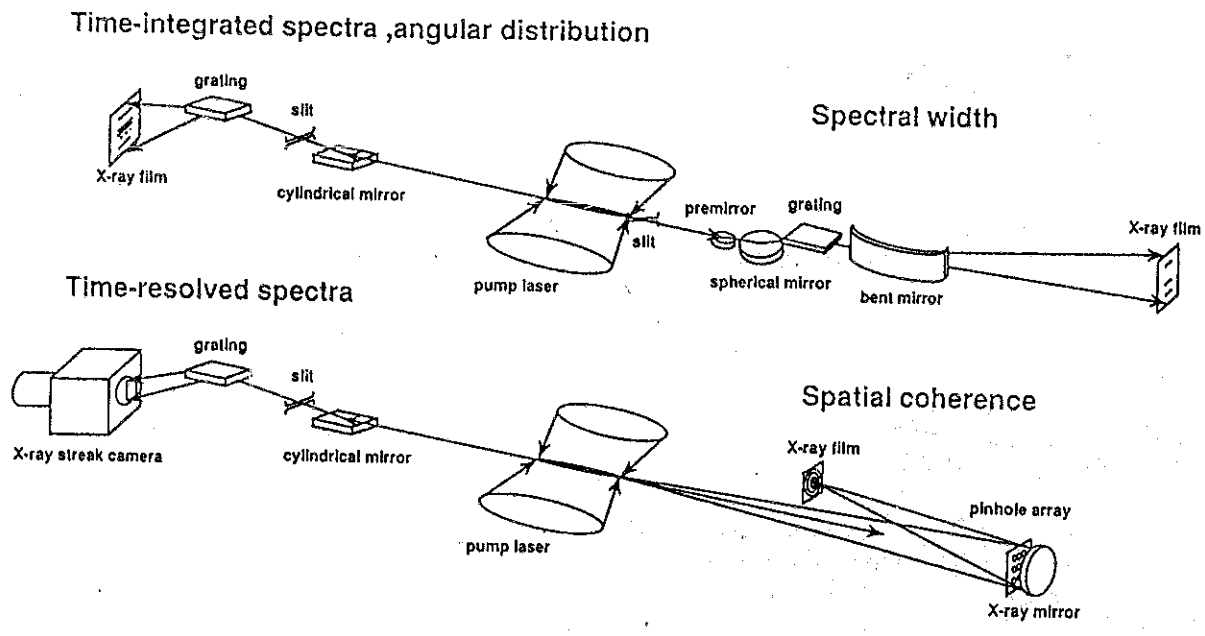

Fig.5 Diagnostics of the X-ray laser beam

3. Results and Discussion

3.1 Time integrated intensity and angular divergence

The time-integrated intensity and the angular divergence of the Ge soft X-ray laser was measured by the grazing incidence spectrometer. Figure 6 shows a result for the 50 mm slab target. The lasing lines are refracted away from the target surface due to electron density gradient. The 232 Å and 236 Å lines due to J=2-1 transitions are stronger than other lasing lines.

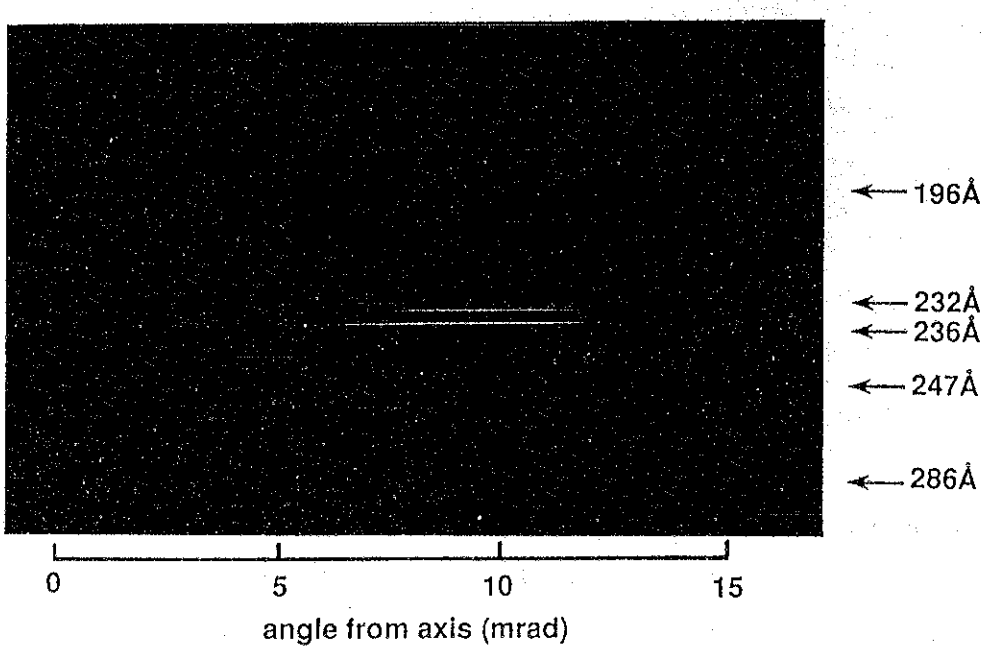

Fig.6 Angular divergence of X-ray laser. Positive angle corresponds to the direction away from target surface.

The intensities of these 2 lasing lines at different target lengths are plotted in Fig.7. Both intensities show exponential growth with the target length. The time-integrated gain coefficients for the two lines are approximately 2.4 cm^{-1}. Increase in the gain-length product should lead to reduction in the angular divergence. The experimental results shown in Fig.8 demonstrates that the angular divergence indeed becomes narrower for the longer target, except for the 50mm target where edge effect due to lower irradiance becomes significant.

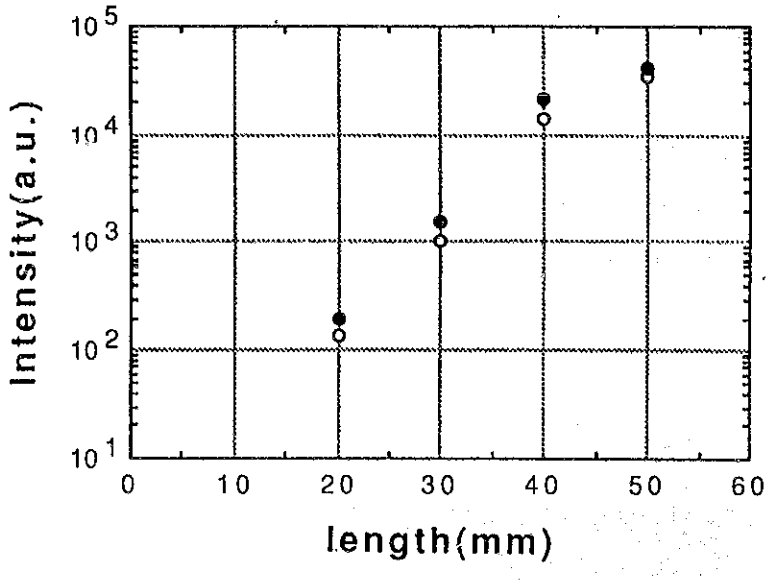

Fig.7 Time-integrated peak intensities emitted from slab targets versus target length. Open circles are for the 232Å line and closed circles are for the 236Å line.

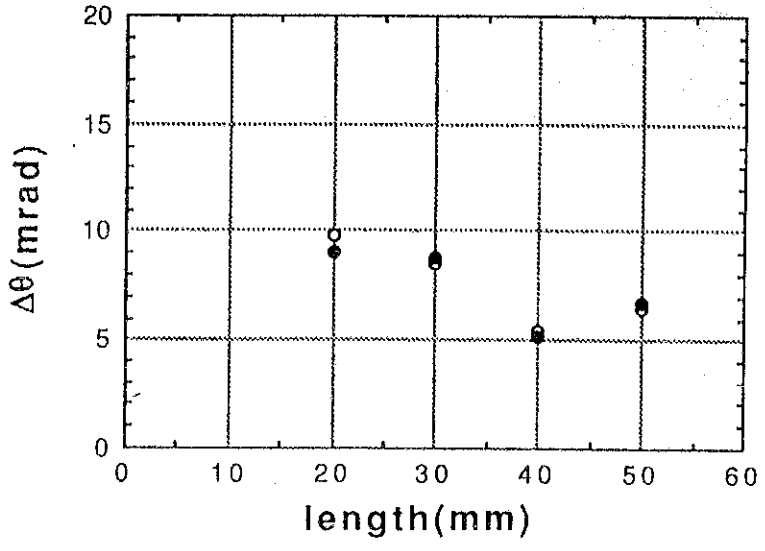

Fig.8 Time-integrated divergence angles emitted from slab targets versus target length. Open circles are for the 232Å line and closed circles are for the 236Å line.

3.2 Spectral Width

The amplification narrowing of the spectral width is given by

$$\Delta\lambda = \frac{\Delta\lambda_D}{\sqrt{gl}} \qquad (1)$$

where $\Delta\lambda$ is the spectral width of the lasing line, $\Delta\lambda_D$ is the Doppler width, and gl is the gain-length product of the lasing line.

The high spectral resolution grazing incidence spectrometer(HIREFS) with a resolving power($\lambda/\Delta\lambda$) exceeding 10^4 was used to measure the spectral width. The measurement result is shown in Fig.9. A 0.8 μm thick Al filter was used to cover half of the X-ray film in order to increase the dynamic range of measurement. For the 232 Å line, the spectral width is 22 mÅ that is almost the limit of the spectral resolution of this spectrometer. Assuming that the ion temperature of the Ge plasma is about 700 eV, the Doppler line broadening is 55 mÅ for the 232 Å line. The observed spectral narrowing is considered to be due to the high gain-length product of the 232 Å and 236 Å lines.

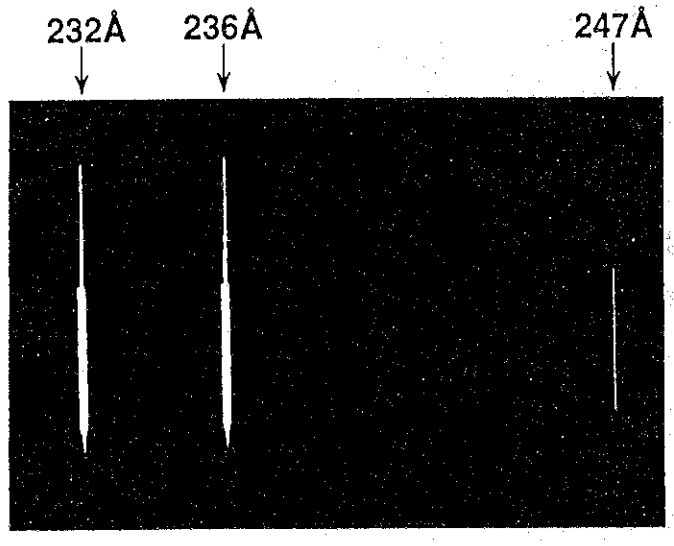

Fig.9 High resolution spectrum of the Ge soft X-ray laser

3.3 Brightness of the 232 Å and 236 Å lines

Spectral brightness is expressed as follows;

$$B = \frac{N}{\tau\, \Delta A\, \Delta\Omega \left(\frac{\Delta\lambda}{\lambda}\right)} \qquad (2)$$

where N is the number of photons of the lasing line, τ is the temporal width, ΔA is the cross sectional area of the X-ray source, $\Delta\Omega$ is the divergence angle of the beam, and $\Delta\lambda$ is the spectral width.

The beam energy of the 232 Å and 236 Å lines was measured with the beam line exposing a photoresist (PMMA) with the X-ray laser. The beam energy was measured to be approximately 0.1 mJ for each line. The temporal width measured with the X-ray streak camera was 700 ps. The source size was approximately 50 μm in diameter deduced from the width in the HIREFS recording without using the slit at the source position.

For the 40 mm slab target, the calculated brightness for the 232 Å and 236 Å lines is about 2.8×10^{23} photons/s•mm^2•mrad^2•0.01%BW. From this measurement, it is derived that the brightness of the Ge soft X-ray laser in our experiment is much higher than other X-ray sources such as synchrotron radiation and incoherent X-rays from laser plasmas(see Fig.10).

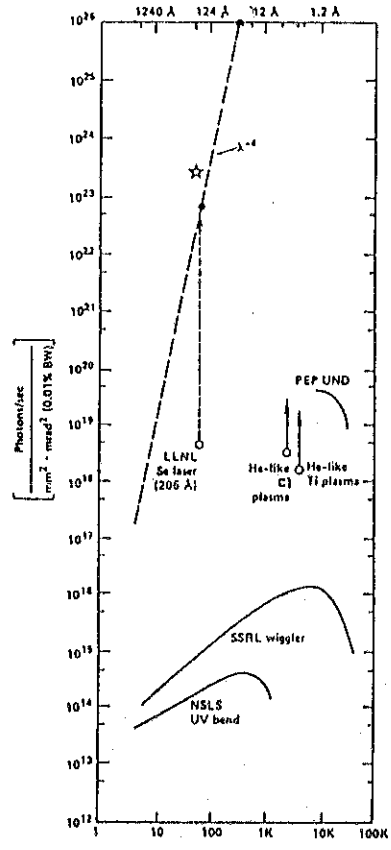

Fig.10 Peak spectral brightness versus wavelength for various X-ray sources[7]
Star indicates the brightness of our Ge soft X-ray laser emitted from a 40mm slab target.

3.4 Spatial Coherence of the 232 Å and 236 Å lines

The temporal and spatial coherence are important parameters in applying the X-ray lasers to lithography and holography. The temporal coherence is estimated from the spectral width. The relationship between the coherence time τ_{coh} and the spectral width $\Delta\lambda$ is given by[6]

$$\tau_{coh}\,\Delta\nu \approx 1 \quad ,$$

$$\Delta\nu = \frac{\Delta\lambda}{\lambda^2}\,c \qquad (3)$$

where c is the speed of light. The calculated coherence time is 0.8 ps which corresponds to the longitudinal coherence length of 250 μm.

The interference pattern was observed using the pinhole array shown in Fig.11. This pinhole array and a concave X-ray mirror was located at the distance of 2.4 m from the target. The reflectivity of this X-ray mirror was 35% at 232 Å and 236 Å. Figure 12 shows the interference pattern obtained with an exploding foil target. Figure 13 shows the intensity distribution of this pattern along the horizontal direction of Fig.12. This shows that the Ge soft X-ray laser we have developed has the coherence size of approximately 300 μm at the pinhole array.

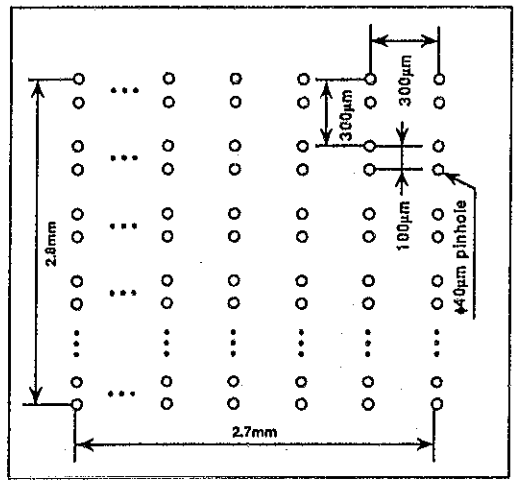

Fig.11 Pinhole array used for spatial coherence measurement

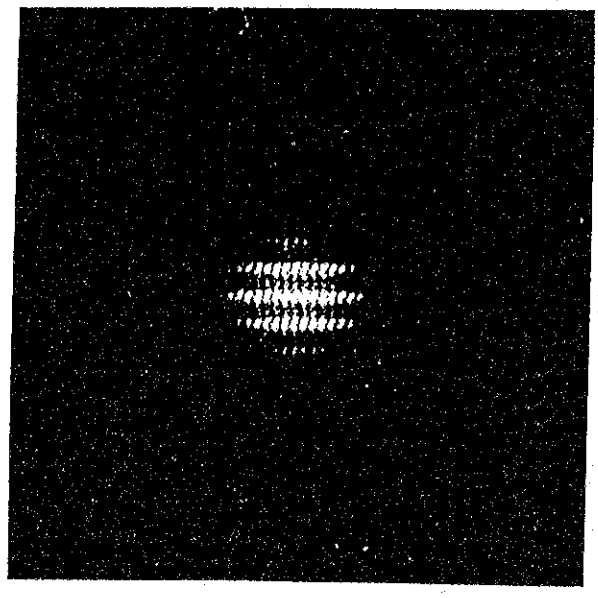

Fig.12 Interference pattern due to pinhole array for the exploding foil target

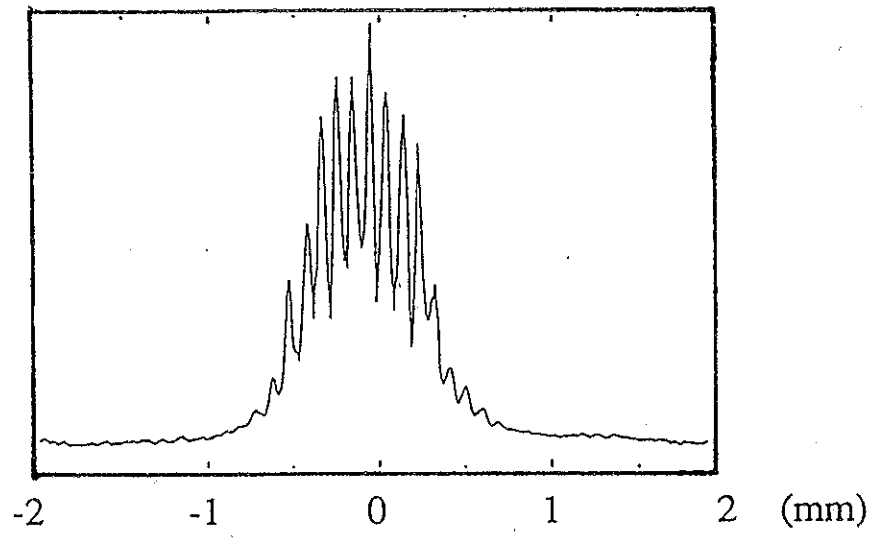

Fig.13 Interference pattern due to 300μm spacing of the pinholes

4.Conclusion

We have obtained amplification of 5 lasing lines due to 3p-3s transitions in the Ne-like Ge ions. Especially, 232 Å and 236 Å lines due to J=2-1 transitions are stronger than other lasing lines. The time-integrated gain coefficients for the 232 Å and 236 Å lines are approximately 2.4 cm^{-1} for the slab target. The measured spectral widths of these lines are much narrower than the calculated Doppler widths. The divergence angle becomes narrower with the gain-length product.

The brightness of the soft X-ray laser emitted from the 40 mm slab target is 2.8×10^{23} photons/s•mm^2•$mrad^2$•0.01%BW which is significantly higher than other X-ray sources.

In addition, we have succeeded in observing the interference pattern which is due to spatial coherence of the X-ray laser beam. The results show that the spatial coherence of the X-ray laser is approximately 300 μm at 2.4 m from the source position.

5.Acknowledgement

This work was performed as a joint research between the Institute of Laser Engineering, Osaka University and the Central Laser Facility, Rutherford Appleton Laboratory.

References

[1] T.N.Lee *et al*, Phys.Rev.Lett. **59**,1185,(1987)

[2] D.Naccache *et al.*, Phys. Rev. A **42**,3027,(1990)

[3] C.J.Keane *et al*, Appl.Phys.B **50**,257,(1990)

[4] D.M.O'Neill *et al.*, Opt. Comm. **75**,406,(1990)

[5] T.Boehly *et al*, Opt.Comm. **79**,57,(1990)

[6] R.C.Elton, 'X-RAY LASERS' (Academic,New York 1990)

[7] D.Matthews *et al*,J.Opt.Soc.Am.B **4**,575,(1987)

Study of a Compact Soft-X-Ray Laser

T. Hara, K. Ando, H. Hirose*,

F. Negishi, H. Yashiro**, and Y. Aoyagi

The Institute of Physical and Chemical Research(RIKEN),

Wako-shi, Saitama 351-01

*Shimadzu, Corp. Nakagyo-ku, Kyoto 604

**Faculty of Engineering, Saitama University,

Shimo-ohkubo, Urawa, Saitama 338

Abstract

To pave the way for many applications, soft X-ray lasers need to be improved in the pumping efficiency and to be excited by a compact-size laser with high repetition rate. Amplified spontaneous emissions (ASE) of Li-like and Be-like ions were observed in recombining Al and Si plasmas produced by a low-power driving laser. These ASEs were achieved by heating plasma by a train of laser pulses with short intervals, and by sharply focusing a pumping glass laser to a line 40 μm wide and 12 mm long onto a slab target for rapid cooling of plasmas through adiabatic expansion. The measured gain coefficients are 3.4, 4.5, 1.1 and 0.6 cm^{-1} for the 105.7 Å (3d-5f) and 154.7 Å (3d-4f) in Al XI and for the 88.84 Å (3d-5f) and 130.0 Å (3d-4f) in Si XII, respectively. The gain in a Al plasma was observed in large area of 500 μm x 600 μm around the position 0.8 mm apart from a target surface. As Al XI line emissions continue during about 6 ns (FWHM), soft-X-ray laser resonator is expected to be effective. Mechanism of plasma heating by a train of laser pulses and the optimum shape of the laser pulse for pumping of soft X-ray laser were investigated.

1. Introduction

Recently, considerable progress has been made in the development of soft x-ray laser since 1985 and soft x-ray lasing of 4.48 nm and 4.32 nm was reported last year[1]. It is believed that it is important to produce high ion density at a higher ionization stage to obtain a large gain. So it is necessary to use a high-power laser of more than several hundred joules/pulse for pumping soft X-ray lasers. For many practical applications a table-size soft X-ray laser should be developed. Until now a powerful laser of a single pulse has often been used to produce high density plasma. Recently we observed ASE(Amplified Spontaneous Emission) in some lines of Al X and Al XI in a recombining plasma produced by a very low power laser which was composed of a train of many pulses separated by about 350 ps.

2. Experimental arrengement and results[2 - 6]

A Nd-doped glass laser was operated at a wavelength of 1.05 μm in a 5 ns-FWHM pulse. A 12 mm-long line focus was formed on an slab target with the use of a cylindrical-spherical lens system. A high density plasma was produced on the target surface by the laser irradiation and then recombined due to cooling by adiabatic expansion and other processes. In the recombination scheme, rapid cooling of the plasma leads to improvement of the laser efficiency. For rapid cooling of the plasma, the width of the focus line was set at less than 40 μm. This narrow width leads to a large volume ratio in plasma expansion. The soft X-ray spectra (time integrated) emitted from the recombining plasma in the 5 - 50 nm region were recorded on Kodak SWR plates with a flat-field-type grazing incidence spectrograph to view the plasma axially.

When an expanding Al plasma was produced by a laser beam of 2 J, amplified spontaneous emissions of Al ions were observed in a recombining plasma. At a position of 0.8 mm from a target surface, the measured gain coefficients are 3.4, 4.5, 3.4 and 3.5 cm^{-1} for the 10.57 nm 3d-5f and 15.47 nm 3d-4f transitions in Al

XI and for the 12.35 nm 3d-5f and 17.78 nm 3d-4f transitions in Al X, respectively. Gain length products of four spectral lines are in the range of 4.1-5.4. If the input energy increases, electron temperature of a laser produced plasma becomes higher and it will be difficult to cool sufficiently the temperature by free expansion. This rapid cooling of plasmas leads to high gain coefficients.

In a recombining Si plasma, amplified spontaneous emissions of Si ions were also observed at the position 0.6 mm apart from target surface. The gain coefficients are 1.1 and 0.6 cm^{-1} for the 8.88 nm 3d-5f and 13.00 nm 3d-4f transitions in Si XII and are 0.6 and 0.4 cm^{-1} for the 10.23 nm 3d-5f and 14.76 nm 3d-4f transitions in Si XI, respectively. These transitions are same ones in Al XI and X. It is expected from these experiments that in Li isoelectronic sequence, the wavelength of ASE should be shortened if heavier target elements are used.

To study the effect of multi-pulse irradiation on the production of laser plasma and on X-ray emissions including ASE in detail, we constructed a pulse train forming system and investigated the emitted soft X-ray spectra for various pulse trains. A 100-ps laser pulse from a mode locked oscillator was injected into an optical pulse stacker[9] to get a 8-pulse train with the interpulse time of 400 ps. Laser plasmas were produced by focusing the laser pulse train with an irradiance of 6×10^{12} W/cm^2 on Al slab targets. Soft X-ray spectra observed at z = 0.4 mm are shown in Fig. 1. The number of laser pulses was changed by controlling the laser paths in the optical pulse stacker and the effects of the pulse number on soft X-ray spectra were investigated. It should be noted that strong lines of Al X and Al XI appear for more than 2-pulses irradiation. This data shows that plasmas are sequentially heated up to high temperature by a chain of laser pulses with the short interpulse time.

It is important to study variation of plasma for time interval between laser pulses while keeping the peak power and the pulse number constant. Surprisingly, in the spectrum of 800 ps time interval, Li-like lines disappeared and only Al X (Be-like) line remained. The spectrum of 600 ps interval was very

similar to that of 800 ps. Line intensities of three different kind of ionization stages (Al VI, Al X and Al XI) are plotted as a function of interpulse time for a train of four pulses in Fig. 2. Line intensities are normalized at 400 ps. From this figure, optimum time interval for efficient heating of plasma is estimated to be about 200 ps.

3. Discussion

The above results have shown very clearly the effect of pulse train laser on the soft X-ray spectra and give understanding of the production mechanism of highly ionized atoms in a high density plasma. Electron temperature plays an important role to produce high ionization stages of plasma. Our experimental results show that multi-pulse irradiation creates hotter plasma than single-pulse irradiation and therefore higher ionization stages such as a Li-like ion can be attained. Each pulse may act as a pre-pulse for next incoming pulses, a part of which is absorbed by the pre-formed plasma, and therefore raises the electron temperature of plasma effectively. As a result, efficient and successive heating near the target surface may occur with increasing the number of pulses. In this consideration, interpulse time is an important factor in order to attain the higher electron temperature of plasma, because such a plasma heating must be done successively before electron temperature decreases due to adiabatic expansion. Our experimental result shows that efficient heating must be achieved within the 400 ps.

As we used a long laser pulse of 5 ns and a slab target in the present experiment, a long time duration of gain can be expected. We observed that the pulsewidth of Li-like Al ion line is 6.2 ns FWHM. This pulsewidth is so long that the cavity experiment will be very useful. Therefore, it is expected that a soft X-ray oscillator can be constructed with high reflective resonator mirrors.

4. Summary

We have observed soft X-ray amplified spontaneous emissions of Al and Si ions in a recombining plasma produced by a low-power driving laser. These lasings were achieved by sharply focusing a pumping glass laser to a line 40 μm wide onto a slab target, of which pulse shape consisted of a chain of picosecond pulse train. As line emissions of Al XI continue about 6 ns (FWHM), a compact soft X-ray oscillator with a high repetition rate can be expected. The soft X-ray lasers will have several important applications such as X-ray microscopes and X-ray holography. Based on the pumping method reported here, we will develop the true tabletop soft X-ray laser.

REFERENCES

1) B. J. MacGowan, S. Maxon, L. B. Da Silva, D. J. Fields, C. J. Keane, D. L. Matthews, A. L. Osterheld, J. H. Scofield, G. Shimkaveg and G. F. Stone, Phys. Rev. Lett. **65**, 420(1990).
2) T. Hara, K. Ando, N. Kusakabe, H. Yashiro, and Y. Aoyagi, Jpn. J. Appl. Phys. **28**, L1010(1989).
3) T. Hara, K. Ando, Y. Aoyagi and H. Yashiro, Proceedings of Fifteenth Int. Conf. on X-Ray and Inner-Shell Processes (Knoxville, Tennessee), 197(1990).
4) T. Hara, K. Ando, F. Negishi, H. Yashiro, and Y. Aoyagi, Proceedings of 2nd Int. Conf. on X-Ray Lasers (York, UK), (1990).
5) H. Yashiro, T. Hara, K. Ando, F. Negishi, S. Ido and Y. Aoyagi, ibid.
6) H. Hirose, T. Hara, K. Ando, F. Negishi, H. Yashiro and Y. Aoyagi, Proceedings of Short-Wavelength Coherent Radiation (Monterey, California), (1991).

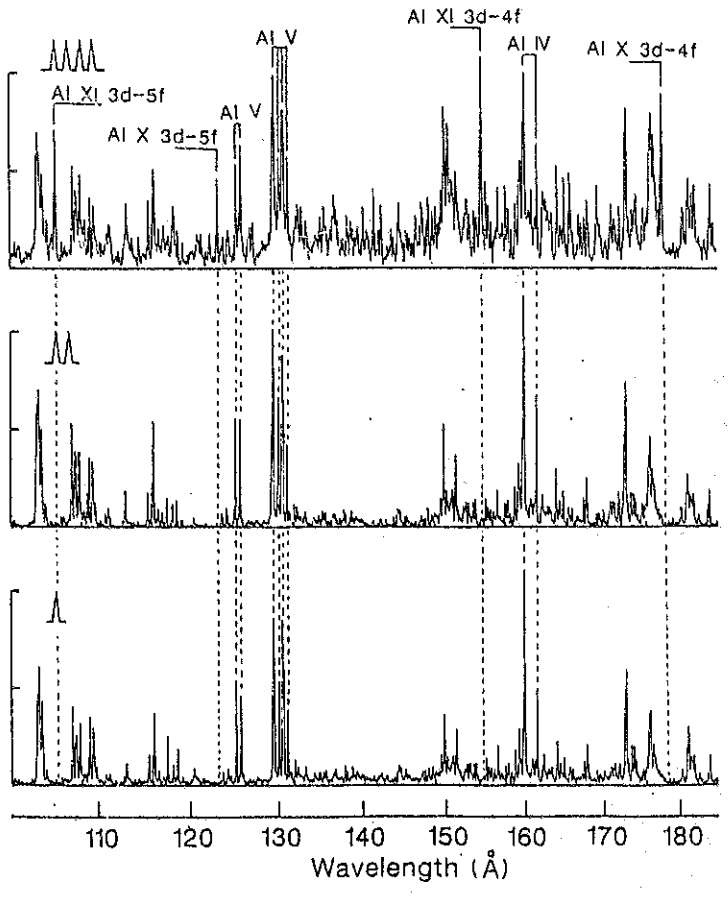

Fig. 1 Microdensitometer traces of spectrograms taken with a flat-field spectrograph for 1, 2, and 4 pulse trains. Exposures for 1, 2, and 4 pulses are 16, 8, and 4 shots, respectively.

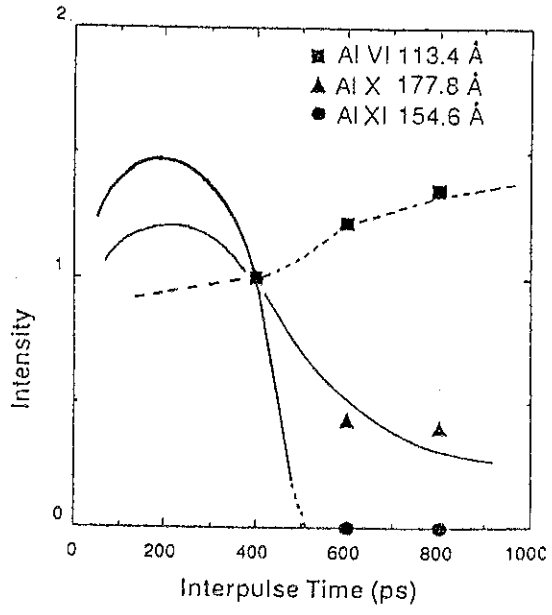

Fig. 2 Line intensity as a function of interpulse time for three defferent kinds of ion spcies (Al VI, X, XI). Intensities are normalized at 400 psec.

Numerical Simulation for Recombination X-Ray Laser

Takayuki AOKI

Department of Energy Sciences, the Graduate School at Nagatsuta,
Tokyo Institute of Technology, 4259 Nagatsuta, Midori-ku, Yokohama 227, Japan

Abstract

Recombination x-ray laser is investigated by the numerical simulation which includes atomic process, hydrodynamics, thermal conduction, and radiation transport. A laser-irradiated aluminum fiber is examined, and the gain of heliumlike 3–2 transition and the time-resolved x-ray spectra are obtained. As a new target structure, a hollow microcylinder target is proposed for a recombination x-ray laser, and studied by using numerical simulation. It appears that there is a possibility to increase the efficiency of x-ray laser generation, and enhance the gain duration time.

1. Introduction

In the x-ray laser schemes using laser-produced plasma, recombination lasing is so effective in comparison with the pumping method using an electron collisional excitation. Recently, the experiments of the laser-irradiated fiber show the gains of the recombination x-ray laser[1]–[2]. The population inversion occurs in which the laser-heated hot plasma expands into free space. In the recombination pumping process, atomic physics, hydrodynamics, thermal transport and so on are coupled closely. When we carry out a numerical simulation, we have to take into account for all the above processes and solve them self-consistently. In this paper, an aluminum target irradiated by a short pulse and short wave length laser is investigated by a numerical simulation. The population inversion in the heliumlike 3–2 transition is discussed, however the transport of the resonance line is neglected. There is no sufficient theory of the radiation trapping which is able to explain the gain characteristics of the experimental data. In the simulation code, an adaptive mesh

CIP (Cubic-Interpolated Pseudo-particle) scheme[3]–[4] is applied to the hydrodynamic motion, and a flux limited diffusion method is used in the thermal conduction.

A new type of the target structure is also proposed in this paper, instead of slab or fiber targets. In fig.1, a hollow microcylinder target is shown schematically. The line focused laser irradiates the inner wall surface of the cylinder through the axial slit. This structure had been proposed[5], however the aim was not a recombination x-ray laser.

2. Atomic kinetics

The atomic model employed in the simulation is based on the collisional-radiative (CR) model. The detail configuration is accounted, however each level is determined by the screened hydrogen model[6]. Only the principle quantum numbers and the charge states are distinguished. The processes included in this model are collisional ionization, three-body recombination, radiative recombination, dielectronic recombination, collisional excitation, collisional deexcitation, and radiative decay[7]. The photoionization and photoexcitation which should be coupled with the radiation transport are neglected. The time-dependent CR model with 53 energy levels is solved at all the spatial mesh points. If the detail atomic data are obtained, it is seemed to be necessary to calculate more levels. When we discuss the gain of 3–2 transition, the radiation trapping of the resonance line becomes quit important, because the n=2 level population changes greatly. In such a case, a kind of the escape probability method should be introduced.

3. Simulation results

By using the 1-D simulation code, the gain characteristics of a recombination x-ray laser are computed. The intense laser of 10^{14}-W/cm^2, 100-ps pulse, 0.53-μm wave length irradiates an aluminum fiber of 10 μm radius. The gain profiles of heliumlike 3–2 transition are shown in fig.2. The gain appears at 150 ps from the end of the laser irradiation. The plasma is expanding and the recombination rate becomes large in this cooling phase. The peak of the gain shifts toward the outer radius in time because of the plasma expansion. The maximum gain coefficient is 4.6 cm^{-1}.

The time-resolved x-ray spectrum has been calculated with the simulation, and that of 200 ps is shown in fig.3. The opacity and the emissivity of bound-free and free-free transition are calculated for the continuum spectra, and the multi-group radiation

transport method is used with respect to the photon energy. The specified line spectra are treated individually, however the bound-bound opacity is neglected. The other line spectra are included in the multi-group of continuum spectra by taken average. The x-ray spectrum obtained by the simulation is similar with the experiment, however there is no detail comparison with the experimental data.

4. Hollow Microclynder Target

The simulation code is applied to the new target structure shown in fig.1 in order to predict the plasma characteristics. The radius of the aluminum cylinder is about 100 μm, and the azimuthal width of the slit is seemed to be less than 20 μm. It depends on the laser intensity. The laser through the axial slit is absorbed at the surface of the inner wall of the cylinder. The hot plasma is ablated toward the center. When the laser of 2×10^{13}-W/cm^2, 200-ps pulse is assumed to heat the plasma, the void is closed at 300 ps from the start of the laser irradiation. Inside the cylinder, the hot and dense plasma is confined for rather long time, and the plasma temperature has a uniform profile. The x-ray radiation emitted in the inside is also confined by the cool wall of the cylinder. The photoexcitation and photoionization keep the plasma higher excitation states effectively. At this time, the hot plasma blows off toward the outside through the slit due to the pressure difference between the inside and the outside. The blow-off plasma is cooled in the outer space. The population inversion is expected for a long duration, because there is a large amount of hot plasma in the cylinder and these play a role of a reserver of the higher charge state ions.

The simulations of two phases are carried out separately. First, the phenomena which occurs inside the cylinder are investigated. The electron temperature, the charge state and the density of the created plasma are obtained. Second, it is assumed that such a plasma blows off from the axial slit and the plasma characteristics at the slit keeps constant. The blow-off plasma is cooled by free expansion and the population inversion occurs due to the recombination processes. The gain history of heliumlike 3–2 transition is shown in fig.4. The gain duration time is longer than the case of the fiber target, because the source of the highly excited plasma is supplied from the cylinder interior. Using this type of the target, we have a possibility to increase the efficiency of the x-ray laser generation. In order to know the feasibility of this scheme, a two dimensional calculation is required and the two phases which were computed separately have to be combined to the continuous processes.

References

[1] C. Chenais-Provics, et al, *Phys. Rev. Lett.*, **59**, 2161 (1987).

[2] S. Carillon, et al, *J. Phys.*, **B 23**, 147 (1990).

[3] T. Yabe and T. Aoki, Comp. Phys. Comm., (to be published) (1991).

[4] T. Aoki and T. Yabe, *Research Report of National Institute of Fusion Science*, NIFS-82 (1991).

[5] J. E. Balmer, R. Weber, P. F. Cunningham, and P. Ladrach, *proceedings of 19th European Conference on Laser Interaction with Matter edited by G. Veralde, E. Minguez, and J. M. Perlado*, Madrid, Spain, 292 (1988).

[6] M. More, Lawrence Livermore National Laboratory Report No.UCRL-84991 (1981).

[7] M. Itoh, T. Yabe, and S. Kiyokawa, *Phys. Rev.* **A**, **35**, 233 (1987).

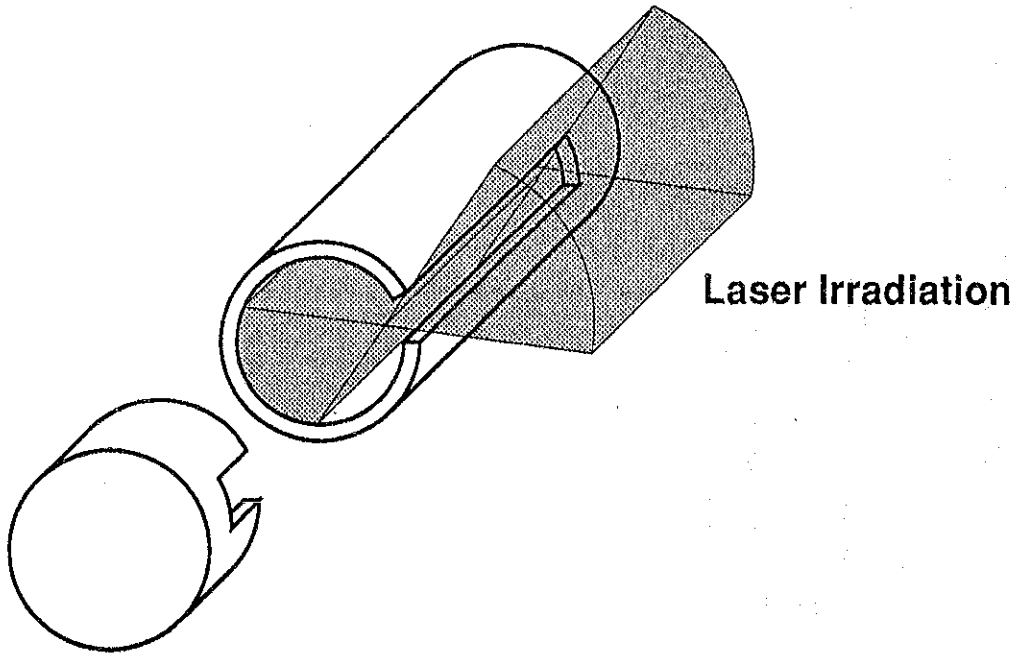

Fig.1 Schematic picture of hollow microcylinder target.

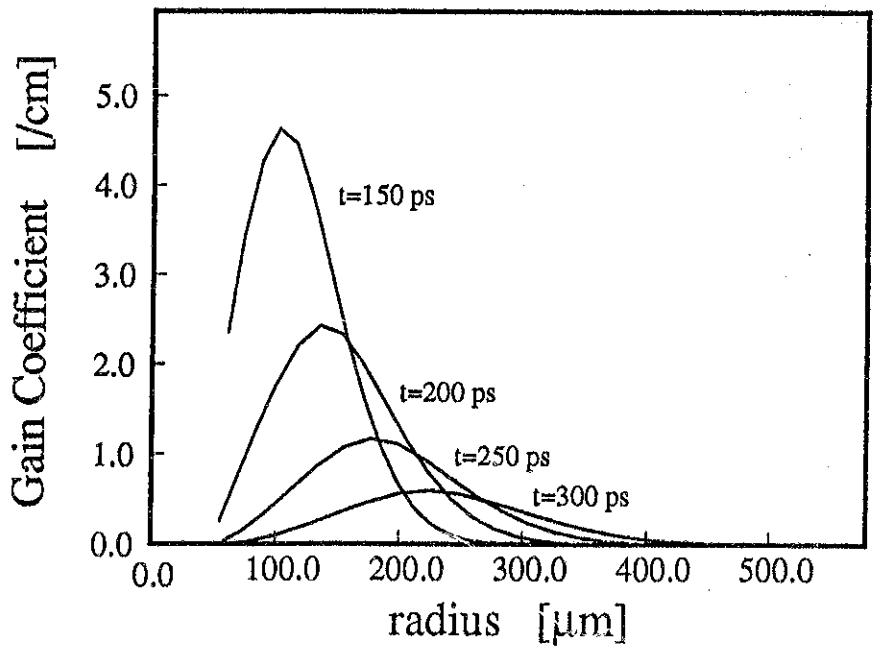

Fig.2 Gain profiles of heliumlike Al 3-2 transition.

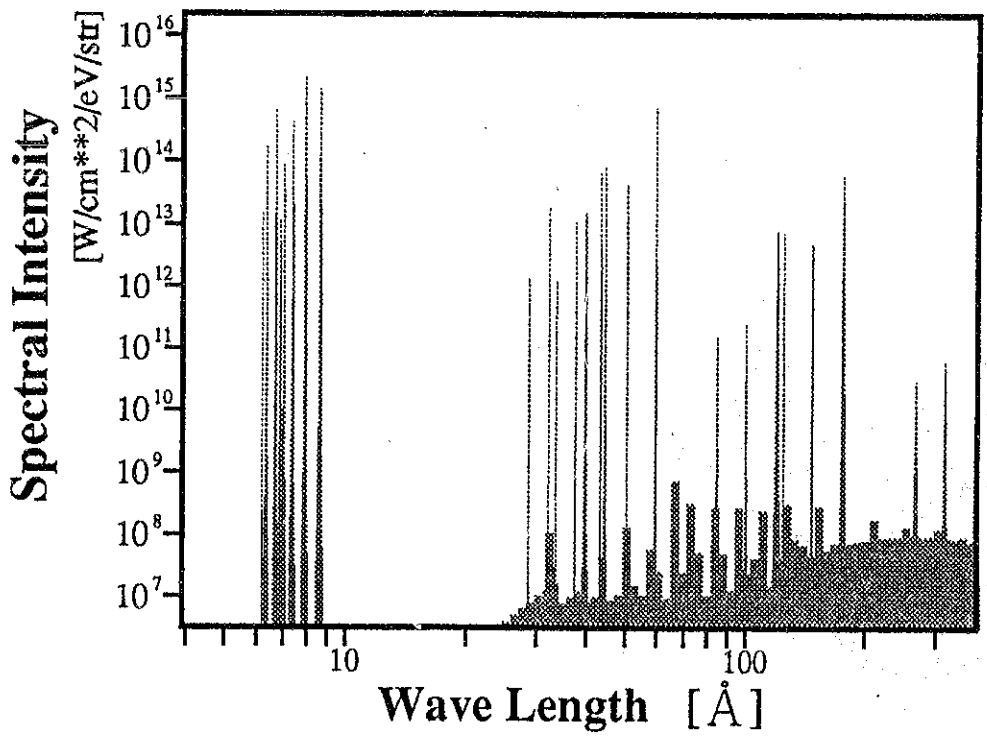

Fig.3 Time-resolved x-ray spectrum. After 200 ps from the end of laser irradiation.

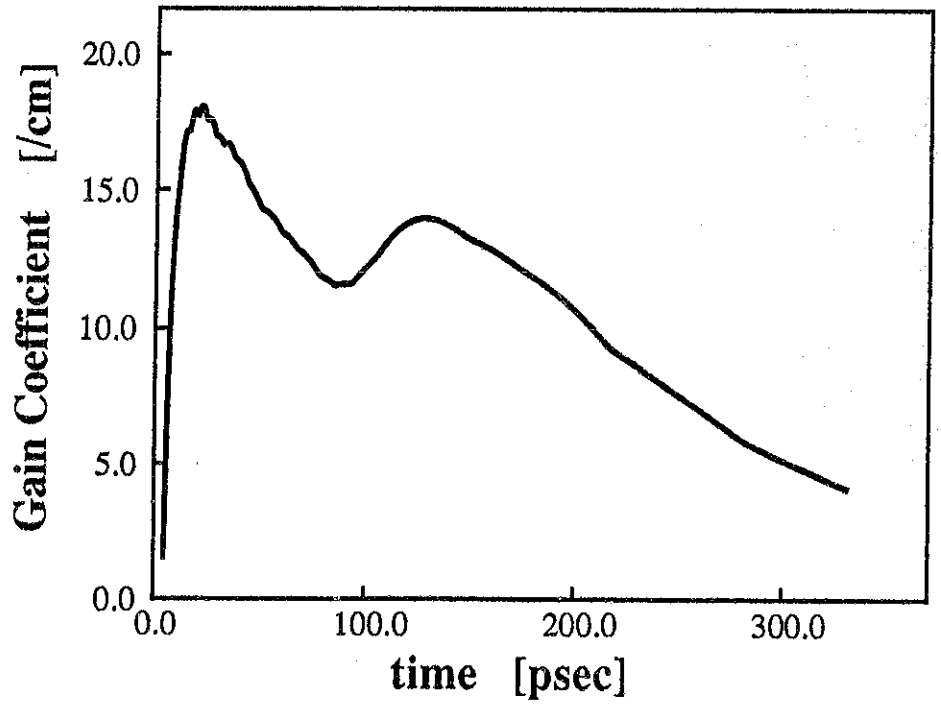

Fig.4 Gain history of heliumlike 3-2 transition. Hot plasma is blown off from the hollow microcylinder target.

X-ray Emission Spectra from Laser-Produced Plasmas

Guan-ming Zeng

Institute of Laser Engineering, 2-6 Yamada-oka, Suita, Osaka 565,Japan

ABSTRACT

X-ray emission in the spectral range of 2～13nm from 21 kinds of materials($_{6}$C～$_{50}$Sn) irradiated by a slab glass laser and a Nd:YAG laser was recorded by a grazing incidence spectrometer with a multichannel detector. The difference of the spectra produced by the two lasers is explained. The electron density and electron temperature of the carbon plasmas were derived from the x-ray spectra and the conditions for intense emission are discussed. The emission spectra from the materials strontium to molybdenum were found to show very similar structures. The spectra from the molybdenum plasmas were studied. The absolute spectral brightness of the line emission from carbon and molybdenum plasmas is estimated.

1. INTRODUCTION

Laser-produced plasmas have been recognized to be of great practical interest as intense sources of soft x-ray radiation(1,2). There are significant advantages of laser-plasma x ray source compared with other x-ray source such as synchrotron radiation machines, discharge machines, and so on(3).

In this paper, detailed spectral distributions of the x-ray emission from 21 kinds of materials($_{6}$C ～ $_{50}$Sn) are reported in the wavelength range of 2～13nm. A high repetitive(10Hz) Nd:YAG laser and a slab glass laser are utilized as the source's drivers. The properties of the line emission from carbon and molybdenum plasmas are studied

and the intensity of the line emission from carbon and molybdenum plasmas is absolutely calibrated by simultaneous measurement of the emission using a grazing-incidence spectrometer and a transmission grating spectrometer. A Hartree-Fock code is used to calculate the energy levels of molybdenum ions.

2. EXPERIMENTAL CONDITIONS

A Q-switched slab glass laser and a Q-switched Nd:YAG laser are used to generate the plasma x-rays. As for the slab glass laser, the spot size is 100 μm, giving an irradiance of 1.4×10^{12}W/cm^2(wavelength: 1.053μm, 4J/35ns). The YAG laser employed in this work is a Quantel International YG682 Nd:YAG laser which produces 8 ns FWHM pulses of 1.06 μm and 0.53 μm wavelength with energies up to 1.0 J and 0.5 J, respectively. The spot size is measured to be 75 μm.

A grazing incidence spectrometer with a multichannel detector has been constructed to record the plasma emission per laser shot. The x-ray spectra from a target material can be obtained in one minute by using the multichannel detector. Moreover, more than 10 kinds of target materials can be set on the rotating target holder once, so it is easy to get the x-ray spectra of many kinds of materials under the same condition.

3.EXPERIMENTAL RESULTS AND DISCUSSION

The x-ray spectra in the region of 2~ 13nm recorded by the multichannel detector from 21 kinds of materials irradiated by the slab glass laser are shown in Fig. 1. The spectral distributions obviously differ greatly for different materials. Therefore, suitable target material can be selected for a given application. For x-ray microscopy experiment, monochromatic emission in the water window spectral region(wavelength: 2.3nm~ 4.4nm) is suitable for biological observations. From Fig.1, it is apparent that

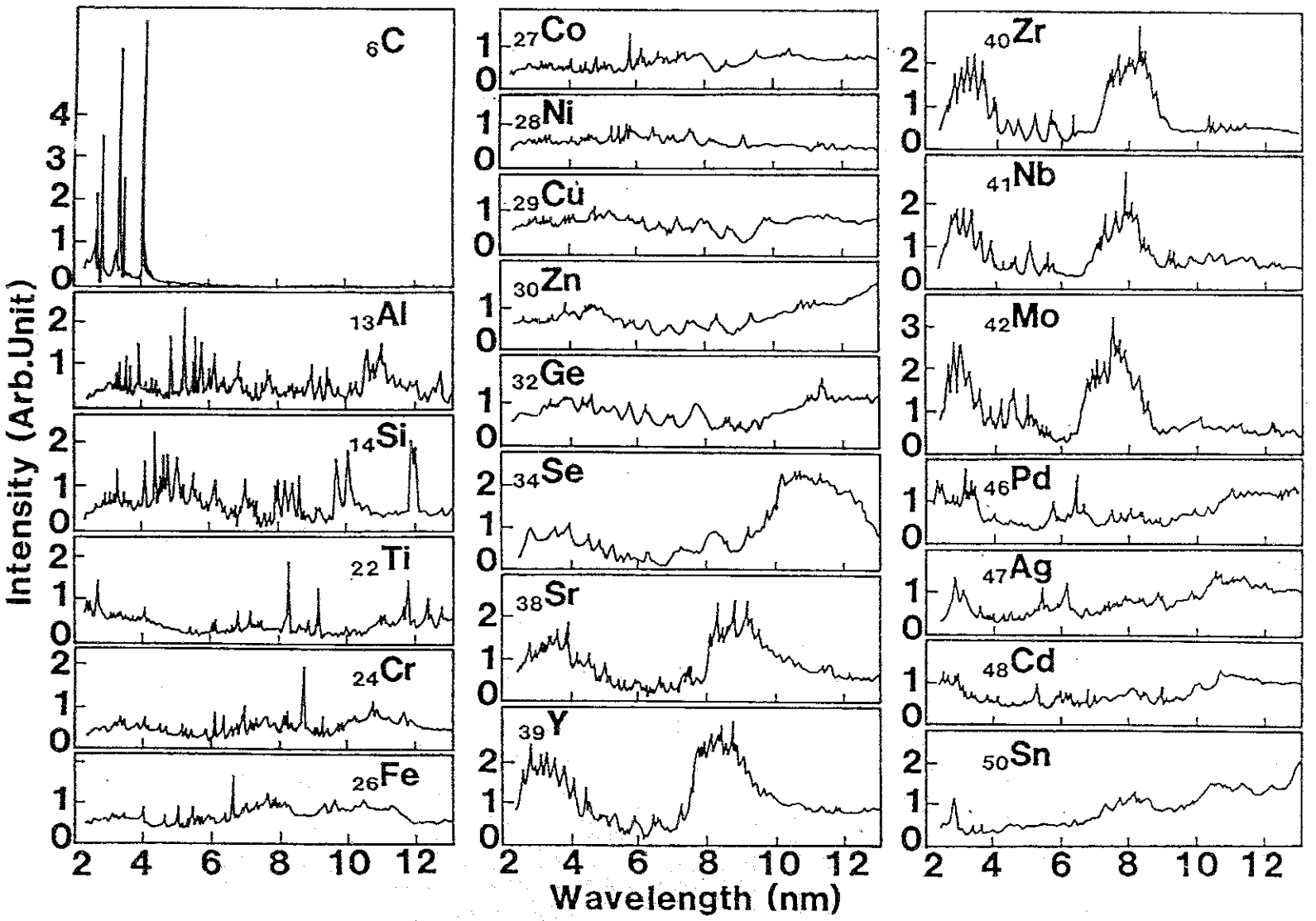

Fig.1 X-ray emission spectra from 21 kinds of materials irradiated by the slab glass laser with a intensity of 1.4×10^{12}W/cm^2. The spectra were recorded by a grazing incidence spectrometer with a multichannel detector. The intensity scales are the same for all spectra.

carbon is the optimum target material. For reduction lithography experiment, different target material may be used to obtain the required x-ray emission. For example, for a system using 12nm radiation, silicon and titanium are advisable. Aluminum and silicon are suitable for x-ray emission around 11nm and 10nm, respectively. To obtain intense x-ray emission in the spectral region from 6.5nm to 9.5nm, a material with atomic number from 38 to 42 may be used as the target material. For x-rays with wavelength below 6.5nm, target materials with atomic number lower than 14 are suitable.

The emission spectra from the 21 kinds of materials irradiated by the 1ω and 2ω YAG lasers were also recorded with the multichannel detector. For simplicity, only the spectra from the molybdenum plasmas are presented in Fig.2 to show the difference. Similar results for the other

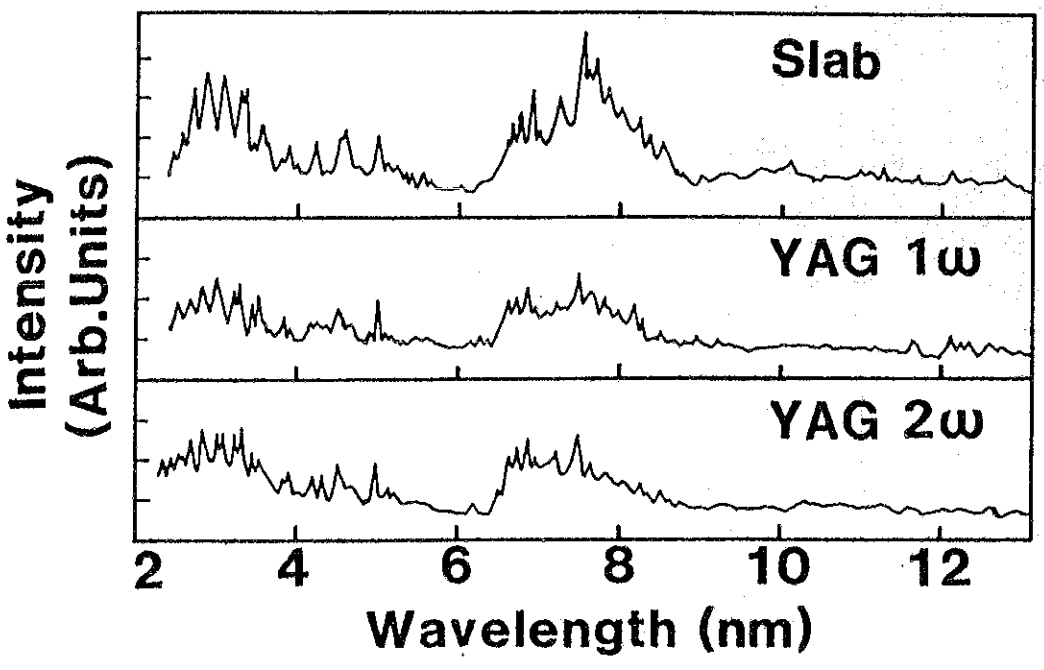

Fig.2 X-ray emission spectra from the molybdenum plasmas produced by the slab laser and the YAG laser of different wavelengths. The laser intensity was the same for all cases and was equal to $1.4\times 10^{12}W/cm^2$. The intensity scales are the same for all spectra.

materials were obtained. Due to the higher energy of the slab laser, the produced x-rays are stronger than that produced by the YAG laser(the measured x-ray signals are proportional to the photon numbers reaching the detector). However, the plasmas produced by the YAG laser emit more intense x-rays at shorter wavelength region relative to that at longer wavelength region due to the fact that the YAG laser has a much narrower pulse width, so the produced plasmas exhibit a shorter gradient length of the electron density and the laser energy can penetrate into the higher density region more easily to generate more highly stripped ions.

In order to get the absolute spectral brightness of each line emitted from the carbon plasmas, the x rays were recorded on Kodak 101-07 films with a transmission grating spectrometer and the grazing-incidence spectrometer simultaneously. The film was absolutely calibrated by using a proportional counter to count the L-shell x rays (930eV) from a copper target bombarded with an electron beam. As a result, the absolute monochromatic spectral brightness of the lines was found to be approximately one order of magnitude greater than that obtained with the transmission grating spectrometer. The peak source brightness of the CVI 1s-2p line was calculated to be about 1.0×10^{16} photons / sec / mm^2 / $mrad^2$ in 0.1% bandwidth, which is comparative to the peak brightness of the SSRL wiggler(SSRL: Stanford Synchrotron Radiation Laboratory)(4).

In a laser-generated carbon plasma, the lower the electron density, the weaker the intensity of Lyman α line will be because the radiative decay becomes weak due to the low population of the upper level. As the electron density increases at a constant electron temperature, according to the simulation results of Duston et al.(5), though the power coefficient (power density divided by electron density divided by ion density) of the line emission from a shell(K-shell or L-shell) decreases due to the increase in

electron collisional quenching of the photons as the density is increased, the power density(W/cm^3) increases because of the increase in emitting ions. On the other hand, at very high ion density, the continuum emission from the plasmas dominates over the line emission, leading to the merging of the series limit, but the total emission power density approaches to the black-body limit. At an electron temperature of 80 eV(which was obtained as the electron temperature of the carbon plasmas), the black-body radiation intensity of the CVI 1s-2p line was calculated to be 1.6×10^{17} photons/ sec/ mm^2/ $mrad^2$ in 0.1% bandwidth. This value is about one order of magnitude greater than that from the laser produced carbon plasmas obtained above. The electron density at which the collisional rate becomes ten times the radiative rate at a certain principal quantum number is called Griem boundary. Above this boundary, the electron distribution approaches a state of local thermodynamic equilibrium. As for the electron temperature, it should rise above a value at which the ions are almost all hydrogenlike or fully ionized. According to our calculation based on the steady state collisional radiative model, the optimum electron temperature is around 100eV. At this temperature, the Griem boundary for n=2 takes a value of about $10^{21}\sim 10^{22}cm^{-3}$.

It is well known that the emission due to free-bound transitions in a plasma can be used to measure electron temperatures. Two radiative recombination continua on the short-wavelength sides of the CVI and CV series limits are observed in the spectra of Fig.1. As a result, the average electron temperatures of the CVII and CVI plasma emission regions were found to be 43eV and 34eV, respectively. The intensity ratio of the H-like to He-like resonance line also gives the electron temperature, which may correspond to the peak temperature around the plasma region that emits intense H-like and He-like resonance lines. The temperature obtained by this method becomes 82eV on the basis of coronal

equilibrium.

The electron density are derived from the intensity ratios of satellite lines. Seely et al. calculated the ratio of the intensity of the $2p^2\,^3P$-$1s2p\,^3P$(3.459nm) satellite line to that of the $2s2p\,^3P$-$1s2s\,^3S$(3.453nm) satellite line as a function of electron density and temperature(6). The measured intensity ratio was 0.65~ 1.0(the range was determined by changing the slope of the background $1s^2$-1s3p line), leading to an electron density of $(0.52\sim 1.0)\times 10^{20}cm^{-3}$. The intensity ratio of the total "triplet" lines ($(1s2s\,^3S$-$2s2p\,^3P)$ + $(1s2p\,^3P$-$2p^2\,^3P)$) to a singlet-D line($2p^2\,^1D$-$1s2p\,^1P$) was ion density-sensitive and its density dependence was calculated by Duston et al.(7). The measured total triplet-to-singlet line intensity ratio was 1.7~ 2.4, leading to an ion density of $(0.35\sim 1.8)\times 10^{19}cm^{-3}$. The satellite lines come from the plasmas where He-like ions dominate, so the electron density was calculated to be $(0.14\sim 0.72)\times 10^{20}cm^{-3}$, which was very close to that obtained with Seely's method. So the electron density of the plasmas that emit intense x rays was on the order of $10^{19}\sim 10^{20}cm^{-3}$. This density is two order of magnitude lower than the Griem boundary.

In order to get a more intense CVI Lyman α line, a higher laser intensity is needed to highly ionize the atoms in higher ion density region. Actually, when the laser energy was increased from 3.0J to 5.5J at a constant laser pulse duration, the CVI Lyman α line became 1.6 times greater in intensity. The electron temperature was found to increase from 75 eV to 85 eV from the intensity ratios of the H-like to He-like resonance line, so more H-like and fully ionized ions were produced.

The elements strontium to molybdenum present the most interesting spectra. A Hartree-Fock approximation code is used to calculate the energy levels of the molybdenum ions. The line identifications of the spectra from molybdenum plasmas could be summarized as follows. The emission in the range

from 3.6nm to 5.0nm is due to 3d-4p transitions in the ionization stages MoX V to X I X . The 3d-4f transitions in MoX X to MoX X II contribute to the emission in the range from 2.3nm to 2.7nm. The spectra between 2.7nm and 3.6nm are a result of the overlapping of the two series of transitions. A number of lines satellite to 3d-4p transitions in the 5.0~ 5.5nm region could be classified in MoX IV and MoX III . The broad band of emission which starts above 6.5nm may be identified with $3p^6 3d^n - 3p^5 3d^{n+1}$ transitions in MoX VI and higher degree of ionization stages. Because of the l-degeneracy with increasing ionic charge, the transitions move to longer wavelengths as the degree of ionization increases. The strong line at 7.6nm was assigned to be $3p^6 3d^9 - 3p^5 3d^{10}$ transition in MoX VI . The same transition in NbX V corresponds to a wavelength of about 8nm, with a wavelength shift close to the calculated value according to Moseley's law. Even for this single line, it is possible to get strong line emission with a dynamic spectral range of 2nm by using the materials in this group. The peak source brightness of the line at 7.6nm was measured to be about 1.0×10^{16} photons / sec / mm^2 / $mrad^2$ in 0.1% bandwidth, which is also comparative to the peak brightness of the SSRL wiggler.

4. CONCLUSIONS

A plasma x-ray source produced by a slab glass laser and a Nd:YAG laser was developed. The x-ray spectra from 21 kinds of materials was recorded by a grazing incidence spectrometer with a multichannel detector. The properties of carbon and molybdenum plasmas were investigated and the absolute spectral brightness were estimated. Finally, a Hartree-Fock code was used to make line identifications of the molybdenum spectra.

REFERENCES

1. G. M. Zeng, M. Takahashi, H. Daido, T. Kanabe, H. Aritome, M. Nakatsuka, and S. Nakai, J. Appl. Phys. 67, 3597

(1990).
2. G. M. Zeng, H. Daido, T. Togawa, M. Nakatsuka, S. Nakai, and H. Aritome, J. Appl. Phys. 69, 7460 (1991).
3. N. M. Ceglio, J. X-ray Sci. Techno. 1, 7(1989).
4. D. Attwood, K. J. Kim, N. Wang, and N. Iskander, Journal de Physique Colloq. 6, C6-203 (1986).
5. D. Duston and J. Davis, Phys. Rev. A 23,2602(1981).
6. J. F. Seely, R. H. Dixon, and R. C. Elton, Phys. Rev. A 23, 1437(1981).
7. D. Duston, J. E. Rogerson, J. Davis, and B. Blaha, Phys. Rev. A 28, 2968(1983).

THERMAL STRUCTURE OF ASTROPHYSICAL PLASMAS

- Outline of Atomic and Radiation Processes -

Kuniaki MASAI
National Institute for Fusion Science
Nagoya 464-01, Japan

ABSTRACT

Thermal characteristics of the astrophysical plasmas are discussed in their various environments. The presence of early-type stars affects the interstellar medium through the UV radiation and the supersonic stellar wind therefrom. Also does the supernova explosion with the huge kinetic energy. The accretion matter on to a compact star (neutron star or black hole) is irradiated by X-rays from the star. In view of atomic processes, these effects on the thermal structure are classified into two regimes whether the plasma is ionizing or recombining as a result. The discussion here is also an introduction to the subsequent three articles about grey atmosphere and Comptonized X-ray spectrum of neutron star, Rydberg atom detected in radio wavelengths, and X-ray emission from supernova remnant.

1. Introduction

Atomic processes of emission in astrophysical plasmas are classified into two regimes by the ionization structure of the plasma. First of all, we define the ionization temperature T_z, which characterizes the ionization degree, as follows. When the ion abundances (fraction) of an element at a given electron temperature T_e are approximated by those of collisional ionization equilibrium at an electron temperature T_e^*, then we set $T_z = T_e^*$. According to this definition, $T_z < T_e$, $T_z = T_e$ and $T_z > T_e$ are attained for plasmas of ionizing condition, ionization equilibrium and recombining condition, respectively, from the point of view of collisional atomic processes.

When the ionization structure of a plasma is close to that of collisional ionization equilibrium, collisional excitation and dielectronic recombination are the dominant processes for line emission, which follows excitation from lower atomic levels of larger population. When plasma is ionizing, excitation (including innershell excitation) and innershell ionization are of practical importance for line emission. Also for these processes larger population of lower levels is responsible. In contrast to the above situation, in a recombining plasma, population of upper levels is important for line emission via radiative recombination and cascade. Hence, we have two characteristic regimes of the population responsible for line emission.

Now, we consider a plasma irradiated by ultraviolet (UV) and/or soft X-rays, which can influence the ionization structure. The presence of ionizing photons results in $T_z > T_e$ in the ionization-recombination balance of the plasma. In other words, the plasma looks recombining in a sense described above when the contribution of photoionization can not be ignored. One can find this situation in the vicinity of early-type stars emitting UV photons and of compact objects such as neutron stars and black holes emitting X-rays, in supernova explosions with UV flash, and so forth. In these cases, the energy from radiation is distributed into the ionization state of internal freedom, which does not immediately come to the thermal energy of the plasma. The energy stored into the internal freedom is larger than the electron kinetic energy of thermal pool.

On the other hand, ionizing condition can be found in the remnants of supernova, where the thermal energy dominates over the energy contained in the ionization states. Because the density in the ambient medium is very low, for instance, lower than 1 cm^{-3} in the inter-stellar/cloud medium, it takes considerable time for collisional ionization compared to shock wave heating. Thus, the plasma is underionization with much energy stored in the thermal pool. The similar situation is found naturally in the case that the heating time scale is much shorter than the ionization time scale. One can see an example in the early phase of solar flares, which are the phenomena of much shorter time scale than the supernova remnants though the density is much higher to be $10^{10}\,cm^{-3}$.

2. Effect of irradiation

We consider a plasma in the vicinity of strong radiation source, an early-type star or a neutron star. For simplicity we assume a spherically symmetric distribution of matter about the central star. The ambient matter corresponds to the interstellar matter in the case of early-type stars and to the accretion matter in neutron stars. The radiation from these sources is represented by e-folding spectrum with characteristic radiation temperature T_r. So we consider the radiation spectrum in a form

$$dL/dE\ dE \propto E^{-\gamma} \exp(-E/T_r)\ E\ dE, \qquad (1)$$

where L is the luminosity, total radiation energy emitted per unit time, and γ is the parameter to represent the spectral steepness of photons with energy $E \ll T_r$. In the following discussion T_r is of interest, so that we here set $\gamma = 1$ to simplify the mathematical treatment. We approximate the photoionization cross section as $\sigma_z(E) = \sigma_{z0}(E/E_z)^{-3}$, where σ_{z0} is the cross section at the ionization potential E_z of the ion specified by z. Then the photoionization rate per unit time is expressed as $\beta_z = (L/4\pi R^2 T_r)\sigma_{z0} I_{4z}(E_z) \equiv F\sigma_{z0} I_{4z}(E_z)$ with the i-th exponential integral $I_i(x)$.

Recombination rate and collisional ionization rate per unit time are expressed as $n_e\alpha_{z+1}$ and $n_e S_z$ with the coefficients α_{z+1} and S_z, respectively. From the ionization-recombination balance we can determine a radius of the ionized sphere of a given ion z as,

$$R_0(z+1) = (L\sigma_{z0} I_{4z}/4\pi n_e \alpha_{z+1} T_r)^{1/2}(1+S_z/\alpha_{z+1})^{1/2}. \qquad (2)$$

In practice, S_z is negligibly small compared to α_{z+1} for the plasmas concerned here. In the above discussion, we ignore the attenuation or the reprocess of the primary photons emitted from the central source. In the astrophysical plasmas, photo-absorption by abundant hydrogen and helium with $n_{He}/n_H \sim 0.1$ are the dominant opacity source. The relative abundances of heavier elements to hydrogen are on the order of 10^{-4} or less. Therefore, this sphere is attained for less abundant species highly ionized, e.g., He-like iron inside the fully ionized He region.

Now we consider the case that the optical thickness for the primary photons is much larger than unity. Then, for the ionization-recombination balance coupled with the radiative transfer, we have

$$F \int d\tau_z/dr \exp(-\tau_z) \exp(-E/T_r)\, dE/E + \int 4\pi j\, dE/E = n_{z+1} n_e \alpha_{z+1}, \qquad (3)$$

where $\tau_z(E) = \int n_z \sigma_z(E)\, dR$ is the optical thickness, and j is the emissivity. For an optically thick limit with $\tau_z(E_z)(E_z/T_r)^3 \gg 1$ or $E_z/T_r > 1$, eq. (5) gives a radius,

$$R_{UV}(z+1) = (3LI_{1z}/4\pi n_{z+1} n_e \alpha'_{z+1} T_r)^{1/3}, \qquad (4)$$

where α'_{z+1} is the rate coefficient of recombination into $n > 1$ levels, and $\alpha_{z+1} - \alpha'_{z+1}$ accounts for j. Eq. (4) corresponds to the Stromgren sphere well known by HII region, which is formed around early type stars emitting UV

with T_r of a few eV. On the other hand, for another optically thick limit with $1 \ll \tau_z(E_z) < (E_z/T_r)^{-3}$ or $E_z/T_r \ll 1$, an approximate solution is obtained as

$$R_X(z+1) = (\sigma_{z0}/\delta n_{z+1})^{1/5}(LI4_z/4\pi n_e \alpha_{z+1} T_r)^{2/5}, \qquad (5)$$

where δ is a parameter related to the thickness of the ionization front, which depends on L as well as T_r, and is close to unity. This is the case for the accretion plasma on a compact star with T_r of a few keV. Hence, $R_0(z+1)$ is realized only when it is smaller than the HII region R_{UV}(HII) around early type stars or the He III region R_X(He III) around compact X-ray stars. The electron temperature of the photoionized sphere is determined substantially by the balance of heating due to photoabsorption and cooling due to L-shell excitation. In the region so close to X-ray stars as iron/nickle is fully ionized, the thermal balance is dominated by Compton scattering, heating and cooling, with a little contribution of free-free emission to cooling.

The three radii obtained are important to bound the two regimes described in Section 1. Inside the HII region, recombining condition should be taken into account for the atomic processes. Then the upper atomic levels are subject to population, and the transition between extremely high levels (n>100) may be observed in radio wavelengths. Current topics of such Rydberg atoms are presented by Sakimoto. The ions for which $R_0(z+1)$ would be nearly equal to or larger than R_{UV}(HII) for early-type stars or R_X(He III) for compact stars are subject to radiative transfer. Then the simple collisional-radiative model fails. Finally, one should keep it in his mind that the structure discussed above is not applied to the central star itself, the photosphere and the atmosphere, but to the ambient matter. In the atmospheres of the stars as considered here, hydrogen is fully or almost fully ionized and the opacity is dominated by the scattering of free electrons. This subject is discussed by Hanawa in relation to the grey atmosphere of a neutron star and to the Compton hardening of X-ray photons by energetic electrons.

3. Effect of dynamics

In the interstellar medium away from UV/X-ray radiation sources, ionization is dominated by electron impact. The thermal energy of electrons sometimes comes from the mechanical energy of shock waves driven by

supernova explosion, by supersonic wind of early type stars, and so on. The kinetic energy of a supernova is as huge as 10^{50}-10^{51} erg, though it is less than ten percent of the total energy released in the explosion. In the supersonic wind of early-type stars, the kinetic energy of 10^{35}-10^{36} erg is emitted per second, and the energy integrated over the life ~ 10^6 yr is about 10^{49} erg, which is one tenth the kinetic energy of Type I supernova. In ordinary interstellar media, the Alfven velocity is only 10^6 cm s^{-1} on account of the week magnetic field of 10^{-6} G while the velocity of supernova explosion reaches 0.1c and the early-type stellar wind 10^8 cm s^{-1}. As well the thermal pressure is much higher than the magnetic pressure. Therefore, the magnetic field plays little role in the above dynamics in contrast to the solar and space plasmas.

We consider a simple example of the interaction of the stellar wind with the ambient medium under a spherically symmetric configuration. The interaction causes two shock waves at the contact surface, one propagates forward (outward) into the ambient medium and the other inward into the stellar wind. The forward shock forms a dense shell into the ambient medium. This interaction can be described by the following couple of equations.

$$d/dt(2\pi R_c{}^3 p) = (1/2)\Delta M_w V_w{}^2 - 4\pi R_c{}^2 dR_c/dt, \quad (6a)$$

$$d/dt(M_s dR_c/dt) = 4\pi R_c{}^2 p, \quad (6b)$$

$$M_s = (4/3)\pi\rho_0 R_c{}^3, \quad (6c)$$

where R_c is the radius of the contact surface, p the pressure to drive, ΔM_w and V_w the mass loss rate and the velocity, respectively, of the wind, M_s the mass of the dense shell and ρ_0 is the preshock density in mass of the ambient matter. From these equations, we obtain the radius of the contact surface i.e. the location to which the stellar wind is extended, as

$$R_c(t) = 9\times10^{19}\ (L_w/10^{36})^{1/5}\ (t/10^6 yr)^{3/5}\ n_0{}^{-1/5}\ \ cm, \quad (7)$$

where $L_w = (1/2)\Delta M_w V_w{}^2$ is the kinetic energy emitted per unit time in the stellar wind, and n_0 is the density in number. This radius is compared to the Stromgren sphere given by eq. (4)

$$R_{UV}(HII) = 3\times10^{20}\ (L_p/10^{49})^{1/3}\ n_0{}^{-2/3}\ \ cm, \quad (4')$$

where L_p is the luminosity in units of ionizing photons per second. The photoionized ambient matter is swept by the stellar wind, and the inward-shock forms a hot bobble in the HII region. This bobble expands with time to be comparable to the Stromgren sphere at the end of the blue supergiant stage.

In the HII region formed by the stellar radiation, $T_e \sim 1$ eV $< T_z$ on account of photoionization. However, the interaction with the stellar wind can raise the electron temperature rapidly by the shock wave to be $T_e > T_z$. Taking into account the electron thermal conduction with eqs. (6), we estimate the electron temperature and the density of the bobble as

$$T_e = 1\times10^2 \, (L_w/10^{36})^{8/35} \, (t/10^6\mathrm{yr})^{-6/35} \, n_0^{2/35} \quad \mathrm{eV}, \qquad (8a)$$

$$n_e = 2\times10^{-2} \, (L_w/10^{36})^{6/35} \, (t/10^6\mathrm{yr})^{-22/35} \, n_0^{19/35} \quad \mathrm{cm^{-3}}. \qquad (8b)$$

In comparison with those of the preshock H II region, the temperature increases and the density decreases by about two orders of magnitude. Hence, in the vicinity of early-type stars, the kinetic energy of the wind as well as the radiation energy influences the atomic processes. The plasma is ionizing and/or recombining depending on $R_c(t)$ and $R_{UV}(\mathrm{HII})$.

In the case of supernovae, UV photons are strongly emitted just at the moment of explosion. This UV flash is too short to affect the ambient matter considerably. Through the evolution of the supernova remnants or the interaction with the ambient medium, the kinetic energy of explosion plays a dominant role via shock waves. By the reverse (inward) shock and the forward shock, the supernova ejecta and the ambient matter, respectively, are heated up enough to emit thermal X-rays. The dynamics for the ejecta expanding into the ambient medium is similar to the case for the stellar wind. The supernova ejecta expand almost freely in the early phase till the mass of the ambient matter swept-up thereby increases to be comparable to the initial ejecta mass. In the ambient medium of density of 1 $\mathrm{cm^{-3}}$, this free expansion phase lasts for several hundred years after explosion. In this phase, the envelope of the ejecta is responsible for the interaction with the ambient matter, and dominates the resultant thermal emission from the supernova remnant. A self-similar analysis for the density distribution $\rho \propto r^{-n}$ of the ejecta envelope and $\rho \propto r^{-m}$ of the ambient matter gives the radius of the contact surface, and the density ratio and the temperature ratio of the two shocks as

$$R_c = [(3-m)(4-m)u_0/(n-3)(n-4)\rho_0]^{1/(n-m)}\ t^{(n-3)/(n-m)}, \quad (9a)$$

$$\rho_r/\rho_f = [(n-3)(n-4)/(3-m)(4-m)], \quad (9b)$$

$$T_r/T_f = (3-m)^2/(n-3)^2, \quad (9c)$$

where u_0 is the initial expansion velocity, and the quantities of the reverse shock and those of the forward shock are designated by r and f, respectively.

From eqs. (9b) and (9c), we could estimate the luminosity ratio of the two shocks, as $L_r/L_f = (n-4)^2/(4-m)^2$ if ionization equilibrium as well as the equipartition between electrons and ions were established. However, the ions (protons) are much efficiently heated at the shock front unless the magnetic field is significant, and the equipartition requires $10^{13}\ n_e^{-1}$ s for the shock velocity $V_s = 3\times10^8$ cm s^{-1} at around the end of the expansion phase. At time much shorter than the equipartition time, the electron temperature at the post shock region is approximately expressed by a function of time as

$$T_e = 2\ \mu^{2/5}\ n_e^{2/5}\ (V_s/3\times10^8)^{4/5}\ (t/500yr)^{2/5}\ \ keV, \quad (10)$$

where μ is the mean molecular weight. In $10^{10}\ n_e^{-1}$ s, the electron temperature is raised up to a few keV at which free-free emission would dominate if ionization equilibrium were the case. In practice, the atomic processes of emission are ruled by the longer time scale of the order of $10^{12}\ n_e^{-1}$ s for collisional ionization equilibrium. Then, bound-bound emission still enhances due to (innershell) excitation and innershell ionization by electron impact reflecting $T_z < T_e$, ionizing condition.

The solutions above are valid for $n > 5$ and $m < 3$ in the free expansion phase. In general, n = 7-12 from Type I to Type II supernovae corresponding to the polytropic stellar structure, and m=0 and m=2 are attained for Type I and Type II , respectively. The latter occurs in the rich stellar wind matter emitted by its progenitor, red supergiant. Supernova 1987A is classified into Type II because the observed H lines mean the presence of hydrogen-rich envelope of the progenitor. However, various observations, e.g., the time difference of the optical detection from the neutrino one, suggest that the progenitor is not a red supergiant but a blue supergiant at the moment of explosion. In this sense, SN 1987A is unusual Type II and is thought as follows; the progenitor evolved to be a blue supergiant after it had once been a red supergiant. Because of the interaction of the blue supergiant wind with the earlier red supergiant one, the circumstellar structure of SN 1987A

is unlikely expressed by the simple distribution of m = 2. Actually, a ring-like structure is found about SN 1987A by Hubble Space Telescope. The expanding ejecta will collide with the ring matter and emit thermal X-rays in about one decade. This interaction is discussed by Suzuki with numerical calculations based on the SPH method.

After the free expansion phase, the core of the supernova ejecta is responsible for the interaction. Then the ambient mass shocked or swept-up is larger than the ejecta mass, and dominates thermal emission from the supernova remnant. The dynamics in this phase is well described by Sedov solutions well known, so that the phase is called Sedov phase. The phase lasts for about 10 thousand years till the radiation cooling dominates over the initial kinetic energy of explosion. In other words, during the Sedov phase and the earlier free expansion phase, the supernova remnants are well approximated by the adiabatic evolution. Nonequilibria in the shock-heated matter described before are still important issues also in the Sedov phase. The shock velocity decreases with expanding the remnant, and in the radiative cooling phase thermal emission no longer dominates in X-ray wavelengths. Consequently, the X-rays observed from supernova remnants are always under the influence of nonequilibria.

4. Remarks

Physics required for the astrophysical plasmas is different from that for solar and space plasmas and for laboratory plasmas of magnetic confinement. In astrophysical situation, the internal freedom of particle is sometimes of practical importance for the thermal structure of the plasma. For instance, in photoionized plasmas, most of the radiation energy absorbed by the plasma is stored in this freedom, and does not immediately come to the thermal energy of the plasma or the kinetic energy of particles. As a result, we can see an example that He-like iron is most abundant at only 100 eV in X-ray irradiated accretion plasma on to a neutron star. The two regimes, ionizing and recombining, discussed here are determined just by the energy stored into the internal freedom.

Radiative Processes in Accreting Neutron Stars

Tomoyuki HANAWA

Department of Astrophysics, School of Science, Nagoya University

Chikusa-ku, Nagoya 464-01, JAPAN

ABSTRACT

The physical condition of a neutron star atmosphere is similar to that of a laser fusion plasma. We review the radiative transfer in a neutron star atmosphere with focusing on two topics, gray emission and Comptonization by bulk motion of plasma. It is shown that electron scattering plays important roles in the radiation transfer.

1. Introduction

First we review nuetron stars for those who are not familiar with astrophysics. Neutron star mass and radius are typically 1.4 $M_\odot$ and 10 km, respectively. Thus far a variety of neutron stars have been found and observed. Some have a companion star and accretes gas from the companion. They are named accreting neutron stars and their energy source is the gravitational energy release of accreting gas. Some accreting neutron stars have strong magnetic field ($B \sim 10^{12}$ G) and their X-ray luiminosity show pulsation (X-ray pulsars). Some other neutron stars have weaker magnetic fields and show X-ray bursts during which the X-ray luminosity increases suddenly (X-ray bursters). Radio pulsars are magnetized spinning neutron stars and some of them have a companion star. Gamma-ray burst sources are supposed to be isolated magnetized neutron stars.

In the following we are concentrated in the case when the magnetic field is weak ($B \ll 10^{10}$ G) and the cylotron emission is unimportant. Then the most frequent radiative process is the electron scattering in a neutron star atmosphere, where the temperature is typcially 10^7 K and the density ranges from 10 g cm^{-3} to 10^{-6} g cm^{-3}. Because of the strong gravity, the atmosphere is strongly stratified

and the density changes steeply in the radial direction. The gas consists mostly of hydrogen (72 % in mass) and helium (25 % in mass) and is almost fully ionized. The most abundant partially ionized element is iron (Fe). The abundance of Fe is about 0.01 % in mass. Then the electron scattering plays important roles in an neutron star atmosphere.

In this paper we discuss two topics in the radiative processes in a neutron star atmosphere. Gray emission from an X-ray burster is discussed in section 2. Hard X-ray production in an accreting neutron star is discussed in section 3.

2. Gray Emission

Some neutron stars named X-ray bursters, repeat sudden rise and gradual decay in their X-ray luminosity. The X-ray spectrum of the burst resembles a blackbody one with a decreaing temperature. Astrophyisists derived the blackbody temperature from the spectral fitting and estimated the size of the X-ray burster from the equation,

$$L = 4\pi R^2 \sigma {T_b}^4 = 4\pi d^2 f_x , \tag{1}$$

where L, R, σ, T_b, d, and f_x denote the luminosity, the radius of the neutron star, the Boltzmann costant, the blackbody temperature, the distance to the source, and the observed X-ray flux, respectively. Under the assumption of $d = 10$ kpc, R was estimated to be about 10 km (see, e.g., van Paradijs 1978). The result was first thought to be an evidence for the X-ray bursters to be a neutron star. It was pointed out later that the luminosity exceeds the Eddington limit if $d > 6$ kpc. When the luminosity is higher than the Eddington limit, the radiation pressure overcomes the gravity and the atmosphere expands appreciably ($R \gg 10$ km). On the other hand, the X-ray burster is much smaller than a standard neutron star model if the distance is shorter than $d < 6$ km. Based on this argument some astrophysists doubted whether the X-ray burster is really a neutron star.

The above problem has been resolved as follows. As shown in introduction, the electron scattering dominates in a neutron star atmosphere. It does not change

the energy of a photon except for the Compton effect and photons are not thermalized in the upper atmosphere of the optical depth $\tau \sim 1$. Emitted photons are produced mostly in the lower atmosphere of $\tau \sim \sqrt{\kappa_e/\kappa_{abs}}$, where κ_e and κ_{abs} denote the electron scattering opacity and the absorption opacity, respectively. The color temperature of the emitted X-ray spectrum is close to the temperature thereof. The X-ray flux is, however, lower than that of the blackbody radiation of the color temperature, $f_x < \sigma T^4$, since electron scattering slows down photon diffusion. According to recent numerical computations (London, Taam, and Howard 1986; Ebisuzaki 1987; Madej 1991), the ratio of f_x to σT^4 is typically 4. The X-ray burst spectrum is not a blackbody one but that of gray emission.

3. Comptonization

Some accreting neutron stars have a power law (non-thermal) component in the hard X-ray spectrum of $E > 10$ keV when the rate of gas accretion is low (see, e.g., Mitsuda et al 1989; Kawai et al. 1990). In such a situation, the neutron stars are covered with a gas stream which is partially transparent ($\tau \sim 1$). The density of the gas stream is still lower than that of the neutron star atmosphere. Then the absorption opacity is much lower than the electron scattering opacity and the Compton effect is the most efficient process to change the energy of a photon.

The electron scattering transfer energy and mometum from electron to photon. Some X-ray photons are scattered repeatedly and become hard X-rays. Thus, the electron scattering "accelerate" photon statistically. Electron in the gas stream has thermal energy and kinetic energy of bulk motion. The former is often assumed to be the main energy source in the literatures. This assumption, however may not be valid. First there is no independebt evidence for the existence of a high temperature electron cloud. Second the electron temperature cools down in a short timescale unless unknown heating mechanism works. Since the accreting gas has a velocity of a half light speed, the bulk motion is likely to be the main energy source. According to the Monte-Carlo simulations (Hanawa 1991a. b), high energy X-rays are produced

efficiently when the gas stream has a semi-realtivistic velocity ($v \sim 0.5c$) and is semi-transparent ($\tau \sim 1$).

REFRENCES

Ebisuzaki, T. 1987, *Pub. Astr. Soc. Japan*, **39**, 287.

Ebisuzaki, T., Hanawa, T., and Sugimoto, D. 1984, *Pub. Astr. Soc. Japan*, **36**, 551.

Hanawa, T. 1991a, *Ap. J.*, **366**, 495.

Hanawa, T. 1991b, *Ap. J.*, **373**, 222.

Kawai, N. et al. 1990, *Publ. Astr. Soc. Japan*, **42**, 115.

Lonodn, R. A., Taam. R. E., and Howard, W. M. 1986, *Ap. J.*, **306**, 170.

Madej, J. 1991, *Ap. J.* (in press).

Mitsuda, K. et al. 1989, *Publ. Astr. Soc. Japan*, **41**, 97.

van Paradijs, J. 1978, *Nature*, **274**, 650.

Note that the above reference list is not a complte list of the papers in this field.

Interstellar Recombination Lines of Carbon — Giant atoms with a diameter of 0.1 mm ! —

K. Sakimoto
Institute of Space and Astronautical Science
Yoshinodai, Sagamihara 229

Abstract. This report briefly sumarises the present status of the study of interstellar radio recombination lines at lower frequencies. Noticeable findings have been made recently in the observation of carbon recombination lines. Rydberg atoms of carbon with an extremely large principal quantum number ($n \sim 700$) were found to exist in interstellar spaces.

We consider a Rydberg atom. The mean diameter is roughly given by $1.5 \times 10^{-8} n^2$ cm, where n is the principal quantum number. Since n takes values up to infinity theoretically, we can have a Rydberg atom with arbitrally large size. However, a Rydberg atom with an extraordinary large diameter would be easily destroyed even if there exists only small perturbation from the surrounding area. Hence, the surrounding must be quiet enough to make a very large Rydberg atom alive. On the other hand, there must be a sufficient energy source to keep an atom in a high Rydberg state. In which space are the both conditions satisfied at the same time? What is the size record of a Rydberg atom that has been observed so far?

In astronomy, atoms in Rydgerg states have been detected in measurements of radio recombination lines. The first observation of a Rydberg atom in an extremely highly excited state (n=631) was made by measuring the recombination lines of carbon in the direction of the strong radio source Cassiopeia A (Cas A) (Konovalenko and Sodin 1980, Blake et al 1980). Later, Konovalenko (1984) also found that a carbon atom with $n = 732$ is present in the same direction. This is the record of the largest n that have been ever observed. The diameter of this Rydberg atom is roughly 0.1 mm. Toward Cas A, many other recombination lines of carbon with large principal quantum numbers have been now detected over a wide range of frequencies (Payne et al 1989).

The interstellar radio recombination line is rather well known for hydrogen because hydrogen is the most abundant element. However, the hydrogen atom with n larger than 300 has not been detected so far. Furthermore, although all the observed recombination lines of hydrogen are in emmision, those of carbon with n larger than 360 are in absorption (Payne et al 1989). Therefore, there must be a clear difference between the formation mechanisms of the hydrogen and the carbon Rydberg atoms.

Recombination lines of hydrogen is emitted from an HII region. In an HII region, the temperature is usually higher than 1000 K and the density is larger than 100 cm^{-3}. Therefore, the line emission and absorption from high Rydberg states suffers significant collisional broadening. For this reason, the recombination lines of hydrogen with n larger than 300 would not be detected (Shaver et al 1976).

Toward Cassiopeia A, no recombination lines of hydrogen are detected. This means that the cloud is not an HII region. Furthermore, from the hydrogen 21cm observation, the (spin) temperature should be less than 100 K and the density of neutral hydrogen should be below 500 cm^{-3}. Therefore, it is expected that the Rydberg carbon atoms with very large principal quantum numbers exist in a gentle CII region. From the observed broadening of carbon recombination lines, the temperature and density of the electron

must be 10∼100 K and 0.5∼0.05 cm^{-3}, respectively. This is consistent with the above consideration.

The intensity of hydrogen recombination lines is somewhat well explained by a simple collisional radiative model (Osterbrock 1974, Shaver 1975, Salem and Brocklehurst 1979). In this model, the population distribution of a hydrogen atom in degenerate states within the same n is assumed to be statistical. However, Watson et al (1980) and Wamsley and Watson (1982) pointed out that the hydrogenic model cannot explain the absorption-emission feature of the carbon recombination lines when the temperature and density of the electron are taken to be 50-100 K and 0.01-0.1 cm^{-3}, respectively.

Watson et al further introduced an interesting model for the carbon recombination lines. They considered a process similar to dielectronic recombination. The ground state of singly ionised carbon has a fine structure splitting ($^2P_{\frac{1}{2}}$ and $^2P_{\frac{3}{2}}$) of 92 K. When the electron temperature is about 100 K, the following resonance scattering occurs efficiently.

$$e + C^+(^2P_{\frac{1}{2}}) \rightleftharpoons C^{**}(^2P_{\frac{3}{2}}, nl)$$

However, since the radiative stabilisation ($^2P_{\frac{3}{2}} \rightarrow ^2P_{\frac{1}{2}}$) is slow ($\sim 2 \times 10^{-6} s^{-1}$), dielectronic recombination is not efficient. Watson et al considered lifetime lengthening of the resonance state induced by collisions with free electrons. The resonance process occurs at small angular momentum l. If the rapid l-changing collision makes it effective that the resonance state comes to have a large angular momentum, the autoionising decay becomes slow and thus that results in temporary stability. Wamlsey and Watson (1982) made a calculation including this effect and could explain observed the absorption-emission feature qualitatively (Payne et al 1989).

However, later Ershov et al (1987) pointed out that it is not necessary to introduce the dielectronic-like process to explain the carbon recombination lines. They extended the calculation of the hydrogenic model to very low temperatures ($\sim$ 15 K) and somewhat higher densities ($\sim$ 0.5 cm^{-3}). The hydrogen model also gave a qualitative agreement with the observation (Payne et al 1989).

Which model is more realistic? The key point is to know the actual electron temperature in the gas producing carbon recombination lines. If the temperature is higher than 50 K, the dielectronic-like process is important. If the temperature is less than 20 K, the resonance process does not occur. However, it is not easy now to determine the actual electron temperature. Further observations and detailed calculations are needed.

References

Blake D H, Crutcher R M, and Watson W D, 1980 *Nature* **287** 707.

Ershov A A, Lekth E E, Smirnov G T, and Sorochenko R L, 1987 *Soviet Astr. Letters* **13** 8.

Konovalenko A A, 1984 *Soviet Astr. Letters* **10** 353.

Konovalenko A A and Sodin L G, 1980 *Nature* **283** 360.

Osterbrock D E, 1974 *Astrophysics of Gaseous Nebulae* Freeman and Company

Payne H E, Anantharamaiah K R, Erickson W C, 1989 *Ap. J.* **341** 890.

Salem M and Brocklehurst M, 1979 *Ap. J. Suppl.* **39** 633.

Shaver P A, *Pramana* **5** 1

Shaver P A, Pedlar A, Davis R D, 1976 *Mon. Not. R. Astr. Soc.* **177** 45

Walmsley C M and Watson W D, 1982 *Ap. J.* **260** 317.

Watson W D, Western L R, and Chritensen R B, 1980 *Ap. J.* **240** 956.

INTERACTION OF SUPERNOVA EJECTA 1987A WITH CIRCUMSTELLAR RING

T. Suzuki[†], T. Shigeyama[‡], and K. Nomoto[†]

[†] *Department of Astronomy, University of Tokyo, Bunkyo-ku, Tokyo 113, Japan*
[‡] *Max-Planck Institut für Astrophysik, 8046 Garching bei München, F.R.G.*

Abstract

The ejecta of SN1987A will eventually collide with the surrounding ring discovered by the Hubble Space Telescope. To investigate the hydrodynamical interaction of the ejecta with the ring, we perform 2 dimensional hydrodynamical calculations and estimate the X-ray emission from the free-free transitions of electrons during the first two years since collision.

1. Introduction

A ring was discovered around SN1987A by the Hubble Space Telescope (Jacobsen *et al.* 1991; Panagia 1991). Its radius is $\sim$ 0.6 ly and the inclination is $\sim$45 degree. No detection of UV echo for the first 80 days since explosion is clearly explained by these features of the ring. The physical parameters of this ring such as its position, the electron density, and the total mass have been determined by the modeling of UV echo (e.g., Lundqvist and Fransson 1991). According to Lundqvist and Fransson, the location of the ring is about 5×10^{17} cm from the center of the ejecta, the gas density 4×10^{-20} g cm^{-3}, the total mass $0.03 M_{\odot}$.

The ejecta of SN1987A will collide with this ring in a few years. The collision will convert some of the kinetic energy of the ejecta into thermal energy through shock waves and emit X-ray photons. The emission will provide us with information about the composition of the ejecta, the interaction between the stellar winds at different evolutionary stages of the progenitor, and the origin of the ring. Therefore it is important to investigate the propagation of shock waves in the ejecta, ring and circumstellar matter. We model the ring and its environment assuming an axial symmetry and perform 2 dimensional hydrodynamical calculation by the smooth particle method (Lucy 1977; Gingold and Monaghan 1977; Benz 1989).

We describe our models in the next section. We discuss the shock propagation and X-ray emission in the sections 3 and 4, respectively. Dependencies on the model parameters are discussed in section 5.

2. Models

Our model consists of three parts, the ejecta, the ring, and matter around the ring which is originally the red giant wind from the progenitor. We presume that the blue giant wind have mostly escaped in the polar direction so that the density of the matter confined between the ejecta and the ring is negligibly low. We neglect the initial thermal energy. No gravity is included. We assume that no cooling affects the dynamical behavior and that the ratio of specific heats γ is 5/3 throughout the matter. The abundance we assume is $X = 0.75$, $Y = 0.25$. The number of particles in our calculation is about 3500. Particles have different masses.

(a) *Ejecta* : We take the ejecta model 14E1 (Shigeyama and Nomoto 1990) which is expanding homologously before the collision. At the collision, the velocity, $v_{\rm edge}$, and the density, $\rho_{\rm edge}$, at the leading edge are respectively assumed to be 3×10^9 cm s^{-1} and 4×10^{-22} g cm^{-3}. The density distribution is power law with the index of -8.6 (model 14E1).

(b) *Ring* : The ring is located at 5×10^{17} cm from the center. We assume that the ring has a circular cross section with a 10^{16} cm radius and uniform density of 4×10^{-20} g cm^{-3}; its total mass is $0.03 M_{\odot}$.

(c) *Wind* : The density of the wind is assumed to be constant which is ten times lower than that of the ring. The velocity of the wind is neglected.

The finite time of equipartition of energy between ions and electrons [equation (5-31) in Spitzer (1962)] is taken into account to calculate the temperature of electrons. We then calculate the emission from free-free transitions of electrons.

3. Hydrodynamics

Figure 1 show a time change in the density contour since collision. Three shock waves are seen in Figure 1. In the ejecta, the shock wave is almost stationary propagating at approximately the same velocity as that of the ejecta. Inside the ring, the surface of the shock wave is deformed because the velocity component tangential to the surface of the ring is much reduced through the boundary between the ejecta and the ring. In the red giant wind, the shock wave propagates at $\sim 1 \times 10^9$ cm s^{-1} to accelerate the wind matter to $\sim 7.5 \times 10^8$ cm s^{-1}. The shock fronts deformed around the ring collide with each other behind the ring in $\sim 3 \times 10^6$ s. The contact discontinuity between the ejecta and the wind is also deformed around the ring. Eventually the ring is almost surrounded with the ejecta.

Among the three regions, the highest ion temperature is attained in the ejecta because the temperature behind the shock is proportional to square of the velocity difference through the shock. The shock in the ring arrives at the edge of the opposite side in $\sim$ 1.5 years, which corresponds to the peak of the luminosity from the ring (see the next section).

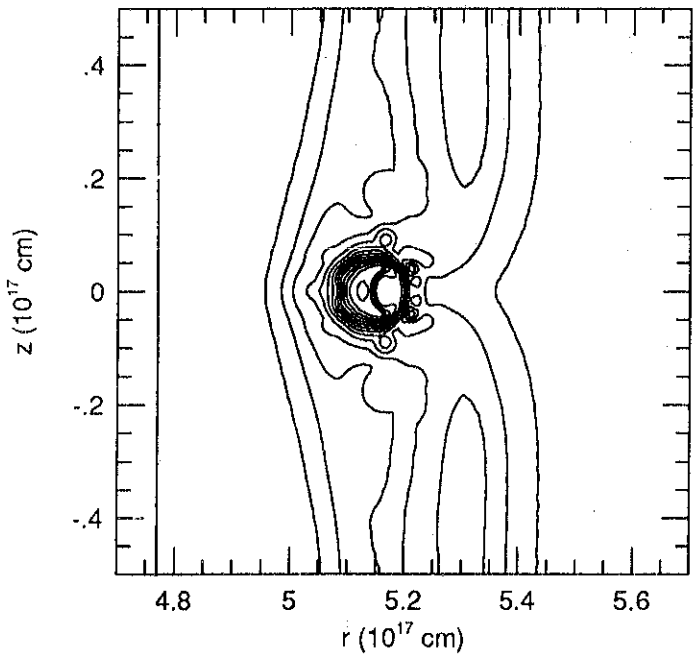

Figure 1. The density contours at $t = 1$ year.

4. Light Curves and Spectra

The X-ray spectra and luminosity are calculated for free-free transitions of electrons. Two peaks appear in the light curve (Figure 2). (The contribution of the matter around the ring is uncertain, because we do not know its occupying solid angle.) The peak luminosity from the ring is about 4×10^{37} erg s^{-1} and its continuum spectrum is the free-free spectrum for the electron temperature of $\sim 2 \times 10^7$ K. (Note that the luminosities from the ejecta in Figure 2 take into account only the calculated region assuming axial symmetry.)

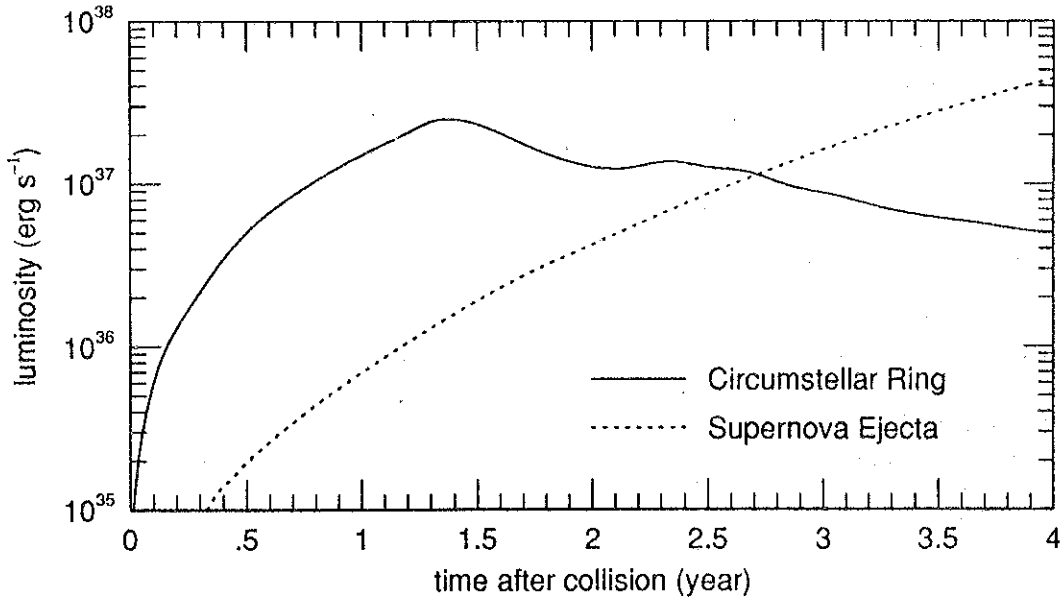

Figure 2. The time changes of luminosities from the ring and ejecta.

5. Discussion

The X-ray emissions from the colliding ejecta and the ring depend on the initial configurations. In the more realistic explosion model, the density at the leading edge of the ejecta is lower at the collision than in the above model. The velocity there would also be lower because of possible deceleration by the blue supergiant wind matter (Itoh *et al.* 1991).

We investigate such a model dependence by assuming that $v_{\rm edge} = 1 \times 10^9$ cm s^{-1} and $\rho_{\rm edge} = 4 \times 10^{-23}$ g cm^{-3}. Because of the smaller $v_{\rm edge}$ and $\rho_{\rm edge}$, the X-ray luminosity increases more slowly and reaches its maximum at ~ 9 years after the collision. Despite the smaller kinetic energy of the ejecta, the peak luminosity from the ring is almost the same as in the previous model. Therefore, X-ray emissions from the collision will be observable with future X-ray Astronomy satellites, from which we can learn the material distribution around the ring.

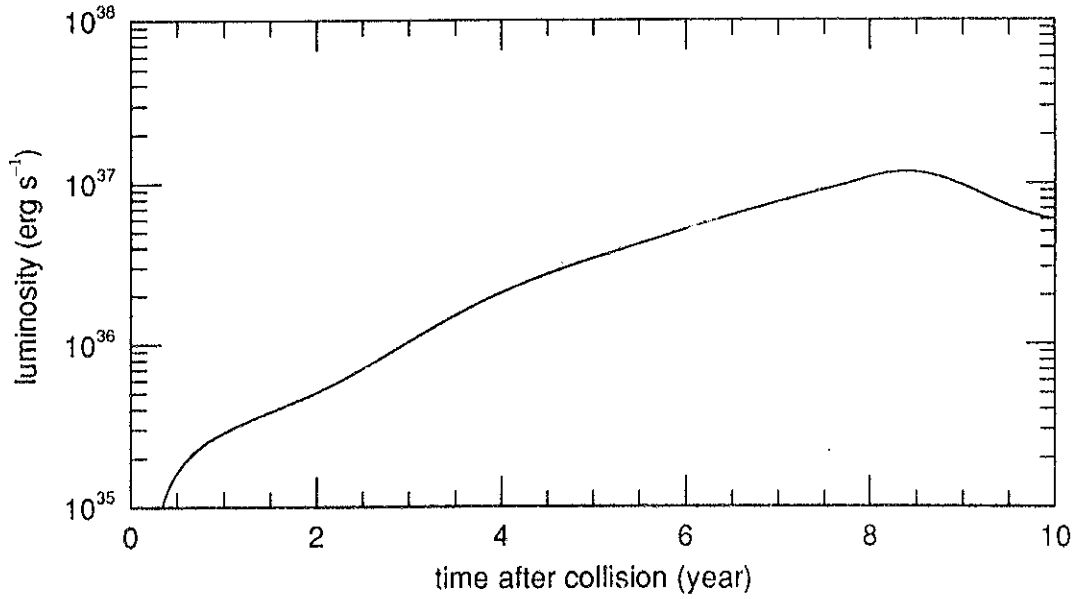

Figure 3. The time changes of luminosity from the ring in the case $v_{\rm edge} = 1 \times 10^9$ cm s^{-1} and $\rho_{\rm edge} = 4 \times 10^{-23}$ g cm^{-3}.

Acknowledgements

We would like to thank H. Itoh, K. Masai, and I. Hachisu for useful discussion.

References

Benz, W., 1989, in "*Numerical Modeling of Non-Radial Stellar Pulsation*", Ed. J. R. Buchler.
Gingold, R. A., Monaghan, J. J. 1977, *Mon. Not. R. astr. Soc.*, **181**, 375.
Itoh, H., Masai, K., Nomoto, K. 1991, in "*Frontiers of X-Ray Astronomy*", Ed. Y. Tanaka and K. Koyama, in press.
Jacobsen, P. *et al.* 1991, *Astrophys. J.*, **369**, L63.
Lucy, L. 1977, *Astron. J.*, **82**, 1013.
Lundqvist, P., Fransson, C. 1991, *Astrophys. J.*, in press.
Panagia, N. 1991, in "*SN1987A and Other Supernovae*", Ed. I. J. Danziger, in press.
Shigeyama, T., Nomoto, K. 1990 *Astrophys. J.*, **360**, 242.
Spitzer, L. Jr. 1962, in "*Physics of Fully Ionized Gases*", p. 135.

Atomic Physics and Plasma Simulation

Kazumi Fujima
Yamanashi University,
Faculty of Engineering

Abstract

A new workshop which connects atomic data for collisional and radiative model and rate-equation is proposed. Features of atomic data base and codes for varieties of atomic models as well as their interface to rate-equation are discussed.

The analysis of an individual atomic process which occurs in hot and dense plasmas is really important for the better understandings of plasmas. Comparison of cross sections of each elementary process can tell which process gives a major contribution for a particular property of plasmas. However, it is inadequate by itself for the quantitative discussion. For example, we can not know how much the process change the portion of ions in a specified state without detailed calculation. An orthodox approach to this problem is to solve what we call rate-equation. That teaches us which channel will open at what plasma parameter. So, every time we find a new interesting mechanism, we have to bring a new state and rates into the rate-equation and to see what will happen. This procedure always requires another crosssection related to the new state.

There are few codes which are now working. They are used as add-in programs of the hydrodynamics of ICF and X-ray laser simulation and so on. Since they are designed for as a special purpose, fast and concise programs are indispensable. This makes them useful at the limited plasma parameters and specific ions such as H and He-like. Generally, there is no need to cover all the atomic date for the various ions and states. The usage of the present rate-equation being so, necessary atomic data can be picked up form handbooks and be written down as data statements

in the computational code. However, these codes are not suitable for our purpose because of the lack of extensibility. So I would like to propose to organize a workshop to prepare a new code of rate-equations which covers the present and future requirement.

The forthcoming computational code should have following characters. First, it can handle many kinds of atomic data or atomic code. This means the code itself includes a function to search necessary atomic data from the database or to calculate by itself. To make this possible, we should find a robust method to check the accuracy, reliability and consistency of the atomic data. Second, the code can be easily enlarged for taking huge number of ion species and charge states into account and reduced for rapid and concise operation. The development of preprocessor of the code may be the solution. Some accessories may also be useful for practical application such as a plasma diagnostics tool. This includes utilities of as averaging the results over azimuthal quantum number of spin multiplicity or states for easy comparison with observed data.

Though these are the preferable features of the code, the resource of the computer is indeed limited. So , we should take a practical design of the code. The collaboration between atomic and plasma physicists in the field is really necessary to make this project work efficiently.

I hope this proposal also has a side effect to activate the communication between atomic physics , plasma physics as well as astrophysics and to stimulate collaboration between these fields.

Analytical Transport Modeling of Divertor Plasma with Radiation Cooling

Michiya Shimada
Japan Atomic Energy Research Institute
Naka-machi, Naka-gun, Ibaraki-ken, Japan 311-01

Abstract

Plasma fluid equations(equations of continuity, pressure balance and heat conduction) of the divertor plasma are solved analytically with the neutral particle. Radiative cooling is also included.

1. Introduction

Divertor models are useful in understanding high density, low temperature divertor plasmas observed in experiments. Analytic divertor models were developed by number of authors. Ohyabu[1] and Mahdavi[2] solved heat conduction equation and pressure balance equation along the field line. Post[3] and Sugihara[4] solved equation of continuity along the field line and demonstrated multiple solutions. Sugihara reproduced the multiple solutions by solving two dimensional plasma transport code coupled with Monte-Carlo neutral transport code. An analytical transport model was proposed[5] to analyze dense, cold and radiative divertor plasma observed in JT-60. In this report, we fully describe the model which solves the three fluid equations (equations of continuity, pressure, and heat conduction) consistently with neutral particle and radiative loss. In addition, the model was improved to include temperature dependence of ionization rate coefficient of hydrogen particles.

2. Analytical Model

2.1 Assumptions

We solve steady state equations of one fluid plasma in one dimension. Effects of momentum loss by charge exchange are neglected. Neutral particles are assumed to have reflection energy given at the divertor plate. These processes neglected in this paper for simplicity might be important for more quantitative comparison with experimental results. The effects of these processes therefore will be discussed in the future work. Omission of these processes, however, should not affect the qualitative features of the discussion.

2.2 Transport Equations

x coordinate is taken along the field line. Suffix 's' corresponds to separatrix point(x = 0). Suffix 'd' corresponds to divertor plate (x=L).

$$\frac{\partial \phi}{\partial x} = S_n \quad \text{----------(2-1)}$$

$$\frac{\partial}{\partial x}\left(2p+mv\phi\right) = S_p \quad \text{----------(2-2)}$$

$$\frac{\partial q}{\partial x} = S_E \quad \text{----------(2-3)}$$

In eq. (2-1), ϕ is the particle flux density along the field line,

$$\phi = nv \quad \text{----------(2-4)}$$

n is plasma density, v is flow velocity, and S_n is particle source.

In eq. (2-2), p is electron pressure,

$$p = nT \quad \text{----------(2-5)}$$

T is plasma temperature, m is ion mass, and S_p is the momentum source, which is neglected in this analysis.

In eq. (2-3), q is heat flux density along the field line,

$$q = -\kappa \frac{\partial T}{\partial x} \quad \text{----------(2-6)}$$

κ is electron heat diffusivity along the field line,

$$\kappa = \kappa_o T^{5/2} \quad \text{----------(2-7)}$$

S_E is the energy source, and convection loss is neglected except at the sheath.

2.3. Boundary conditions

at x = 0 (separatrix point)

$$\phi = \phi_s = \frac{\Gamma_s}{A} \quad \text{----------(3-1)}$$

$$q = q_s = \frac{P_s}{A} \quad \text{----------(3-2)}$$

at x = L (divertor plate),

$$v = v_d = C_{sd} \quad \text{----------(3-3)}$$

$$T = T_d = \frac{P_d}{e\gamma\Gamma_d} = \frac{q_d}{e\gamma\phi_d} \quad \text{---------- (3-4)}$$

In eq. (3-1), ϕ_s is particle flux density from the main plasma, Γ_s is total particle flux from the main plasma,

$$\Gamma_s = \frac{N}{\tau_p} \quad \text{----------(3-5)}$$

N is total number of particles in the main plasma volume, τ_p is particle confinement time of the main plasma, A is effective cross section of the scrape-off layer,

$$A = 2\pi R\, \delta\, \theta \quad \text{---------- (3-6)}$$

R is major radius, δ is scrape-off layer thickness, and θ is pitch of the field line,

$$\theta = \frac{B_p}{B_T} \quad \text{---------- (3-7)}$$

B_p is poloidal field, and B_T is toroidal field.

In eq. (3-2), P_s is total power from the main plasma,

$$P_s = P_{in} - P_{rad} \quad \text{----------(3-8)}$$

P_{in} is input power, and P_{rad} is radiation and charge exchange loss power in the main plasma.

In eq. (3-3), C_{sd} is sound velocity at the divertor plate,

$$C_{sd} = \sqrt{\frac{2eT_d}{m}} \quad \text{----------(3-9)}$$

e is electronic charge.

In eq. (3-4), γ is heat transmission coefficient at the sheath.

2.4. Solution of the transport equations

From eqs. (2-1) and (3-1),

$$\phi = \phi_s + \int_0^x S_n \, dx \quad \text{----------(4-1)}$$

From eqs. (2-2), (2-4), (2-5), (3-3), (3-9),

$$v = \frac{4n_d T_d - 2nT}{m\phi} \quad \text{---------- (4-2)}$$

From eqs. (2-3), (2-6), (2-7),

$$-\frac{2}{7}\kappa_o \frac{\partial}{\partial x} T^{7/2} = q_s + \int_0^x S_E \, dx' \quad \text{---------- (4-3)}$$

By integrating this equation from x to L, we obtain

$$T = \left(T_d^{7/2} + \frac{7}{2\kappa_o} \left(q_s (L-x) + \int_x^L dx \int_0^x S_E \, dx' \right) \right)^{2/7}$$

---------- (4-4)

If S_E can be neglected,

$$T = \left(T_d^{7/2} + \frac{q_s (L-x)}{\frac{2}{7}\kappa_o} \right)^{2/7} \quad \text{---------- (4-5)}$$

2.5. Neutral Transport

$$S_n = n n_o \langle \sigma v \rangle = f_g \, n \, n_{od} \langle \sigma v \rangle \exp\left(- \int_{\theta x}^{\theta L} \frac{d\xi}{\lambda} \right) \quad \text{----- (5-1)}$$

In eq. (5-1), n_o is neutral particle density, f_g is particle reflection coefficient at the divertor plate times the geometrical factor, n_{od} is neutral particle density at the divertor plate, $\langle \sigma v \rangle$ is the ionization rate coefficient of electron impact, ξ is the coordinate normal to the divertor plate($\xi = \theta x$), λ is ionization mean-free-path.

$$n_{od} = \frac{\phi_d \, \theta}{v_{od}} \quad \text{---------- (5-2)}$$

v_{od} is neutral particle velocity, which is assumed to be a function of ion speed accelerated at the sheath.

$$v_{od} = R_E \sqrt{\frac{5eT_d}{m}} \qquad \text{---------- (5-3)}$$

where R_E is the energy reflection coefficient at the divertor plate.

$$\lambda = \frac{v_{od}}{n\langle\sigma v\rangle} \qquad \text{----------(5-4)}$$

With eq. (5-1), (5-4), and (5-2), we obtain

$$S_n = f_g \frac{n_{od}\, v_{od} \quad \exp(-\theta \int_x^L \frac{n\langle\sigma v\rangle dx}{v_{od}})}{\frac{v_{od}}{n\langle\sigma v\rangle}}$$

$$S_n = f_g\, n_{od}\, n\langle\sigma v\rangle \quad \exp(-\frac{\theta}{v_{od}} \int_x^L n\langle\sigma v\rangle dx)$$

$$\int_0^x S_n dx = f_g\, n_{od} \int_0^x n\langle\sigma v\rangle \exp(-\frac{\theta}{v_{od}} \int_x^L n(x')\langle\sigma v\rangle dx')\, dx$$

$$\int_0^x S_n dx = f_g\, \phi_d \left(\exp(-\frac{\theta}{v_{od}} \int_x^L n\langle\sigma v\rangle dx) - \exp(-\frac{\theta}{v_{od}} \int_0^L n\langle\sigma v\rangle dx) \right) \text{ -- (5-5)}$$

In order to evaluate this integral, we find an approximate solution of n. Assuming that v<<Cs, which is valid for most of the divertor volume, we obtain from eq. (4-2),

$$nT = 2n_d T_d \qquad \text{---------- (5-6)}$$

From eqs. (2-4) and (3-4),

$$n_d = \frac{\phi_d}{C_{sd}} = \frac{\phi_d}{\sqrt{\frac{2eT_d}{m}}} \qquad \text{---------- (5-7)}$$

Using eq. (5-7), eq.(5-6) becomes

$$nT = 2 \frac{\phi_d}{\sqrt{\frac{2eT_d}{m}}} T_d = 2 \sqrt{\frac{mT_d}{2e}} \phi_d$$

Using eq. (4-5), we obtain

$$n = \frac{2\sqrt{\frac{mT_d}{2e}}\,\phi_d}{\left(T_d^{7/2} + \frac{q_s(L-x)}{\frac{2}{7}\kappa_o}\right)^{2/7}} \quad \text{---------- (5-8)}$$

which can be integrated.

$\langle\sigma v\rangle$ can be given as a function of electron temperature, T [6]:

$\langle\sigma v\rangle = \alpha_0 + \alpha_1 T + \alpha_2 T^2 + \alpha_3 T^3$ ($3<T<100$ eV), 3×10^{-8} m^3/s ($T>100$ eV)

where $\alpha_0 = -3.5487 \times 10^{-9}$, $\alpha_1 = 1.0847 \times 10^{-9}$,

$\alpha_2 = -1.2032 \times 10^{-11}$, $\alpha_3 = 4.6103 \times 10^{-14}$.

Let us define I(x) by:

$$I(x) = \int_x^L n\langle\sigma v\rangle dx = \int_x^L (\alpha_0 n + \alpha_1 nT + \alpha_2 nT^2 + \alpha_3 nT^3)dx$$

$$= \alpha_0 \int_x^L n dx + nT\left(\alpha_1(L-x) + \alpha_2 \int_x^L T dx + \alpha_3 \int_x^L T^2 dx\right)$$

$$\int_x^L n dx = \frac{\frac{4}{5}\kappa_o}{q_s}\phi_d\sqrt{\frac{mT_d}{2e}}\left(\left(T_d^{7/2} + \frac{q_s(L-x)}{\frac{2}{7}\kappa_o}\right)^{5/7} - T_d^{5/2}\right)$$

---------- (5-9)

$$\int_x^L T dx = \frac{\frac{2}{9}\kappa_o}{q_s}\left(\left(T_d^{7/2} + \frac{q_s(L-x)}{\frac{2}{7}\kappa_o}\right)^{9/7} - T_d^{9/2}\right)$$

$$\int_x^L T^2 dx = \frac{\frac{2}{11}\kappa_o}{q_s}\left(\left(T_d^{7/2} + \frac{q_s(L-x)}{\frac{2}{7}\kappa_o}\right)^{11/7} - T_d^{11/2}\right)$$

Using (5-9), eq. (5-5) becomes

$$\int_0^x S_n dx = f_g\,\phi_d\left(\exp(-\theta\frac{I(x)}{v_{od}}) - \exp(-\theta\frac{I(0)}{v_{od}})\right) \text{---- (5-10)}$$

$$= f_g\,\phi_d\,J(x)$$

where $J(x) = \exp(-\theta\frac{I(x)}{v_{od}}) - \exp(-\theta\frac{I(0)}{v_{od}})$ ---- (5-11)

From eqs.(4-1), (5-10), and (5-11), we obtain

$$\phi = \phi_s + f_g\,\phi_d\,J(x) \quad \text{---------- (5-12)}$$

$$\phi_d = n_d v_d = \frac{\phi_s}{1 - f_g J(L)} \quad \text{---------- (5-13)}$$

$$\phi = \frac{1 - f_g J(L) + f_g J(x)}{1 - f_g J(L)} \phi_s \quad \text{---------- (5-14)}$$

From eqs. (3-1), (3-3), (3-4), (4-5), (5-8) and (5-13), n_s, v_s, T_s, n_d, v_d, T_d can be calculated.

2.6 Radiation Power

The radiative cooling rate was calculated in a manner described as follows[7].

The rate equations of impurity particles with nuclear charge k are given by:

$$-n_e n_0 S_0 + n_e n_1 \alpha_1 + n_n n_1 \beta_1 - \frac{n_0}{\tau_p} = 0$$

$$-n_e n_i S_i + n_e n_{i-1} S_{i-1} + n_e n_{i+1} \alpha_{i+1} - n_e n_i \alpha_i + n_n n_{i+1} \beta_{i+1} - n_n n_i \beta_i - \frac{n_i}{\tau_p} = 0$$

$$(i=1,\ldots,k-1)$$

$$n_e n_{k-1} S_{k-1} - n_e n_k \alpha_k - n_o n_k \beta_i - \frac{n_k}{\tau_p} = 0$$

where n_e is the electron density, n_i is the impurity density with charge i(i=0 means impurity neutral particle), S_i is the rate coefficient for electron-impact ionization from i to i+1, α_i is the rate coefficient for recombination(radiative+dielectronic) from i to i-1, b is the rate coefficient for charge-exchange between hydrogen neutral particles(with density n_n) and ions with charge state i. The last term corresponds to the loss to the divertor plate. The loss rate is assumed to be the same for all the impurity species. All the rate coefficients and radiative cooling rates for each ionization state are calculated using the ADLHAX code developed by R. Hulse[8].

Using this procedure, we calculated the ionization equilibrium as a function of electron temperature, particle recycling time, and neutral particle density. The ionization equilibrium is very much affected by charge exchange recombination[9].

After calculating the ionization equilibrium, radiative cooling rate L(T) was computed.

The volume-integrated radiative power loss can be calculated as following[7]:

$$q = -\kappa_0 T^{5/2} \frac{\partial T}{\partial x}$$

$$\frac{\partial q}{\partial x} = S_E = -n^2 f L(T)$$

where f is impurity concentration and L(T) is radiative cooling rate.

By multiplying these eqs. and by integrating, we obtain

$$\frac{1}{2}(q_s^2 - q_d^2) = \kappa_0 p^2 f \int_{T_d}^{T_s} T^{1/2} L(T) dT$$

where electron pressure and impurity concentration are assumed to be constant along the field line.

By defining a function g,

$$g(T) = 2\kappa_0 \int_0^T T^{1/2} L(T) dT$$

we can calculate the radiation loss power in the divertor consistently with divertor parameters.

$$q_s^2 - q_d^2 = p^2 f (g(T_s) - g(T_d))$$

Figure 1 shows a comparison of two cases; neutral particles 1% of electron density, and with neutral particle density 10% of electron density. For these cases, g factors discussed above is calculated(Fig. 2). These figures indicate that radiative cooling rate is significantly enhanced with particle recycling and charge exchange recombination.

3. Summary

Analytical solution of the divertor fluid equations is presented. The divertor parameters are solved consistently with neutral particles and remote radiative cooling.

Acknowledgement

The author would like to express sincere gratitude to Drs. Y. Shimomura, H. Kishimoto, S. Tamura, T. Iljima, and M. Yoshikawa for continuous support and encouragement. The author appreciates Dr. Russel Hulse for providing them a powerful impurity physics package, which was indispensable in the impurity analysis described in this paper. The author also appreciates Drs. S. A. Cohen and M. Sugihara for fruitful discussion on the neutral particle modelling results. The author appreciates fruitful discussion on divertor models with Drs. R. D. Stambaugh, K. H. Burrell, G.

M. Staebler, and M. Ali Mahdavi in General Atomics and Dr. N. Ohyabu in National Institute for Fusion Science.

Reference

[1] Ohyabu, N., Nucl. Fusion 21 (1981) 519.
[2] Mahdavi, M. A., et al., Phys. Rev. Lett.47 (1981) 1609.
[3] Post, D. E. et al., J. Nucl. Mat. 121 (1984) 171.
[4] Sugihara, M. et al., J. Nucl. Mat. 128 & 129 (1984) 114.
[5] Shimada, M. et al., J. Nucl. Mat. 176 & 177 (1990) 122.
[6] Janev, R. K. et al., "Elementary Processes in Hydrogen-Helium Plasmas", Springer Verlag (1987).
[7] Shimada, M. et al., Nucl. Fusion 22 (1982) 643.
[8] Hulse, R. A. , Nucl. Technology/Fusion 3 (1983) 259.
[9] Hulse, R. A. , et al., J. Phys. B 13 (1980) 3895.

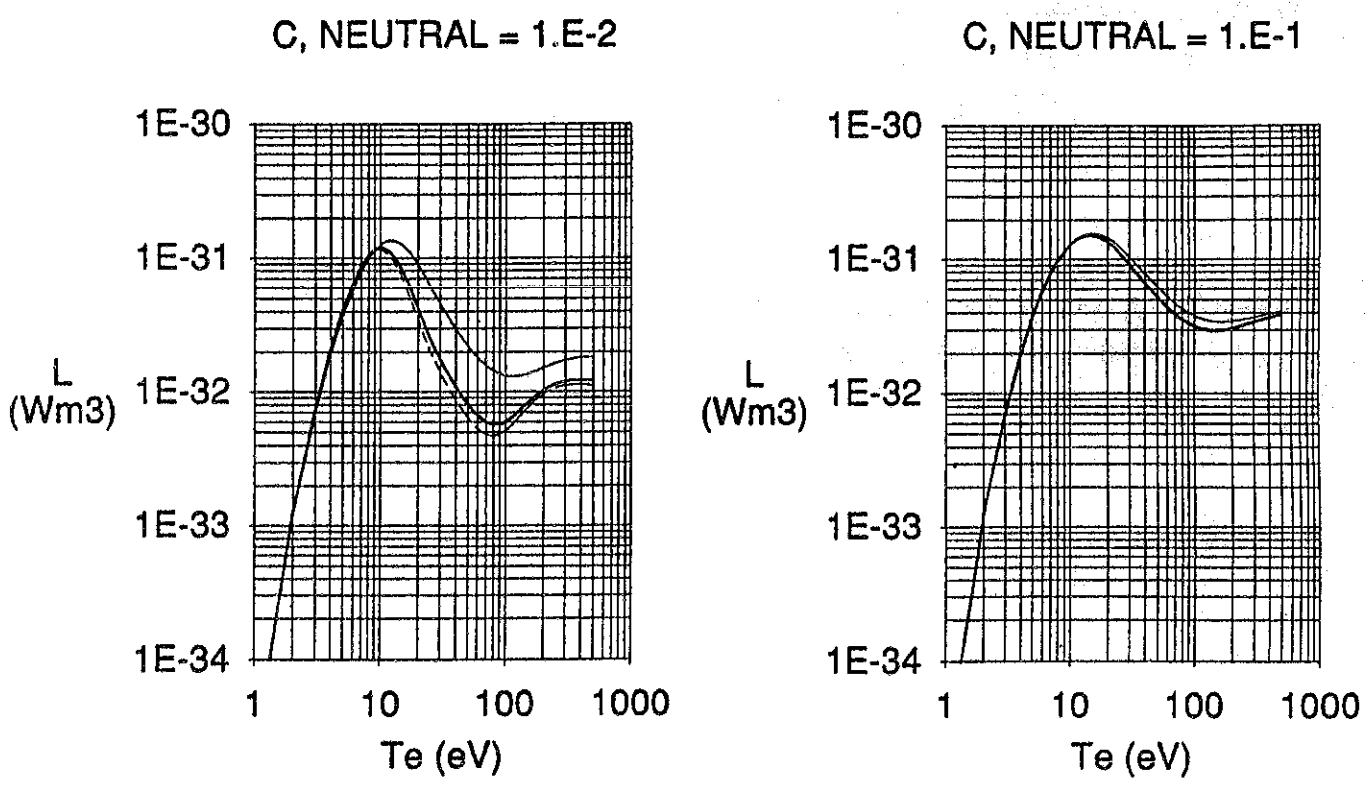

Figure 1. Radiative cooling rate of carbon. (a) neutral particles 1 % of electron density (b) neutral particles 10% of electron density. Three curves represent:dash line: coronal equilibrium, thick line: the product of electron density and particle recycling time $n\tau$ of 10^{17} $m^{-3}sec$, thin line: $n\tau$ of 10^{16} $m^{-3}sec$.

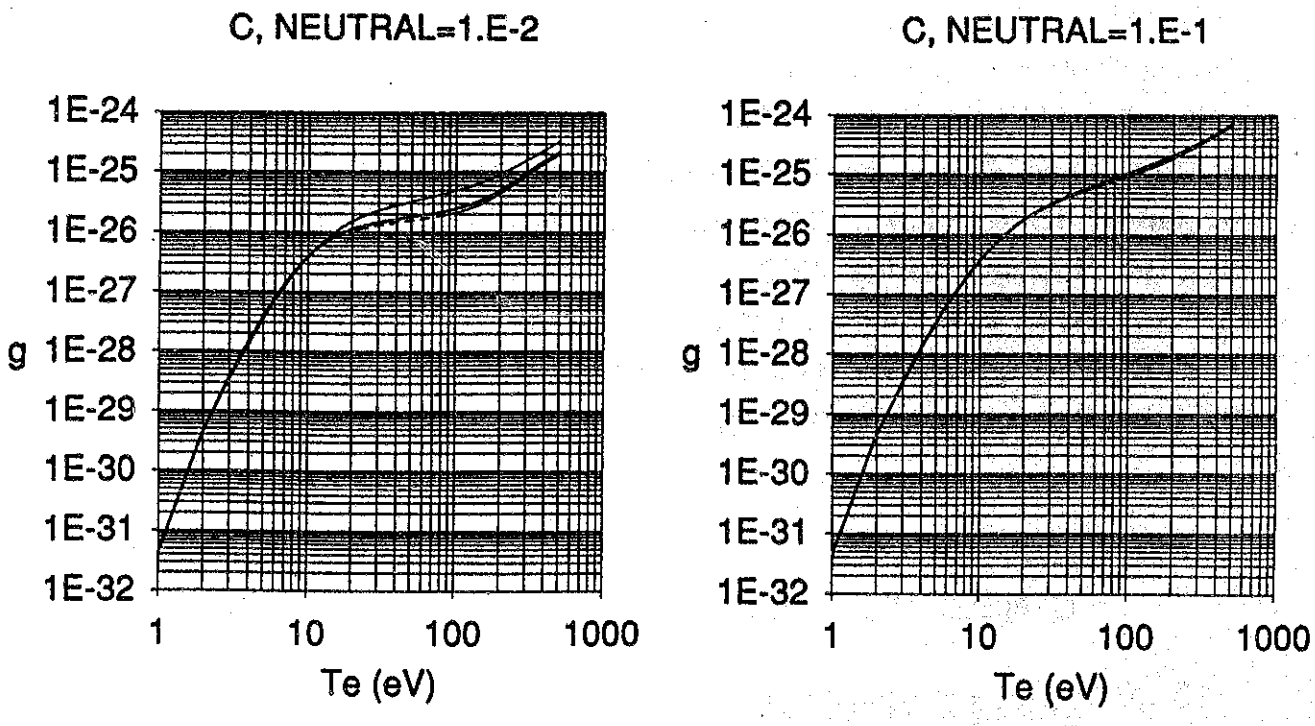

Figure 2. g factor for remote radiative cooling calculation. The same notation was used as in Figure 1.

H_2 AND H_2^+ DENSITIES AT THE PLASMA BOUNDARY

KEIJI.SAWADA and TAKASHI.FUJIMOTO
(Department of Engineering Science,
Kyoto University, Kyoto, Japan)

With regard to recycling of hydrogen in torus and especially to the physics of the H-mode in tokamaks, one of the key issues is what hydrogen species is present in the outer region of these plasmas. We have proposed a method [1] of using the observed intensities of hydrogen emission lines, for example the Balmer series lines, for determination of the electron density, the atomic hydrogen density, and the molecular hydrogen density. We have applied this method to the WT-3 tokamak[2]. The result is shown in Fig.1.

In the above model, the population density of an excited level with principal quantum number p is given by

$$n(p) = R_0(p)n_in_e + R_1(p)n_Hn_e + R_2(p)n_{H2}n_e \qquad (1)$$

where $R_0(p)$,$R_1(p)$,$R_2(p)$ are called the population coefficients, which are solutions of the population balance equation, and n_i, n_H, n_{H2} are the densities of protons, hydrogen atoms and hydrogen molecules, respectively.

Under the condition of an ionizing - phase plasma

like hydrogen in tokamaks, the first term in Eq.(1) dose not contribute to the population density. We have derermined n_e, n_H and n_{H2} from the measured intensities of Balmer α, β and γ lines.

In the above analysis, we have neglected the contribution from the dissociative excitation process of molecular ions. In order to include this contribution another term is included on the right hand side of Eq.(1); i.e., $R_3(p)n_{H2^+}n_e$. It is expected that the p dependence of the dissociative excitation cross section from molecular ion is rather similar to that of the excitation cross section from the ground state atoms ($\propto \tilde{p}^3$) than that of the dissociative excitation cross section of neutral molecules($\propto \tilde{p}^6$). Therefore, the p dependence of $R_3(p)$ is similar to that of $R_1(p)$. If we write $R_3(p) = kR_1(p)$ ($k \approx 10$), the procedure[1] is valid with n_H replaced by ($n_H + kn_{H2^+}$). The ratio n_{H2^+}/n_H is not determined by the present method.

We estimated the ratio n_{H2^+}/n_{H2} as follows.
If the plasma is in a steady state, the amount of molecular hydrogen ions produced in unit time should be equal to that lost. They are produced mainly by

$$e + H_2 \rightarrow e + H_2^+ + e \quad .$$

They are lost mainly by

$$e + H_2^+ \rightarrow H + H^*$$
$$e + H_2^+ \rightarrow H^+ + H^* + e$$
$$e + H_2^+ \rightarrow H^+ + H^+ + 2e \quad .$$

The estimated $n_{H_2^+}/n_{H_2}$ value is about 15% at r=0.21(m). The measured value $(n_H + kn_{H_2^+})/n_{H_2}$ in our experiment is about 3%, too small in comparison with the above estimated value. We are now trying to resolve this discrepancy.

REFERENCES

[1] T.Fujimoto, K.Sawada and K.Takahata, J. Appl. Phys. 66, 2315 (1989)

[2] T.Fujimoto et al, NUCLEAR FUSION, Vol.29,No.9 (1989)

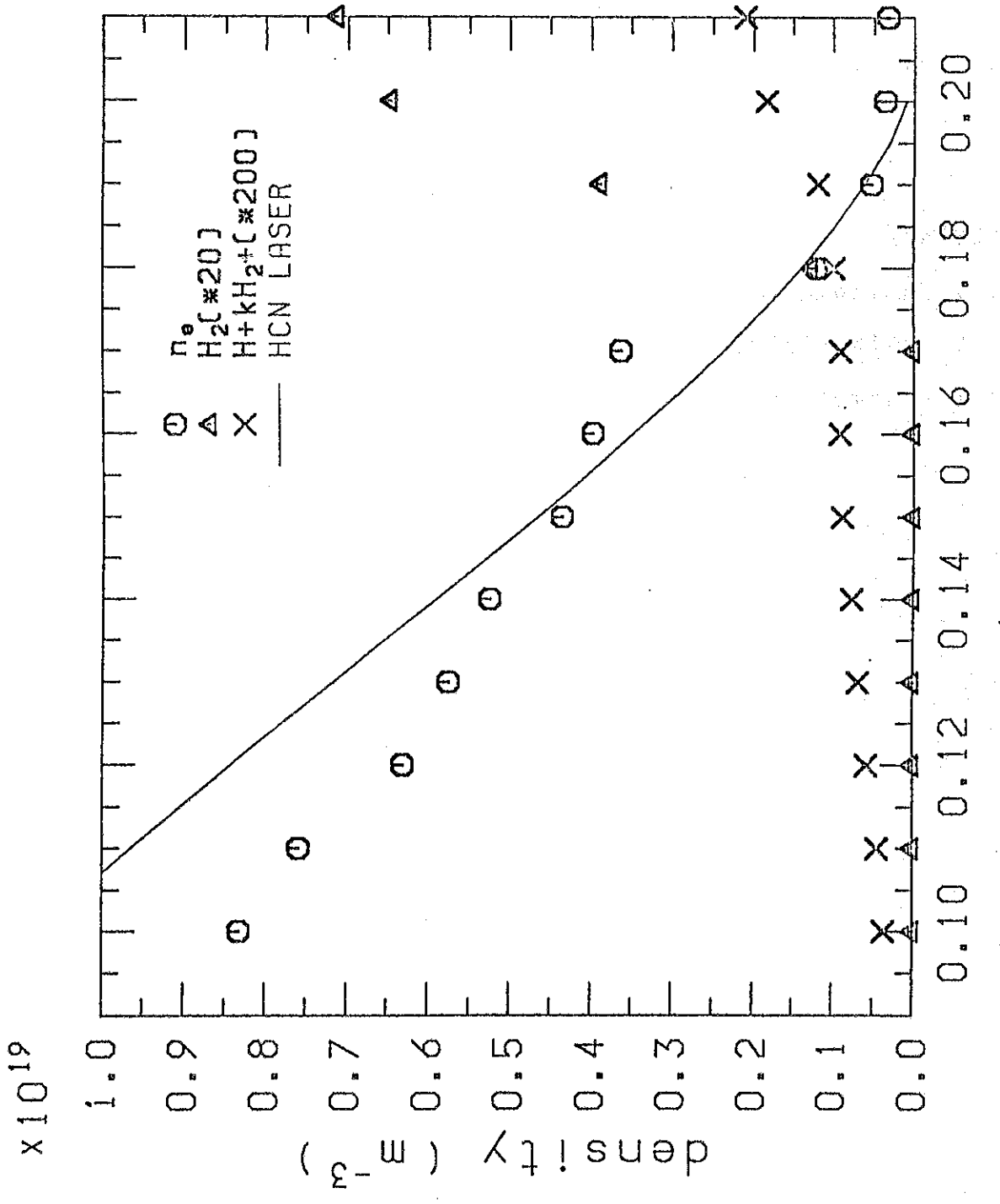
density (m^{-3})
x 10^{19}
1.0
0.9
0.8
0.7
0.6
0.5
0.4
0.3
0.2
0.1
0.0
0.10
0.12
0.14
0.16
0.18
0.20
radius (m)
n_e
H_2(*20)
$H+kH_2^+$(*200)
HCN LASER

Fig.1

COLLISIONAL-RADIATIVE MODEL FOR Li-like ION

TETSUYA KAWACHI and TAKASHI FUJIMOTO
(Department of Engineering Science,
Kyoto University,KYOTO,JAPAN)

Li-like ion is of considerable interest in spectroscopic study of high-temperature plasma like Tokamak. However, the question whether the recombining plasma component can always be neglected in interpreting the obserbed excited-level population has not been answered for these ions. In the case of hydrogen-like ion and, to some extent, helium-like ions this problem has been well established:for ionizing plasma, the recombining plasma component can well be neglected. For the purpose of answering this question in general as well as interpreting experiment, we are now constructing a collisional-radiative model program.

In the following,atomic parameters and the source of numerical data are given.

1 Energy levels

Each of the levels with principal quantum number $n<5$ is considered separately acocording to its angular momentum, and its energy is taken from Grotrian Diagram [1]. Other levels with principal quantum number $n>5$ are treated as screened hydrogen-like levels. The energy level diagram of Li-like oxygen we considered is shown in Fig.1.

2 Spontaneous transition probability

The data by A.Lindgard and S.E.Nielsen (1977)[2] is used for the transitions from higher energy levels to 2s,2p,3s,3p,3d,4s,4p, 4d,4f. For other transitions, the result by Johnson(1972)[3], in which the A coefficient for the neutral hydrogen atom is given, is used.

3 Excitation cross sections and Ionization cross sections

The results by D.H.Sampson (1990)(1981)(1981), in which the collision strength is caliculated by the distorted wave theory [4] or the scaled collision strength is caliculated by the Z= method[5][6], are used for excitations from sublevels 2s,2p,3s,3p, 3d,4s,4p,4d,4f. For excitations from the energy-levels with principal quantum number n>5 , the semi-empirical cross section due to Johnson[3] is used. The results of Sampson is compared with those of others workers in Fig.2.

4 De-excitation and 3 body recombination cross sections

The cross section for de-excitation and 3 body recombination are caliculated from those for excitation and ionization according to the principle of detailed balance.

5 Radiative Recombination cross section

The Z scaled radiative recombination cross section by McLaughlin (1990)[7] is used.

The result of the present collisional-radiative caliculation will appear soon.

(REFERENCE)

[1] S.Bashkin and J.O.Stoner,Jr.
Department of Physics.Univ.of Arizona(1978)

[2] A.Lindgard, S.E.Nielsen
Atomic Data and Nuclear Data table 19,533-633 (1977)

[3] L.C.Johnson
Astrophysical Journal 174,227-236 (1972)

[4] H.L.Zhang, D.H.Sampson, C.J.Fontes
Atomic Data and Nuclear Data table 44,31-77 (1990)

[5] R.E.H.Clark, D.H.Sampson, S.J.Goett
The Astrophysical Journal Suppl. 49,545-554 (1981)

[6] L.B.Golden, R.E.H.Clark, S.J.Goett, D.H.Sampson
The Astrophysical Journal Suppl. 45,603-612 (1981)

[7] D.J.McLaughlin, Yukap Hahn
Physical Review A 43,1313-1323 (1990)

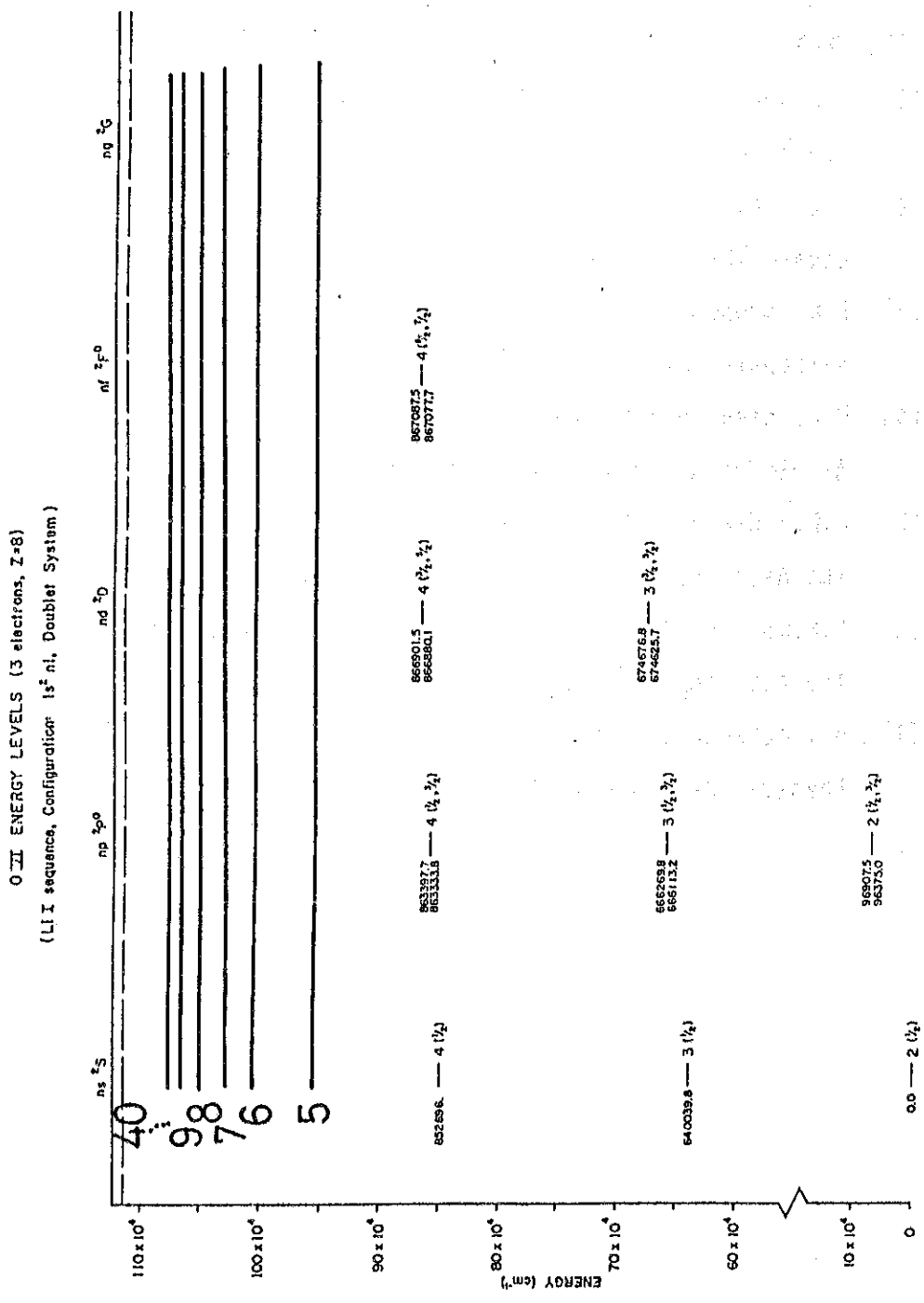
O III ENERGY LEVELS (3 electrons, Z=8)
(Li I sequence, Configuration 1s² nl, Doublet System)
ENERGY (cm⁻¹)
110 x 10⁴
100 x 10⁴
90 x 10⁴
80 x 10⁴
70 x 10⁴
60 x 10⁴
10 x 10⁴
0
ns ²S
np ²P°
nd ²D
nf ²F°
ng ²G
852896. — 4 (½)
8633927.7
8633333.8 — 4 (½, 3/2)
8669015
8668801 — 4 (½, 3/2)
8670875
8670777 — 4 (½, 3/2)
640039.8 — 3 (½)
6662698
6661132 — 3 (½, 3/2)
6746768
6746625.7 — 3 (½, 3/2)
0.0 — 2 (½)
969075
963750 — 2 (½, 3/2)
40
9 8
7 6
5

Fig. 1

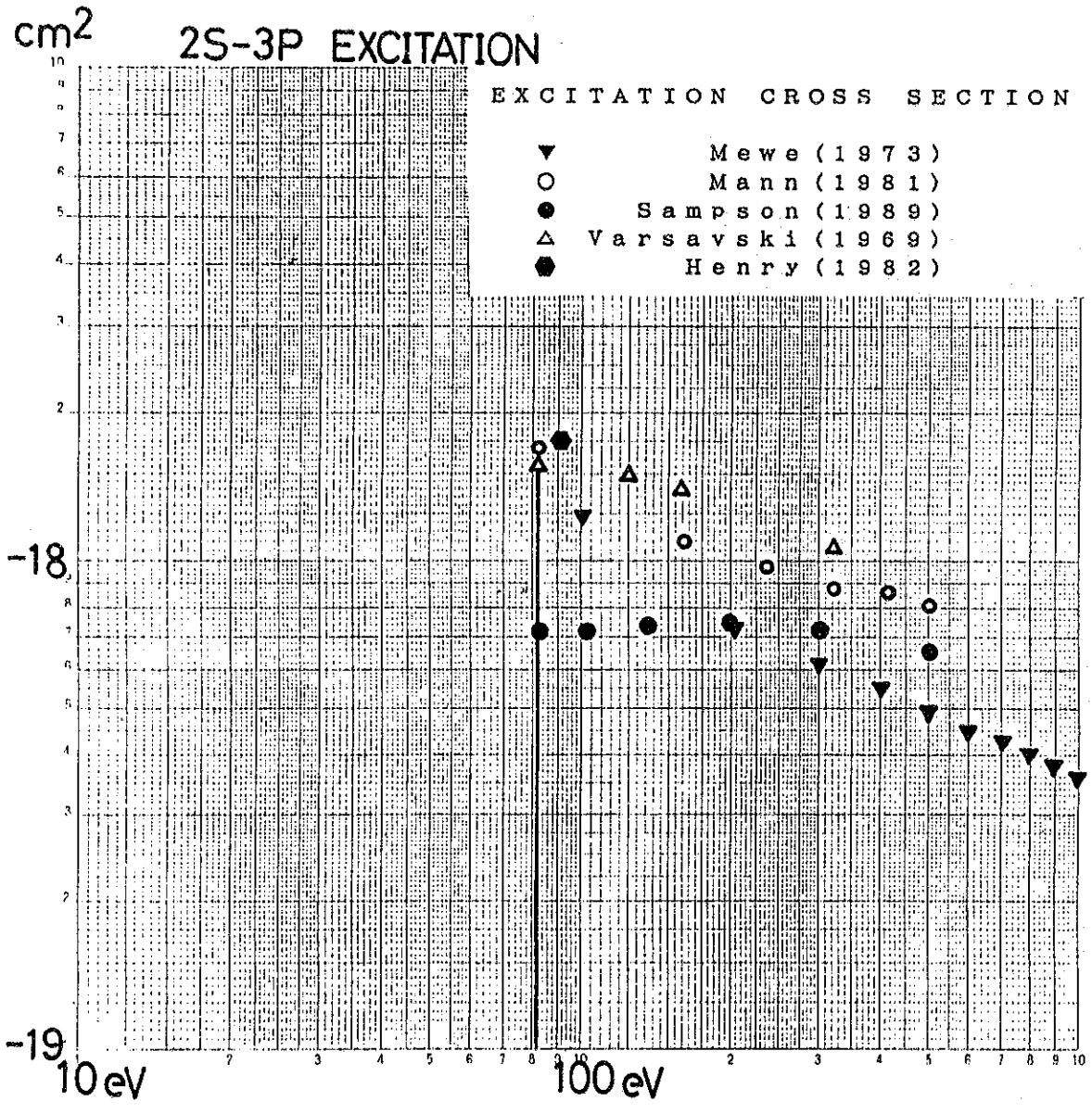
cm2
2S-3P EXCITATION
EXCITATION CROSS SECTION
Mewe (1973)
Mann (1981)
Sampson (1989)
Varsavski (1969)
Henry (1982)
-18
-19
10 eV
100 eV

Fig. 2

Recent Issues of NIFS-PROC Series

NIFS-PROC-1 *U.S.-Japan Workshop on Comparison of Theoretical and Experimental Transport in Toroidal Systems Oct. 23-27, 1989* ; Mar. 1990

NIFS-PROC-2 *Structures in Confined Plasmas –Proceedings of Workshop of US-Japan Joint Institute for Fusion Theory Program–* ; Mar. 1990

NIFS-PROC-3 *Proceedings of the First International Toki Conference on Plasma Physics and Controlled Nuclear Fusion –Next Generation Experiments in Helical Systems– Dec. 4-7, 1989* ; Mar. 1990

NIFS-PROC-4 *Plasma Spectroscopy and Atomic Processes –Proceedings of the Workshop at Data & Planning Center in NIFS–*; Sep. 1990

NIFS-PROC-5 *Symposium on Development of Intensed Pulsed Particle Beams and Its Applications*; Oct. 1990

NIFS-PROC-6 *Proceedings of the Second International TOKI Conference on Plasma Physics and Controlled Nuclear Fusion , Nonlinear Phenomena in Fusion Plasmas -Theory and Computer Simulation-;* Apr. 1991

NIFS-PROC-7 *Proceedings of Workshop on Emissions from Heavy Current Carrying High Density Plasma and Diagnostics;* May 1991

NIFS-PROC-8 *Symposium on Development and Applications of Intense Pulsed Particle Beams, December 6 - 7, 1990;* Jun. 1991